PhD degree in Molecular Medicine (curriculum in Molecular Oncology)

European School of Molecular Medicine (SEMM),

University of Milan and University of Naples "Federico II"

Settore disciplinare: BIO/10

Molecular implications of Afadin and Aurora-A–mediated phosphorylation of NuMA in spindle orientation

Manuel Carminati

European Institute of Oncology (IEO), Milan

Matricola n. R10333

Supervisor: **Dr. Marina Mapelli**

European Institute of Oncology (IEO), Milan

Internal Advisor: **Prof. Giorgio Scita**

IFOM, The FIRC Institute of Molecular Oncology, Milan

External Advisor: **Prof. Neil Q. McDonald**

The Francis Crick Institute, London

Anno accademico 2015-2016

TABLE OF CONTENTS

GLOSSARY

ABL1	Ableson Leukemia Kinase-1
ACD	Asymmetric Cell Division
AJ	Adherens Junction
BD	Binding Domain
Caco-2	Human Colorectal Adenocarcinoma Cells
CC	Coiled-Coil
CDK1	Cyclin-Dependent Kinase 1
Coot	Crystallographic Object-Oriented Toolkit
DIC	Differential Interference Contrast Microscopy
Dlg	Disc Large
DMSO	Dimethyl Sulfoxide
Dvl	Dishevelled
ECM	Extracellular Matrix
F-actin	Filamentous Actin
FRAP	Fluorescence Recovery After Photobleaching
FRET	Fluorescence Resonance Energy Transfer
Fz	Frizzled Receptor
GEF	Guanine Nucleotide Exchange Factors
GL2	Luciferase
GoLoco	G Alpha (i/o) - Loco
GSH	Glutathione Sepharose
GTP/GDP	Guanosine Triphosphate/Diphosphate
$G\alpha_i$	The Alpha Subunit Of Adenyl-Cyclase-Inibitory Heterotrimeric G Protein
HEK293t	Human Embryonic Kidney 293 Cells
HeLa	Human Cervical Cancer Cells
hTERT-RPE-1	Human Telomerase-Immortalized Retinal Pigment Epithelial Cell Line
ISC	Intestinal Stem Cell
Lgl	Lethal Giant Larvae
LGN	Leu-Gly-Asn Repeat-Enriched Protein
MDCK	Madin-Darby Canine Kidney Cells
MT	Microtubule
NB	Neuroblast
NLS	Nuclear Localization Signal
NuMA	Nuclear Mitotic Apparatus
Par	Partitioning-Defective
PHENIX	Phyton-based Hierarchical Environment for Integrated Crystallography
Pins	Partner of Inscuteable
Plk1	Polo-Kinase-1
Ran	Ras Related Nuclear Protein
RCC1	Regulator Of Chromosome Condensation
Ric8A	Resistance To Inhibitors Of Cholinesterase 8
RNAi	RNA Interference
S2	*Drosophila* Shneider-2 Embryonic Cells
SEC	Size Exclusion Chromatography
shRNA	Short-Hairpin RNA
SLK	Ste20-Like Kinase
SOP	Sensory Organ Precursor
+TIPs	Microtubule Plus-End Tracking Proteins
TPR	Tetratrico-Peptide Repeats

INDEX OF FIGURES

ABSTRACT

Oriented cell divisions contribute to tissue morphogenesis and homeostasis. Planar divisions occurring with the spindle within the epithelial plane enlarge sheets and tubules, while asymmetric cell divisions with the spindle aligned to the apico-basal polarity axis sustain differentiation programs. Several pathways have been involved in establishing correct spindle orientation, both in cultured cells and *in vivo*. Most of these pathways impinge on the evolutionarily conserved $G\alpha_i$/LGN/NuMA complexes that orient the spindle by generating pulling forces on astral microtubules (MTs), via direct interaction of NuMA with the *MT-motors* Dynein/Dynactin.

My PhD projects focused on the molecular mechanisms underlying the spindle orientation function of Afadin, and on the relevance of NuMA phosphorylation by Aurora-A for spindle orientation.

During planar cell divisions, $G\alpha_i$/LGN/NuMA assemblies are restricted to the lateral cortex, for molecular reasons that are still unclear. Studies conducted during this thesis indicate that LGN interacts directly with the junctional and F-actin binding protein Afadin, and define the TPR domain of LGN (hereon LGN^{TPR}) and a C-terminal peptide of Afadin ($Afadin^{PEPT}$) as the minimal interacting regions retaining micromolar binding affinity. The crystal structure of the LGN^{TPR}-$Afadin^{PEPT}$ fusion protein shows that the $Afadin^{PEPT}$ threads along the LGN^{TPR} superhelix with opposite chain directionality, similarly to what observed for LGN in complex with other ligands, including NuMA. Consistently, we provided evidence that Afadin competes with NuMA for binding to LGN. Afadin knock-down in HeLa cells leads to reduced LGN cortical levels, and unexpectedly also to complete loss of cortical NuMA and Dynein/Dynactin, and hence spindle misorientation. Importantly, we discovered that Afadin interacts concomitantly with F-actin and LGN *in vitro*. Furthermore, we showed that loss of Afadin impairs correct cystogenesis of Caco-2 cells, suggesting that it plays essential functions in epithelial planar cell divisions. Altogether our data suggest a model whereby in metaphase Afadin mediates cortical

recruitment of Dynein/Dynactin, by targeting LGN at the lateral cortex via direct and concomitant interaction with LGN and with cortical F-actin. Later, LGN engages with NuMA and Dynein/Dynactin to exert pulling forces on the mitotic spindle. Thus, Afadin represents the first described mechanical anchor between the acto-myosin cell cortex and the Dynein/Dynactin *MT-motors.*

Besides being spatially regulated, the cortical recruitment of $G\alpha_i$/LGN/NuMA is timely controlled by mitotic kinases coordinating spindle orientation with mitotic progression. It was reported that the activity of the mitotic kinase Aurora-A is required for correct spindle orientation in human cells in culture, and that NuMA is among its phosphorylation targets. However, whether NuMA is phosphorylated directly by Aurora-A and how molecularly its kinase activity affects spindle orientation was still unknown when we started our studies. Analyses in HeLa and RPE-1 cells revealed that, in metaphase, depletion or inhibition of Aurora-A leads to aberrant accumulation of NuMA at the spindle poles and loss from the cortex, despite LGN localizes normally at the cortex. FRAP experiments revealed that Aurora-A governs the dynamic exchange between the cytoplasmic and the spindle pole-localized pools of NuMA. Our experiments *in vitro* and in cells showed that Aurora-A phosphorylates directly three serine residues on the C-terminus of NuMA, and mutation of Ser1969 into alanine recapitulates the aberrant polar accumulation of NuMA and the spindle orientation defects observed upon Aurora-A inhibition. Thus we concluded that phosphorylation on Ser1969 of NuMA by Aurora-A controls NuMA distribution between the spindle poles and the overlying cortex, and allows proper spindle orientation. Intriguingly, Ser1969 lies within a previously characterized microtubule (MT)-binding domain. However, *in vitro* co-sedimentation and bundling assays revealed that the binding affinity of NuMA for MTs is unaltered by Aurora-A-mediated phosphorylation, suggesting that unphosphorylated NuMA accumulates at spindle poles via a receptor other than MTs. Most interestingly, with our experiments we also identified a new MT-binding domain of

NuMA positioned downstream of the LGN binding motif. This result is consistent with our finding that NuMA can simultaneously interact with LGN and MTs. Based on these data, we propose that in metaphase the MT-binding activity of NuMA may contribute to anchor astral MT +TIPs at cortical sites together with LGN.

1 INTRODUCTION

1.1 Oriented cell divisions in development

During development and adult life, oriented divisions shape epithelial architecture contributing to both tissue formation and homeostasis. Oriented divisions imply an active process whereby the mitotic spindle aligns along a specific axis, determined by cellular polarity, generally inherited by the epithelial tissue in which the cell is embedded. Epithelial polarity is set up via antagonizing forces between the apical Par3/Par6/aPKC polarity complex (referred to as Par proteins hereon) and baso-lateral Scribble/Dlg/Lgl proteins. The orientation of the mitotic spindle with respect to the apico-basal axis determines whether the outcome of the cell division is symmetric (SCD) or asymmetric (ACD). In prototypic SCDs the spindle is positioned perpendicularly to the apico-basal axis, so that the cytosolic content is equally partitioned, and two daughter cells with identical cellular content will be generated upon cytokinesis (Fig. 1a, top). Conversely, in ACDs the spindle becomes aligned along the apico-basal axis, producing two cells with unequal inheritance of cytoplasmic components, ultimately following a different fate (Fig. 1a, bottom). ACDs occur only in stem cells and are particularly relevant for a process known as stem cell self-renewal, in which upon division one cell retains stemness while the other one becomes committed to differentiation. Stem cells can also divide via proliferative symmetric divisions to amplify the stem cell pool. The right balance between stem cell ACDs and SCDs ensures proper combination of proliferation with differentiation, which is essential for tissue development and homeostasis. Indeed, deregulation of stem cell proliferation via aberrant SCDs in *Drosophila* neuroblasts (NBs) results in brain tissue overgrowth with tumor-like phenotype [1]. Oriented SCDs contribute to the maintenance of tissue integrity by orienting the mitotic spindle within the plane of the epithelial sheet, a process known as planar cell division (see paragraph 1.1.2). The relevance of planar cell division for proper tissue maintenance came from recent studies in the *Drosophila* cuboidal follicle epithelium, the columnar embryonic ectoderm, and the pseudostratified

neuroepithelium. In these epithelia, ectopic expression of the stem cell-specific adaptor Inscuteable (Insc) induces aberrant ACDs, thus generating cells that are positioned outside of the epithelium upon cell division. Surprisingly, live imaging studies revealed that these cells are readily reintegrated into the cell layer, through a mechanism dependent on lateral adhesions [2]. In support to the role of planar SCDs in maintaining epithelial integrity, depletion of epithelial junctions in the *Drosophila* imaginal discs leads to cell delamination and cell death [3]. Consistently, blocking apoptotic pathways in misaligned cells is sufficient to induce the formation of tumor-like masses.

The molecular mechanisms underlying ACDs' execution have been a matter of long debate. In the case of *intrinsic* ACDs, stem cells polarize cell-autonomously and daughter cells acquire different fates by inheriting unequal cytoplasmic components. In other cases, the external tissue instructs stem cell polarity, in particular by contacts with cellular microenvironments known as *niches*. In this case, unequal partitioning of *niche* contacts, determined by the orientation of the division, defines differential positioning of daughter cells and results in differential fate. These types of oriented divisions are commonly referred to as *extrinsic* ACDs [4, 5]. The concept of *niche* is defined as a "specific anatomic location that regulates how stem cells participate in tissue regeneration, maintenance and repair" [6].

One of the most studied adult stem cell *niche* in vertebrates is the base of intestinal crypts, likely because of its high rate of regeneration. Intestinal stem cells (ISCs) localize at the bottom of the crypts interspersed with Paneth cells that work as *niche* (Fig. 1b). The restriction of Paneth cells to the base of the crypts has been ascribed to repulsion forces occurring between EphrinB1 and its receptor EphB3 [7]. More recently, ablation of the adherens junction protein Afadin has been shown to cause mislocalization of Paneth cells leading to stem cell overproliferation [8]. In fact, Paneth cells are responsible for the generation of a Wnt3 gradient, which is crucial to maintain stemness limited to the crypt base (Fig. 1b). In general, the Wnt pathway has emerged as a major short-range

morphogen driving tissue formation via stem cell regulation (see paragraph 1.2.3). Importantly, experiments carried out in isolated ES cells demonstrated that Wnt3a-ligand-coated beads were able to induce orientation of the mitotic spindle perpendicular to the bead, suggesting that localized Wnt-signaling is sufficient to reorient stem cell divisions. In this *in vitro* system, after cytokinesis the daughter cell proximal to the Wnt bead expressed pluripotency genes, while the more distal one showed hallmarks of differentiation [9].

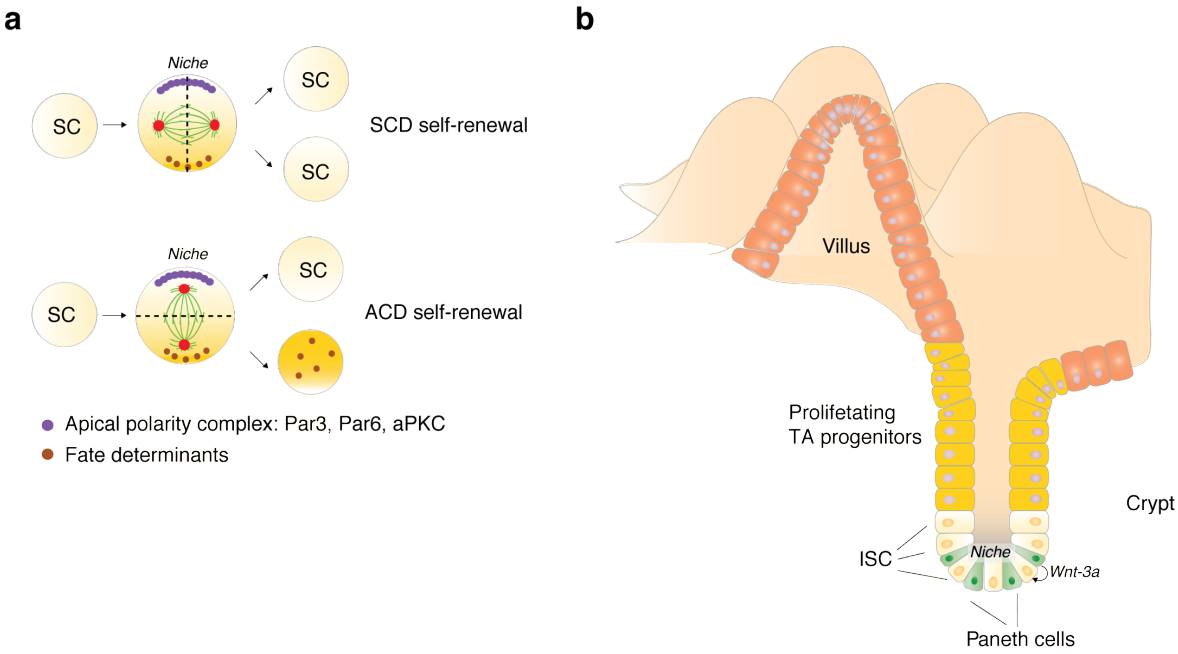

Fig. 1. Oriented cell divisions sustain tissue morphogenesis and integrity. a) Scheme of asymmetric versus symmetric self-renewing stem cell divisions. In SCDs (top) stem cells proliferate by equally distributing cellular components between the two daughter cells, generating two stem cells. In ACDs (bottom) self-renewal is attained by unequal partitioning of *fate determinants* and niche contacts, so that only one cell retains stemness (pale yellow) while the other one is committed to differentiation (gold). The mitotic spindle is in green, while spindle poles are depicted in red. A dashed line indicates the plane of the cell division. **b)** The small intestine is formed by a monolayered epithelium folding into villi and crypts. At the crypt base, ISCs intercalate with Paneth cells (green) secreting Wnt ligands and thus acting as *niche*. Upon proliferation ISCs move upward along the crypt wall, experience reduced Wnt-signals, and differentiates into transit-amplifying (TA) progenitors. TA progenitors, in turn, differentiate into the variety of cells populating the villi to replace the epithelial cells, which are shed into the intestinal lumen at the villus tip.

In the next two paragraphs I will describe how oriented cell divisions are attained in different cellular systems and contexts, via combination of intrinsic and external cues.

1.1.1 Spindle orientation in asymmetric cell divisions

Much has been learnt about the molecular bases of ACDs in invertebrate systems such as *Drosophila* neuroblasts (NBs, the stem cells of the central nervous system), *Drosophila* sensory organ precursors (SOPs, the stem cells of the peripheral nervous system), and the *Drosophila* germ line stem cells (GSC). For a summary of proteins involved in ACDs, and the nomenclature, please see Table 1.

Drosophila	**Vertebrates**
Pins	LGN
$G\alpha_i/G\alpha_o$	$G\alpha_i$
Mud	NuMA
Canoe	Afadin
Insc	mInsc
Bazooka	Par3
Par6	Par6
aPKC	aPKC ζ/ι/λ
Dlg	Dlg1
Dsh	Dvl1/2/3

Table 1. Spindle orientation proteins in flies and in vertebrates.
Orthologs of proteins involved in spindle orientation and in cell polarity in vertebrates, and in *Drosophila melanogaster.*

In all these systems, spindle coupling to polarity cues is attained through cortical recruitment of Dynein/Dynactin-based *microtubule-motors (MT-motors),* assembled on $G\alpha_i$/LGN/NuMA complexes (Fig. 3) (described in paragraph 1.2.1). Cortical clustering of *MT-motors* connected to astral-MTs results in the generation of pulling forces on the spindle, through the MT-minus-end directed motion of Dynein. While force generation mechanisms are evolutionarily conserved, the localization of Par proteins and of *MT-motors* in dividing cells, and their distribution between daughter cells is strongly system and context-dependent. *Drosophila* NBs, after delamination from the neuroepithelium,

give rise to one self-renewing NB that remains attached to the epithelial layer, and to one ganglion mother cell (GMC) producing either two neurons or glial cells (Fig. 2a). *Drosophila* NBs are the prototype of *intrinsic* ACDs, which are executed in a cell-autonomous manner. After cell division, Par proteins (Bazooka/Par6/aPKC) are retained by the NB stem cell, while the set of molecules called *fate determinants* such as Prospero, Numb and Brat are confined into the differentiating cell [10]. In this system, the *MT-motors* built on $G\alpha_i$/Pins/Mud complexes (the fly counterpart of $G\alpha_i$/LGN/NuMA) segregate with Par proteins into the NB, through the action of the adaptor protein Insc, which binds physically to both Bazooka [11] and Pins [12]. In fact, in this system, loss of Insc [10] or of Mud/Pins [13, 14] compromises spindle coupling to the polarity axis, and hence the asymmetric outcome of the division.

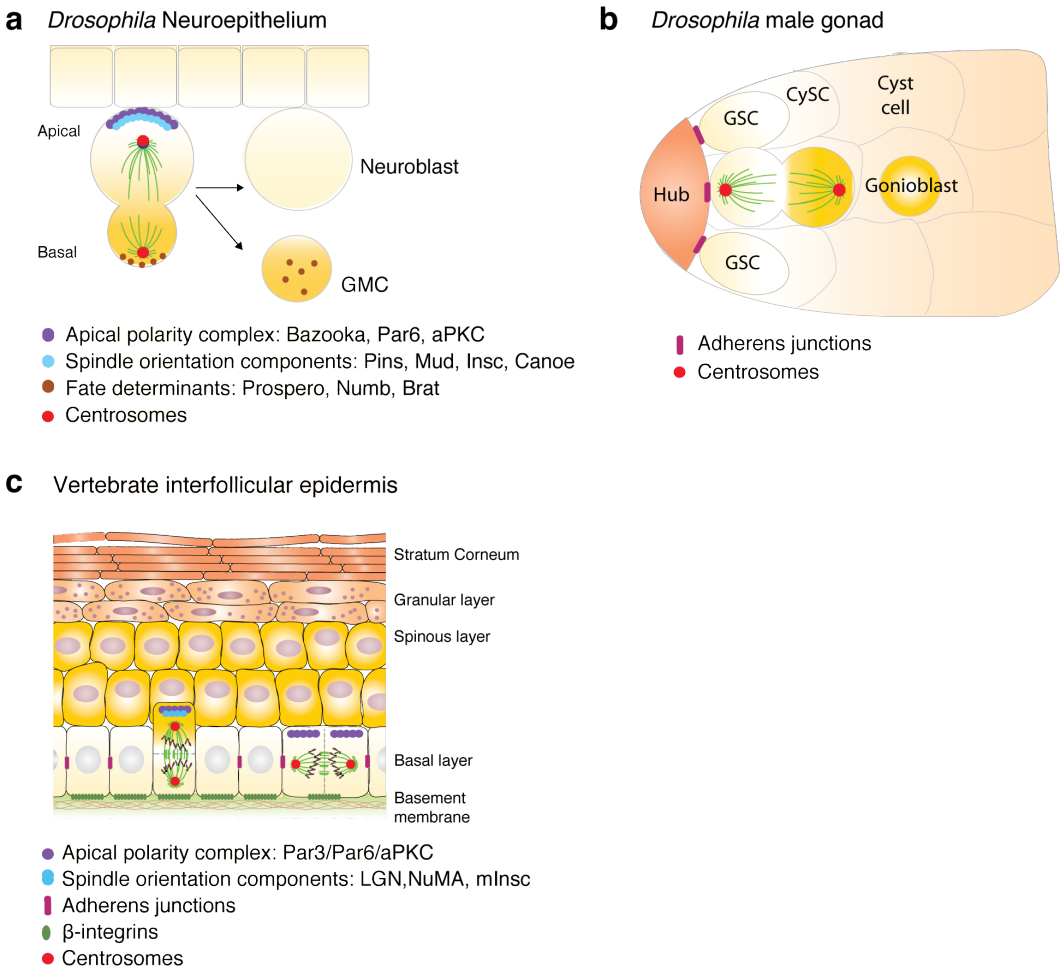

Fig. 2. Spindle orientation in model systems of ACD. a) Intrinsic ACDs of *Drosophila* neuroblasts delaminated from the neuroepithelium generating two differently sized daughters: one neuroblast and one ganglion mother cell (GMC). The larger neuroblast, that maintain stemness, inherits the apical Baz/Par6/aPCK polarity complex (purple crescent), and the spindle orientation proteins Pins, Mud, $G\alpha_i$, Inscuteable, and Canoe (cyan crescent). The smaller GMC inherits *fate determinants* (brown dots) that activate a neuronal differentiation program. **b)** *Drosophila* male GSCs divide asymmetrically producing one stem cell contacting the *niche* (Hub) through adherens junctions (magenta rods), and a distal daughter differentiating into a gonioblast and positioned among somatic cyst cells. **c)** During development, murine epidermal progenitors balance ACDs and SCDs to stratify the skin. Basal progenitors adhere to the basement membrane (*niche*) through β-integrins (green), and to neighboring cells through adherens junctions (magenta rods). These contacts and the apical localization of the Par complex Par3/Par6/aPKC (purple dots) define the progenitor apico-basal polarity. Vertical ACDs (left) occur with the spindle aligned to the apico-basal polarity axis, and generate a basal progenitor and a differentiating suprabasal cell inheriting Par3, Insc, LGN and NuMA (cyan dots). Planar SCDs expand the basal progenitor pool (right).

Like NBs, *Drosophila* germ-line stem cells (GSCs) achieve self-renewal by ACDs. However in this case, fate asymmetry is not cell-autonomous, but relies on the influence of a *niche* called "Hub". In the male gonad, GSCs adhere through E-cadherins to the Hub cells, which activate Jak-STAT signaling in the nearby cells [15] (Fig. 2b). As GSCs cells divide with their spindle perpendicular to the Hub, cells maintaining contact with the *niche* will retain stemness, while the distal ones will differentiate into a gonioblast.

The influence of the proximity to a *niche* has been reported also for vertebrate ACDs. It is worth mentioning that although the role of Par proteins in coordinating cellular polarity with the spindle axis is a common feature throughout evolution, and the players involved in spindle orientation are often conserved, transferring the molecular knowledge acquired in invertebrates to vertebrate systems has proven difficult. One of the best-characterized vertebrate systems dividing asymmetrically is the stem cell compartment of the developing murine skin. During embryonic development, murine basal skin progenitors exist as a monolayer attached to a basement membrane (Fig. 2c). Being rich in growth factors and in extracellular matrix (ECM) ligands, the basement membrane is assumed as *bona fide niche.* Skin progenitors are attached to the basement membrane via integrins, and

connected to one another by E-cadherins. This configuration establishes their apico-basal polarity, with Par proteins apically restricted. At the early stages of skin development, until day E10, the progenitors divide planarly with their spindle parallel to the basement membrane to enlarge the stem-cell pool and to expand the epithelium (Fig. 2c, right). At a later stage, to allow skin stratification, progenitor divisions switch to vertical with their spindles perpendicular to the basement membrane (Fig. 2c, left). As a result, one cell remains in the basal layer as a basal progenitor, while the other one is displaced in the suprabasal layer, and differentiates in a Notch-dependent manner [16]. In skin progenitors, the molecular mechanism underlying the switch from planar SCDs to vertical ACDs relies on the apical localization of mInsc (the mammalian ortholog of Insc), LGN, NuMA, and Dynein/Dynactin (Fig, 2c, cyan crescent) [17]. Consistently, ablation of LGN, NuMA or Dynactin in asymmetrically dividing progenitors by *in utero* electroporation, reverted perpendicular divisions and prevented skin stratification [16]. A more recent study in the same system reported that the kinase aPKCλ is also essential for setting the correct balance between SCDs and ACDs throughout epidermal embryonic development [18].

1.1.2 Spindle orientation in symmetric cell divisions

As already mentioned, planar cell divisions orient the mitotic spindle within the plane of an epithelium. The mechanisms underlying these oriented divisions have been extensively studied in both isolated cells and in tissues. A model system widely used to study polarized SCDs in monolayered epithelia consists of three-dimensional cultures of MDCK and Caco-2 cells. These 3D-cultures grow as monolayered spheres by planar cell divisions, in which the apical side of cells faces the inner hollow lumen [19-21]. A more simple system to study basic mechanisms of orientation in symmetrically dividing cells, regardless of cortical polarity, are HeLa cells plated on fibronectin coverslips, where the mitotic spindle aligns to a fibronectin-coated substrate, in a β1-integrin dependent manner [22] (Fig. 8a). A plethora of studies exploiting these models of SCDs indicated a prominent role of LGN

and NuMA in maintaining proper spindle orientation. In metaphase, LGN is recruited at the plasma membrane by interaction with $G\alpha_i$ subunits, and targets to the membrane Dynein/Dynactin motors through NuMA [23, 24] (Fig. 3). Accordingly, knock-down of NuMA prevents cortical enrichment of Dynein/Dynactin and randomizes the spindle. Furthermore, overexpression of either LGN or $G\alpha_i$ causes excessive spindle oscillations and misoriented divisions [23, 25], indicating that appropriate levels of $G\alpha_i$/LGN/NuMA are required for correct spindle orientation. Intriguingly, as explained in more detail in paragraph 1.4.2, studies in HeLa cells showed that Ran-GTP prevents cortical enrichment of LGN and NuMA above the metaphase plate, thus confining their localization to the regions of the cortex above the spindle poles [26] (Fig. 10a, left). In chick neuroepithelial cells dividing planarly, $G\alpha_i$/LGN/NuMA complexes localize in an equatorial cortical belt [27], while LGN is enriched at the lateral cortex of mitotic cells in MDCK cysts, where its depletion causes spindle misorientation and defective cystogenesis [20]. How LGN becomes restricted at the lateral cortex during vertebrate planar cell divisions (Fig.3) is not known. Studies in MDCK cysts revealed that the kinase aPKC prevents apical localization of LGN by phosphorylating its linker domain on Ser401. Upon phosphorylation, recruitment of 14-3-3 proteins would displace multiple $G\alpha_i$ subunits from LGN, thus excluding it from the apical cortex [19]. As will be discussed in paragraph 1.2.2, the interaction with the baso-lateral protein Dlg1 (Dlg in *Drosophila*) has been shown to mediate lateral recruitment of LGN in chick neuroepithelium [28] and in *Drosophila* follicular epithelium [29]. However, whether these are the only cortical cues targeting LGN at the lateral cortex of planar mitoses remains an open issue.

1.2 Mitotic spindle orientation pathways

In both ACDs and SCDs, cells respond to specific cues that instruct spindle orientation by influencing the distribution of the Dynein/Dynactin motors, which in turn capture the plus-ends of astral MTs to exert pulling forces on the spindle poles towards the cortex. Stimuli

instructing spindle orientation derive from intrinsic factors, such as membrane associated proteins localizing in specific cortical domains, from cell geometry, as well as from extrinsic signals including growth factors, cell-matrix contacts, and cell-cell contacts [30]. Different pathways responsible for the recruitment of *MT-motors* convey external and intrinsic cues to the mitotic spindle, all impinging on the common $G\alpha_i$/LGN/NuMA assembly.

1.2.1 Structural organization of the $G\alpha_i$/LGN-dependent spindle orientation machinery

The core components of the force generating machinery pulling on astral MTs are trimeric complexes formed by the Dynein/Dynactin interactor NuMA (Nuclear Mitotic Apparatus), the switch protein LGN (Leu-Gly-Asn repeat-enriched protein) and the $G\alpha_i$ subunit of the heterotrimeric G proteins (Fig. 3). Notably, FRET-based studies demonstrated that LGN behaves as a conformational switch that in interphase is held in an inactive closed conformation by a head-to-tail interaction between its N-terminal and its C-terminal domains [25] (Fig. 4a, right). The domain structure of LGN consists of eight N-terminal tetratricopeptide-repeats (TPRs) and of four GoLoco motifs at the C-terminus, joined by a linker region of about 100 residues (Fig. 4a). At mitotic entry, LGN is targeted to the plasma membrane by direct interaction of its C-terminal GoLoco motifs (LGN-GoLoco) with multiple $G\alpha_i$-GDP subunits, whose myristoyl group inserts into the phospholipid bilayer. The N-terminal TPR region of LGN (LGN^{TPR} hereon) acts as cortical receptor for NuMA, which after nuclear envelope breakdown is released into the cytoplasm, and recruits Dynein/Dynactin to the cortex, resulting in the generation of pulling forces on the spindle [23] (Fig. 3). Importantly, structural studies revealed that LGN-GoLoco associates exclusively with the GDP-loaded form $G\alpha_i$ [31, 32], acting as guanine dissociation inhibitor (GDI). Timely regulation of the assembly of active $G\alpha_i$/LGN/NuMA/Dynein complexes at the cortex involves a non-canonical G-protein pathway, whereby $G\alpha_i$

dissociates from Gβ/γ by action of a guanine exchange factor (GEF), and a localized pool of $G\alpha_i$-GDP forms to bind LGN. The GEF Ric-8 catalyzes the release of GDP from isolated $G\alpha_i$ subunits, thus limiting the concentrations of $G\alpha_i$-GDP molecules available for interacting with LGN-GoLoco. Ric-8 has been implicated in asymmetric cell division execution in *Drosophila* [33] and in *C. elegans* [34], as well as in symmetrically dividing HeLa cells, where its depletion reduces cortical localization of *MT-motors* and causes spindle misorientation [24]. As $G\alpha_i$-GDP localizes uniformly at the cortex, what restricts the localization of LGN/NuMA above the spindle poles is still unclear [25, 27, 35].

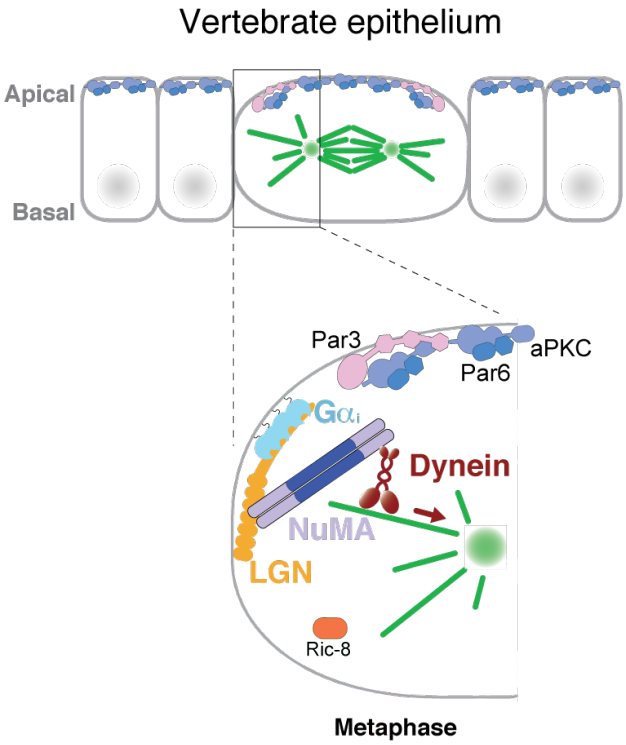

Fig. 3. The evolutionarily conserved spindle orientation machinery built on $G\alpha_i$/LGN/NuMA complexes. Model of the spindle orientation machinery at work in dividing vertebrate epithelial cells, where cortical polarization is established by apical distribution of the conserved Par3/Par6/aPKC complex. Cortical trimeric $G\alpha_i$/LGN/NuMA assemblies are required to orient the mitotic spindle by anchoring astral MTs to the cell cortex. At mitotic entry, LGN (depicted in orange) is targeted to the plasma membrane by direct interaction of its C-terminal GoLoco motifs with multiple $G\alpha_i$-GDP subunits (cyan), whose myristoyl group inserts into the phospholipid bilayer. The N-terminal TPR region of LGN acts as cortical receptor for NuMA (violet), which after nuclear envelope breakdown is released into the cytoplasm, and recruits Dynein (shown in

brown) to the cortex. The minus-end directed movement of Dynein/Dynactin generates pulling forces on the astral MTs, ultimately resulting in spindle positioning towards $G\alpha_i$/LGN/NuMA lateral crescents. The GEF Ric-8 (dark orange) controls the timely activation of the $G\alpha_i$/LGN/NuMA by catalyzing the release of GDP from isolated $G\alpha_i$ subunits.

During asymmetric division, a crosstalk exists between the $G\alpha_i$/LGN/NuMA complexes and apical Par proteins, mediated by mInsc. Such link has been documented in fly NBs by genetic and imaging studies [10, 14]. Similarly, imaging analyses in murine skin progenitors dividing vertically revealed that Par proteins, mInsc, NuMA, and LGN colocalize in a crescent above the apical spindle pole to orient the mitotic spindle along the apico-basal axis [17] (Fig. 2c, cyan spheres). Based on this evidence, a simple spindle orientation model has been proposed in which Par proteins/Insc/LGN/NuMA and Dynein would be part of the same macromolecular complexes (Fig. 2a,c). Nevertheless, more recent biochemical and structural data with mammalian and insect proteins showed that mInsc/Insc and NuMA are competitive interactors of LGN/Pins [12, 36] (Fig. 5), thus challenging the model of a single macromolecular complex. LGN and Pins share the same domain structure, although Pins has only three GoLoco motifs instead of four (Fig. 4a). TPR motifs consist of a couple of antiparallel α-helices termed A and B connected by a short turn. They stack to one another creating arrays of repeats, which form superhelical scaffolds (Fig. 4b, top). LGN^{TPR}/$Pins^{TPR}$ show distinct structural features compared to the canonical TPR motifs. First, the fourth TPR-repeat of both $Pins^{TPR}$ and LGN^{TPR} presents an insertion between helices A and B (Fig. 4b, bottom), resulting in a longer repeat that distorts the superhelix by an outward displacement with respect to the helical axis [12, 36, 37] (Fig. 4b, top). Second, the presence of a set of asparagines, belonging to the invariant *NLGN* motifs, within the αA-helices of each TPR generates an asparagine ladder providing a docking ridge for LGN/Pins ligands [12] (Fig. 4b).

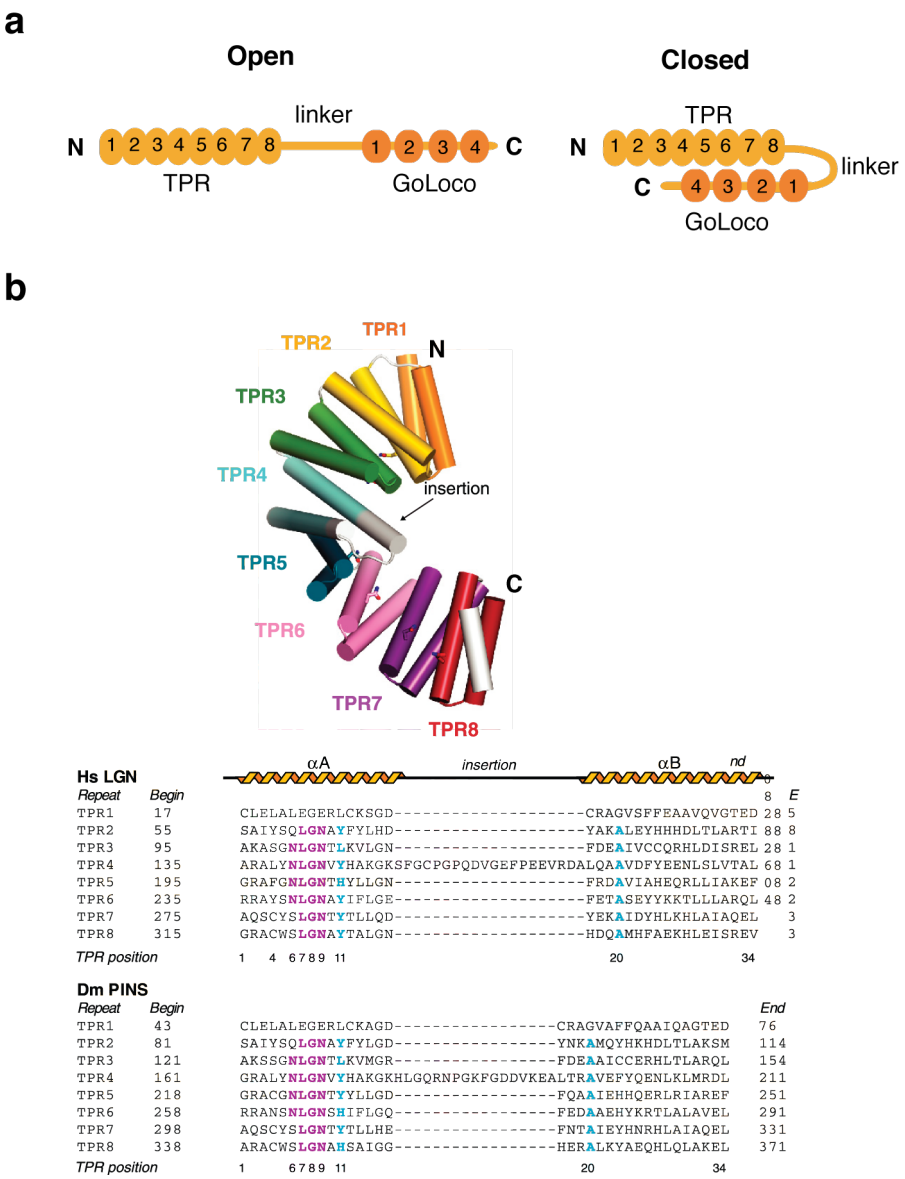

Adapted from Culurgioni, S., Proc. Natl. Acad. Sci. USA 2011

Fig. 4. Peculiar architecture of the TPR motifs of LGN/Pins. a) Domain structure of the full-length LGN with the eight N-terminal TPRs represented in bright orange, and the four C-terminal GoLoco motifs in darker orange. LGN is active in the open conformation (left), while the N- and the C-terminus engage in a head-to-tail arrangement to inhibit its activity in interphase (right). **b)** Top. Cartoon representation of the architecture of LGN^{TPR}. Each TPR motif is shown in a different color, and consists of two antiparallel α-helices shown as cylinders. The invariant asparagines within the *NLGN* motifs are shown in sticks. Bottom. Structure-based alignment of the TPR sequences of LGN and Pins. The insertion between the A and the B α-helices of TPR4 is visible in both proteins. The *NLGN* motifs in the A α-helices are shown in purple, while the conserved hydrophobic residues conforming to the canonical TPR consensus are depicted in cyan.

Because of these peculiarities, LGN^{TPR}/$Pins^{TPR}$ are endowed with a structural versatility in binding to diverse target proteins. Despite sharing very low sequence similarity (Fig. 5e), LGN/Pins ligands including mInsc [37], Insc [12], NuMA [36], Frmpd1/4 [38, 39], and the LGN-GoLoco itself [40] dock to the same surface of the TPR domain, within the inner concave groove formed by the TPRs' A α-helices (Fig. 5a-d, bottom). The crystal structures of LGN^{TPR}/$Pins^{TPR}$ in complex with Insc, mInsc, and NuMA show that all the fragments of the LGN interactors are about 32-40 residues long and thread along the internal surface of LGN^{TPR} with an extended conformation and with opposite chain directionality (Fig. 5 a-c). The LGN-GoLoco3-4 fragment behaves differently, as it binds only partially to the extended surface of the LGN superhelix, with two out of five key residues conserved with the other LGN ligands (Fig 5d,e). Due to the similarity in LGN-binding, these interactors are all competitive ligands of LGN [12, 36]. In particular, mInsc and NuMA compete for the binding to LGN with mInsc displaying a five-fold higher affinity compared to NuMA. In the same study, the preferential binding of mInsc has been confirmed in the presence of full-length LGN/$G\alpha_i$ [12]. The higher binding affinity displayed by mInsc is reflected in its more extended interaction surface as compared to the other proteins in complex with LGN. In fact, NuMA, and LGN-GoLoco3-4 contact only TPRs 1-6 or TPRs 5-8 respectively (Fig. 5c,d), while Insc/mInsc, besides binding to the core TPRs 1-6 module, further extend on TPR6-8 with an N-terminal α-helix that strenghtens the interaction (Fig. 5a,b). Structure-based sequence alignment of the LGN-binding peptides from Insc (residues 303-340), mInsc (residues 23-58), NuMA (residues 1900-1928) and the mouse LGN-GoLoco3-4 peptide (residues 618-632), suggests that the key residues involved in the interaction are conserved (Fig. 5e), although the overall sequences share little similarity.

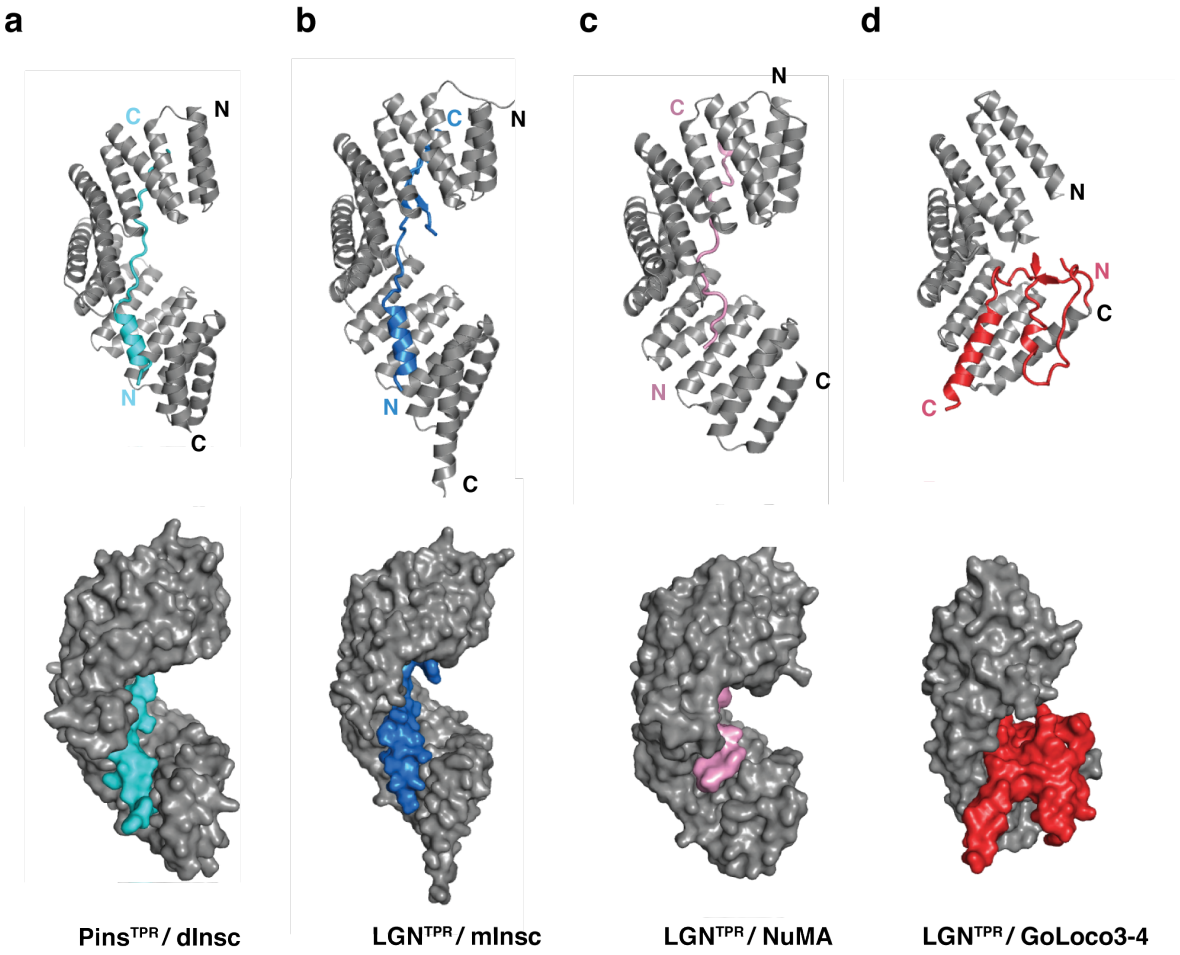

e

Dm Insc	303	KHPEPVASWMSEQRWAGEPEVMCTLQH-KSIAQEAYK	340
Hs Insc	23	MQVDSVQRWMEDLKLMTECECMCVLQA-KPISLEEDA	58
Hs NuMA	1900	NSFYMGTC---QDEPEQLDDWNR-IAELQQRNR	1928
Hs LGN-GoLoco	632	QSRLILSFF--------DEDPVT----------	618

Fig. 5. Architecture of Pins^{TPR}/LGN^{TPR} in complex with its ligands. a) Cartoon (top) and surface (bottom) representation of the Pins^{TPR}/Insc$^{303-340}$ complex (PDB ID 4A1S). Pins is shown in gray, while Insc in cyan. **b)** LGN^{TPR}/mInsc$^{23-69}$ complex (PDB ID 3SF4) where LGN is show in gray, whereas mInsc in blue. **c)** Topology of LGN^{TPR}/NuMA$^{1900-1928}$ (PDB ID 3RO2), with the NuMA peptide shown in pink. **d)** LGN^{TPR} in complex with GoLoco$^{593-651}$ (PDB ID 4JHR). The GoLoco fragment encompasses the 3rd and the 4th GoLoco motif, and is shown in red. **e)** Structure-based sequence alignment of the LGN^{TPR} interactors. The conserved residues involved in the binding to LGN are highlighted in red.

Thus all LGN ligands are competitive interactors, with Insc displaying the highest affinity, followed by NuMA and by LGN-GoLoco3-4 [12, 36, 40]. Such a hierarchy of binding affinities seems to be crucial for the temporal and spatial regulation of spindle orientation.

In fact, besides competing with each other, mInsc and NuMA are both capable of displacing LGN-GoLoco from LGN^{TPR} into an LGN^{TPR}/LGN-GoLoco reconstituted complex [12, 25], meaning that they play a role in the opening of the head-to-tail interaction holding LGN in the inhibited state. In contrast, it has been reported that the activation of full-length LGN/Pins in cells requires the synergistic binding of NuMA/Mud and several $G\alpha_i$ subunits [41], suggesting that the linker of LGN contributes to strengthen the intra-molecular interaction keeping LGN in the closed conformation. Biochemical and imaging studies showed that in *Drosophila* NBs, $G\alpha_i$ binds to the first GoLoco motif to recruit Pins at the apical cortex without opening it, but rather priming the molecule for subsequent cooperative binding of other $G\alpha_i$ subunits and Mud to GL2-3 and to $Pins^{TPR}$, respectively [42]. As the determinants involved in LGN^{TPR}/$Pins^{TPR}$ binding are conserved, designing mutants on either Insc or NuMA aimed at uncoupling their role in the opening of the LGN-switch might be a challenge. The competitive interaction observed for mInsc and NuMA to bind LGN^{TPR} argues against the hypothesis whereby mInsc is the molecular bridge recruiting $G\alpha_i$/LGN/NuMA complexes to the apical cortex in asymmetric mitoses. Thus, how Insc contributes to oriented apico-basal division still remains unexplained. Another question arising from the current model is how $G\alpha_i$/LGN/NuMA complexes remain restricted at the apical site in ACDs. As will be described in the next paragraph, in *Drosophila* NBs cortical Dlg interacts with the phosphorylated linker of Pins, thus providing an apical anchorage independent of the Insc/Par complex [43]. In addition, as will be introduced in paragraph 1.3.3, the F-actin binding protein Canoe (Afadin in vertebrates) may serve a similar purpose, thus keeping $G\alpha_i$/Pins/Mud at the apical cortex to orient the mitotic spindle along the apico-basal axis [44].

1.2.2 The Dlg/LGN pathway

The polarity protein Dlg has been implicated in spindle orientation in the *Drosophila* follicular epithelium and in the vertebrate neuroepithelium, through a mechanism relying

on its direct binding with LGN/Pins. In flies, the direct interaction between Dlg and Pins depends on Aurora-A-mediated phosphorylation on Ser436 of the Pins linker. The relevance of the Dlg/Pins interaction has been investigated in the so-called "induced cell polarity system" in *Drosophila* S2 cell-doublets, developed by Johnston and colleagues [43]. In this system, fusion to the cell-cell junction protein Echinoid is used to localize a protein/domain of choice to the contacts between clustered cell pairs. Then, the orientation of the spindle axis compared to the cell-cell junction domain is measured. In particular, by fusing phosphorylated Pins to Echinoid (Ed-Pins) the authors monitored the spindle orientation with respect to the Ed-Pins cortical enrichment, and found the existence of an Aurora-A/Pins-Linker/Dlg spindle orientation pathway that captures astral MT plus-ends through the kinesin Khc-73. The same authors showed that this pathway works synergistically with $G\alpha_i$/Pins/Mud to drive mitotic spindle orientation in metaphase. In *Drosophila* epithelial cells such as SOP and the ovary follicular ones, Dlg regulates Pins localization. Indeed, in SOP cells Dlg localizes and restricts Pins at the anterior cortex to generate asymmetric planar cell divisions [45]. On the other hand, in the follicular epithelium, Dlg classical baso-lateral localization at septate junctions instructs lateral distribution of Pins, thus inducing symmetric planar cell divisions [29]. The crystal structure of the guanylate kinase (GK) domain of Dlg1 in complex with phospho-Ser401 LGN peptide (Fig. 6a) [46] supports the evidence that LGN/Dlg1 interaction is conserved in vertebrates [47], even though in this case *in vitro* experiments indicate that LGN Ser401 might be phosphorylated by aPKC [19, 46]. Consistent with a role of Dlg1 in driving planar spindle orientation also in vertebrates (Fig. 6b), its depletion in chick neuroepithelium and HeLa cells causes a reduction of LGN cortical levels and spindle misorientation [28]. However, as already mentioned in paragraph 1.1.2, the phospho-Ser401-LGN lateral distribution in MDCK planar mitoses seems to rely on a mechanism of exclusion from the apical cortex, rather than being actively instructed by Dlg1.

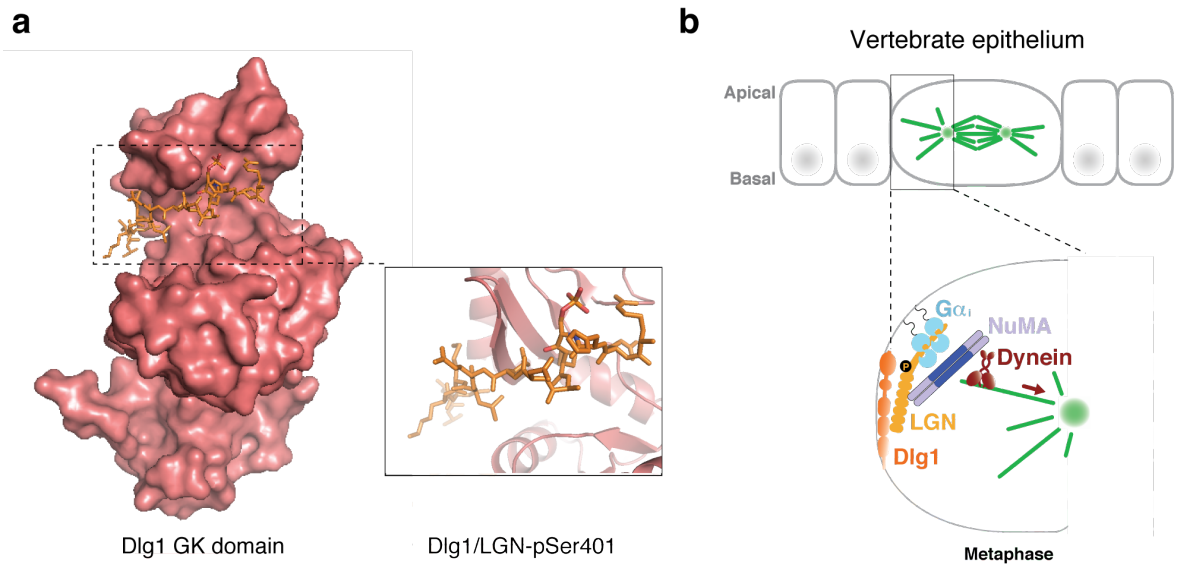

Fig. 6. Role of the Dlg1/LGN^{linker} interaction in vertebrate planar mitoses. a) Crystal structure of the GK domain of Dlg1 in complex with a phospho-Ser401 peptide of the LGN linker (PDB ID 3UAT). The entire Dlg1 GK domain is in in pale red surface representation, while the LGN peptide is in bright orange sticks (left). At right is a close-up view of the interaction, with Dlg1 shown in cartoon. **b)** Cartoon model depicting the proposed role for Dlg1 in anchoring LGN at the lateral cortex of epithelial cells in metaphase. Upon aPKC/Aurora-A-mediated phosphorylation of Ser401 on the LGN linker, cortical Dlg1 recruits LGN, which in turn bind to NuMA/Dynein to generate pulling forces on the spindle.

1.2.3 The Dishevelled/NuMA pathway

Spindle orientation responds to the combination of intrinsic and external cues. The role of signal transduction pathways governing cell growth and differentiation in determining the orientation of cell division has been documented for the Wnt [48], the Hippo [49, 50] and the EGFR signaling [51]. Two different branches of the Wnt signaling exist, known as the canonical and the non-canonical or planar cell polarity (PCP) pathways. The main effector transducing Wnt signaling is the cytoplasmic protein Dishevelled (Dvl), which becomes activated upon binding of Wnt-ligands to frizzled receptors (Fz). Dvl is a scaffolding protein consisting of a DIX domain, followed by a PDZ and a DEP domain (Fig. 7a). In the canonical pathway Dvl mediates the stabilization of the transcription factor and junctional protein β-catenin, whereas in the PCP it induces a cascade of actin-cytoskeleton rearrangements, and coordinates epithelial cell polarization with planar spindle orientation.

Ségalen and colleagues reported, that in *Drosophila* SOP and in zebrafish epiblast cells, Dvl interacts through its DEP domain with the C-terminal portion of NuMA to control spindle orientation. In *Drosophila*, Wnt signaling orients SOP cells along the anterior-posterior axis, with Dsh (*Drosophila* Dvl) and Mud localized posteriorly (Fig. 7b), while Pins and Dlg are enriched at the anterior side. Similarly, Dvl and NuMA are necessary to position the mitotic spindle along the animal-vegetal axis in zebrafish epiblast cells [48]. Using the above-mentioned "induced cell polarity assay", it was shown that the Dsh-DEP domain interacting with Mud is not sufficient for robust spindle orientation [52], which requires also the C-terminus of Dsh. More specifically, Johnston and coworkers demonstrated that the last 10 residues of Dsh, which are conserved across species, interact directly with the PDZ region of the F-actin binding protein Canoe (Fig. 7b).

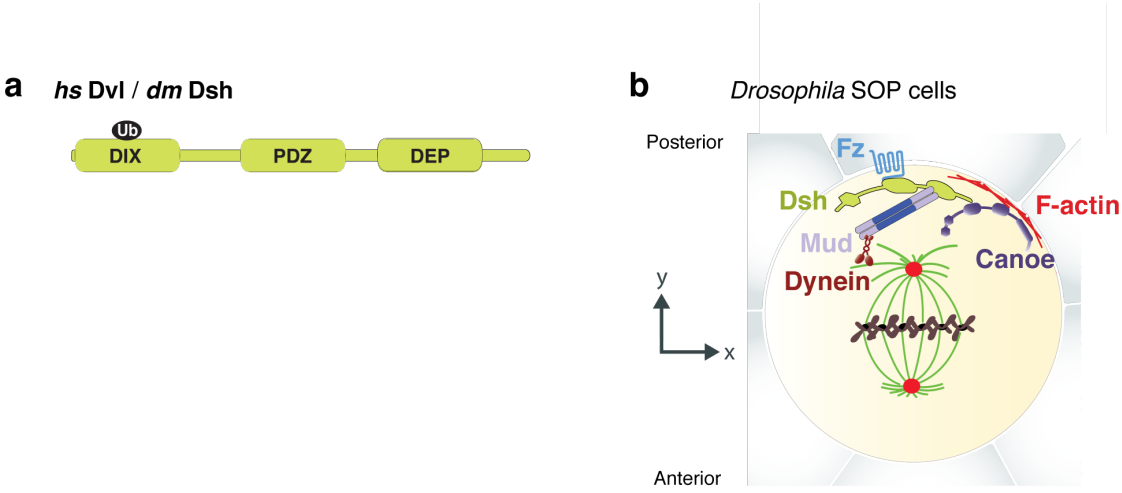

Fig. 7. The Dishevelled/Mud pathway in SOP cell planar divisions. a) The domain structure of Dishevelled, depicted in green, is conserved between humans (*hs* Dvl) and flies (*dm* Dsh). It consists of a DIX domain, followed by a PDZ and a DEP domain. The ubiquitination site lying in the DIX domain is indicated as a black sphere. **b)** Model of planar spindle orientation in asymmetrically dividing *Drosophila* SOP cells. Upon Fz receptor activation, Dsh is recruited at the plasma membrane of the posterior side of the cell, where it interacts with both Mud and Canoe to orient the mitotic spindle via Dynein/Dynactin. The x,y axis indicates the orientation within the epithelial layer.

Three isoforms of Dvl exist in vertebrates, two of which have been implicated in spindle orientation [53, 54]. In particular, the spindle orientation functions of Dvl3 depend on its interaction with NuMA, that in mitotic HeLa cells is enhanced by the activity of the deubiquitinase CYLD [53]. Consistently, structural and biochemical studies showed that ubiquitination events on the DIX domain of Dvl hamper its self-oligomerization [55] as well as the binding affinity for its interactors [56]. The spindle orientation function of Dvl2 seems to be related to its localization at the spindle poles, where it associates with and is phosphorylates by Plk1 kinase on Thr206 [53, 54].

Altogether these data point to the existence of a conserved LGN-independent cortical anchoring and spindle orientation pathway executed through the Dvl/NuMA/Dynein axis.

1.3 Afadin and spindle orientation

1.3.1 Role of the acto-myosin cell cortex in spindle orientation

Several lines of evidence indicate that spindle orientation and positioning require cortical actin, together with a number of actin regulators including members of the ezrin/radixin/moesin (ERM) family [3, 57] and Cdc42 [21, 58]. In mammalian cells, ERM proteins are activated at mitotic entry via Ste20-like kinase (SLK)-mediated phosphorylation [57]. In preparation for mitosis, the actin cytoskeleton of animal cells undergoes dramatic changes and reorganizes in a process known as mitotic “round-up”, where the interphase actin cytoskeleton is remodeled into the so called “acto-myosin cell cortex” [59]. In this context, interphase actin structures including focal adhesions disassemble and filamentous actin (F-actin) is recruited directly underneath the plasma membrane to form the mitotic cortex, which is thinner but more rigid as compared to the interphase one. The mitotic acto-myosin cortex consists of a cross-linked network of actin, myosin, and associated actin-binding proteins such as activated ERMs. Mitotic round-up is essential to achieve a cell geometry that provides enough space for mitotic spindle formation, and enough stiffness to counterbalance the traction forces exerted by *MT*-

motors pulling on astral MTs during spindle orientation and positioning [60]. Notably, most cells in culture do not detach completely from the substratum as they round. Instead, the cell margin retracts leaving thin tubular strands of cytoplasm called "retraction fibers", rich in F-actin and in activated ERM proteins [59] (Fig. 8a). Chemical depolymerization of cortical F-actin by treatment with Latrunculin-A generates orientation defects in cultured cells [61] as well as in *Drosophila* wing discs *in vivo* [3]. Importantly, the same treatment perturbs LGN cortical localization in HeLa cells in culture [57]. These results indicate that an intact cell cortex is required for the correct recruitment of *MT-motors,* which in turn orient the spindle. Whether the mitotic cortex works just as a rigid tethering platform for *MT-motors*, or it plays an active role in instructing spindle orientation is a matter of intense debate [30].

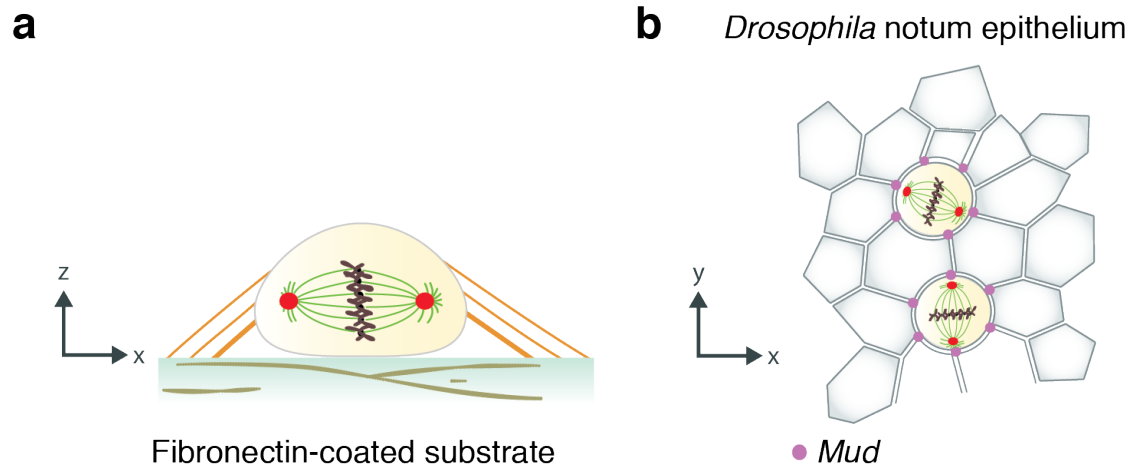

Fig. 8. Role of the acto-myosin cell cortex and of cell-cell junctions in instructing spindle orientation. a) Cartoon of a HeLa cell in metaphase plated on a fibronectin-coated support, where the mitotic spindle is oriented parallel to the substrate via β1-integrin. The actin-rich retraction fibers that form upon mitotic round-up are shown in orange. **b)** Model of the x,y view of the *Drosophila* notum epithelium. The mitotic spindles align towards Mud clusters (violet spheres) localized at TCJs, where at least three cells meet.

Different actin-binding proteins have been recently identified as possible mediators of the crosstalk between the acto-myosin cytoskeleton and astral MTs [60]. For example, the cortical actin-associated protein MISP controls spindle orientation in HeLa cells, in a Plk1 dependent manner [62]. Phosphorylated MISP forms a complex with Dynein/Dynactin,

regulates their cortical distribution, and is required for astral MT stability, thus providing a connection between the cell cortex and the mitotic spindle [62]. SLK-activated ERM proteins cross-link F-actin with the plasma membrane, and also contribute to spindle orientation by mediating the attachment of MTs to the cell cortex. Molecularly, in HeLa cells ERM proteins ensure proper LGN/NuMA cortical localization, and in the apical progenitors of the embryonic mouse neocortex contribute to planar spindle orientation [57]. Other evidence on the crosstalk between the acto-myosin cortex and MTs was provided by the discovery in mitotic cells in culture of subcortical actin clouds. Actin clouds are polarized actin structures with spindle orientation function exerted by the unconventional actin motor and MT-binder Myosin-10 [63], which seems to be involved in the communication between retraction fibers and astral MTs [64]. In addition, either in culture or *in vivo,* cells are subjected to external constraints, like retraction fiber forces and tissue packing compression, which modify cell shape and impact on spindle orientation. The influence of cell shape on spindle orientation has long been under debate. Based on the "Hertwig rule" cells divide accordingly to their long axis, thus implying that spindle orientation depends passively on cell shape and external physical constraints. Although this notion seems to contradict the idea of spindle motors, it is also possible that motors localize in cortical domains accounting for cell shape.

Apart from physical constraints that cells can experience within tissues, other external signals such as ECM [65] or cell-cell junctions [30] contribute to orient the mitotic spindle.

1.3.2 Role of cell-cell junctions in instructing spindle orientation

Epithelial cells maintain their intercellular junctions throughout divisions. This has been documented in MDCK cells, which maintain E-cadherin-based AJs laterally [66], and also in basal keratinocytes *in vivo* [67]. In the mouse skin epithelium, basal progenitors adhere to each other through E-cadherin-based AJs. In mitosis, junctions maintain cells within the epithelium, and also contribute to spindle orientation. It has been reported that in the basal

layer of murine developing skin, absence of the AJ-protein α-catenin causes loss of Par3 and LGN from the apical cortex, and aberrant NuMA distribution, thus leading to spindle misorientation [17]. Consistently, experiments carried out in MDCK cysts revealed that a number of cell-cell junction molecules controls planar spindle orientation, including E-cadherins [68], the junctional adhesion molecules-A (JAM-A) [69], and Plexin/Semaforin complexes [70]. Furthermore, epithelial tricellular junctions (TCJs) of the *Drosophila* pupal notum epithelium, that form where at least three cells meet, have recently been suggested to influence spindle orientation (Fig. 8b). In this system, Mud localizes at TCJs since G2-phase and promotes the recruitment of *MT-motors* independently of Pins. Hence, TCJs act as interphase cell shape sensors to orient the mitotic spindle [71]. Notably, this mechanism cannot be transferred to vertebrates, as NuMA is nuclear and has not been detected at cellular junctions in polarized epithelia.

1.3.3 Canoe

The *Drosophila* protein Canoe is an F-actin binding protein involved in cytoskeletal organization and in signal transduction during morphogenesis. The domain structure of Canoe, which is conserved also in vertebrates (paragraph 1.3.4), includes two Ras-association (RA) domains, a Fork-Head associated (FHA) domain, one PDZ domain that mediates the interaction with Nectin [72], and a C-terminal F-actin binding domain (Fig. 9b, top). In embryonic mesodermal cells Canoe localizes to AJs, and connects the junctions to the actin cytoskeleton by direct binding to F-actin [73]. Speicher and colleagues reported that Canoe is required for spindle orientation in NBs and in muscle progenitors. In NBs Canoe colocalizes at the apical cortex with Bazooka/Par6/aPKC and the Pins/Mud complex, and controls the basal distribution of fate determinants such as Numb (Fig. 2a) [44]. Interestingly, a recent study reported that the Hippo pathway kinase Warts (LATS1-2 in vertebrates), which associates in vivo with Bazooka/Insc, is required for the apical recruitment of Canoe via direct phosphorylation of Ser1196, Thr1380 and

Thr1394 [50]. Previous studies exploiting the "induced cell polarity assay" demonstrated that cortically fused $Pins^{TPR}$ is able to target Canoe at the cortex by direct interaction with its C-terminal region ($Canoe^{Cter}$), suggesting that $Pins^{TPR}$ and $Canoe^{Cter}$ can interact. In turn, the RA domains of Canoe, which bind physically to Ran-GTP, are required for cortical recruitment of Mud, for unclear molecular reasons [74]. As introduced in paragraph 1.2.3, Canoe has been also implicated in the Fz/Dsh/Mud spindle orientation pathway through direct interaction of its PDZ with the very C-terminal residues of Dsh [52]. In summary, Canoe has been implicated in spindle orientation in several ways: i) by interaction of its C-terminal portion with PinsTPR; ii) by interaction of its PDZ with the last 10 residues of Dsh; iii) by a molecularly unclear role of the RA domain in targeting Mud at the cortex.

1.3.4 Afadin

The vertebrate ortholog of Canoe is Afadin, which in humans is coded by the ubiquitously expressed MLLT4 (or AF-6) gene (Fig. 9a), and shares the same domains structure of Canoe (Fig. 9b, bottom). Afadin has six different splicing variants, three of which possess a C-terminal region mediating F-actin association [75-77] (Fig 9a, isoforms 3,4,5). In vertebrate epithelia, Afadin localizes and contributes to the formation of AJs [78] by direct interaction of its PDZ domain with the C-terminus of Nectin [72]. In addition, it connects physically AJs to cortical F-actin [73]. Consistent with the function in adhesion and tissue integrity, Afadin knock-out is embryonically lethal in mice [79], while its tissue specific ablation has been reported to cause severe morphogenetic defects in the brain [80], nephrons [81] and lymphatic system [82]. Furthermore, as already discussed in paragraph 1.1 Afadin ablation in the mouse small intestine leads to Paneth cell dislodging from the base of the crypts and ISC overproliferation, indicating that it plays a prominent role in the maintenance of ISC compartment [8]. Consistently, Afadin has been implicated in different types of tumors. For instance, its loss correlates with bad prognosis in severe pancreatic

cancers [83]. Molecularly, in pancreatic cell lines Afadin has been shown to interact with the Wnt-effector Dvl2, restraining its association with the transcription factor FOXE1. In the absence of Afadin, constitutive binding of Dvl2 to FOXE1 causes uncontrolled *Snail* expression, leading to proliferation and metastasis [83]. The same phenotype has been observed in breast cancer [84], where AF-6 has been recently identified as one of the more frequently mutated genes [85]. However, whether and how Afadin plays a role in spindle orientation was unexplored before our findings.

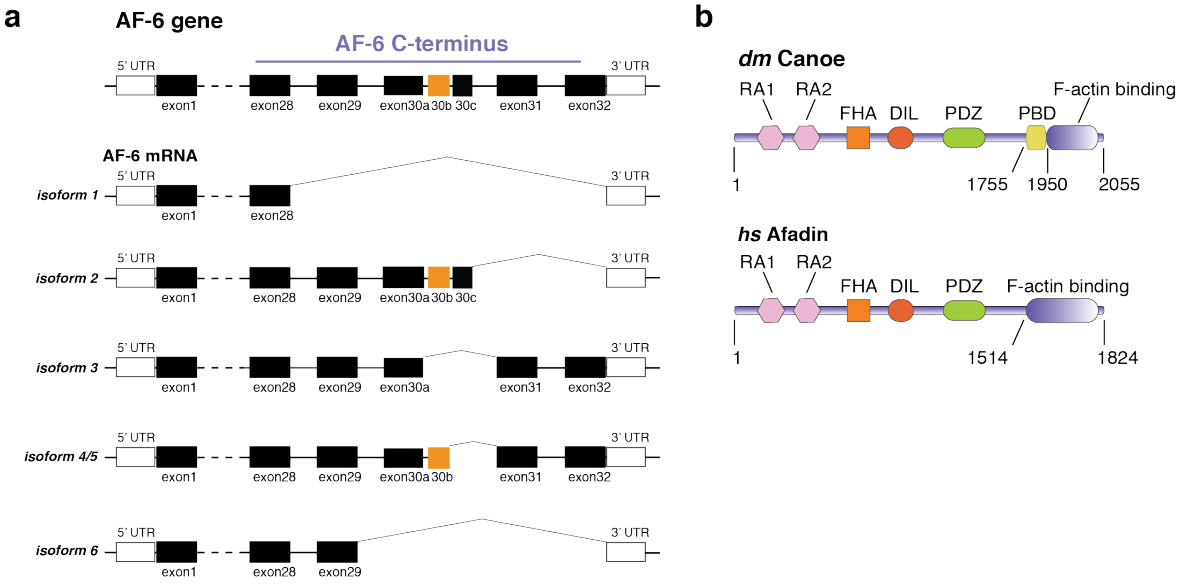

Fig. 9. Schematic representation of the human Afadin gene and its protein domain structure. **a)** Scheme of human Afadin (also known as AF-6 or MLLT4) gene, and its splice variants. The AF-6 gene is located on human chromosome 6, and consists of 32 exons. Alternative splicing produces six transcripts differing in their C-terminal region. Human Afadin isoforms 1 and 6 stop at exons 28 and 29 respectively, and are similar to short variant of rat Afadin (also known as s-Afadin), which was reported to be unable to bind to F-actin. Human Afadin isoforms 2, 3, 4 and 5 are similar to long rat Afadin (l-Afadin), which binds to F- actin. Isoforms 4 and 5 differ for the presence of additional 11 residues between exon 28 and 29. The LGN-binding site of Afadin characterized in this study is coded by exon 30 (highlighted in orange), and is present in all human long isoforms except isoform-3. **b)** Schematic representation of the domain structure of long isoforms of *Drosophila* Canoe (top), and human Afadin (bottom) consisting of two Ras-association domains (RA1 and RA2), a Fork-Head-associated domain (FHA), a Dilute domain (DIL) and a PDZ domain, followed by a C-terminal F-actin binding region. The C-terminal portion of Canoe contains also a Pins binding region (yellow).

1.4 NuMA and spindle orientation

1.4.1 Mitotic spindle assembly

The mitotic spindle consists of a bipolar array of MTs focused and anchored at the spindle poles. Three classes of MTs form the mitotic spindle: kinetochore MTs, interpolar MTs, and astral MTs. Astral MTs grow from the spindle poles and anchor the mitotic spindle to the cell cortex sustaining spindle alignment in metaphase and elongation in anaphase [86]. MTs are hollow cylindrical structures formed by α/β-tubulin dimers that associate head-to-tail in polarized polymers with a plus-end where β-tubulin is exposed, and a minus-end where α-tubulin emerges. MT nucleation occurs at centrosomes, formed around two barrel-shaped centrioles embedded in a protein matrix known as pericentriolar material. At G2/M transition centrosome maturation requires the activity of several mitotic kinases such as the cyclin-dependent kinase 1 (CDK1), the Polo-like kinase 1 (Plk1) and Aurora-A [87]. Chromosome derived signals transduced by the small GTP-ase Ran are also necessary for mitotic spindle assembly. Ran was first identified as a regulator of nuclear transport in association with importins and exportins. The Ran-GTP cycle is regulated by the chromatin associated GEF RCC1, which promotes the exchange of GDP for GTP, generating a Ran-GTP gradient centered on chromosomes (Fig. 10a, left). Molecularly, Ran-GTP promotes the spindle assembly by inducing the release of spindle assembly factors from importins. As will be explained in the next paragraph, mitotic kinases together with Ran-GTP control the centering of the mitotic spindle in metaphase and its elongation in anaphase. A fundamental role in mitotic spindle assembly is also played by the motor protein Dynein, which localizes with NuMA at the spindle poles to focus and tether the minus-end of MTs to the centrosomes [88, 89].

1.4.2 Coordination of orientation with mitotic progression

In vertebrate cells, the mitotic spindle forms in prometaphase with a random orientation, and than rotates during metaphase to achieve the final axis of division observed in

anaphase [27]. Kiyomitsu and Cheeseman demonstrated that, in HeLa cells, LGN is initially recruited all around the cell cortex in prometaphase, while in metaphase it becomes restricted to two cortical crescents facing the spindle poles, together with NuMA [26]. To explain their observation, the authors proposed that spindle pole- and chromosome-derived signals regulate Dynein localization at metaphase. More specifically, the chromosome-derived Ran-GTP gradient would prevent cortical enrichment of LGN and NuMA above the metaphase plate, thus confining their localization to the regions facing the spindle poles (Fig. 10a, left). How molecularly Ran-GTP mediates this process is not clear yet. In the same study, the authors observed that in metaphase Dynein displays an asymmetric cortical distribution that is negatively regulated by spindle pole proximity, thus generating oscillations that contribute to spindle centering. The spindle pole signals governing the cortical asymmetric distribution of Dynein derive from Plk1 activity, which disrupts the association between Dynein/Dynactin and LGN/NuMA at cortical sites in proximity of the spindle pole [26] (Fig. 10a, right). During anaphase, the cortical levels of NuMA above the spindle poles increase in an LGN-independent manner, resulting in an enrichment of Dynein/Dynactin that generates robust pulling forces elongating the spindle. The cortical enrichment of NuMA in anaphase has been linked to its phosphorylation state. During metaphase CDK1 phosphorylates NuMA on Thr2055 (Fig. 10b) negatively regulating the direct binding of NuMA to the plasma membrane [90], likely through charge repulsion [91]. In anaphase, when CDK1 becomes inactive, unphosphorylated NuMA binds directly to the phospholipid-bilayer [90, 91]. This way, CDK1 activity couples mitotic progression with cortical NuMA/Dynein functions. An alternative mechanism that has been put forward to explain the LGN-independent NuMA cortical enrichment observed in anaphase, involves members of the 4.1G/R families of cytoskeletal proteins. Studies from the Cheeseman and Lechler laboratories indicated that residues 1788-1810 of NuMA mediate cortical targeting of the protein [35, 92], by direct association with 4.1R [93] (Fig. 10b). However, later studies showed that loss of cortical NuMA upon depletion of 4.1G/R

might result from indirect effect of cortical disruption. The same study by Kotak *et al.* [94], proposed that the region containing the 4.1G/R binding site, encompassing residues 1699-1876, is rather an additional phosphoinositides interacting region.

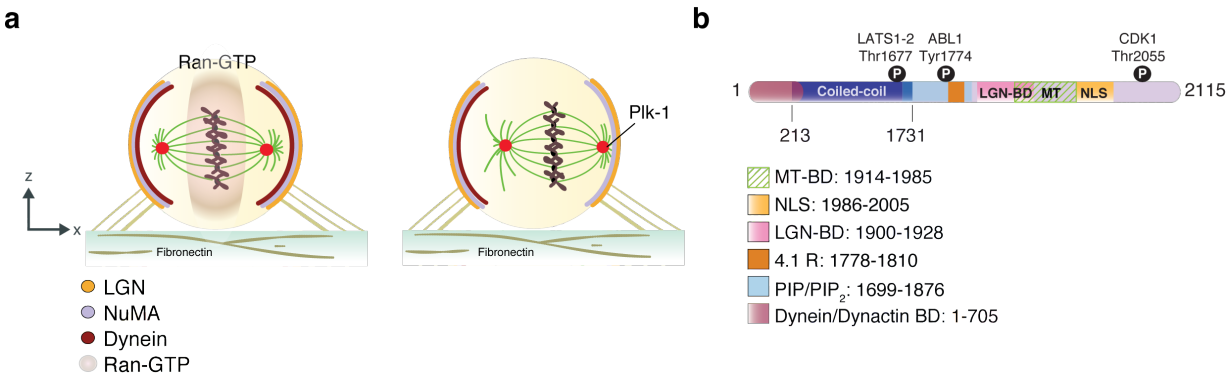

Fig. 10. Regulation of NuMA cortical localization in metaphase and anaphase. a) Schematic representation of the Ran-GTP gradient that in metaphase excludes LGN/NuMA complexes from the cortical regions near chromosomes, thus restricting their localization to crescents overlying the spindle poles (left). The kinase activity of Plk1 mediates spindle centering by inhibiting LGN/NuMA interaction with Dynein/Dynactin (right). **b)** The domain structure of NuMA is made of a globular N-terminus that mediates the interaction with Dynein/Dynactin, a long coiled-coil domain that induces dimerization, and a C-terminal tail that includes the LGN and 4.1R–binding domains, a nuclear localization signal (NLS), and a MT-binding domain. In addition the C-terminus contains a charged motif interacting with phopsholipids that mediates direct membrane association of NuMA in anaphase. NuMA phosphorylation events are represented as black spheres. Thr2055 is phosphorylated by CDK1 in metaphase to inhibit NuMA binding to phospholipids until anaphase onset, when the kinase becomes degraded by Cyclin-B. Tyr1774 is a substrate of ABL1, which contributes to maintain LGN/NuMA cortical levels in metaphase. Thr1677 would be phosphorylated by LATS1/2 to release the intramolecular interaction that may exist between the NuMA C-terminal tail and the upstream CC.

Together these findings demonstrate that localization of NuMA/Dynein is tightly regulated throughout mitosis to ensure mitotic spindle positioning in metaphase and elongation during anaphase.

1.4.3 NuMA

Human NuMA is a 2115-residue-long protein (238 kDa) that in interphase localizes into the nucleus. In mitosis, NuMA is distributed at the spindle poles and at the regions facing the spindle poles, where it contributes to spindle organization and positioning. Its domain structure consists of a globular N-terminal domain, a central extended coiled-coil (CC) that mediates homodimerization, and of an unstructured C-terminal region (Fig. 10b). While the N-terminal region spanning residues 1-705 reported to interact with Dynein/Dynactin [23] has been poorly characterized, the C-terminal tail of NuMA has been extensively studied. The NuMA C-terminus contains a number of interaction domains including the ones for LGN (residues 1900-1928) [12, 36] (see paragraph 1.2.1), for phospholipids [90, 94] (as detailed in paragraph 1.4.2), for MTs, and a nuclear localization signal (NLS) (Fig. 10b). One of the most studied functions of NuMA is its MT-binding ability. Experiments with *Xenopus* extracts revealed that a portion of the NuMA C-terminus is involved in MT aster formation by MT-bundling [89]. Further analysis of the identified region demonstrated that its overexpression in HeLa cells induces MT-bundling *in vivo*. Co-sedimentation experiments with Taxol-stabilized MTs revealed that human NuMA interacts physically with MTs through a region spanning residues 1914-1985 [95] (Fig. 10b, dashed green). The finding that the MT-binding domain of NuMA was partially overlapping with the LGN-interacting region raised the question as to whether LGN and MTs could compete for the association with NuMA. Experiments performed with Taxol-stabilized MTs and *in vitro* translated NuMA-1580-2115 in the presence of LGN^{TPR} seemed to indicate that binding of LGN inhibits the interaction of NuMA with MTs. Furthermore, a NuMA fragment encompassing residues 1892-2015 failed to bundle MTs in an *in vitro* bundling assay in the presence of LGN^{TPR}. Unexpectedly, in the same study the authors found that NuMA-1914-1985, was able to bundle MTs efficiently even when LGN^{TPR} was present [96]. Based on the structural evidence of LGN^{TPR} in complex with NuMA-1900-1928 ($NuMA^{PEPT}$), this result is most likely due to the lower binding affinity

of LGN^{TPR} for NuMA-1914-1985 that compared to $NuMA^{PEPT}$ lacks 13 residues, among which some are crucial for docking within the LGN concave groove (Fig. 5c,e).

At mitotic entry, NuMA contributes to MT focusing and tethering to the centrosomes [89, 97], in association with Dynein/Dynactin. Although in mitosis, the bulk of NuMA localizes at the spindle poles, a portion of NuMA is recruited at the cortex in crescents overlying the spindle poles by direct interaction with LGN [12, 36]. In turn, this NuMA population recruits Dynein/Dynactin to drive spindle orientation [23].

As already mentioned in paragraph 1.4.2, in HeLa cells in culture, NuMA is targeted to polar cortical crescents by LGN. However its recruitment is also regulated by several phosphorylation events. The ABL1 kinase has been implicated in spindle orientation in HeLa cells and in keratinocytes by direct phosphorylation of NuMA on Tyr1774. This phosphorylation would favor NuMA recruitment to LGN crescents in metaphase, through an unknown mechanism [98]. Furthermore, recently Dewey and colleagues showed that in *Drosophila* S2 cells the Hippo pathway kinase Warts contributes to spindle orientation by phosphorylating Mud on Ser1868, within its C-terminal coiled-coil (CC) domain. Of note, this phosphorylation would be conserved in NuMA at Thr1677. Molecularly, such phosphorylation event would relieve an intramolecular interaction occurring between the CC domain and the C-terminal portion of Mud/NuMA, this way exposing the Pins/LGN binding domain [49]. Whether other mitotic kinases control NuMA cortical enrichment in metaphase was unknown when I started my PhD. Interestingly, a phosphoproteomic screening performed by Kettenbach and colleagues in HeLa cells revealed that NuMA is a substrate of Aurora-A [99, 100]. Aurora-A is a Ser/Thr-kinase that from prometaphase to metaphase localizes at spindle poles and controls centrosome maturation and separation, assembly of a bipolar spindle, and alignment of chromosomes [87]. Through the phosphoproteomic screening, several Aurora-A phosphosites were found on the C-terminus of NuMA, including Ser1969, which lies within a previously identified MT-binding domain [95]. Interestingly, chemical inhibition of Aurora-A with MLN8237

induces orientation defects in U2OS cells [101]. Nevertheless, whether Aurora-A regulates the localization of NuMA at the spindle poles and at the cortex, and how it controls spindle orientation is unclear.

1.5 AIM OF THE PROJECTS

Over the past years, many efforts have been made to identify cellular pathways and external stimuli that contribute to spindle orientation. However, the molecular mechanisms underlying this process are still far from being fully understood.

My PhD project focused on the biochemical and structural characterization of the junctional protein Afadin, and its interaction with LGN, F-actin and NuMA. In addition, I characterized the Aurora-A-mediated phosphorylation of NuMA, and its implications for MT-binding and spindle orientation.

Aim 1: Role of Afadin in spindle orientation

In epithelial planar divisions LGN localizes at the lateral cortex to align the mitotic spindle within the plane of the epithelium. Several mechanisms have been proposed to explain the lateral restriction of LGN, including the interaction of LGN with cortical Dlg1 [28, 46] and its aPCK-mediated apical exclusion [19]. Whether other molecules contribute to maintain LGN at the lateral cortex during planar mitoses is still unclear.

Growing evidence points to a role for the acto-myosin cell cortex in instructing spindle orientation. The stiffness of the cortex is required to counterbalance Dynein-based forces, however direct molecular links between F-actin and the *MT-motors* might exist. Interestingly, in *Drosophila* epithelia the F-actin binding protein Canoe was shown to be essential for spindle orientation via direct binding with Pins [74]. Because the ortholog of Canoe in vertebrates, named Afadin, localizes at adherens junctions, we consider it an interesting candidate for being the mechanical connection between the lateral cortex and *MT-motors* assembled on Dynein/Dynactin. Therefore, the first aim of my PhD research was to test whether Afadin would interact directly with LGN, to characterize their interaction biochemically and by X-ray crystallography, and to investigate its relationship with F-actin and with NuMA. My molecular findings have then been transferred in cells to

analyze the relevance of the LGN/Afadin/F-actin interaction for spindle orientation in HeLa cells, and in three-dimensional epithelial Caco-2 cysts.

Aim 2: Effect of NuMA phosphorylation by Aurora-A on spindle orientation

During metaphase and anaphase, proper spindle orientation relies on the distribution of NuMA at the spindle poles and at the cortex. The levels of cortical NuMA, in turn, depend on a wide range of factors including phosphorylation events by Plk1 [26], ABL1 [98] and CDK1[90]. Whether other factors affect the enrichment of NuMA above the spindle poles in metaphase is an interesting open question. The mitotic kinase Aurora-A has been involved in spindle orientation both in *Drosophila* NBs and in vertebrate systems. Data generated in our lab revealed that either depletion or chemical inhibition of Aurora-A induces aberrant accumulation of NuMA at the spindle poles, and loss of cortical localization. This phenotype was accompanied by spindle misorientation in HeLa and RPE-1 cells. Based on these findings, the second part of my PhD research aimed at investigating how molecularly Aurora-A balances the pool of NuMA localizing at the spindle poles with the pool recruited at the cortex with LGN. Of note, a recent phospho-proteomic study reported that NuMA is a substrate of Aurora-A [99, 100], and that most of the identified Aurora-A phosphosites of NuMA lie in its C-terminal portion that was reported to bind LGN and the MTs [96]. For these reasons, I first set out to test whether the C-terminus of NuMA could be phosphorylated directly by Aurora-A *in vitro,* and whether its phosphorylation could hamper its interaction with MTs or with LGN, thus providing a molecular explanation for the aberrant localization phenotype observed in conditions of Aurora-A inactivation.

2. RESULTS: Afadin in spindle orientation

Recently, converging evidence has accumulated for the role of the acto-myosin cortex and of cell-to-cell junctions in instructing mitotic spindle orientation. Importantly, the F-actin binding protein Canoe has been implicated in the execution of asymmetric cell divisions in *Drosophila* NBs [44]. Thus we reasoned that Afadin, the vertebrate ortholog of Canoe, could be an ideal candidate to study F-actin-mediated spindle orientation. Afadin is an adherens junction component, whose known function is to connect cadherins with the actin cytoskeleton [102]. Afadin was first identified in rat brain where it is expressed in two splice variants: longer l-Afadin and shorter s-Afadin. Of note, rat l-Afadin but not s-Afadin contains an F-actin binding domain in its C-terminus [75-77], while human Afadin (*hs* Afadin hereon) has six splice variants (Fig. 9a). Because *hs*Afadin-isoform4 shares high similarity to the rat l-Afadin, we decided to select it for our studies. It is established that accurate spindle orientation in metaphase depends on the association between LGN and NuMA, which occurs via direct interaction between the LGN^{TPR} and the C-terminal region of NuMA [12]. Thus, to start investigating the contribution of Afadin in spindle orientation I set out to determine its biochemical relationship with LGN and NuMA.

Afadin binds directly to LGN *in vitro*

2.1 $Afadin^{Cter}$ interacts physically with LGN^{TPR}, but not with NuMA

Studies exploiting an induced-cell polarity system in *Drosophila* S2 cells revealed that $Pins^{TPR}$ (the fly ortholog of LGN^{TPR}) binds directly to the C-terminal portion of Canoe, in a region overlapping with its F-actin binding domain [74] (Fig. 9b, top). Similarly to Canoe, *hs*Afadin consists of two N-terminal Ras-associating (RA) domains, a Dilute domain, a PDZ domain, and an F-actin-binding domain at its C-terminus (Fig. 9b, bottom). To test whether the interaction of Canoe with Pins is conserved in their human orthologs, I first purified to homogeneity the C-terminal domain of Afadin encompassing residues 1514-1824 ($Afadin^{Cter}$ hereon) and the N-terminal TPR-domain of LGN spanning residues 15-

350 (LGN^{TPR}). I then conducted analytical size exclusion chromatography (SEC) experiments by loading equimolar amounts of LGN^{TPR} and Afadin^{Cter} on a Superdex-200 5/150 column, from which they eluted as a stoichiometric 1:1 complex (Fig. 11a), indicating that they interacts physically. On the other hand, when I repeated the same experiment with Afadin^{Cter} and a C-terminal fragment of NuMA containing the LGN-binding domain (NuMA$^{1861-1928}$), the two proteins eluted in two separate peaks (Fig. 11b), meaning that they do not interact with one another.

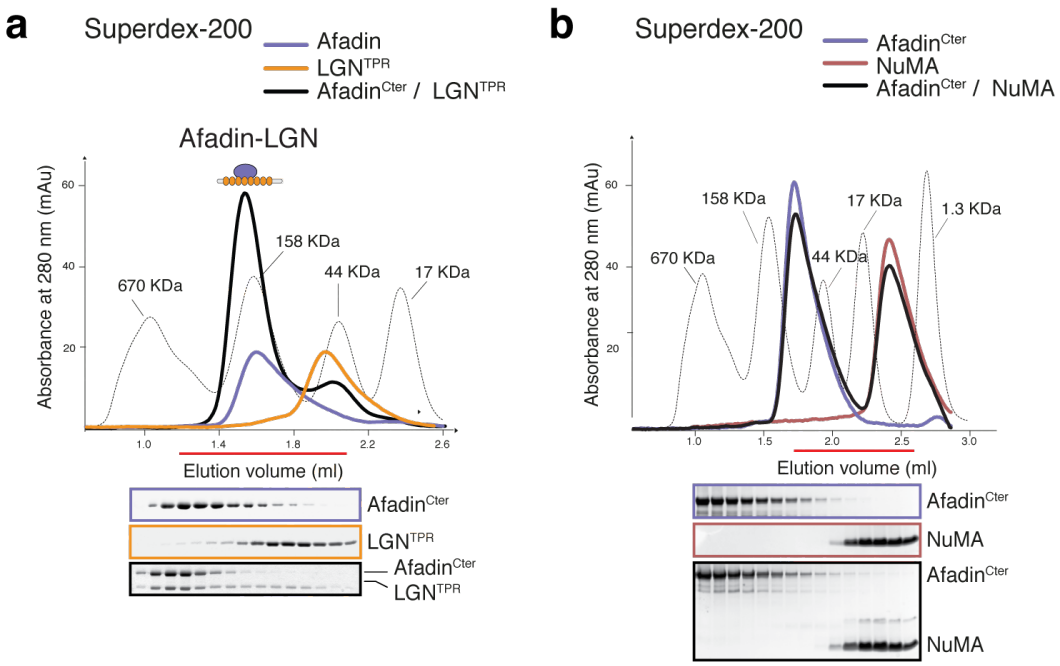

Fig. 11 Afadin^{Cter} interacts physically with LGN^{TPR}, but not with NuMA. a) SEC elution profile of the stoichiometric complex formed between Afadin^{Cter} and LGN^{TPR} mixed at 15 µM concentration, and Coomassie-stained SDS-PAGE of the peak fractions corresponding to the horizontal red bar. The elution profile of globular markers is reported in a dashed gray line. Individual runs of Afadin^{Cter} and LGN^{TPR} are shown for comparison. Notably, Afadin^{Cter} (about 37 kDa in size) elutes near the 158 kDa molecular weight marker, in spite of being monomeric in solution according to Static-Light-Scattering experiments (not shown), thus suggesting that it adopts an elongated conformation. **b)** An analogous incubation of Afadin^{Cter} with NuMA$^{1861-1928}$ does not result in a complex formation, as evident by the absence of a peak eluting earlier than the two proteins in isolation.

2.2 Afadin^{Cter} binds to LGN^{TPR} with micromolar affinity

To further characterize the interaction between LGN^{TPR} and Afadin^{Cter}, I measured the strength of the binary interaction by Isothermal Titration Calorimetry (ITC). ITC is a technique that allows the determination of the thermodynamic parameters of a binding reaction including the dissociation constant (K_D) and the stoichiometry. This technique is based on the measurement of the heat exchange occurring during the formation of a complex, where small amounts of a ligand molecule are titrated to saturation into a cell containing the receptor. The heat being released or absorbed is then plotted as a function of time and fitted with a non-linear model, generating a sigmoidal curve that allows the calculation of the thermodynamic parameters (see Mat. & Meth. section 5.2.3). I first exploited this approach to determine the K_D of the binding between Afadin^{Cter} and LGN^{TPR} by subsequent injections of 10 µl of LGN at a 0.8 mM concentration into a cell containing 60 µM Afadin. Unfortunately, I could not obtain a sigmoidal isotherm because of the low binding affinity (Fig. 12a). Ideally, to obtain a sigmoidal isotherm, the affinity between the receptor and the ligand should be high enough compared to the reactant concentrations that a plateau of equal exchanged heats forms at the first injections, when the ligand associates completely to the receptor, and a second plateau forms at the last injections, when all available receptor is saturated by the ligand, and only heats of dilutions are recorded. Thus, for 5-30 µM affinities, ligand and receptor proteins should at be at millimolar concentration to achieve such experimental conditions. In the case of Afadin and LGN, the solubility was limiting to perform a standard ITC experiment. Therefore, I decided to perform a "displacement experiment", as previously reported [103]. In a displacement experiment, a high affinity interaction is coupled to a low-affinity one via a competition experiment, in which the higher-affinity ligand is titrated into the cell containing the receptor in complex with the lower-affinity partner. As a result, the sigmoidal isotherm will be shallower than the one recorded for the high-affinity ligand titrated in the receptor alone, to an extent reflecting the low-affinity interaction. Based on these considerations, I

decided to couple the low interaction between Afadin^{Cter} and LGN^{TPR} with the high affinity interaction reported for LGN^{TPR} and a peptide of human Insc (hInsc) spanning residues 23-58 (hInsc^{PEPT}) [12]. I first measured the affinity of LGN^{TPR} for hInsc^{PEPT} by a conventional ITC experiment, in which 90 µM of the peptide were injected into 12 µM LGN^{TPR}. This experiment yielded a K_D of 15 nM, in line with previous findings [12]. I then repeated the hInsc^{PEPT} titration in a cell containing 30 µM Afadin^{Cter} in complex with LGN^{TPR}. The perturbed isotherm obtained under these conditions (Fig. 12b) was used to derive the K_D of 2.0 ± 0.6 µM between Afadin^{Cter} and LGN^{TPR}, as described in the Mat. & Meth. section 5.2.3.

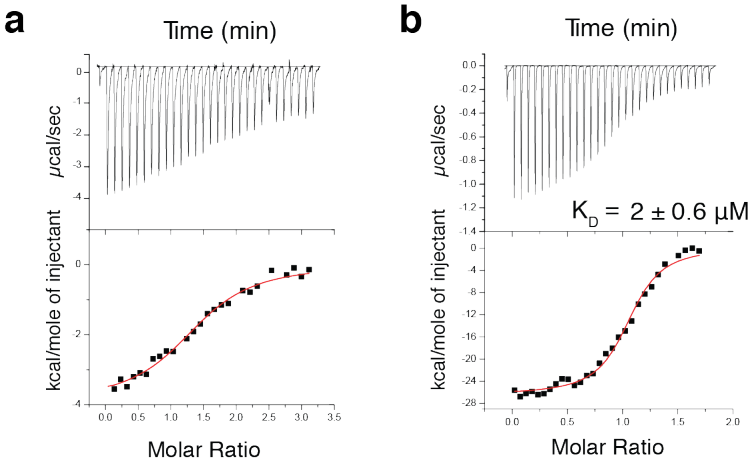

Fig. 12. Afadin^{Cter} binds to LGN^{TPR} with micromolar affinity. a) Measurement of the binding affinity between Afadin^{Cter} and LGN^{TPR} through isothermal titration calorimetry (ITC) by injecting 0.8 mM LGN into a cell containing 60 µM Afadin. Data fitting does not result in a sigmoidal curve. **b)** ITC displacement experiment in which 90 µM of the high affinity LGN-ligand hInsc^{PEPT} were injected in a cell containing 30 µM Afadin^{Cter} in complex with LGN^{TPR}. The sigmoidal curve obtained was used to derive the K_D of 2.0 ± 0.6 µM between Afadin^{Cter} and LGN^{TPR}. K_D is reported as mean ± error of fitting of the ITC data with the isotherm (red line).

2.3 Afadin$^{1709-1746}$ is the shortest fragment retaining full binding to LGN^{TPR}

To produce a crystallization quality sample, I mapped the minimal interacting domains on both sides of the Afadin/LGN complex through GST pull-down assays. According to secondary structure prediction, Afadin^{Cter} folds into two helical domains joined by an unstructured linker region (Fig. 13).

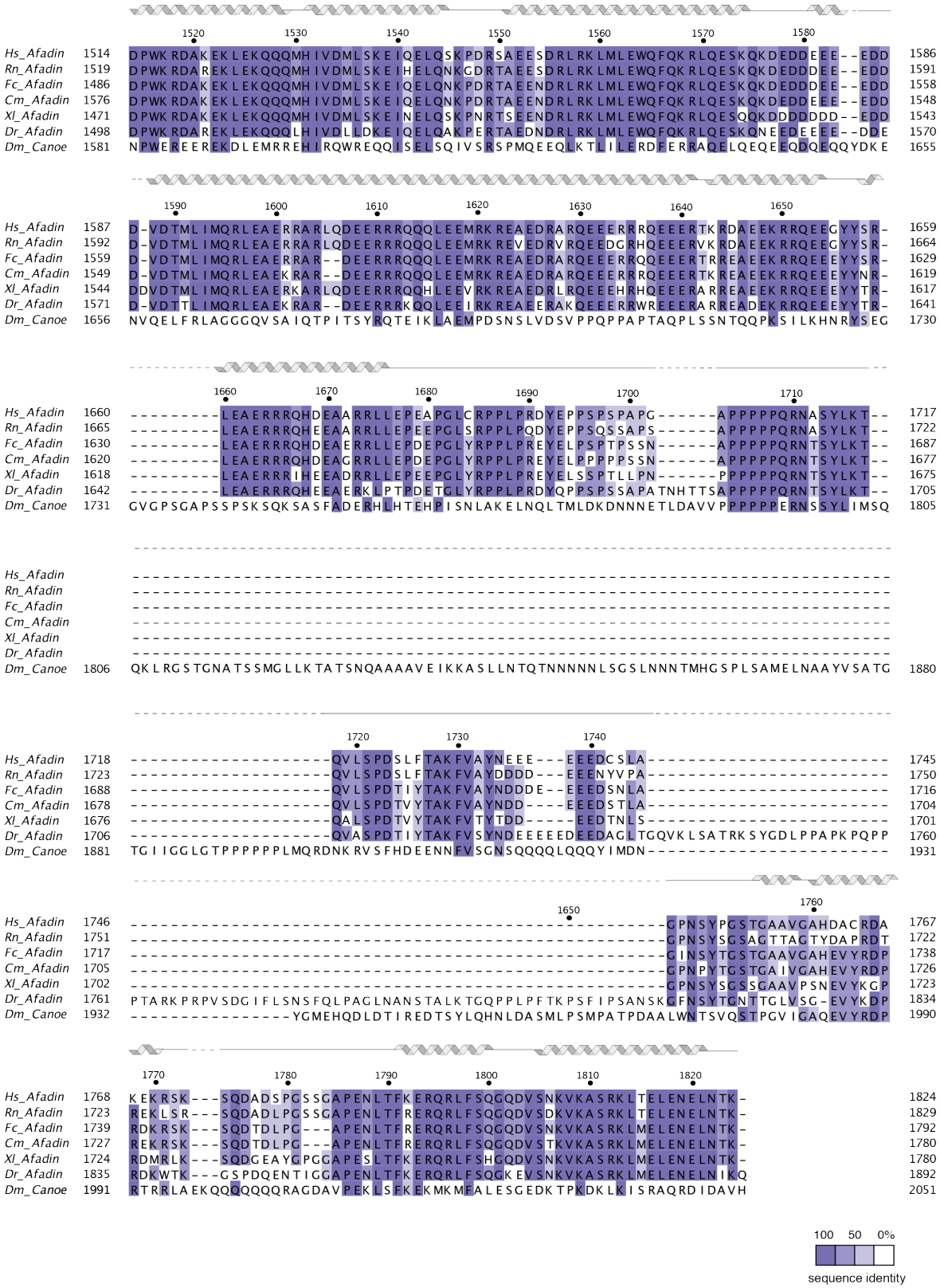

Fig. 13. Sequence alignment of the C-terminus of Afadin *long* isoforms.

Afadin residues are colored based on the conservation calculated on the alignment of seven orthologues of *Homo sapiens, Rattus norvegicus, Falco cherrug, Chelonia mydas, Xenopus laevis, Danio rerio and Drosophila melanogaster.* According to secondary structure prediction (using the server https://www.predictprotein.org/), Afadin^{Cter} folds into two helical domains (depicted in light gray) joined by an unstructured linker region.

On these bases, I designed a set of complementary Afadin fragments encompassing the whole Afadin^{Cter} (Fig. 14a, top), which I fused to a GST-moiety. To screen the ability of the Afadin fragments to bind LGN^{TPR}, I immobilized the GST fusions on glutathione-Sepharose (GSH) beads at 1 μM concentration, and incubated them with 5 μM LGN^{TPR} in solution. After washes, the species retained on beads were separated on an SDS-PAGE. This analysis revealed that the small peptide Afadin$^{1709-1746}$ (Afadin^{PEPT} hereon) binds to LGN^{TPR} to the same extent of the entire Afadin^{Cter} (Fig. 14a, bottom). In a second experiment, I mapped the minimal portion of LGN^{TPR} able to interact with Afadin^{PEPT}. To this aim I immobilized 1 μM GST-Afadin^{PEPT} on GSH beads, and tested its interaction with LGN proteins lacking either the first or the last TPR repeat. As both the LGN truncations failed to bind to Afadin^{PEPT} (Fig. 14b), I concluded that all eight TPRs of LGN are necessary for the interaction. To confirm that Afadin^{PEPT} encompasses the entire LGN^{TPR} binding region, I measured its affinity for LGN^{TPR} by fluorescence polarization (FP). I conducted the experiment using 40 nM of a fluorescently labeled Afadin^{PEPT}, in which I titrated increasing concentrations of LGN^{TPR}. Fitting of the residual polarization with a hyperbolic curve yielded a K_D of 5.6 ± 0.5 μM (Fig. 14c) (see Mat. & Meth. section 5.2.4), consistent with the 2 μM K_D measured by ITC for the entire Afadin^{Cter} and the same LGN^{TPR}. Further GST pull-down experiments with trimmed versions of the Afadin^{PEPT} led to the identification of shorter fragments of Afadin retaining binding to LGN^{TPR} (Fig. 14d). However, these fragments showed a reduced affinity for LGN^{TPR} when tested by FP assays (Fig. 14e). Therefore, I decided to use the Afadin^{PEPT} spanning residues 1709-1746 for crystallographic studies.

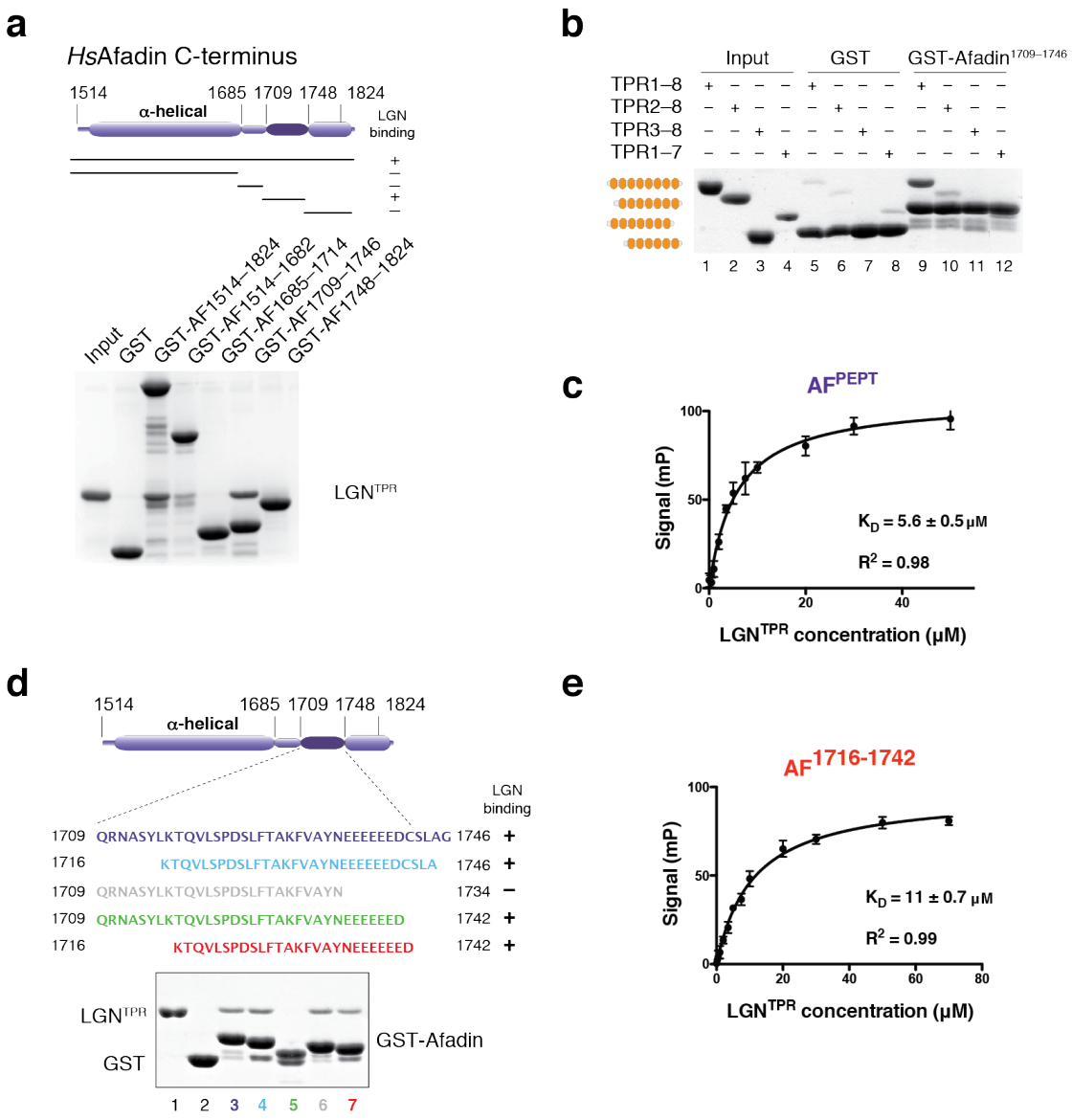

Fig. 14. Afadin$^{1709-1746}$ is the shortest fragment retaining full binding to LGN^{TPR}. a) Mapping of the minimal region of Afadin^{Cter} retaining binding to LGN^{TPR} by GST pull-down. Complementary fragments of Afadin^{Cter} (1 µM) were adsorbed on glutathione (GSH) beads, and incubated with 5 µM of purified LGN^{TPR}. After washes, species retained on beads were separated by SDS-PAGE **b)** Binding assay with 1 µM of GST-Afadin$^{1709-1746}$ on GSH beads, incubated with 5 µM of LGN constructs encompassing different sets of TPRs. **c)** Fluorescence polarization measurement of the binding affinity between a synthetic fluorescein-labeled Afadin^{PEPT} and LGN^{TPR}. **d)** Trimmed versions of the GST-Afadin^{PEPT} (1 µM) were adsorbed on GSH beads and screened in a GST pull-down assay for their ability to bind 5 µM LGN^{TPR} in solution. **e)** Fluorescence polarization measurement of the binding affinity between a synthetic fluorescein-labeled Afadin$^{1716-1742}$ and LGN^{TPR}.

2.4 Biochemical characterization of the chimeric fusion protein

Because of the relatively low affinity between LGN^{TPR} and Afadin^{PEPT}, I decided to generate a chimeric protein carrying the Afadin^{PEPT} sequence fused downstream of LGN^{TPR} (Fig. 15a, top) (see Mat. & Meth. section 5.3.1 for the cloning approach). To characterize the fusion protein biochemically, I loaded it on a SEC column from which it eluted as a monodispersed monomer, similarly to what observed for the LGN^{TPR}/Afadin^{PEPT} reconstituted complex (Fig. 15a, bottom). I further checked the homogeneity of the LGN^{TPR}-Afadin^{PEPT} chimera by using a 12% Tris-Glycine native PAGE (Fig. 15b). Whereas LGN^{TPR} in isolation runs as a smear of multiple bands, LGN^{TPR}-Afadin^{PEPT} runs with a higher mobility as a single population, meaning that the fused Afadin^{PEPT} stabilizes a compact conformation of the LGN^{TPR} super-helical scaffold. I observed the same behavior for the LGN^{TPR}/Afadin^{PEPT} reconstituted complex, that however runs more retarded than the fusion protein, suggesting that it is a more heterogeneous sample. Taken together these analyses indicated that in the fusion protein the Afadin^{PEPT} binds to LGN^{TPR} intra-molecularly, stabilizing a compact conformation. I therefore decided to use the chimera for crystallization experiments.

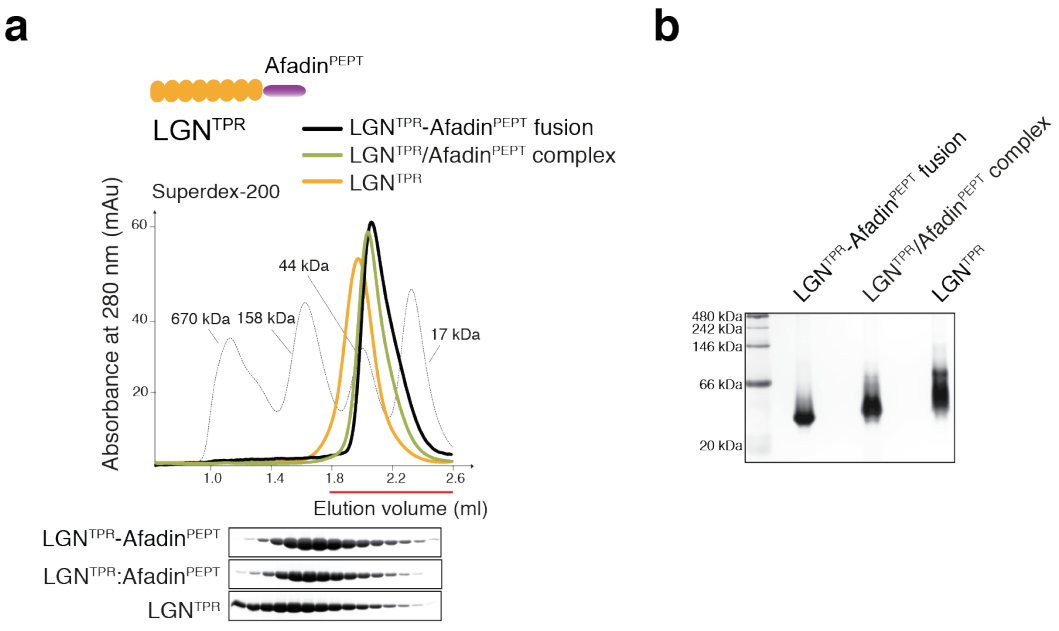

Fig. 15. Biochemical characterization of the LGN^{TPR}-Afadin^{PEPT} fusion protein. a) Comparative SEC analysis of LGN^{TPR}-Afadin^{PEPT}, LGN^{TPR} and the LGN^{TPR}/Afadin^{PEPT} complex performed on a Superdex 200 5/150 column (GE Healthcare) at 100 μM concentration. For this analysis, the LGN^{TPR} complex was assembled by mixing synthetic Afadin^{PEPT} with LGN^{TPR} in a 1:1.3 molar ratio. The protein elution profiles are overlaid with the trace of globular molecular-weight markers (grey dashed line). For all samples, the peak fractions were separated by SDS–PAGE and visualized by Coomassie staining. At the top left corner a schematic representation of the domain structure of the chimeric protein is shown, with LGN^{TPR} colored in orange and Afadin^{PEPT} in purple. **b)** The conformational heterogeneity of the LGN^{TPR}-Afadin^{PEPT} fusion, the LGN^{TPR}/Afadin^{PEPT} complex and LGN^{TPR} was assessed by native PAGE followed by Coomassie staining. Native molecular-weight markers are displayed in the first lane (labeled in kDa).

2.5 Crystals of the LGN^{TPR}-Afadin^{PEPT} chimera

I conducted initial crystallization attempts with the LGN^{TPR}-Afadin^{PEPT} chimera by using commercial sparse-matrix screens, as detailed in the Mat. & Meth. section 5.3.3 and in our manuscript published in Acta Crystallographica Section F [104]. Cubic crystals grew in about 20% of the salting-out conditions containing sulfate, phosphate, formate and malic acid ions at pH values ranging from 7.0 to 8.5. Of note, the same crystallization trials performed on a sample of LGN^{TPR} in complex with Afadin^{PEPT} were unsuccessful. To obtain larger crystals, I reproduced manually the positive hits and obtained many small crystals (Fig. 16a) or multiple crystals (Fig. 16b). I further optimized the crystallization conditions by changing the temperature, the protein concentration, or by streak seeding (Fig. 16c).

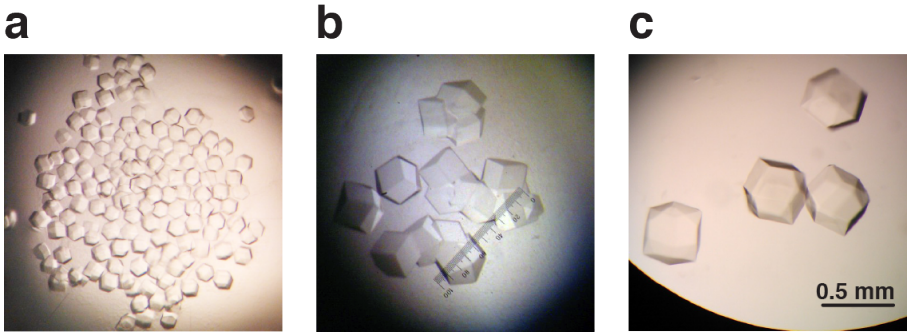

Fig. 16. Crystals of the LGN^{TPR}-Afadin^{PEPT} chimera. a,b) Initial crystals of LGN^{TPR}-Afadin^{PEPT} grown manually by hanging-drop vapor diffusion in ammonium sulfate or malic acid. **c)** After

optimization at 15 °C or seeding at 4 °C, single cubic crystals of about 0.5 mm in size appear after 1 day of crystallization.

Using LGN^{TPR}-$Afadin^{PEPT}$ crystals about 0.5 mm in size, we collected X-ray diffraction data at the Swiss Light Source, that were processed using XDS [105] implemented in *xia2* [106]. Crystals diffracted to a resolution of 2.9 Å (Fig. 17a) and belonged to the space group $P2_13$. The Matthews coefficient of 4.8 $Å^3$ Da^{-1} was compatible with two copies of LGN^{TPR}-$Afadin^{PEPT}$ per asymmetric unit (a.s.u). The structure was solved by molecular replacement with *Phaser* [107] using the coordinates of mouse LGN^{TPR} [36] as a search model (PDB ID 3RO2). The $Afadin^{PEPT}$ (Fig. 17b, purple molecule) was built manually by iterative cycles in *Coot* [108], and the structure refined with *Phenix* [109] to a final R_{free} of 25.2% and R_{work} of 20.6%. The data collection and refinement statistics are reported in Table 2.

Table 2. Data collection and refinement statistics.

	LGN-Afadin
Data collection	PXIII – SLS
Space group	$P2_13$
Cell dimensions	
a, *b*, *c* (Å)	169.8
α, β, γ (°)	90.0
Resolution (Å)	45.4 - 2.9 (2.98 – 2.9)*
R_{sym} or R_{merge}	5.7 (71.6)
I / σI	14.6 (1.5)
Completeness (%)	96.3 (95.8)
Redundancy	3.4 (3.2)
Refinement	
Resolution (Å)	45.4 – 2.9
No. reflections	34,817
R_{work} / R_{free}	20.6 / 25.5
No. atoms	
Protein	5732
Ligand/ion	15
Water	-
B-factors	
Protein	82.8
Ligand/ion	74.8
R.m.s. deviations	
Bond lengths (Å)	0.09
Bond angles (°)	1.13

*Values in parentheses are for highest-resolution shell.

The final model contains two copies of the LGN-Afadin chimera. Interestingly, analysis of the crystal contacts revealed that the packing is promoted by sulfate ions coordinated by charged side-chains of both LGN^{TPR} (Arg86 and Arg120) and the Afadin^{PEPT} (Gln1718) (Fig. 17d). The packing is further strengthened by contacts between the very C-terminal residues of Afadin^{PEPT} of one molecule in the a.s.u., and residues on the TPR-region of the second molecule. The overall structure (Fig. 17b) indicates that the Afadin^{PEPT} traces along the inner surface of the LGN^{TPR} scaffold with the exception of the first 12 residues that run parallel to the last TPR. We reasoned that the initial Afadin^{PEPT} stretch spanning residues 1709-1720 and containing Gln1718^{AF} was instrumental in promoting crystallization because this native linker provided chemical active side chains mediating crystal contacts.

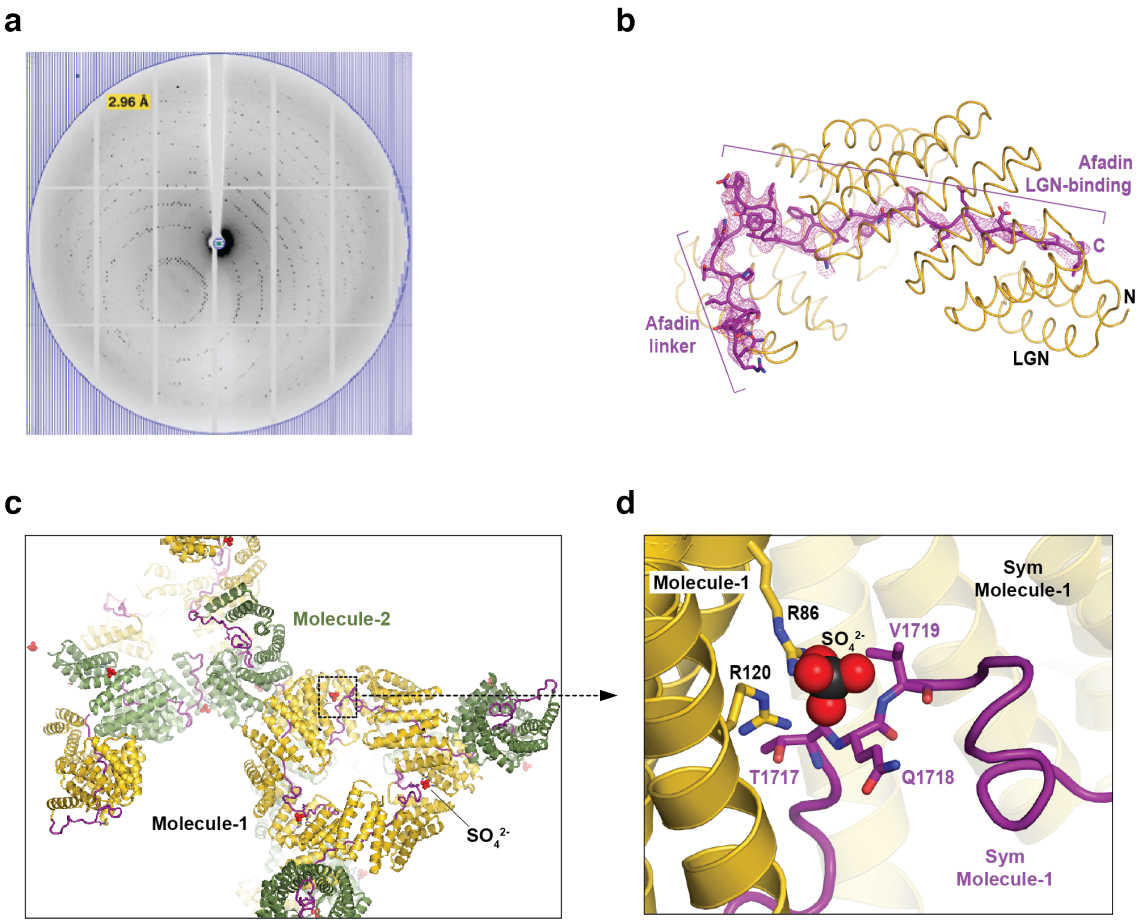

Fig. 17. Diffraction and packing of the LGN^{TPR}-Afadin^{PEPT} crystals. a) 2.9 Å resolution X-ray diffraction pattern of LGN^{TPR}-Afadin^{PEPT} obtained using a synchrotron-radiation source on beamline X06DA at the Swiss Light Source. **b)** LGN^{TPR}-Afadin^{PEPT} model and composite OMIT electron-density map displayed around the Afadin^{PEPT} region contoured at the 1.0 σ level. **c)** Crystal

lattice of LGN^{TPR}-$Afadin^{PEPT}$ with the two molecules of the asymmetric unit shown as gold and green cartoons and the sulfate ions shown as red spheres. For all molecules, the native linker of $Afadin^{PEPT}$ is displayed in purple. **d)** Enlarged view of the crystal contacts contributed to by the side chains of $Arg86^{LGN}$ and $Arg120^{LGN}$ and $Gln1718^{AF}$ of the two LGN^{TPR}-$Afadin^{PEPT}$ fusion proteins present in the asymmetric unit.

2.6 Architecture of the LGN/Afadin interface

The final model of the LGN^{TPR}-$Afadin^{PEPT}$ fusion protein includes residues 15-350 of LGN and 1709-1745 of Afadin, of which the last ten are visible only in one of the two molecules present in the a.s.u. The overall structure shows that LGN^{TPR} folds as a right-handed super-helix that buries the elongated $Afadin^{PEPT}$ into its concave groove (Fig. 18a). The TPR scaffold of LGN is formed by eight TPR repeats, each consisting of two antiparallel helices, named A and B, connected by short loops. The TPR repeats stack to one another to form a right-handed α-solenoid in which A-helices face the inner surface and contact the Afadin peptide in an extended interaction surface. The $Afadin^{PEPT}$ runs with opposite chain directionality compared to LGN. Invariant Leu-Gly-Asn (LGN) triplets present on the A-helices of the LGN scaffold stabilize the interaction with Afadin primarily via hydrogen bonds with main chain atoms of $Afadin^{PEPT}$. In addition, the specificity of the interaction is provided by side chain contribution that can be subdivided into three modules (Fig. 18b). The N-terminal residues 1720–1731 of Afadin stretch on TPR-6–7 of LGN creating a hydrophobic pocket contributed by $Phe1730^{AF}$, $Ile246^{LGN}$ and $Phe247^{LGN}$ (Fig. 18c). The second Afadin portion, spanning residues 1732–1741, contacts the central TPRs of LGN via polar interaction between glutamic acids of Afadin and the conserved Arg235-236 of LGN (Fig. 18d). The last module comprises residues 1742–1745 of Afadin, where $Leu1744^{AF}$ protrudes into a conserved hydrophobic pocket between TPR-1 and TPR-2 of LGN (Fig. 18e).

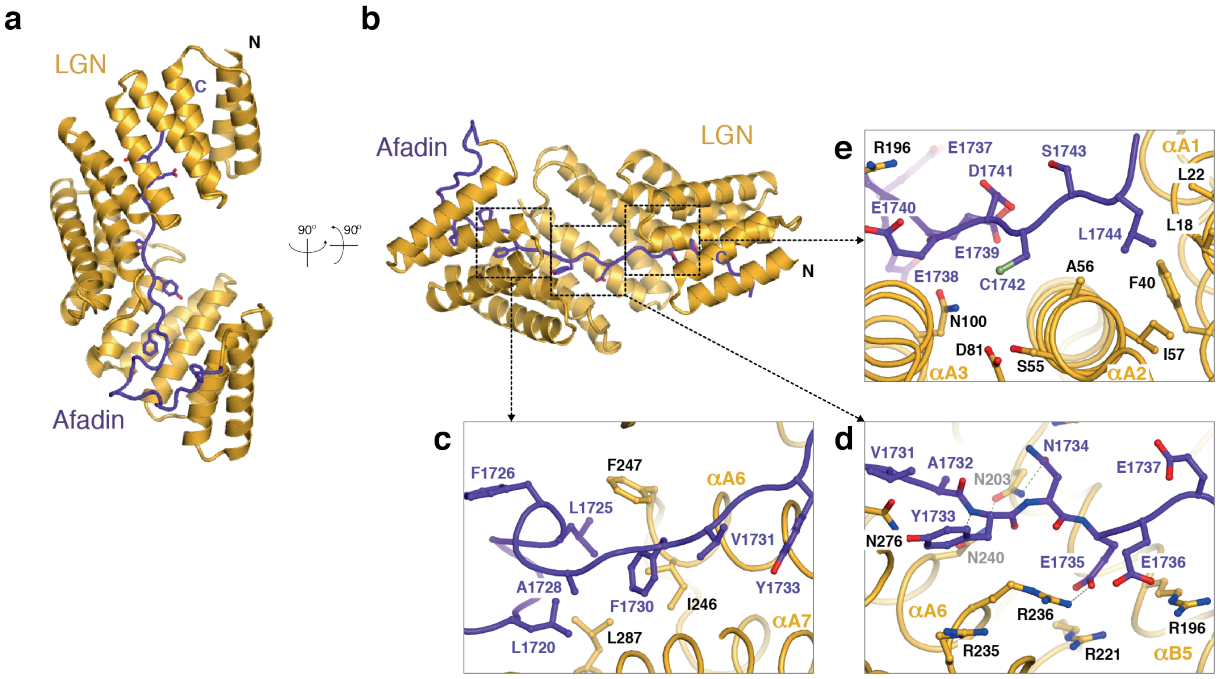

Fig. 18. Architecture of the LGN/Afadin interface. a,b) Cartoon representation of the LGN^{TPR}-Afadin^{PEPT} fusion protein viewed at the indicated orientations. LGN^{TPR} is depicted in gold, while Afadin^{PEPT} is in purple. The side-chains of key residues of Afadin protruding towards the LGN^{TPR} α-solenoid are shown in balls-and-sticks. **c,d,e**) Enlarged views of three modules of the interaction interface between LGN^{TPR} and Afadin^{PEPT}. The N-terminal region of the Afadin^{PEPT} organizes a hydrophobic pocket centered on Phe1730^{AF}, Leu246^{LGN} and Phe247^{LGN}, whereas the middle part of the Afadin peptide forms several hydrogen bonds and polar interactions mediated by negatively charged residues of Afadin and conserved arginines present on TPR5-6 of LGN. On the peptide C-terminal end, Cys1742^{AF} and Leu1744^{AF} fits in the grooves between TPR2-3 and TPR1-2 respectively.

The structure suggests that all three modules work together to dock the Afadin^{PEPT} onto the LGN^{TPR} scaffold. To identify the determinants of the interaction, I designed specific mutants on both sides of the dimer interface, and tested the residual binding in GST pull-down assays. Single substitution of either Phe1730^{AF} or Glu1735^{AF} with alanine abrogated binding to LGN^{TPR} (Fig. 19a). Consistently, double replacement of Ile246^{LGN}-Phe247^{LGN} to glutamic acids, or Arg235^{LGN}-Arg236^{LGN} to alanines completely abolished the interaction (Fig. 19b). FP experiments confirmed that the binding strength of the LGN^{TPR} mutants for Afadin^{PEPT} decreases 15 to 30-folds as compared to wild-type LGN^{TPR} (Fig.

19c). In summary, our structural analysis indicates that the LGN^{TPR} scaffold wraps around the Afadin^{PEPT}, and that the determinants of the interaction are Phe1730^{AF} and Glu1735^{AF}.

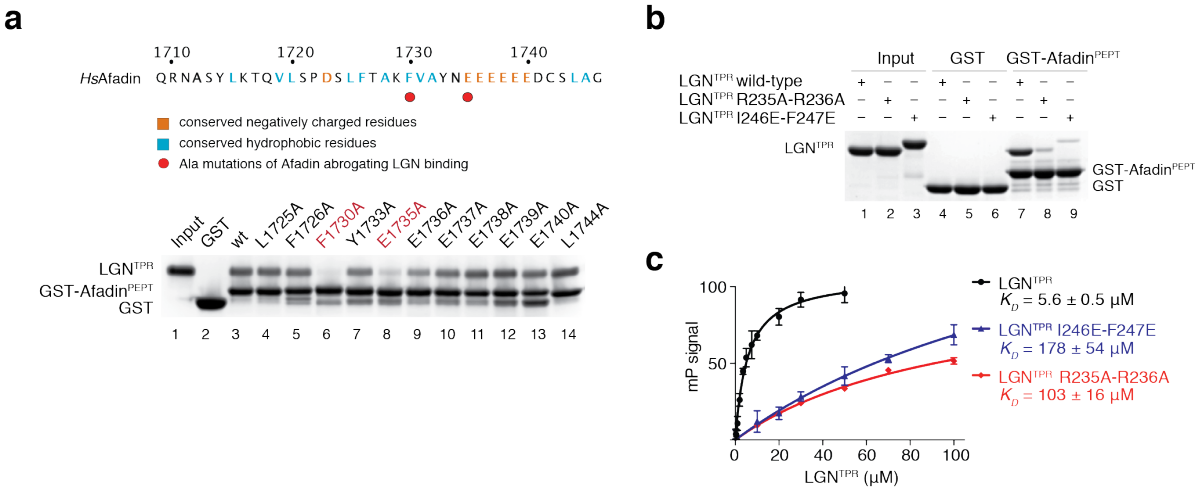

Fig. 19. Structure validation by mutational analysis. a) Top: Primary sequence of Afadin^{PEPT} colored according to conservation with hydrophobic and negatively charged residues colored in cyan and orange. Bottom: Biochemical validation of the Afadin-LGN interface by mutational analysis on GST-Afadin^{PEPT} carrying the indicated alanine substitutions. **b)** Analogous GST pull-down assays performed with LGN^{TPR} variants carrying double mutations in residues facing Phe1730^{AF} and Glu1735^{AF}. **c)** Fluorescence polarization measurements of the binding affinity between a synthetic fluorescein-labeled Afadin^{PEPT} and LGN^{TPR}, either wild-type or mutated on the LGN-Afadin interface.

Afadin and NuMA are competitive ligands of LGN

The overall conformation of the LGN^{TPR}-Afadin^{PEPT} chimera is reminiscent of the topology observed for LGN^{TPR} in complex with its interactors, such as mInsc [37], NuMA [36], and Frmpd1/4 [38, 39]. Indeed, structural superposition of LGN^{TPR}-Afadin^{PEPT} with LGN^{TPR} in complex with NuMA$^{1900\text{-}1928}$ (Fig. 20a, top) shows that Afadin interacts with LGN via residues whose side chain chemical properties are conserved in NuMA and in other LGN known ligands (Fig. 20a, bottom). This observation raised the question as two whether Afadin and NuMA compete for LGN binding. To address this question, I performed a SEC experiment in which I loaded simultaneously equimolar amounts of Afadin, NuMA and LGN on a Superdex-200 sizing column. Under these conditions,

LGN^{TPR} co-eluted with NuMA$^{1861-1928}$, while Afadin^{Cter} eluted in isolation in earlier fractions (Fig. 20b), indicating that Afadin and NuMA are competitive ligands of LGN, with NuMA displaying higher affinity. Of note, I obtained the same results for the *Drosophila* orthologs Canoe, Mud and Pins (Fig. 20c) supporting the notion that the relationship among these spindle orientation proteins is evolutionarily conserved.

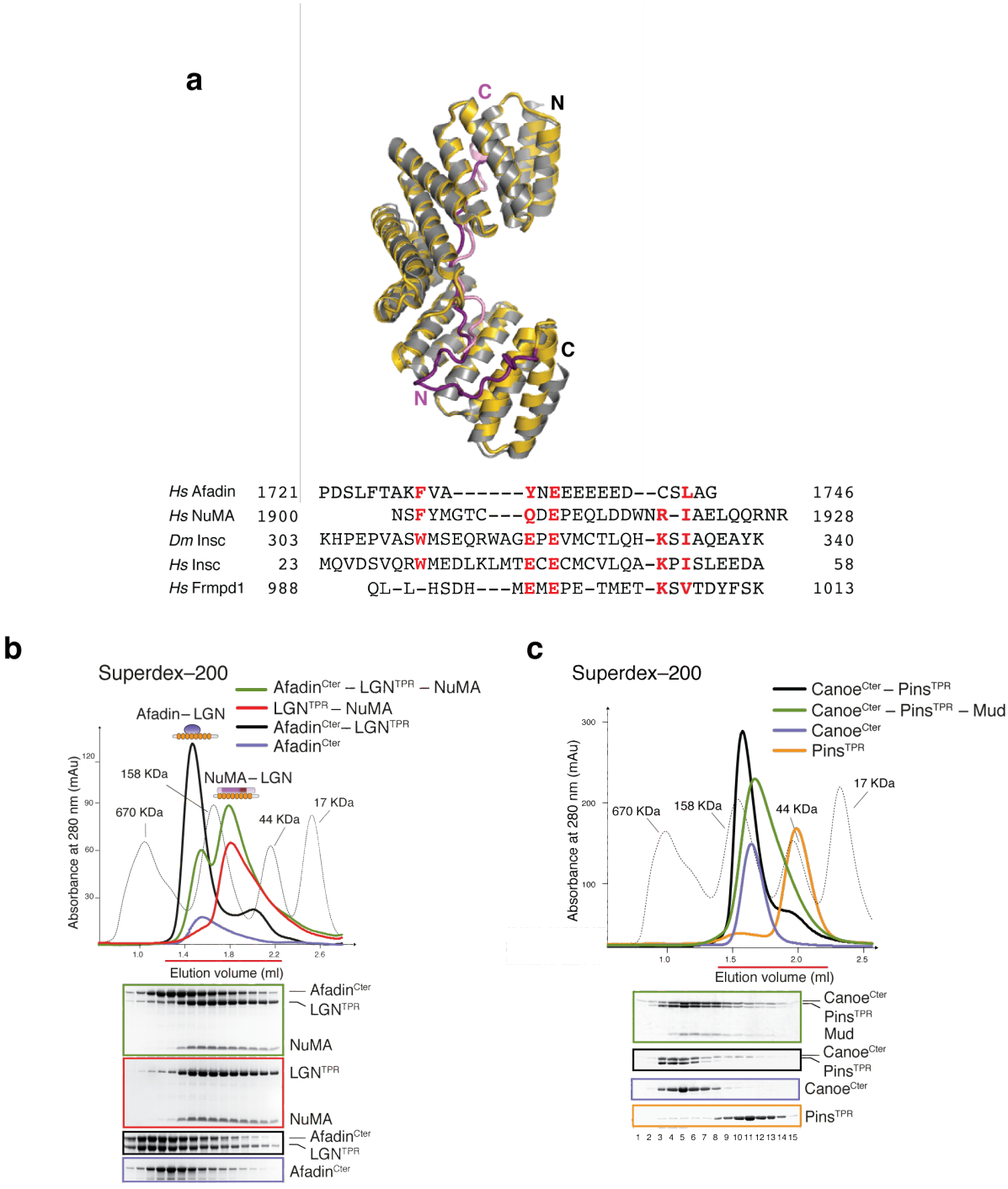

Fig. 20. Afadin and NuMA are competitive ligands of LGN. a) Structure superposition of LGN^{TPR}-Afadin^{PEPT} (gold-purple) with the LGN^{TPR}/NuMA$^{1900-1928}$ complex (gray/pink). **b)** Structure-based sequence alignment of the already known LGN^{TPR} ligands, and the newly

identified Afadin^{PEPT}. The conserved key residues for the interaction with LGN^{TPR} are highlighted in red. **c)** When loaded simultaneously on a SEC column in equimolar amounts, Afadin^{Cter}, LGN^{TPR} and NuMA$^{1861-1928}$ elute in two distinct peaks (green trace). The early eluting peak consists only of Afadin^{Cter}, while the slower migrating peak contains LGN^{TPR} in complex with NuMA$^{1861-1928}$. This result indicates that Afadin and NuMA are mutually exclusive ligands of LGN, with NuMA displaying higher affinity. **c)** SEC analysis showing Canoe^{Cter} enters a stoichiometric complex with Pins^{TPR} eluting in fractions 3-6 (black trace). Addition to the mix of equimolar amounts of Mud$^{1895-2094}$ results in a complex of Mud$^{1895-2094}$/Pins^{TPR} eluting slightly earlier than Canoe^{Cter} in isolation (fractions 4-7). This analysis demonstrates that the mutually exclusive interaction between NuMA and Afadin is conserved in the *Drosophila* orthologs.

Afadin recruits *MT-motors* to the cell cortex through LGN to drive mitotic spindle orientation

2.7 Afadin loss causes spindle misorientation in HeLa cells

To assess the functional role of the Afadin/LGN interaction on spindle orientation, Sara Gallini with the help of Laura Pirovano in our group, analyzed the effect of Afadin depletion in HeLa cells. Immunostaining of mitotic HeLa cells with a polyclonal antibody raised against Afadin^{Cter} revealed that Afadin localizes to the cell cortex from prometaphase to telophase, and that it in metaphase it co-localizes with LGN and NuMA in cortical regions above the spindle poles (Fig. 21a, top). To further analyze the spindle orientation functions of Afadin, we generated HeLa cell lines stably interfered for Afadin using two lentiviral short-hairpin vectors (shRNA-1/2) targeting human Afadin, with shRNA-2 being more efficient (not shown). For spindle orientation analyses, these HeLa cells were grown on fibronectin-coated slides, synchronized by single thymidine block, and imaged in the x-z plane by confocal microscopy (Fig. 8a). Under these conditions, wild-type HeLa cells divide with the spindle aligned to the substratum (α-angle, Fig. 21a, bottom), whereas cells with compromised orientation mechanisms undergo oblique divisions. Quantifications of the metaphase spindle angle revealed that wild-type HeLa cells divide with an average α-angle of 7.6°, while Afadin-depleted cells by the shRNA-2 showed a spindle randomization with 15.4° (Fig. 21a, bottom left and Fig. 21e). Together

these findings indicate that Afadin is essential for correct spindle orientation of HeLa cells in culture.

2.8 The LGN/Afadin interaction is required for cortical LGN/NuMA/Dynein localization, and proper metaphase spindle orientation

Correct spindle orientation relies on the recruitment of Dynein/Dynactin (*MT-motors*) at cortical sites, that in metaphase is mediated by $G\alpha_i$/LGN/NuMA complexes. Therefore, to understand the molecular contribution of Afadin to spindle orientation, we studied the effect of its depletion on the localization of LGN, NuMA and Dynein/Dynactin. Confocal images revealed that in wild-type HeLa cells LGN, NuMA and the Dynactin subunit $p150^{Glued}$ localize in a crescent above the spindle poles (Fig 21b, control). Conversely, in Afadin knock-down cells, the cortical localization of LGN is strongly decreased, and both NuMA and Dynactin completely disappear from the cortex (Fig. 21b, shRNA-2), indicating that Afadin is essential for the cortical recruitment of *MT-motors*. Based on the direct interaction between Afadin and LGN that I had uncovered, we hypothesized that Afadin might bring LGN to the cortex by interacting directly with its TPR-domain. To test this possibility, we performed spindle orientation rescue experiments in Afadin-depleted HeLa cell lines expressing sh-resistant Afadin mutants. As the LGN/Afadin interaction is contributed both by side-chains and by a number of main chain hydrogen bonds (Fig. 18), for the rescue experiments we decided to use an Afadin mutant lacking the whole LGN-binding peptide ($Afadin^{\Delta LGN}$). Spindle orientation analysis and immunostainings revealed that wild-type Afadin ($Afadin^{WT}$) restored LGN localization at the cortex as well as horizontal spindle orientation, while $Afadin^{\Delta LGN}$ mutant did not (Fig. 21c-e). These results indicate that in HeLa cells the interaction of Afadin with LGN mediates LGN-cortical recruitment, and instructs correct spindle orientation.

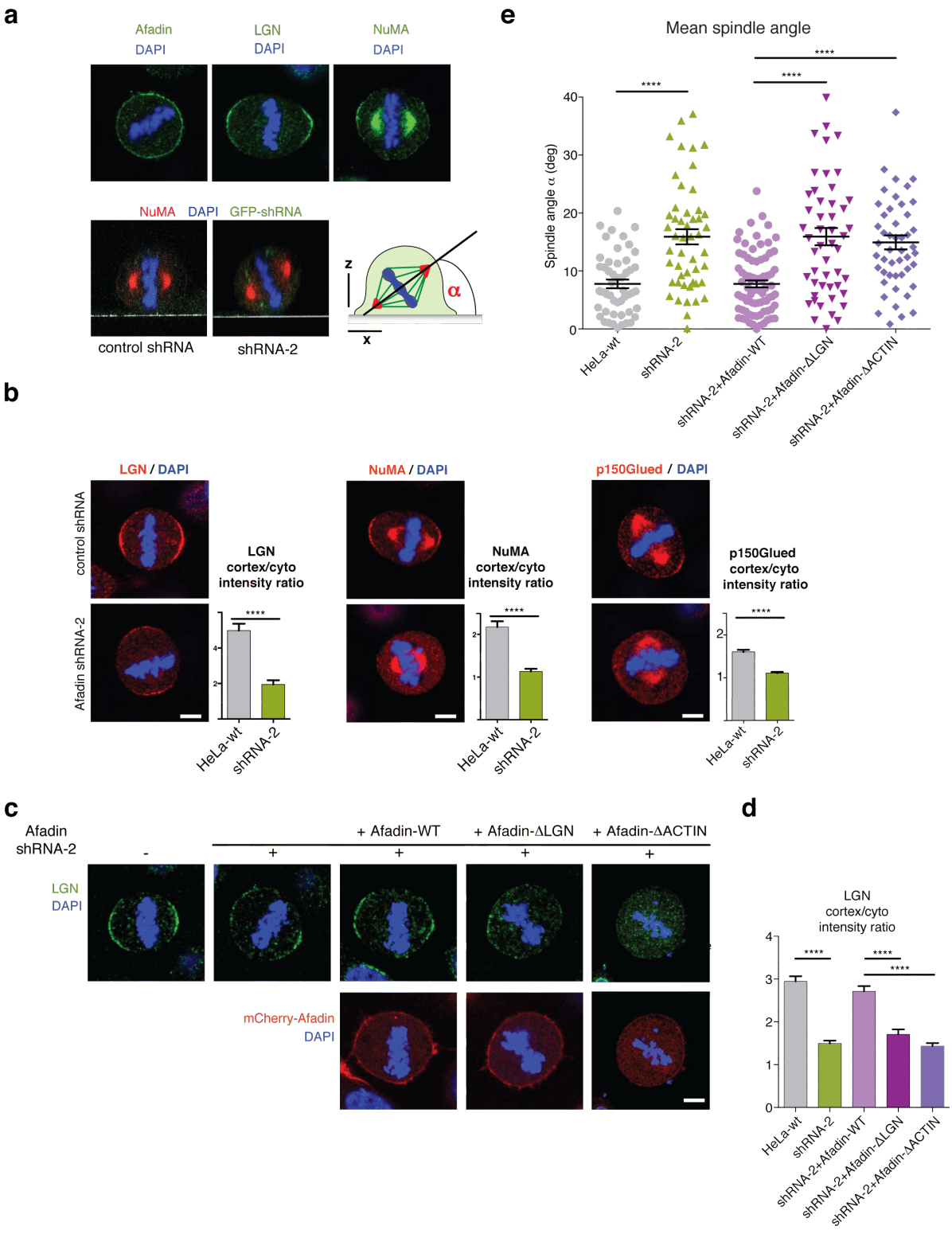

Fig. 21. The direct LGN/Afadin interaction is required for cortical LGN/NuMA/Dynein localization in metaphase, and proper spindle orientation.

a) Top. Cortical localization of endogenous Afadin, LGN, and NuMA in HeLa cells cultured on fibronectin-coated coverslips. Bottom. Representative confocal z-sections of mitotic HeLa cells infected with control or Afadin-targeting shRNAs stained for NuMA and DNA (DAPI). The plane of the coverslip is visible as a white line. The right panel shows a schematic representation of the experimental setting. **b)** Confocal sections of control shRNA (top) and Afadin shRNA-2 expressing

HeLa cells (bottom) in metaphase stained for LGN, NuMA, and p150^{Glued}. Bar graphs show quantification (mean + s.e.m.) of cortical signals from three independent experiments. ****P < 0.0001 by two-sided Mann-Whitney test. **c)** Rescue experiments of cortical LGN in HeLa cell lines stably depleted of endogenous Afadin, and transfected with shRNA-resistant rat mCherry-wild-type Afadin, Afadin lacking the LGN-binding domain (Afadin$^{\Delta LGN}$), or Afadin devoid of the actin-binding domain (Afadin$^{\Delta ACTIN}$). Bottom panels show the localization of the transfected mCherry-Afadin constructs. **d)** Quantification of cortical LGN in three independent rescue experiments (mean + s.e.m.). ****P < 0.0001 by two-sided Kruskal-Wallis test. **e)** Distributions of mitotic-spindle angles in metaphase for Afadin shRNA rescue experiments. Mean ± s.e.m. are shown for three independent experiments. ****P < 0.0001; by one-way ANOVA Tukey's test. Scale bars in **b)** and **c) are** 5 μm.

Afadin bridges the interaction between LGN and F-actin *in vitro* and *in vivo*

2.9 Afadin^{Cter} co-sediments with F-actin *in vitro*

As reported by previous studies, Afadin is an F-actin binding protein that links adherens junctions to the cell cortex. Importantly, F-actin is the main component of the cell cortex, which assembles at mitotic entry to mediate round-up [59]. Although increasing evidence points to a role of the acto-myosin cell cortex in mitotic spindle placement, a physical connection between F-actin and spindle orientation proteins is still missing. To understand whether the F-actin binding domain of Afadin is implicated in spindle orientation function, I characterized the F-actin binding activity of Afadin. First, I tested whether the Afadin^{Cter} construct interacting with LGN^{TPR} associates directly to F-actin. To this aim I performed high-speed co-sedimetation assays with Afadin^{Cter} concentrations ranging from 0.25 to 15 μM and 1 μM of polymeric F-actin. The supernatant (S) and pellet (P) fractions were analyzed separately by SDS-PAGE (Fig. 22a), and the amount of Afadin^{Cter} found in the pellet was quantified and plotted against the total concentration (see Mat. & Meth. section 5.5.1). Data fitting revealed that the binding between Afadin^{Cter} and F-actin occurs with a K_D of 3.8 ± 0.5 μM (Fig. 22b). As the Afadin^{Cter} sequence does not contain any known canonical actin-binding domain, I carried out an additional co-sedimentation experiment with two complementary fragments encompassing the entire C-terminal portion of Afadin

to restrict the F-actin interacting region. This experiment showed that the Afadin portion co-sedimenting with F-actin spans residues 1514-1682, just upstream the LGN binding site (Fig. 22c). Interestingly, SEC analysis revealed that the same Afadin^{Cter} construct does not enter a complex with globular (G) actin (Fig. 22d), even at 10-fold higher concentrations than the ones used in co-sedimentation assays, thus suggesting that Afadin recognizes specific features of the actin filaments' lattice.

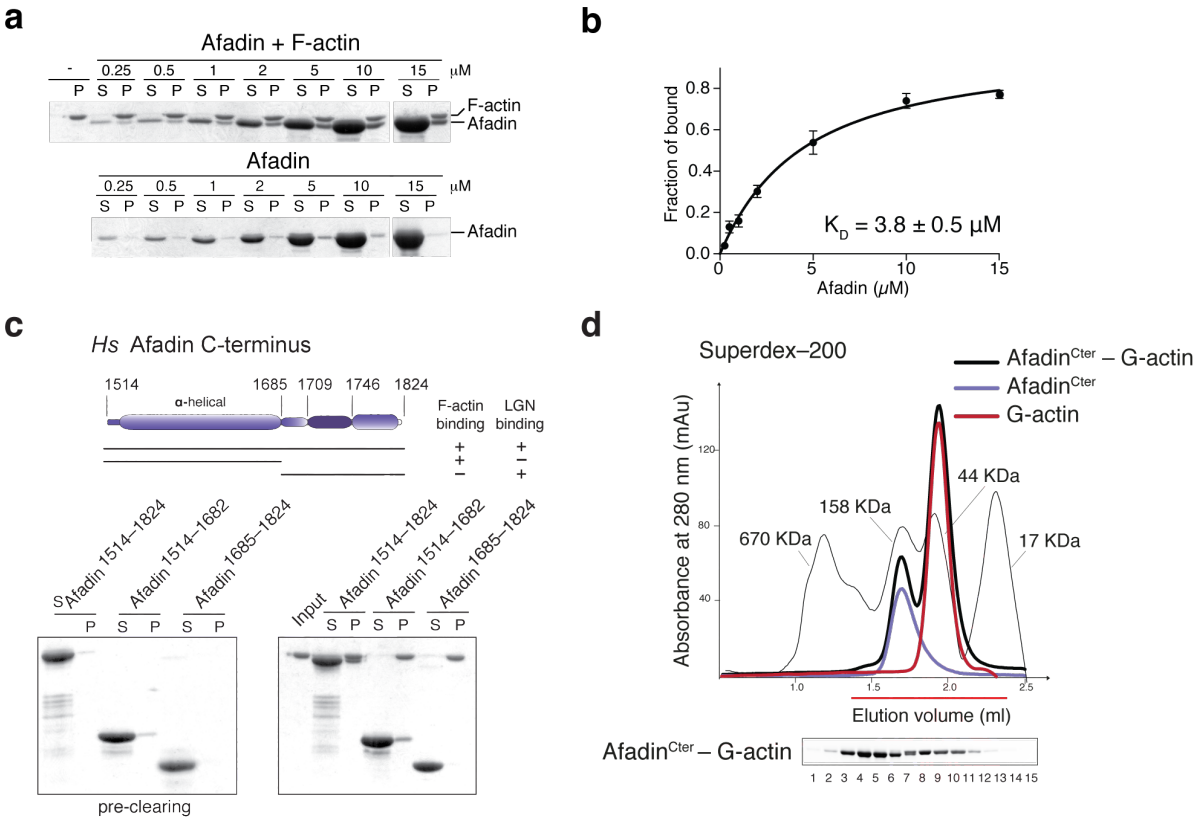

Fig. 22. Afadin^{Cter} co-sediments with F-actin *in vitro*. **a)** High-speed co-sedimentation of increasing concentrations of Afadin^{Cter} with 1 µM of F-actin. Coomassie-stained SDS-PAGE of pellet (P) and supernatant (S) fractions for each Afadin concentration. **b)** Quantification of the co-sedimentation assay by densitometric analysis. Error bars, s.d. (n = 3 independent experiments). **c)** High-speed co-sedimentation assay of two complementary fragments of Afadin^{Cter} (residues 1514-1824) with F-actin. Supernatant (S) and pellet (P) fractions of an analogous high-speed sedimentation experiment performed in the absence of F-actin are shown as a control of co-sedimentation specificity. **d)** SEC analysis and corresponding SDS-PAGE showing that at 150 µM concentration of both species Afadin^{Cter} and monomeric G-actin do not form a complex. The elution profiles of Afadin^{Cter} and G-actin are also shown as references for the individual runs. Despite having similar molecular weight, Afadin^{Cter} elutes near the globular 158 kDa marker (lanes 3-6 of the SDS-PAGE), whereas G-actin elutes in the later fractions 7-10.

2.10 Afadin co-sediments concomitantly with F-actin and LGN

The finding that the LGN and the F-actin binding domains of Afadin are physically separated prompted us to investigate the possibility that Afadin could bind simultaneously to LGN and F-actin. To this aim I co-sedimented Afadin^{Cter} with F-actin in the presence of LGN^{TPR}. As expected, LGN^{TPR} in isolation remained in the supernatant fraction, whereas it co-sedimented with F-actin in the presence of equimolar amounts of Afadin^{Cter} (Fig. 23a, top lanes 6-7,10-11). I then took advantage of the structural knowledge acquired to design mutants on either side of the Afadin^{Cter}/LGN^{TPR} complex impairing the interaction, namely Afadin$^{F1730E-E1735R}$ and LGN$^{R235A-R236A}$. Mutations disrupting the Afadin^{Cter}/LGN^{TPR} interface impaired LGN co-sedimentation with F-actin (Fig. 23a, top lanes 12-13) indicating that Afadin links directly LGN and F-actin *in vitro.*

2.11 Afadin bridges the interaction of LGN with the acto-myosin cell cortex

To prove that Afadin works as a physical anchor between LGN and cortical actin filaments also in cells, we treated mitotic HeLa cells with the actin-depolymerizing drug Latrunculin-A, which disrupts the acto-myosin cell cortex almost completely (Fig. 23b, left). Under these conditions Afadin detached from the plasma membrane and redistributed in the cytoplasm (Fig. 23b, middle), while LGN disappeared from the cortex to accumulate aberrantly on the spindle poles, as previously described [61] (Fig. 23b, right). Most importantly, expression in Afadin-depleted cells of an Afadin mutant devoid of the actin-binding region that I had identified *in vitro* (mCherry-Afadin$^{\Delta ACTIN}$) failed to rescue LGN cortical localization (Fig. 21c-d), and spindle orientation defects (Fig. 21e). Together, these data demonstrate that Afadin acts a mechanical bridge between the acto-myosin cortex and the spindle *MT-motors*.

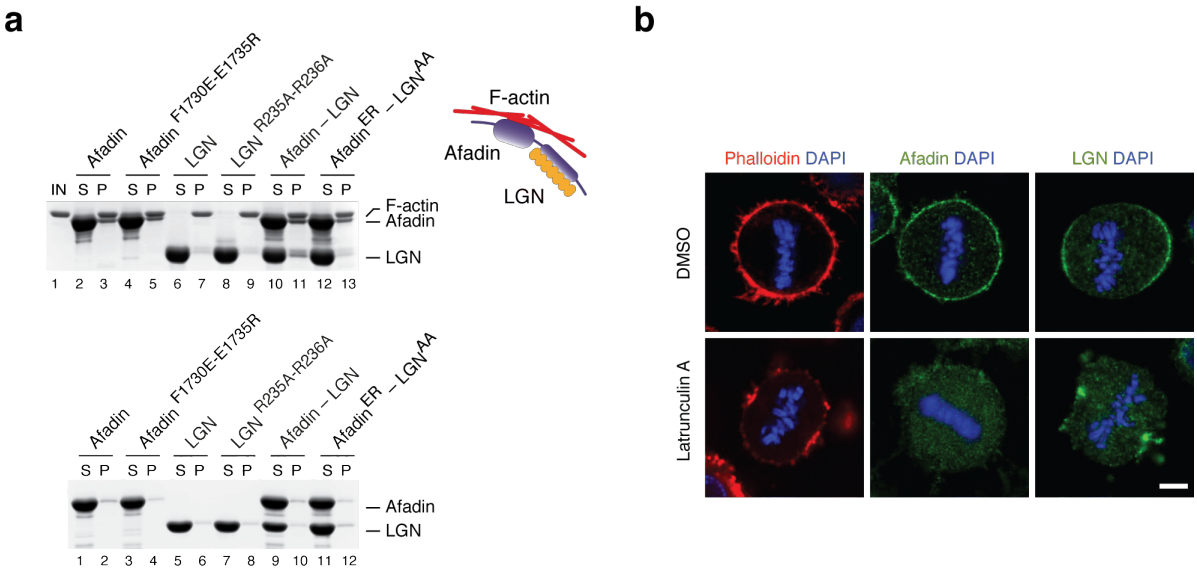

Fig. 23 Afadin bridges the interaction of LGN with F-actin *in vitro* and in cells. a) High-speed co-sedimentation performed at saturating concentrations of Afadin^{Cter} (9 µM) in the presence of equal amounts of LGN^{TPR}. Analyses were carried out with wild-type Afadin^{Cter} and LGN^{TPR} or with the mutants Afadin$^{F1730E\ E1735R}$ and LGN$^{R235A\ R236A}$. **b)** HeLa cells in metaphase treated with DMSO (top row) or 1 µM Latrunculin-A (bottom row), fixed and stained for actin (phalloidin), Afadin or LGN. Scale bar, 5 µM.

Afadin directs planar cell division and correct formation of Caco-2 cysts

Afadin is an adherens junction protein implicated in the formation of polarized epithelia. Thus, we decided to study the relevance of its role in spindle orientation during epithelial formation, when cell-to-cell junctions are present. To this aim we employed as a model system Caco-2 cells that in matrigel undergo planar divisions forming monolayered 3D cysts with the apical side facing the inner lumen (Fig. 24a-b, wild-type). Knock-down of Afadin in Caco-2 cells caused misoriented divisions, and the formation of multi-lumen cysts (Fig. 24a-b, shRNA-2). In summary, these findings suggest that Afadin is required for planar cell division and for correct epithelial morphogenesis.

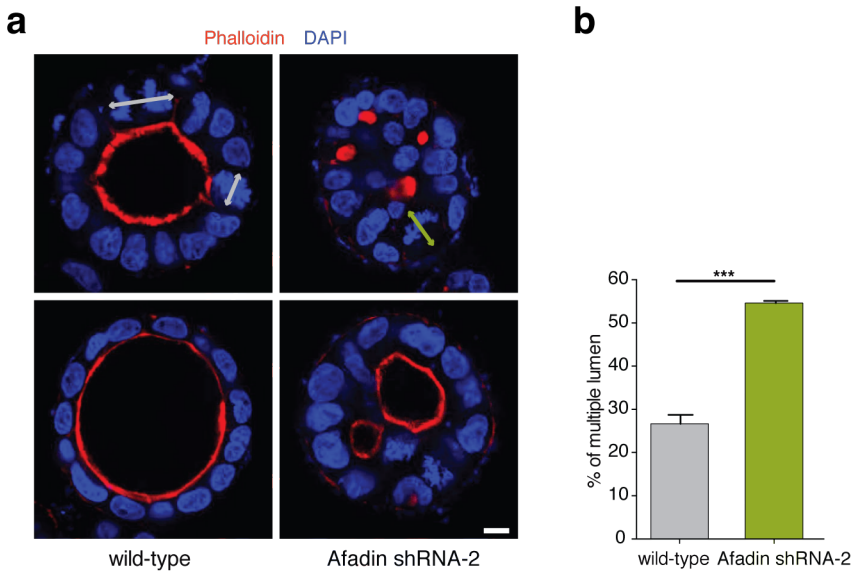

Fig. 24 Afadin directs Caco-2 planar cell divisions and correct cystogenesis. a) Confocal sections of the equatorial region of Caco-2 cysts grown from wild-type cells (left) or cells lacking Afadin (right). The orientation of the spindle axis in mitotic cells is indicated with double-arrowed lines. Scale bar, 10 μm. **b)** Quantification of defective cystogenesis as a percentage of cysts with a single lumen in wild-type or Afadin-ablated Caco-2 cells. Mean ± s.d. are shown. ***$P < 0.001$ by two-sided Fisher's exact test between control cysts and Afadin shRNA-2 expressing cysts.

3. RESULTS: NuMA and Aurora-A in spindle orientation

NuMA is one of the master regulators of spindle orientation, which also plays essential functions in spindle organization and maintenance [110]. At mitotic entry, NuMA localization and activities are tightly regulated by Ran-GTP signaling [111] and by several phosphorylation events. In metaphase, it localizes both at the spindle poles and at the cortex [26]. Recently, a proteomic screening identified NuMA among the mitotic targets of Aurora-A kinase [99]. Like NuMA, in mitosis Aurora-A localizes at the spindle poles where it promotes spindle organization by controlling MT nucleation and dynamics. However, the functional relevance of the phosphorylation of NuMA by Aurora-A is still unclear. We thus set out to investigate the role of the crosstalk between NuMA and Aurora-A biochemically and in cells. For this project Sara Gallini and Laura Pirovano carried out the cell biology experiments, while I validated their findings at the molecular level with different biochemical approaches.

Mitotic inhibition of Aurora-A causes aberrant accumulation of NuMA at the spindle poles and spindle misorientation

To analyze the contribution of Aurora-A to spindle orientation, we established cell culture conditions in which the kinase was either partially inhibited or silenced. Treatment of HeLa and non-transformed hTERT-RPE-1 cells with 50 nM of the Aurora-A chemical inhibitor MLN8237 or depletion of Aurora-A by small-interfering oligos (siRNAs) caused spindle misalignment compared to control cells (Fig. 25a). Under these conditions, in HeLa cells LGN cortical recruitment in metaphase was unaltered (not shown), whereas NuMA enriched aberrantly at the spindle poles and was lost from the cortex (Fig. 25b), indicating that Aurora-A activity is required for the correct localization of NuMA in metaphase. Importantly, artificial tethering of NuMA to the plasma membrane by the generation of a GFP-NuMA-LGN^{GoLoco} chimeric protein was able to by-pass the requirement of Aurora-A for correct orientation, indicating that cortical localization of

NuMA with $G\alpha_i$ is both sufficient and necessary to ensure correct spindle orientation (Fig. 25c). Together these findings suggest that Aurora-A regulates mitotic spindle orientation by controlling NuMA distribution in metaphase.

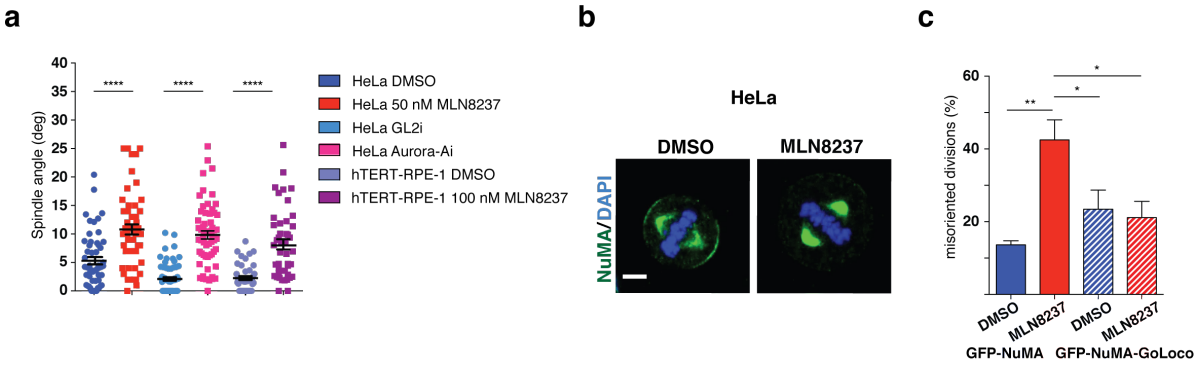

Fig. 25 Mitotic inhibition of Aurora-A causes aberrant accumulation of NuMA at the spindle poles and spindle misorientation. a) Scatter plots illustrating the distribution of the angle measured between the spindle axis and the plane of the coverslip in HeLa cells treated with DMSO or 50 nM MLN8237; GL2i or Aurora-Ai, and hTERT-RPE-1 cells treated with DMSO or 100 nM MLN8237. For the scheme of the experimental setting please see Fig. 21a (bottom, right). Means ± SEM are shown; n > 40 from three independent experiments; for all conditions. ****: $p < 0.0001$. **b)** Immunofluorescence analysis of endogenous NuMA (green) in HeLa cells treated with DMSO or MLN8237. **c)** Quantification (%) of misoriented divisions of HeLa cells expressing GFP-NuMA or GFP-NuMA^{GoLoco} and treated with DMSO or MLN8237. The position of the spindle poles (detected by GFP signal) was monitored by DIC in video-recording time-lapse experiments. Means ± SEM; for all conditions n > 45 from three independent experiments. *$p < 0.05$; *ns*: non-significant statistical difference by unpaired t test.

Aurora-A phosphorylates NuMA to control its localization in metaphase and spindle orientation

3.1 Aurora-A phosphorylates NuMA^{Cter} *in vitro*

To investigate how Aurora-A controls NuMA distribution in mitosis, I started testing whether NuMA could be phosphorylated directly by the kinase. To this aim we focused on the C-terminal portion of NuMA, starting right after the coiled-coil region. We chose the fragment encompassing residues 1821-2115 (NuMA^{Cter} hereon) (Fig. 26a, top) that is monomeric, unable to dimerize with endogenous NuMA, and contains three serines

conforming to the Aurora-A consensus site R/K-X-S/T- Φ, where Φ stands for a hydrophobic residue, while X for any residue [112, 113] (Fig. 26a, bottom). After cloning NuMA^{Cter} into a bacterial expression vector, I purified the protein to homogeneity before subjecting it to an *in vitro* kinase assay with the purified kinase domain of Aurora-A. To analyze the effect of Aurora-A phosphorylation, we decided to use Phos-TAG SDS-PAGEs that delay the runs of phosphorylated bands resulting in a shift to higher molecular weights. This technique is based on the association of the Phos-TAG chemical to the phospho-groups of proteins within the separating gel. Upon incubation with the kinase, NuMA^{Cter} showed three slow-migrating bands compared to unmodified NuMA^{Cter} (Fig. 26b, lanes 1-2). To prove that those bands resulted from Aurora-A phosphorylation I repeated the kinase assay in the presence of 1 mM MLN8237 that was able to revert the phosphorylation completely (Fig. 26b, lane 3). Consistent with previous studies [99], mass spectrometry analysis of the slow-migrating bands confirmed that phosphorylation occurs on the three predicted serines at position 1969, 1991, and 2047. Indeed, when I repeated the experiment with a mutant version of NuMA^{Cter} on which the three serine phosphosites were mutated into alanines (NuMA^{3Ala}), no shifted bands appeared on the Phos-TAG^{TM} PAGE upon addition of Aurora-A (Fig. 26, lanes 4-6). These results showed that Aurora-A phosphorylates directly NuMA^{Cter} on Ser1969, 1991 and 2047 *in vitro*.

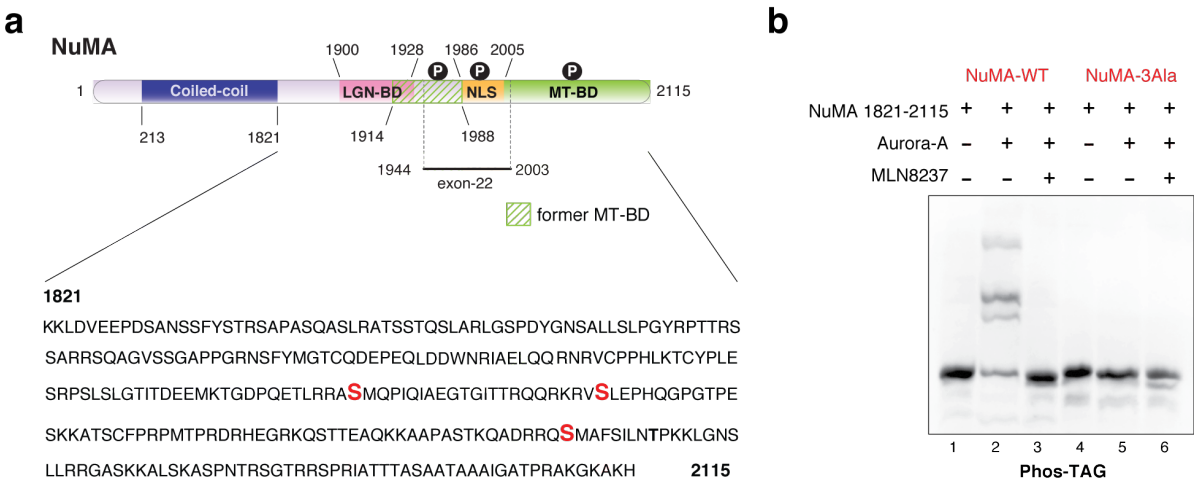

Fig. 26. Aurora-A phosphorylates NuMA^{Cter} *in vitro.* a) Schematic representation of the domain structure of NuMA, enlarged on the C-terminal portion spanning residues 1821-2115 (NuMA^{Cter} in the text and below). Fragments with known functions are highlighted with different colors including the LGN-binding domain (residues 1900-1928, pink), the *former* MT- binding domain (residues 1914-1985, dashed green) and the nuclear localization signal (NLS, residues 1986-2005, orange). The MT-binding domain identified in our study (see paragraph 3.7) encompassing residues 2002-2115 is in green. In the primary sequence of NuMA^{Cter}, the Aurora-A phospho-serines Ser1969, Ser1991 and Ser2047 are in red. **b)** Coomassie blue-stained Phos-TAG SDS-PAGE of the *in vitro* kinase assay performed with the purified kinase domain of Aurora- A and NuMA^{Cter} wild-type (NuMA-WT), or with Ser1969, Ser1991 and Ser2047 mutated into alanine (NuMA-3Ala). Samples in lanes 3 and 6 contained 1 mM MLN8237 in the reaction buffer. The purified NuMA^{Cter} samples used as substrates are loaded in lane 1 and 4 as controls.

3.2 NuMA phosphorylation on Ser1969 controls its localization in metaphase

To address the relevance of the identified phosphosites in cells, we generated HeLa cells stably expressing mCherry-NuMA^{Cter} either wild-type or carrying alanine-mutations in the three identified serines, singularly or in combination. The mitotic localization of the mutants was then analyzed, and the signal at the spindle poles quantified. In unperturbed conditions, mCherry-NuMA^{Cter} wild-type localized both at the spindle poles and at the cortex, while it accumulated aberrantly on the spindle poles upon treatment with MLN8237 (Fig. 27a-b, WT). Conversely, the constructs carrying single substitution of Ser1969Ala or substitution of all three the serines into alanines (3Ala) showed a constitutive accumulation at the spindle poles even in control cells, and became insensitive to MLN8237 treatment (Fig. 27a-b, S1969A and 3Ala). Together these results indicate that Aurora-A phosphorylates NuMA on Ser1969 to regulate its polar accumulation in metaphase. Based on these observations, we hypothesized that Ser1969 might serve as priming site to allow the subsequent phosphorylation of Ser1991 and Ser2047. To test this possibility I compared the phosphorylation kinetics of NuMA^{Cter} and NuMA^{Cter}-S1969A in an *in vitro* phosphorylation time-course experiment. The kinase reactions were stopped at different time points and separated by Phos-TAG SDS-PAGE, revealing that the phosphorylation patterns of NuMA^{Cter} and NuMA^{Cter}-S1969A were identical (Fig. 27c). This experiment demonstrated that the Ser1969 of NuMA does not work as a priming site, but rather it is the main phosphorylation event underlying Aurora-A-mediated control of NuMA localization.

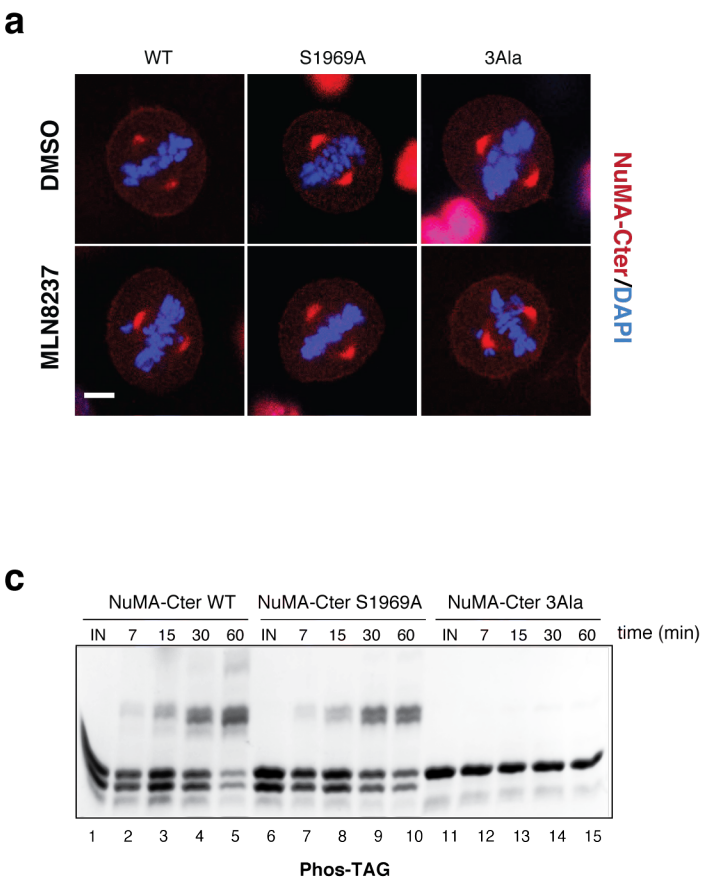

Fig. 27. NuMA phosphorylation on Ser1969 controls its localization in metaphase. a) Confocal images of metaphase HeLa cells stably expressing mCherry-NuMA^{Cter} wild-type, or carrying either S1969A or S1969-S1991-S2047 mutated into alanine (3Ala). Representative images from cultures treated with DMSO (top) or 50 nM MLN8237 (bottom) are shown. **b)** Quantification of the mCherry fluorescence ratio between poles and cytosol in the experimental conditions of panel **a)** (means ± SEM; n > 20 from three independent experiments). **c)** Time-course of NuMA^{Cter} wild type, S1969A, or 3Ala *in vitro* phosphorylation by Aurora A. Reactions were stopped at different time points and analyzed by Phos-TAG SDS-PAGE.

3.3 Phosphorylation on Ser1969 of NuMA controls its mobility at spindle poles and spindle orientation

Based on our observations, it seemed that upon Aurora-A inactivation NuMA was physically trapped on spindle poles, thus reducing the cytosolic fraction available for interaction with cortical LGN in metaphase. To test this possibility, we decided to measure the mobility of full-length NuMA (NuMA-FL-WT) at the spindle poles by Fluorescence Recovery After Photobleaching (FRAP) analysis in Aurora-A inhibited conditions. To

evaluate the effect of Aurora-A inhibition on the cycling rate of NuMA-FL at the spindle poles, we used mitotic HeLa cells transiently transfected with GFP-NuMA. We photobleached the GFP-NuMA signal at one of the two spindle poles in DMSO or MLN8237-treated cells in metaphase, and monitored the dynamics of FRAP recovery (Fig. 28a, top) (see Mat. & Meth section 5.7.5). By comparing the half-time of the recovery and the mobile fraction of bleached GFP-NuMA in untreated cells with those of Aurora-A-inhibited cells, we found that the turnover of NuMA at the spindle poles is significantly slower in MLN8237-treated cells (Fig. 28a, bottom left). In addition, in the same inhibited conditions, the GFP-NuMA fluorescence intensity at the plateau diminished compared to control cells indicating a reduction of the mobile fraction of NuMA at the spindle poles (Fig. 28a, bottom right). To address the relevance of the phosphorylation on Ser1969 for NuMA polar accumulation, we expressed mCherry-NuMA-FL either WT or S1969A in HeLa cells stably depleted for endogenous NuMA, and repeated the FRAP experiments (Fig. 28b, top). While the half-time of recovery of mCherry-NuMA-WT was undistinguishable from the one previously measured for GFP-NuMA-WT, mCherry-NuMA-S1969A displayed a slower-rate (Fig. 28b, bottom left). Most importantly, the mobility of mCherry-NuMA-S1969A (Fig. 28b, bottom right) mirrored the one observed for GFP-NuMA-WT in cells treated with MLN8237, indicating that Ser1969-phosphorylation governs the correct cycling rate of NuMA at the spindle poles in metaphase. To understand whether the spindle misorientation phenotype observed upon treatment of HeLa cells with MLN8237 arises from the lack of NuMA phosphorylation on Ser1969, we set out to perform spindle orientation rescue experiments in NuMA-depleted HeLa cells with either mCherry-NuMA-WT or mCherry-NuMA-S1969A. Spindle angle analysis revealed that while WT NuMA could revert completely spindle placement defects, the phospho-mutants could not (Fig. 28c). In conclusion, our data indicate that Aurora-A contributes to spindle orientation by controlling NuMA accumulation on the spindle poles through phosphorylation on Ser1969.

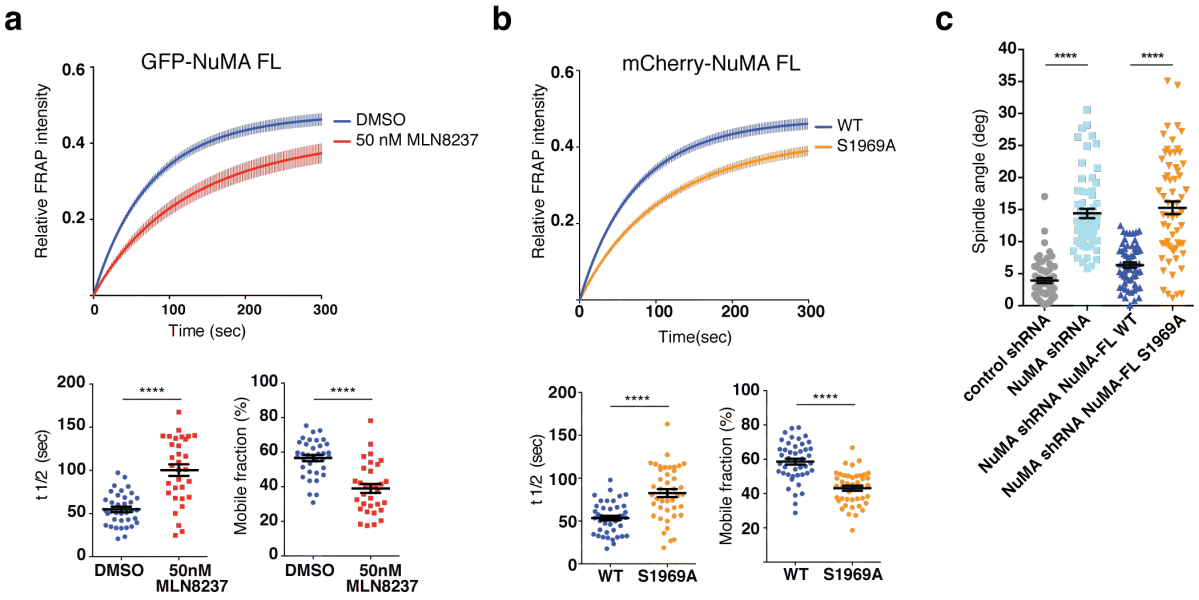

Fig. 28. Phosphorylation on Ser1969 of NuMA controls its mobility at spindle poles and spindle orientation. a) FRAP analysis in HeLa cells of full-length GFP-NuMA in the presence of DMSO or MLN8237. Recovery profiles of bleached GFP spindle poles signal over 5 minutes are plotted (top). The dot-plots (bottom) show the distribution of $t_{1/2}$ (sec) and the mobile fraction (%) of GFP-NuMA at the spindle poles (means ± SEM; n > 40 from three independent experiments). In all statistical analyses, ****: $p < 0.0001$ by unpaired t test. All scale bars: 5 μm. **b)** FRAP analysis in NuMA-ablated HeLa cells transiently transfected with full-length mCherry-NuMA wild-type or S1969A mutant. Recovery profiles of bleached mCherry spindle poles signal plotted over 5 min (left). Dot plots (right) show the distribution of $t_{1/2}$ (sec) and the mobile fraction (%) of mCherry-NuMA proteins at the spindle poles (means ± SEM; n > 44 from three independent experiments). ****$p < 0.0001$ by unpaired t test. **c)** Quantification of mitotic spindle angle of NuMA-depleted HeLa cells transiently transfected with full-length mCherry-NuMA wild-type or S1969A mutant. Means ± SEM; n > 50 from three independent experiments. ****$p < 0.0001$ by Kruskal-Wallis test.

Binding of NuMA to MTs and to LGN is independent of Aurora-A activity

3.4 Phosphorylated NuMA co-sediments with MTs

Starting from the observation that Aurora-A inhibition causes an accumulation of NuMA on the spindle poles, we reasoned that a receptor for NuMA at the spindle poles might exist, whose affinity is modulated by Aurora-A. Interestingly, the phosphosite Ser1969 that we had identified as the major determinant of NuMA mobility at the spindle poles, lies in a region previously reported to bind MTs spanning residues 1914-1985 [95, 96] (Fig. 26a,

dashed green). Thus, we decided to test whether the affinity of NuMA for MTs changes upon phosphorylation. To this purpose I performed *in vitro* co-sedimentation experiments of NuMA^{Cter} with taxol-stabilized MTs. Analysis of the supernatant (S) and pellet (P) fractions upon ultracentrifugation allows the detection of the direct binding between purified proteins and MTs (Fig. 29a). S and P samples separation on Phos-TAG SDS-PAGE revealed that neither phosphorylation of NuMA^{Cter} by Aurora-A, nor the phospho-mimetic replacement of the Ser1969, 1991 and 2047 with aspartic acids affected the binding to MTs *in vitro* (Fig. 29, lanes 9-10 and 11-12). To understand if this finding holds true also in cells, I performed a co-sedimentation experiment on lysates of mitotic HeLa cells stably expressing mCherry-NuMA^{Cter}, treated or not with 50 nM MLN8237. For a better comparison of the binding affinities, I conducted the experiment in the presence of increasing concentrations of taxol-stabilized MTs. SDS-PAGE separation of S and P fractions followed by immunoblotting with an antibody against NuMA revealed that NuMA binds MTs to the same extent in untreated and in MLN8237 treated cells (Fig. 29b, lanes 1-2 and 7-8). These results indicate that Aurora-A-mediated phosphorylation on Ser1969 of NuMA does not influence the affinity of the protein for MTs.

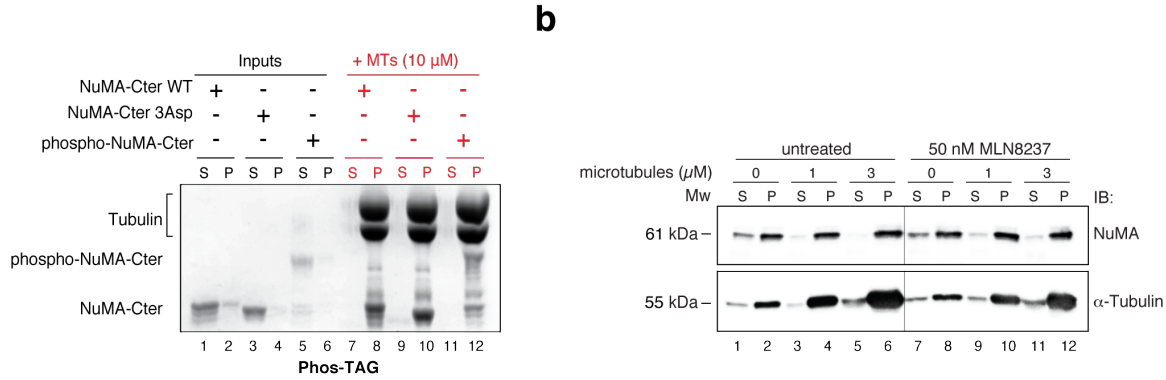

Fig. 29. Phosphorylated NuMA co-sediments with MTs. a) Co-sedimentation of 2 µM NuMA^{Cter} with 9 µM polymeric tubulin (MTs). Wild-type NuMA^{Cter} unmodified or phosphorylated by Aurora-A, and NuMA^{Cter}-3Asp (S1969-S1991-S2047 replaced with Asp) were tested. The supernatant (S) and pellet (P) fractions were analyzed on a Phos-TAG SDS-PAGE followed by Coomassie staining (lanes 7-12). The solubility of NuMA^{Cter} in the absence of microtubules was tested (lanes 1-6). **b)** Lysates of prometaphase-arrested mCherry-NuMA^{Cter}–expressing HeLa cells

were co-sedimented with increasing amounts of exogenous microtubules. The MT-binding ability of mCherry-NuMA^{Cter} was assessed in untreated (lanes 1-6) and 50 nM MLN8237-treated (lanes 7-12) lysates. NuMA^{Cter} and MTs in the pellet (P) and supernatant (S) fractions were detected by immunoblotting using anti-NuMA and anti-α-tubulin antibodies.

3.5 Phosphorylation of NuMA does not affect its MT-bundling activity

Previous studies showed that dimeric GST-NuMA constructs encompassing the MT-binding domain mediate MT-bundling [96, 114, 115]. To explore the possibility that Aurora-A phosphorylation could affect the MT-bundling ability of NuMA, I generated a dimerizing GST-fusion construct of NuMA^{Cter} and of its two complementary sub-fragments spanning residues 1821-2001 and 2002-2115, respectively (Fig. 30a). I then tested these fragments in an *in vitro* MT-forming assay, in which a mixture of unlabeled:rhodaminated tubulin was incubated with the proteins of interest without taxol-induced stabilization. The ability of such NuMA fragments to favor MT-formation from α/β-tubulin heterodimers was then analyzed by wide-field microscopy. Using this approach, I found that GST-NuMA^{Cter} and GST-NuMA$^{2002-2115}$ not only promoted MT formation but also bundled MTs efficiently, regardless of Aurora-A activity. On the other hand GST-NuMA$^{1821-2001}$ only induced polymerization of short MTs, similar to the ones observed in the GST control (Fig. 30b). This evidence indicates that the MT-binding and bundling abilities of NuMA are not affected by Aurora-A phosphorylation, and at the same time reveals that the spindle pole accumulation of NuMA observed upon inhibition of the kinase occurs via receptors other than MTs.

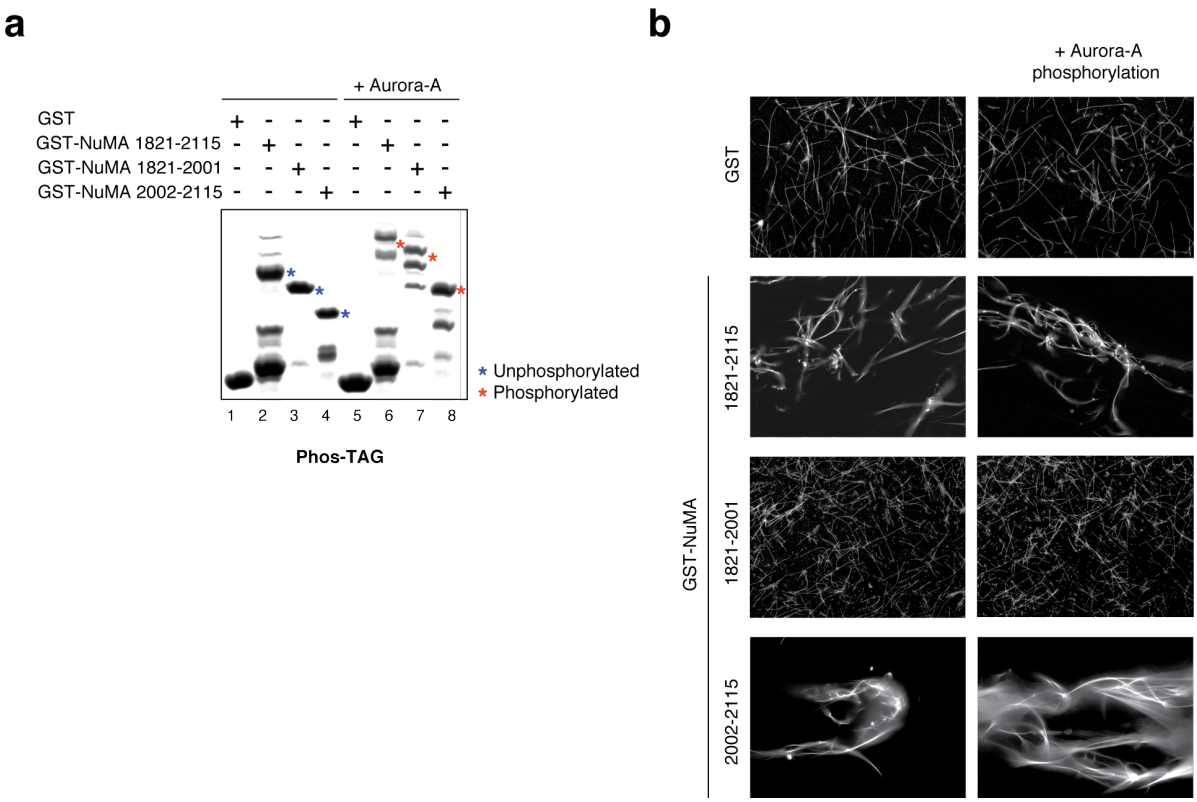

Fig. 30. Phosphorylation of NuMA does not affect its MT-bundling activity. **a)** Coomassie stained Phos-TAG SDS-PAGE of the GST-NuMA^{Cter} fragments used in the *in vitro* bundling assays used in **b)**. Unmodified species are indicated with blue asterisks (lanes 2-4), whereas Aurora-A phosphorylated corresponding bands are marked with red asterisks (lanes 6-8). **b)** Representative images of *in vitro* microtubule bundling assays performed with rhodamine labeled tubulin in the presence of GST-NuMA$^{1821-2115}$, GST-NuMA$^{1821-2001}$ and GST-NuMA$^{2002-2115}$, or GST as control. Experiments were performed both with unmodified (left panels) and phosphorylated NuMA fragments.

3.6 Phosphorylation of NuMA does not increase LGN-binding affinity

Another hypothesis that might explain the reduction of cortical NuMA upon Aurora-A inhibition would be that NuMA phosphorylation is required for its direct binding to LGN. It is known that LGN recognizes a portion of NuMA^{Cter} encompassing residues 1900-1928 with the N-terminal TPR-domain [36], and that this interaction is required for spindle orientation in metaphase [27]. To test whether Aurora-A activity could influence NuMA/LGN binding affinity, I performed a GST pull-down assay with 1 µM GST-LGN^{TPR} immobilized on GSH beads and 2 µM phosphorylated NuMA^{Cter} in solution, and

found that the amount of NuMA retained on beads was unchanged upon Aurora-A phosphorylation (Fig. 31, lane 12). Thus I concluded that the Aurora-A does not control the cortical enrichment of NuMA by altering the NuMA/LGN affinity. I further confirmed this result by repeating the GST pull-down experiment with 2 μM of the phospho-mimetic $NuMA^{Cter}$-3Asp in solution (Fig. 31, lane 11), which also did not show increased affinity for LGN.

Identification of a new NuMA MT-binding domain downstream the LGN binding site

3.7 $NuMA^{2002-2115}$ co-sediments with MTs

The unexpected finding that the construct $NuMA^{1821-2001}$ encompassing the *previously identified* MT-binding domain (Fig. 26a, dashed green) was unable to bundle MTs prompted us to evaluate the MT-binding ability of this fragment in a co-sedimentation assay, in parallel with $NuMA^{Cter}$ and $NuMA^{2002-2115}$. Upon ultracentrifugation and SDS-PAGE analysis, I found that both $NuMA^{Cter}$ and $NuMA^{2002-2115}$ co-sedimented with taxol-stabilized MTs (Fig. 32a, lanes 7-8 and 11-12), while $NuMA^{1821-2001}$ remained in the supernatant fraction (Fig. 32a, lanes 9-10). This result identifies a new MT-binding domain of NuMA spanning residues 2002-2115.

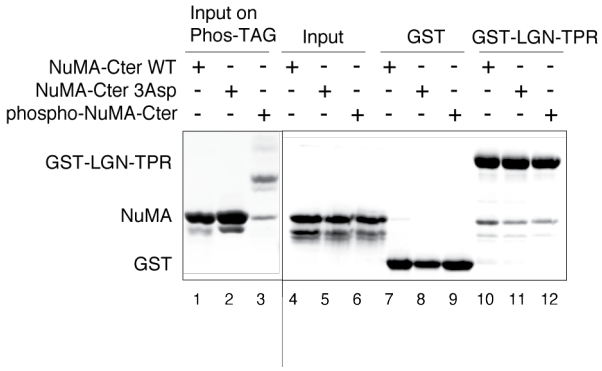

Fig. 31. Phosphorylation of NuMA does not increase LGN-binding affinity. a) *In vitro* pull-down assay performed with GST-LGN^{TPR} adsorbed on glutathione beads and purified NuMA^{Cter} in solution. After washes, species retained on beads were separated by SDS-PAGE and Coomassie-stained. The NuMA^{Cter} samples used in the pull-down experiment were also separately loaded on a Phos-TAG SDS-PAGE to monitor their phosphorylation status (lanes 1-3).

3.8 NuMA co-sediments simultaneously with MTs and LGN

The fact that the newly identified MT-binding domain lies downstream of the LGN-binding stretch (Fig. 26a, green) rather than overlapping with it as previously reported [96], raised the question as to whether a single molecule of NuMA could associate with LGN and MTs at the same time. To test this idea, I repeated the MT-co-sedimentation assay with NuMA^{Cter} and its two subdomains in the presence of equimolar amounts of LGN^{TPR}. As expected, LGN^{TPR} in isolation was found in the supernatant, while it sedimented into the pellet with MTs in the presence of NuMA^{Cter} (Fig. 32b, lanes 9-12). On the other hand, LGN^{TPR} did not sediment with MTs in the presence of NuMA$^{1821-2001}$ that is unable to bind MTs (Fig. 32b, lanes 13-14), nor with NuMA$^{2002-2115}$, that does not contain the LGN binding site (Fig32b, lanes 15-16). Collectively, these experiments identifies a MT-binding region at the very C-terminus of NuMA that is compatible with the concomitant binding of NuMA to LGN and to MTs.

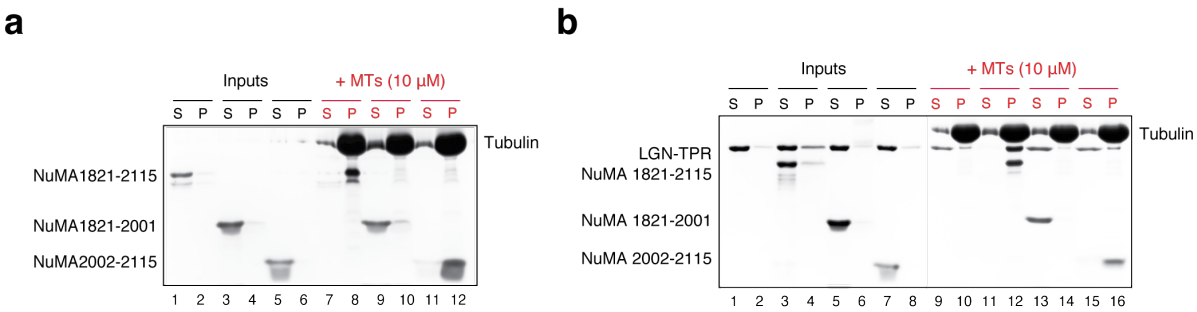

Fig. 32. NuMA co-sediments simultaneously with MTs and LGN. a) Co-sedimentation of the NuMA^{Cterm} fragments (2 µM) used in the bundling assay of Fig. 30b, in the presence of 9 µM MTs. The supernatant (S) and pellet (P) fractions were analyzed on SDS-PAGE followed by Coomassie staining (lanes 7-12). The solubility of the NuMA^{Cter} fragments in the absence of microtubules was tested (lanes 1-6). **b)** MT-co-sedimentation assay performed as in **a)** in the presence of 1 µM LGN^{TPR}.

3.9 Direct binding of NuMA to MTs is not required for its polar localization

The experiments described so far excluded that NuMA phosphorylation on Ser1969 could control its polar accumulation by affecting the affinity for MTs. This finding is consistent with the notion that the new MT-binding domain I have identified does not include Ser1969. Thus, we asked whether the portion of NuMA encompassing Ser1969 was implicated in NuMA localization at the spindle poles. Of note, previous studies reported that the mouse NuMA fragment coded by exon-22 (exon-24 spanning residues 1944-2003 in *hs* NuMA), is essential for centrosome tethering to astral MTs. Indeed, these studies showed that removal of exon-22 in the mouse NuMA gene generates a protein unable to localize at the spindle poles [97]. Based on this observation, we transfected HeLa cells with three NuMA constructs encompassing the previously reported MT-binding domain (NuMA$^{1821-2001}$), the newly identified one (NuMA^{Cter} Δ exon-24) or both of them, and analyzed their ability to localize at the spindle poles in metaphase by confocal microscopy. Consistent with the current knowledge, mCherry-NuMA$^{1821-2001}$ localized at the spindle poles almost to the same extent of NuMA^{Cter}, indicating that the direct binding to MTs is not involved in polar targeting of NuMA. On the other hand, the polar localization of the

mCherry-NuMA^{Cter} Δ exon-24 was severely compromised (Fig. 33). These data suggest that the region of NuMA spanning residues 1944-2003, coded by exon-24, mediates spindle poles localization in spite of not being involved in direct MT-association. This is consistent with our finding that phosphorylation of Ser1969 is the major event controlling NuMA polar accumulation. Altogether our results revealed that 1) the binding of NuMA to MTs and to LGN is independent of Aurora-A activity, 2) the fragment of NuMA encompassing residues 2002-2115 contains the MT-binding domain, while residues 1821-2001 are involved in spindle pole association regulated by Aurora-A, (C) NuMa^{Cter} interacts simultaneously with LGN and MTs.

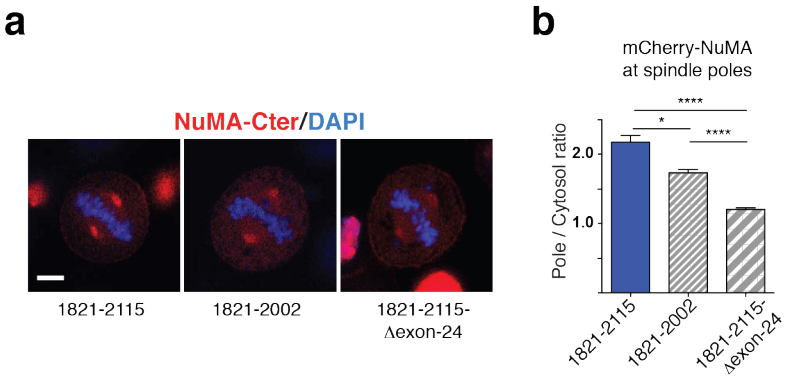

Fig. 33. Direct binding of NuMA to MTs is not required for its polar localization. a) Confocal sections of metaphase HeLa cells transiently expressing the entire mCherry-NuMA^{Cter} (residues 1821–2115) or its deletions D2003–2115 and D1944–2003 (Dexon-24). **b)** Histograms represent the quantification of the mCherry signal at the spindle poles with respect to cytoplasm (means ± SEM; n > 30 from three independent experiments). ****p < 0.0001 and *p < 0.05 by Kruskal-Wallis test. Scale bar, 5 µm.

4. DISCUSSION

4.1 Afadin

During my PhD studies, we provided structural evidence of the direct interaction of Afadin with LGN, and that it is compatible with the simultaneous binding to cortical F-actin. Based on these findings, we demonstrated that in epithelial cells Afadin acts as a molecular bridge between F-actin and LGN, and that this molecular mechanism accounts for the role of Afadin in spindle orientation. Our studies are presented in the paper entitled "Concomitant binding of Afadin to LGN and F-actin directs planar spindle orientation" published in Nature Structural & Molecular Biology on January 2016 [115]. We also published a more technical report describing the strategy adopted to obtain well-diffracting crystals of the Afadin-LGN complex entitled "Crystallization and X-ray diffraction of LGN in complex with the actin-binding protein Afadin" on Acta Crystallographica Section F [104].

My studies started from *in vitro* binding assays demonstrating that the association between $Pins^{TPR}$ and $Canoe^{Cter}$ previously reported [74] is conserved in the human orthologs LGN^{TPR} and $Afadin^{Cter}$. Mapping of the minimal binding interfaces of the two proteins revealed that the stretch of Afadin encompassing residues 1709-1746 binds to LGN^{TPR} with the same strength measured for the entire $Afadin^{Cter}$. Crystallographic analysis carried out on a chimeric construct of LGN^{TPR} fused to $Afadin^{1709-1746}$ revealed that the Afadin peptide runs along the inner groove of the LGN^{TPR} superhelix with opposite chain directionality, and docks onto the LGN^{TPR} surface via a number of main chain hydrogen bonds, and specific contacts of the side chains $Phe1730^{AF}$ and $Glu1735^{AF}$. The topology of LGN^{TPR} in complex with Afadin is reminiscent of that of LGN in complex with other interactors such as mInsc [37], NuMA [36], and Frmpd1/4 [39]. Thus, it is not surprising that SEC analysis showed that Afadin competes with NuMA for binding LGN. Of note, this competition is conserved also between *Drosophila* Canoe and Mud, suggesting that the

molecular function of Afadin is conserved across species. Because the topology of LGN^{TPR} bound to its ligands is similar, it is possible to superimpose the corresponding structures in order to find a putative motif common to all LGN binding partners. Structural superposition of LGN^{TPR} in complex with its known ligands, including the Afadin peptide, led to the definition of an LGN-binding consensus [F/W]-X_{2-8}-[E/Q/Y]-X-E-X_5-[Q/D/E]-X_{1-2}-[K/R/C]-X_{0-1}-[L/I/V], where X stands for any residue (Fig. 20a, bottom). However, this consensus turns out to be poorly predictive due to the variability in the residues accommodated between the conserved positions, and in the manner in which the ligand side chains can rearrange to recognize the LGN surface.

We then demonstrated that in epithelial cells the Afadin/LGN interaction has a functional role in the cortical recruitment of *MT-motors*. Indeed, loss of Afadin in HeLa cells perturbs cortical localization of LGN in metaphase, and abolishes NuMA and Dynein/Dynactin recruitment at the cortex both in metaphase and in anaphase. Thus, Afadin is essential for targeting NuMA at the cell cortex, despite they do not interact directly but are mutually exclusive interactors of LGN. To reconcile this apparent discrepancy, one could hypothesize the existence of higher order oligomers in which multiple LGN molecules engage either with NuMA or Afadin. We believe that this hypothesis is unlikely, as in the absence of limiting concentrations or topological constraints not visible in the LGN crystallographic structures, all the available sites on LGN would be occupied by the higher affinity ligand, which in this case is NuMA. Intriguingly, the observation that in metaphase an Afadin mutant devoid of the LGN-binding motif is unable to mediate the recruitment of NuMA at the cortex indicates that this function impinges on the direct interaction of Afadin with LGN. Consistently, studies exploiting the *Drosophila* S2 "induced cell polarity assay" have shown that the Pins/Mud spindle orientation pathway relies on the physical interaction of Canoe with Pins at the cortex [74]. Collectively, our data support a sequential model, in which LGN is first recruited at the cortex by Afadin, binds to several $G\alpha_i$ molecules (Fig. 34, left), and is later handed to NuMA, that binds LGN with higher

affinity (Fig. 34, right). In addition, our results indicate that, also in anaphase, Afadin is essential for the localization of NuMA at the cortex [115] (not shown here). In anaphase, NuMA cortical levels increase by direct interaction of the protein with phospholipids, independently of LGN [90, 91, 94]. In summary, we suggest a model in which in metaphase Afadin targets LGN at the cortex by direct interaction with its TPR domain, but at the same time it is also involved in cortical recruitment of NuMA/Dynein in more sophisticated ways, whose elucidation will require further localization and biochemical studies. Interestingly, recent evidence suggests the existence of LGN-independent spindle orientation pathways impinging on NuMA and Afadin (Fig. 7b). "Induced cell polarity assays" in *Drosophila* S2 cells have shown that the DEP domain and the C-terminal PDZ-ligand of Dishevelled are both required for spindle orientation [52]. In the same study, the authors demonstrated that the C-terminus of Dishevelled interacts with Canoe [52]. In addition, in fly and fish embryonic cells with active planar cell polarity Wnt-signaling the DEP domain of Dishevelled co-immunopreciptates with the C-terminal region of Mud/NuMA [48]. The interaction of Dishevelled with NuMA as well as the one with Afadin has later been confirmed in human cells [53, 83], suggesting that an Afadin/Dishevelled/NuMA spindle orientation pathway might exist and be conserved across species. Based on this, future biochemical and structural studies aimed at reconstituting the hypothetical Afadin/Dishevelled/NuMA complex would sustain a model in which Afadin mediates the cortical recruitment of NuMA through Dishevelled, independently of LGN.

Growing evidence points to a prominent role of the acto-myosin cortex in instructing spindle orientation in vertebrate cells in culture and *in vivo* [59]. The need of an intact cell cortex for correct spindle positioning is reflected in the requirement of actin regulators including ERM proteins [57], Cdc42 [21, 58], MISP [62] and Myosin-10 [63]. Nevertheless, how the external signals sensed by the acto-myosin cell cortex are communicated to the mitotic spindle is still largely unclear. Our work on the mitotic role of

Afadin contributed to fill this gap. More specifically, our findings describe for the first time a direct connection between the cell cortex and the cortical Dynein/Dynactin. Biochemical assays demonstrated that region of the isoform-4 of human Afadin encompassing residues 1514-1682 co-sediments with F-actin. Most importantly, we found that Afadin binds concomitantly to F-actin and LGN *in vitro*, and that it acts as the first described physical anchor between the cortex and the spindle motors *in vivo*. To prove the relevance of the interaction of Afadin with F-actin in cells we depolymerized cortical F-actin by using Latrunculin-A, and observed that this led to dissociation of Afadin and LGN from the cortex. In addition, depletion of Afadin did not disrupt the integrity of the acto-myosin cell cortex, thus placing Afadin downstream of F-actin. Consistently, expression in Afadin-depleted HeLa cells of an Afadin construct devoid of the F-actin binding site, that localizes poorly at the cortex, prevented LGN cortical localization and correct spindle alignment. Thus we could conclude that, also in cells, Afadin acts as a molecular bridge connecting F-actin and LGN (Fig. 34, left). Being a component of AJs in vertebrate epithelia [78], we reasoned that Afadin could represent a cortical cue that restricts LGN and NuMA laterally to ensure planar cell divisions (Fig. 34). In line with this hypothesis, we showed that Caco-2 cells lacking Afadin grown in three-dimensional cysts are unable to undergo planar cell divisions, and generate cysts with multiple lumens. However, whether defective cystogenesis is a direct cause of misoriented divisions, or an indirect effect due to weakening of cell-cell contacts remains an open question. In summary, the notion that Afadin is a major component of cell-cell junctions and that it acts as a hub for small G-protein signaling, both in vertebrates [116, 117] and in *Drosophila* [118], makes it an ideal candidate to transduce to the mitotic spindle external stimuli such as Wnt signaling, and mechanical properties of the cortex such as cell shape.

Since in flies Canoe regulates asymmetric cell divisions in NBs and muscle progenitors [44], it would be interesting to investigate the role of Afadin in vertebrate systems able to

switch from planar to vertical divisions, including the developing skin and the neuroepithelium.

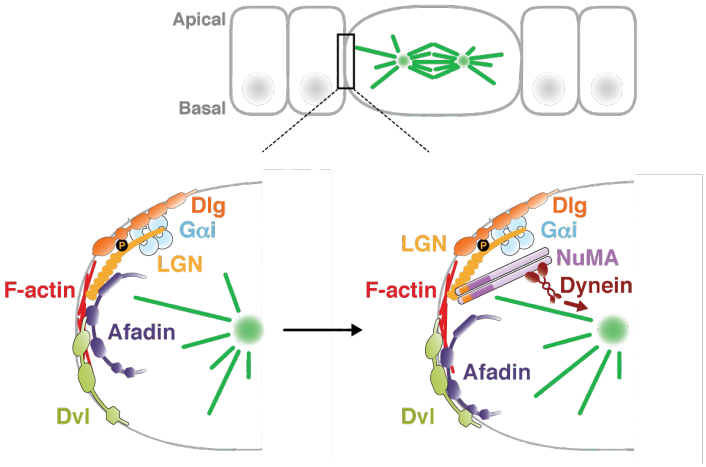

Fig. 34 Schematic representation of the mitotic function of Afadin supported by our study. Afadin localizes at adherens junctions of polarized epithelia and instructs the localization of *MT-motors* by concomitant binding to cortical F-actin and LGN. LGN is anchored to the lateral membrane by direct simultaneous interactions with Afadin, $G\alpha_i$-GDP and Dlg. Dlg recognizes the phosphorylated linker region of LGN (left panel). In the presence of the higher-affinity ligand NuMA, LGN dissociates from Afadin and recruits NuMA/Dynein at the cortex, and microtubule-pulling forces ensue (right panel). Evidence in flies suggests that the direct association of Afadin with Dishevelled (Dvl) might contribute indirectly to targeting NuMA at the cortex.

4.2 NuMA and Aurora-A

Part of my PhD research activities dealt with the characterization of the functional role of NuMA phosphorylations by Aurora-A. Our studies revealed that the kinase activity of Aurora-A controls spindle alignment of HeLa and RPE-1 cells in culture by governing the distribution of NuMA in metaphase. More specifically, we found that mitotic inhibition of Aurora-A causes aberrant accumulation of NuMA at the spindle poles, thus preventing its cortical recruitment with LGN and resulting in misoriented divisions. Through biochemical studies, we identified a new MT-binding domain within the C-terminal region of NuMA, which is dispensable for the localization of NuMA at the spindle poles and it is compatible with LGN binding, thus suggesting a possible role in spindle positioning. Our findings are

reported in the manuscript entitled "NuMA phosphorylation by Aurora-A orchestrates spindle orientation" published in Current Biology on February 2016 [119].

Starting from the evidence that Aurora-A inhibition causes spindle orientation defects, we found that in the same conditions NuMA accumulates aberrantly at the spindle poles, accompanied by NuMA reduced mobility (Schematic representation in Fig. 35, bottom). These observations imply that in unperturbed conditions the affinity of NuMA for spindle pole components is reduced by Aurora-A phosphorylation, to allow NuMA cortical recruitment to LGN crescents (Fig. 35, top).

Intriguingly, in *Drosophila* NBs, Aurora-A has been involved in spindle orientation via Pins phosphorylation within the linker between its TPR and GoLoco domains on a conserved Serine residue, which mediates the interaction with cortical Dlg. It seems that in vertebrates, phosphorylation of the same Serine residue is required to restrict LGN at the lateral cortex during planar mitoses in MDCK cysts [20], and in neuroepithelial cells [28]. Whether LGN is a direct substrate of Aurora-A also in vertebrates is not known. However, our data indicate that neither depletion nor inhibition of Aurora-A hampers cortical localization of LGN in metaphase, meaning that loss of cortical NuMA does not depend on the absence of LGN.

In addition, we demonstrated that, in Aurora-A inhibited conditions, artificial tethering of NuMA to the cell cortex by fusion with the GoLoco region of LGN rescued spindle orientation defects, indicating that the major event causing spindle misorientation in Aurora-A inhibited cells is the lack of cortical NuMA.

How does Aurora-A-mediated phosphorylation regulate NuMA distribution between the spindle poles and the cortex? One possibility is that this phosphorylation event might increase the binding affinity of NuMA for cortical LGN. Alternatively, phosphorylated NuMA may display reduced affinity for a receptor at the spindle poles. To address these two possibilities we made use of a C-terminal tail of NuMA spanning residues 1821-2115, which contains the LGN-binding motif but is unable to dimerize with endogenous NuMA,

and lacks the region binding to Dynein. Upon Aurora-A inhibition, this C-terminal construct of NuMA mimicked the aberrant polar accumulation observed for the full-length protein. For these reasons we decided to use this construct to investigate the effect of the phosphorylation on purified NuMA *in vitro.* We first demonstrated that Aurora-A phosphorylates directly the C-terminus of NuMA on Serines 1969, 1991 and 2047. *In vitro* binding assays indicated that the interaction between LGN and NuMA is not enhanced by Aurora-A phosphorylation. Conversely, we found that substitution of Ser1969 with Alanine recapitulates the NuMA enriched localization at the spindle poles in Aurora-A inhibited HeLa cells. In fact, in unperturbed conditions, a C-terminal construct of NuMA spanning residues 1821-2115 carrying Ser1969Ala mutation accumulates aberrantly at the spindle poles. Of note, the same mutation introduced into full-length NuMA subjected to FRAP at the spindle, in unperturbed conditions, reduces NuMA mobility as observed for the wild-type construct upon Aurora-A inhibition. We thus concluded that Aurora-A phosphorylates NuMA on Ser1969 to ensure its correct distribution and dynamic exchange between the spindle poles and the polar cortex in metaphase (Fig. 35, top). The evidence that the Ser1969 phosphosite, which plays a prominent role in setting normal amounts of NuMA at the spindle poles, lies in a region that had been previously implicated in MT-binding, prompted us to test the idea that Aurora-A-mediated-phosphorylation could modulate the affinity between NuMA and MTs. Through MT co-sedimentation and MT-bundling assays, we found that phosphorylation of Ser1969 neither affects NuMA association with MTs nor its ability to bundle MTs *in vitro,* meaning that non-phosphorylated NuMA accumulates at the spindle poles via receptors other than MTs. Most interestingly, during these analyses we defined a new MT-binding domain confined to NuMA residues 2002-2115, which does not contain Ser1969 (Fig. 26a). The association of the NuMA C-terminal construct encompassing residues 2002-2115 with MTs is not essential for its targeting to the spindle poles. This observation is compatible with previous studies in which removal of the mouse NuMA fragment coded by exon-22 (exon-24

spanning residues 1944-2003 in *hs* NuMA) generated a protein localizing less efficiently at the spindle poles [97]. Of note, the new MT-binding domain we have identified is physically separated from the LGN binding motif. Therefore, not surprisingly but in contrast to previous evidence [96] we found that the association of NuMA with MTs is compatible with its simultaneous binding to LGN. Based on this, we propose that the MT-binding domain might work at the cortex to stabilize the interaction between LGN/NuMA and the MT +TIPs, this way assisting the sliding of the *MT-motors* along the depolymerizing MTs (Fig. 35, top close-up). In line with our model, the binding of NuMA to MTs has been shown to result in frictional forces favoring the minus-end directed movement of Dynein [114].

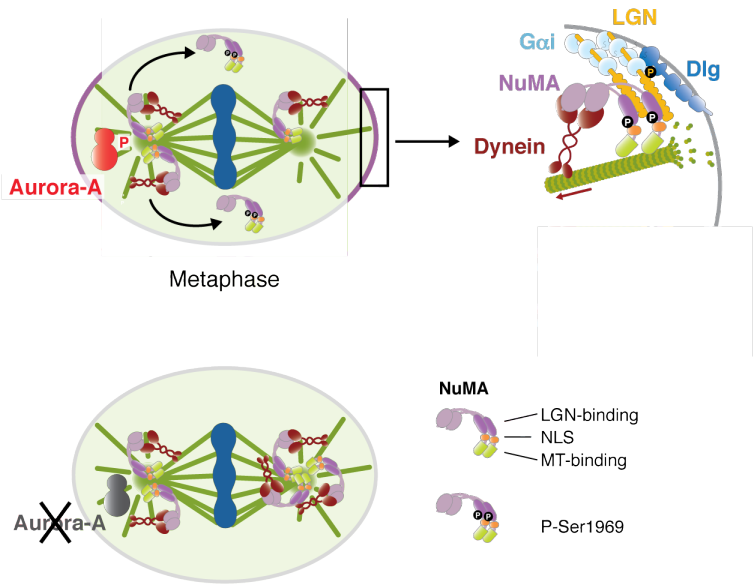

Fig. 35. Schematic representation of the role of Aurora-A in regulating the distribution of NuMA in metaphase. Top) In unperturbed conditions, Aurora-A at the spindle poles phosphorylates NuMA on Ser1969 enhancing its mobility and allowing a pool of NuMA to reach the polar regions of the cortex above the spindle poles (left panel). The receptor for NuMA at the cortex is LGN, which, in turn, is recruited to the plasma membrane by interaction with four $G\alpha_i$ moieties anchored to the lipid bilayer via myristoyl groups. Phosphorylated LGN is further secured to the membrane by interaction with Dlg1. The N terminus of NuMA associates with Dynein/Dynactin, while the C-terminal portion binds concomitantly to LGN and to MTs, this way stabilizing the contacts between the Dynein/Dynactin motors and the depolymerizing microtubule lattice (right panel). **Bottom)** Aurora-A inhibition results in aberrant accumulation of

unphosphorylated NuMA at the spindle poles, and simultaneous loss of NuMA from the cortex. The receptor of NuMA at the spindle poles whose affinity is reduced by Aurora-A phosphorylation is still unknown.

Our finding that Aurora-A controls NuMA distribution in adherent cells in culture provides an additional regulatory mechanism for NuMA recruitment at cortical LGN crescents in metaphase. However, the identity of the receptor/s at the spindle poles, whose affinity for NuMA is modulated by Aurora-A still remains unknown. At this regard, it will be of great interest to look for centrosomal interactors of NuMA regulated by Aurora-A, by performing co-immunoprecipitation experiments from untreated or MLN-treated lysates coupled to mass spectrometry analyses.

In conclusion, many layers of regulation work synergistically to ensure proper levels of LGN/NuMA in metaphase, that ultimately lead to accurate spindle orientation preceding anaphase spindle elongation [35]. Whether our proposed mechanism can be extended to proliferating tissues and to planar cell divisions is currently unknown. Aurora-A has been involved in the regulation of spindle orientation during asymmetric cell divisions in the mammary epithelium [120]. Therefore, the relevance of the Aurora-A/NuMA pathway in stem cell self-renewal would be an exciting direction for future experiments.

In our work we reported the role of the LGN/Afadin/F-actin interaction, and of the phosphorylation of NuMA by the Aurora-A kinase in ensuring proper spindle orientation in metaphase in HeLa cells. We also demonstrated that Afadin regulates planar cell divisions in a three-dimensional epithelial model *in vitro*. Thus, what remains to be established is whether these mechanisms are conserved in developing epithelia *in vivo*. A suitable model to study the functions of Afadin/LGN and of NuMA phosphorylation in metaphase is the mouse stratifying skin. Until day E10 skin progenitors divide planarly with their spindle parallel to the basement membrane to enlarge the stem-cell pool and to expand the epithelium (Fig. 2c, right), while at a later stage progenitor divisions switch to vertical to allow stratification and differentiation (Fig. 2c, left). It is known that during skin

stratification, LGN and NuMA localize apically above one of the poles to orient the mitotic spindle perpendicular to the basement membrane, this way promoting vertical asymmetric cell divisions [4, 17]. Nevertheless, whether in metaphase these proteins localize laterally to drive planar cell divisions when the progenitor pool expands still remains to be determined. Interestingly, LGN and NuMA have been detected at the lateral belt of chicken neuroepithelial cells that divide planarly [27]. It would be informative to visualize the localization of LGN and NuMA in murine skin planar mitoses. Based on the molecular mechanism we have proposed in Fig. 34, we would expect Afadin to localize at the lateral cortex at sites of cell-cell junctions. Immunostaining experiments and *in utero* inactivation of Afadin in the developing skin followed by spindle orientation analysis would be instrumental to monitor Afadin localization and elucidate its function in maintaining skin progenitors' planar cell division. Rescue experiments performed by expressing an Afadin variant lacking the LGN binding region under a skin progenitor-specific promoter would reveal if, in this system, the Afadin/LGN interaction has the same role that we have observed in HeLa and Caco-2 cells.

What makes NuMA timely available at the lateral cortex to ensure the recruitment of the Dynein/Dynactin *MT-motors* in planar mitoses? One possibility is that following the enrichment of LGN at the lateral cortex through Afadin, which localizes at AJs, the mitotic release of NuMA from the nucleus displaces Afadin from LGN because its higher affinity for LGN. The newly formed LGN/NuMA complex then would remain localized laterally through direct interaction of the GoLoco domain of LGN with multiple membrane-bound $G\alpha_i$ molecules. According to this model, Afadin would serve as a cortical landmark to localize LGN at the lateral cortex, priming its subsequent stabilization with $G\alpha_i$ and the recruitment of NuMA. This simplistic sequential model is not completely supported by our data, as we do not have evidence in HeLa cells that LGN/Afadin complexes form and localize at the lateral cortex, before the release of NuMA from the nucleus.

A second hypothesis for the timely recruitment of NuMA at the cortex envisions the existence of regulatory mechanisms controlling NuMA accessibility to cortical LGN throughout mitosis, such as the chromosome-centered Ran-GTP gradient, or the phosphorylation of NuMA by Aurora-A. Ran was originally identified as a regulator of the nuclear-cytoplasmic transport in association with importins and exportins. Later it was found that the GTP-loaded form of Ran catalyzes the release of mitotic spindle assembly factors from importins. As a consequence, proteins containing an NLS, like NuMA, which are bound to β-importin, at mitotic entry are released from this interaction by Ran-GTP in proximity of chromosomes [111]. It has been reported that, in *Drosophila* NBs, Canoe is polarized at the apical cortex where it favors the recruitment of Mud with Pins. In line with the RanGTP-gradient model, the molecular explanation that was pushed forward for this observation is that Canoe binds directly Ran-GTP with its Ras-Association domains, favoring the release of Mud from β-importin, and allowing the interaction of Mud with cortical Pins [74]. Nevertheless, in the vertebrate planar mitoses, or at least in the chicken neuroepithelium, it is unlikely that such a mechanism is at play, as the levels of NuMA and LGN in the lateral belt are not stronger in the proximity of the metaphase plate [27].

An alternative explanation of how NuMA enriches at the LGN sites in vertebrate systems is based on our finding that Aurora-A governs the cortical accumulation of NuMA. More specifically, we can hypothesize that in mitosis the phosphorylation of Ser1969 of NuMA by Aurora-A at the spindle poles mobilizes NuMA from the poles allowing its recruitment at the lateral cortex by LGN. Also in this case the transfer of LGN from Afadin to NuMA would be ensured by the high affinity between LGN and NuMA (Fig. 36). Whether NuMA phosphorylation by Aurora-A works in systems different than HeLa cells remains to be explored.

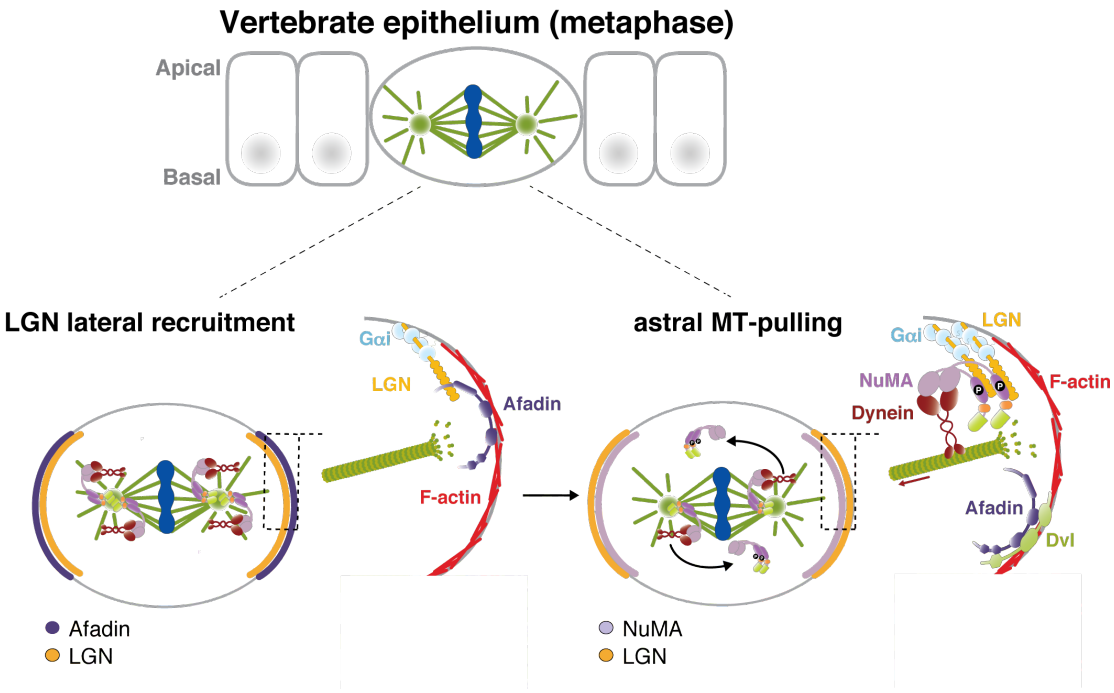

Fig. 36. Integrated model of the role of the Afadin/LGN interaction, and of NuMA phosphorylation in epithelial planar mitoses. Left) At mitosis onset, F-actin-bound Afadin instructs the localization of LGN at the lateral acto-myosin cortex of epithelial cells (close-up view). At this stage most of the NuMA pool is unphosphorylated and accumulates at the spindle poles. Afadin and LGN are represented in dark purple and orange, respectively. **Right)** As NuMA becomes phosphorylated by Aurora-A at Ser1969, it is released from the poles and becomes available to interact with LGN at the lateral cortex by displacing away the lower affinity ligand Afadin (close-up view). This way, Dynein/Dynactin are recruited at the cortex and generate forces to orient the spindle within the plane of the epithelium. NuMA and LGN are represented in violet and orange, respectively.

5. MATERIALS AND METHODS

5.1 Protein expression and purification

Afadin/LGN Project

GST-LGN$^{15-350}$ (LGN^{TPR}), GST-NuMA$^{1861-1928}$, GST-Afadin$^{1514-1824}$ (Afadin^{Cter}) fragments and the chimeric fusion protein GST-LGN$^{15-350}$-Afadin$^{1709-1747}$ (LGN^{TPR}-Afadin^{PEPT} in the text) were cloned into pGEX-6P1 vector (GE Healthcare), and expressed in BL21 *E. coli* cells by overnight induction with 0.5 mM IPTG at 20°C. Cells were lysed in 0.1 M Tris-HCl pH 8, 0.3 M NaCl, 10 % glycerol, 0.5 mM EDTA, and 1 mM DTT, and cleared for 1 h at 100,000 *g*. Cleared lysates were affinity purified by incubation with Glutathione Sepharose-4 Fast-Flow beads (GE Healthcare). After washes, fusion proteins retained on beads were incubated with GST-PreScission protease (GE Healthcare) overnight at 4 °C to remove the GST-tag. The cleaved material was eluted from the beads in a desalting buffer consisting of 20 mM Tris-HCl pH 8, 40 mM NaCl, 5 % glycerol, 1 mM DTT, and loaded on a Resource-Q ion-exchange column. Proteins were eluted from Resource-Q with a gradient of 40-320 mM NaCl in 20 column volumes, pooled and stored at -80 °C. *Drosophila* Canoe$^{1755-2051}$, Mud$^{1895-2094}$, and Pins$^{25-406}$ (Pins^{TPR}) were purified similarly. For crystallization experiments, the fusion protein LGN^{TPR}-Afadin^{PEPT} was further polished on a Superdex-200 column equilibrated in 10 mM Hepes pH 7.5, 0.15 M NaCl, 5 % glycerol. Afadin point mutations were generated by QuickChange strategy (Stratagene) according to manufacturer's instructions. All clones were sequence verified.

Aurora-A/NuMA Project

His-tagged NuMA$^{1821-2115}$ (referred to as NuMA^{Cter} in the text), NuMA$^{1821-2001}$, NuMA$^{2002-2115}$ were cloned into a pETM14 vector (Novagen), and expressed in BL21 *E coli* cells by overnight induction with 0.2 mM IPTG at 20°C. Cells were lysed in 0.1 M Tris-HCl pH 8, 0.3 M NaCl, 10 % glycerol, 5 mM imidazole, and 2 mM β-mercaptoethanol, and cleared for 1 h at 100,000 *g*. Clear lysates were injected on a HiTrap chelating column (GE

Healthcare) loaded with Ni^{2+}. The proteins were eluted by applying a 5-200 mM imidazole gradient, and dialyzed against 20 mM Tris-HCl pH 6.8, 40 mM NaCl, 5 % glycerol, 2mM β-mercaptoethanol prior to injection onto a Resource-S cation exchange column. The His-tag was removed by incubation with His-PreScission protease (GE Healthcare) overnight at 4 °C. His-$NuMA^{Cter}$ constructs were eluted from Resource-S with a gradient of 40-250 mM NaCl in 20 column volumes, pooled and stored at -80 °C.

GST-LGN^{15-350} (LGN^{TPR}), GST-$NuMA^{1821-2115}$ ($NuMA^{Cter}$), GST-$NuMA^{1821-2001}$, and GST-$NuMA^{2002-2115}$ were cloned into a pGEX-6P1 vector (GE Healthcare), and expressed in BL21 *E. coli* cells by 5 hours induction with 0.5 mM IPTG at 20°C. Cells were lysed in 0.1 M Tris-HCl pH 8, 0.3 M NaCl, 10 % glycerol, 0.5 mM EDTA, and 1 mM DTT, and cleared for 1 h at 100,000 *g*. Clear lysates were loaded on a GSTrap FF column (GE Healthcare) in PBS and eluted by 10 mM glutathione after washing the packed beads with 1M NaCl PBS. Proteins were pooled and dialyzed against 10 mM Hepes pH 7.5, 0.15 M NaCl, and 5% glycerol before storage at -80 °C.

5.2 *In vitro* binding assays

5.2.1 GST pull-down

For pull-down assays, 1μM of GST-Afadin fragments were immobilized on GSH-beads, and incubated for 1 hour on ice with 5 μM of LGN^{TPR} proteins in 10 mM Hepes pH 7.5, 0.1 M NaCl, 5% glycerol, 0.1 % Tween20. After washes, proteins bound to beads were separated by SDS-PAGE, and detected by Coomassie staining.

In the Aurora-A/NuMA project the GST pull-down assay was conducted similarly by immobilizing 1μM of GST-LGN^{TPR} on GSH-beads, and incubated for 1 hour on ice with 2 μM of $NuMA^{Cter}$ wild-type, carrying the 3Asp mutation or phosphorylated by Aurora-A in the same buffer as above.

5.2.2 Analytical Size Exclusion Chromatography (SEC)

In the SEC analyses 15 μM of LGN^{TPR}, $Afadin^{Cter}$ and $NuMA^{1861-1928}$ were loaded singularly or in combination on a Superdex 5/150 (GE Healtcare) and eluted in 50 μl fractions in 10 mM Hepes pH 7.5, 0.1 M NaCl, 5% glycerol. The presence of the proteins in the elution volume was monitored by absorbance at 280 nm (expressed as mAu) and subsequently checked by SDS-PAGE followed by Coomassie staining. For the SEC analysis conducted on $Afadin^{Cter}$ and globular Actin (G-actin), 150 μM of both species were loaded on Superdex 5/150 in 5 mM Tris-HCl pH 7.8, 0.2 mM ATP, 1 mM DTT, 0.1 mM $CaCl_2$ (G-buffer).

5.2.3 Isothermal Titration Calorimetry (ITC)

The thermodynamical parameters of the association between $Afadin^{Cter}$ and LGN^{TPR} were measured in an ITC displacement experiment, in which the relatively low-affinity reaction between Afadin and LGN was coupled to the high-affinity binding of LGN^{TPR} to the human Insc peptide spanning residues 23-58 ($hInsc^{PEPT}$) [12]. All reagents were dialyzed overnight against 10 mM Hepes pH 7.5 and 0.15 M NaCl. ITC measurements were performed at 25 °C on a MicroCal VP-ITC calorimeter (MicroCal, Inc). In a first preliminary experiments, 12 μM of LGN^{TPR} in the cell were titrated with 10 μl injections of $hInsc^{PEPT}$ at 90 μM. Heats of ligand binding were corrected by subtraction of the average heat of ligand dilution after saturation, and fitted to a single-site binding model with Origin-7.0 software package (MicroCal). Analysis of the integrated heats yielded an association constant K_{INSC} of $6.3 \pm 1.8 \times 10^7$ M^{-1}, fully in line with previous reports[12]. In a second calorimetric experiment, $hInsc^{PEPT}$, at the same concentration used in the first experiment, was injected in a cell containing 12 μM of LGN^{TPR} and 30 μM of $Afadin^{Cter}$. The presence of the low-affinity ligand in the cell, affected the association of $hInsc^{PEPT}$ with LGN^{TPR}, as revealed by the analysis of the binding isotherm performed with the standard single-site binding model, which results in an apparent association constant K_{APP}

of $4.0\times10^6 \pm 5.7\times10^5$ M^{-1}. The measured K_{INSC} and K_{APP} were then used to derive the association constant K_{AF} for the binding of $Afadin^{Cter}$ to LGN^{TPR} using the following equation [103]:

$K_{AF} = [(K_{INSC}/K_{APP}) -1] * 1/[AF]$

where [AF] is the concentration of Afadin in the cell during the measurement of K_{APP}.

5.2.4 Fluorescence Polarization (FP)

Fluorescence polarization measurements were performed on an Infinite F200 (Tecan). A fixed concentration (40 nM) of fluorescein-labeled $Afadin^{PEPT}$ (United Biosys Inc.) was incubated with increasing concentrations of the indicated LGN^{TPR} construct in 10 mM Hepes pH 7.5, and 0.15 M NaCl. The corresponding K_D were calculated by fitting the fluorescence polarization curves in Prism (GraphPad Software) with the following quadratic equation:

$Y = B* ((0.04+x+ K_D)-sqrt(sqr(0.04+x+ K_D)-4*0.04*X))/(2*0.04)$

where Y is the intensity of the fluorescence polarization signal, B is the maximum polarization signal at saturation, x is the concentration of LGN^{TPR} in micro-molarity, and 0.04 μM is the constant concentration of $Afadin^{PEPT}$.

5.3 Protein crystallization and structure determination

5.3.1 Generation of the LGN^{TPR} - $Afadin^{Cter}$ fusion protein

To stabilize the LGN^{TPR}/$Afadin^{PEPT}$ interaction, the sequence of $Afadin^{PEPT}$ was covalently linked to the C-terminus of LGN^{TPR}. To generate the chimeric construct, a two-step restriction-free cloning approach was employed [121]. Firstly, the coding sequence of $Afadin^{PEPT}$ was amplified using 50-base primers designed for the insertion of the PCR product into a previously generated pGEX-6P1-LGN^{TPR} vector. The forward primer carried a 24-base overlap with the vector, which was complementary to the 3'-end of the LGN^{TPR} construct, followed by 25 bases of $Afadin^{PEPT}$. The reverse primer annealed on the

pGEX-6PI vector with 24 bases complementary to the 3'- end of the point of insertion (see Fig. 36 and Table 3).

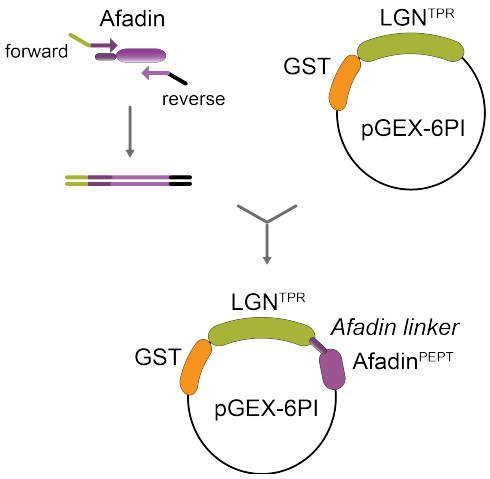

Fig. 37. Schematic representation of the restriction-free cloning strategy adopted to generate the LGN^{TPR}-Afadin^{PEPT} fusion construct.

Table 3. Macromolecule production information.

	LGN and Afadin
Source organism	*Homo sapiens*
DNA source	Synthetic
Expression vector	pGEX-6P1
Expression host	*E. coli* BL21 Rosetta
Sequence of LGN^{TPR}-Afadin^{PEPT}	GPLGSASCLELALEGERLCKSGDCRAGVSFFEAAVQVGTEDLKTLSAIYSQLGNAYFY LHDYAKALEYHHHDLTLARTIGDQLGEAKASGNLGNTLKVLGNFDEAIVCCQRHLDI SRELNDKVGEARALYNLGNVYHAKGKSFGCPGPQDVGEFPEEVRDALQAAVDFYEE NLSLVTALGDRAAQGRAFGNLGNTHYLLGNFRDAVIAHEQRLLIAKEFGDKAAERRA YSNLGNAYIFLGEFETASEYYKKTLLLARQLKDRAVEAQSCYSLGNTYTLLQDYEKAID YHLKHLAIAQELNDRIGEGRACWSLGNAYTALGNHDQAMHFAEKHLEISREVGDQR NASYLKTQVLSPDSLFTAKFVAYNEEEEEEDCSLAG

Residues left after GST-removal are indicated in blue. Afadin^{PEPT} is shown in magenta.

The amplified PCR fragment was cleaned using a PCR purification kit (Qiagen) and diluted to 100 ng/µl. A second amplification was conducted using 2–4 µl of the PCR fragment previously produced to prime the PCR reaction of PfuTurbo polymerase (Agilent

Technologies) on 50 ng pGEX-6P1- LGN^{TPR} vector in 50 µl reaction mixture. The amplification protocol consisted of 35 cycles, with an elongation step of 15 minutes. Once completed, 9 µl of the PCR reaction was treated with DpnI (New England Biolabs) for 2 hours at 37 °C to digest the methylated parental plasmid and subsequently transformed into Escherichia coli DH10 competent cells (Top10, Invitrogen). Positive clones containing the GST-LGN^{TPR}-$Afadin^{PEPT}$ fusion gene were confirmed by DNA sequencing.

5.3.2 Native PAGE analysis of the LGN^{TPR}-$Afadin^{PEPT}$ chimera

Native polyacrylamide gel electrophoresis (Native PAGE) allows the analysis of a protein sample without disrupting its native conformation, its secondary structure, and its native charge. 6 µg of the LGN^{TPR}-$Afadin^{PEPT}$ fusion, of the LGN^{TPR}/$Afadin^{PEPT}$ complex, and of LGN^{TPR} were prepared in a non-denaturing non-reducing sample buffer, without boiling. The samples were then separated, in parallel to native molecular weight standards (NativeMark, Life Technologies), on a 12% Native PAGE run at 150V on ice at 4°C. Protein bands were detected by Coomassie staining.

5.3.3 Crystallization conditions

Initial crystallization trials of the LGN^{TPR}-$Afadin^{PEPT}$ sample utilized the commercial sparse-matrix screens SaltRX (Hampton Research), AmSO4 (Qiagen), JCSG-plus and Structure Screen 1 + 2 (Molecular Dimensions) and were conducted in sitting-drop vapor-diffusion format using a Cartesian Honeybee nanodispenser (Genomic Solutions) in three-square-well CrystalQuick Greiner plates. At the two concentrations tested (10 and 5 mg/ml), 100 nl protein solution was mixed with an equal volume of reservoir solution at 20°C. Crystals appeared at 10 mg/ml after 1 day in about 20% of the salting-out conditions containing sulfate, phosphate, formate or malic acid ions at pH values between 7.0 and 8.5. We selected conditions E10 from the AmSO4 kit (0.1 M Na Hepes pH 7,1.6 M ammonium sulfate) and C7 and C9 from the SaltRX kit (0.1 M Bis-Tris propane pH 7, 3.5 M sodium

formate and 0.1 M Bis-Tris propane pH 7, 1.2 M dl-malic acid pH 7.0, respectively) for manual optimization. All three conditions were reproduced in hanging drops in 24-well VDX plates (Hampton Research) by mixing 1 µl protein solution with 1 µl reservoir solution. To slow the crystal growth, we performed grid screens around 0.1 M Na Hepes pH 7, 1.6 M ammonium sulfate at 15°C. The concentration of ammonium sulfate was varied from 1.35 to 1.6 M in 50 mM increments at pH values ranging from 7.5 to 8.25. Further attempts to slow crystal nucleation were conducted at 4°C, seeding drops set up with a protein concentration of 5 mg/ml and a reservoir solution consisting of 0.1 M Tris–HCl pH 8.0, 1.4 M ammonium sulfate after 3 hours of equilibration (Table 4).

Table 4. Crystallization conditions.

Method	Sitting drop	Sitting drop	Hanging drop	Hanging drop*
Plate type	96 x 3 well	96 x 3 well	24 well	24 well
Temperature (°C)	20	20	15	4
Protein conc.	10 mg ml^{-1}	10 mg ml^{-1}	8 mg ml^{-1}	5 mg ml^{-1}
Composition of protein solution	10 mM Na-Hepes pH 7.5, 0.15 M NaCl, 5 % glycerol, 4.5 mM TCEP	10 mM Na-Hepes pH 7.5, 0.15 M NaCl, 5 % glycerol, 4.5 mM TCEP	10 mM Na-Hepes pH 7.5, 0.15 M NaCl, 5 % glycerol, 4.5 mM TCEP	10 mM Na-Hepes pH 7.5, 0.15 M NaCl, 5 % glycerol, 4.5 mM TCEP
Composition of reservoir solution	0.1 M Na-Hepes pH 7, 1.6 M ammonium sulfate	0.1 M Bis-Tris Propane pH 7, 3.5 M sodium formate	0.1 M Tris-HCl pH 8, 1.4 M ammonium sulfate	0.1 M Bis-Tris Propane pH 7, 1.0 M DL-Malic acid
Initial hit	AmSO4-Qiagen E10	SaltRX-Hampton C7	AmSO4-Qiagen E10	SaltRX-Hampton C9
Drop volume	100 nl (1:1 ratio)	100 nl (1:1 ratio)	1 µl (1:1 ratio)	1 µl (1:1 ratio)
Reservoir volume	100 µl	100 µl	300 µl	300 µl
Screened by X-ray	NO	NO	YES	YES

* this condition was used for seeding after 3 hours equilibration.

Analogous optimizations were conducted around 0.1 M Bis- Tris propane pH 8.0, 3.5 M sodium formate and around 0.1 M Bis-Tris propane pH 7.0, 1.2 M malic acid. Single large crystals suitable for diffraction experiments were obtained at 15° C with 1.3 M ammonium sulfate or 1.0 M dl-malic acid, or by seeding the same conditions at 4 °C (Fig. 16). To

improve the crystal packing an additional additive screen was performed starting from these latter conditions, which unfortunately did not change either the crystal morphology or diffraction properties. As the crystals were fragile, they were cryo-protected by stepwise addition of ethylene glycol directly to the crystallization drops to a final concentration of 20% for 10–30 minutes prior to flash-cooling in liquid nitrogen.

5.3.4 Data collection, processing and structure determination

X-ray diffraction data for LGN^{TPR}-$Afadin^{PEPT}$ crystals were collected on beamline X06DA at the Swiss Light Source (SLS), Villigen, Switzerland. Data were processed using XDS [105] implemented in *xia2* [106]. The crystals diffracted to a resolution of 2.9 Å (Fig. 17a) and belonged to the cubic space group $P2_13$. The unit-cell parameters are consistent with two copies of the fusion protein per asymmetric unit, with a Matthews coefficient of 4.8 $Å^3$ Da^{-1} and a solvent content of 75 %. The high solvent content partly explains the modest resolution of the data despite the relatively large dimensions of the crystals, as often observed by Kantardjieff & Rupp [122] and Weichenberger & Rupp [123]. The structure of LGN^{TPR}-$Afadin^{PEPT}$ was determined by molecular replacement with *Phaser[107]* using the coordinates of mouse LGN^{TPR} solved previously in complex with NuMA (PDB ID 3RO2) as a search model. The Afadin peptide was built manually by iterative cycles in *Coot* [108] and refinement in *Phenix* [109]. The model was refined at 2.9 Å resolution to a final R_{free} of 25.5 % and an R_{work} of 20.6 %, with good stereochemistry. Data-collection statistics are given in Table 3. The structure was illustrated with PyMol (DeLano Scientific LLC).

5.4 *In vitro* kinase assays

Kinase assays were carried out using 1 ng of the purified kinase domain of Aurora-A (generous gift of Prof. Richard Bayliss) incubated with 2 μM of the $NuMA^{Cter}$ fragments. The reagents were incubated for 30 minutes at 30° C in kinase buffer consisting of 20 mM

Hepes pH 7.5, 5 mM $MgCl_2$, 0.2 M KCl, 0.5 mM EGTA, 2 mM DTT, 0.25 mM $NaVO_4$, and 1 mM ATP. To inhibit Aurora-A, 1 mM of MLN8237 was added to the reaction mix. For the phosphorylation time-course, kinase reactions were stopped at 7, 15, 30, or 60 minutes by addition of SDS-loading buffer. To discriminate the phospho-proteins from their non phosphorylated counterparts, samples were separated by Phos-TAG SDS-PAGE (Wako Rure Chemical Industries,Ltd, AAL-107), and stained with Coomassie blue. The Phos-TAG SDS-PAGE is a phosphate-affinity gel electrophoresis technique developed to detect different phosphorylation states of proteins by using a separating gel containing Phos-TAG acrylamide. To prevent excessive heating of the gel, Phos-TAG SDS-PAGEs were run at 80 V for 2 hours at room temperature.

5.5 Co-sedimentation assays

5.5.1 *In vitro* co-sedimentation with F-actin

For co-sedimentation assays, actin was purified as previously described [124] and stored at 4°C in G-buffer (5 mM Tris-HCl pH 7.8, 0.2 mM ATP, 1 mM DTT, 0.1 mM $CaCl_2$). Actin co-sedimentation assays were conducted according to Scita *et al.* [125]. Purified rabbit G-actin was allowed to polymerize into filamentous actin (F-actin) for 20 minutes at room temperature in F-buffer (G-buffer supplemented with 1 mM $MgCl_2$, 0.2 mM EGTA and 0.1 M KCl). Polymeric F-actin (1µM) was incubated with increasing concentration of His-Afadin^{Cter} for 15 minutes at room temperature, and subsequently ultracentrifuged for 25 minutes at 400,000 *g* at 4°C. Pellet and supernatant fractions were separated by SDS-PAGE, and visualized by Coomassie staining. For each concentration of Afadin^{Cter}, densitomeric quantification of the band in the pellet was performed with the software ImageLab (Bio-Rad Laboratories). Normalized binding data were obtained by dividing the values of the pellet fractions at each point by the maximum value of the pellet at saturation. Normalized binding data were fitted to the quadratic equation :

$Y = B* ((1+x+K_D)-sqrt(sqr(1+x+K_D)-4*1*X))/(2*1)$

where Y is the fraction of Afadin in the pellet at each concentration point, B is the maximum value of Afadin in the pellet at saturation, x is the concentration of Afadin incubated with F-actin expressed in micro-molarity, and 1 μM is the constant concentration of F-actin. Fitting and K_D calculation were carried out with the software Prism. Qualitative co-sedimentation assays of Afadin^{Cter} in complex to LGN^{TPR} were carried out similarly using 15 μM of both proteins with 1μM F-actin.

5.5.2 *In vitro* co-sedimentation with microtubules (MTs)

α/β-tubulin (Cytoskeleton Inc.) was polymerized into stable microtubules (MTs) according to the producer's instructions, and MT-cosedimentation assays were carried out as in Ciferri *et al.* [126]. For MT-binding reactions, MTs were diluted to a final concentration of 9 μM in general tubulin (GT) buffer (80 mM PIPES pH 6.8, 1 mM $MgCl_2$, 1 mM EGTA) supplemented with 1 mM GTP, 50 μM Paclitaxel, and 60 mM NaCl. 1 μM NuMA^{Cter} fragments were added to a final volume of 50 μl. Reactions were incubated at room temperature for 15 minutes, transferred onto 100 μl of cushion buffer (80 mM PIPES pH 6.8, 1 mM $MgCl_2$, 1 mM EGTA, 50 μM Paclitaxel, 50 % glycerol), and ultracentrifuged for 15 minutes at 400,000 g at 25 °C. To monitor phosphorylated species co-sedimenting with MTs (Fig. 29a), samples were loaded on a Phos-TAG SDS-PAGE. To assess whether NuMA could associate simultaneously with MTs and with LGN, the co-sedimentation assays were repeated in the presence of 1 μM LGN^{TPR}.

To perform MT-co-sedimentation experiments with cell extracts, HeLa cells stably expressing mCherry-NuMA^{Cter} and synchronized with STLC in prometaphase, with or without MLN8237, as described above, were lysed in JS buffer (75 mM Hepes pH 7.5, 1.5 mM EGTA, 1.5 mM $MgCl_2$, 0.15 M KCl, 0.1 % NP40, 15 % glycerol) supplemented with protease and phosphatase inhibitors. 50 μg of cleared lysates were subjected to ultracentrifugation at 400,000 *g* at 25 °C for 15 minutes with 0, 3, 5 μM of MTs previously polymerized. Supernatant (S) and pellet (P) fractions were analyzed by SDS-PAGE run at

80V for 5 hours, followed by immunoblotting. The mouse monoclonal anti-NuMA antibody was used at a dilution of 1:200, and the anti-α-tubulin at 1:1500 (Abcam ab4074).

5.6 In *vitro* microtubule forming assays

MT-forming assays were performed according to Du *et al*. [96]. Rhodamine-labeled and unlabeled tubulin were mixed at a 1:10 ratio at a concentration of 36 μM with GT buffer supplemented with 1 mM GTP, and incubated with 25 μM GST-NuMA^{Cter} fragments. 5 μl of the reactions were kept at 37 °C for 4 minutes, and later fixed for 3 minutes at room temperature with 45 μl of GT buffer complemented with 1% glutaraldehyde. Fixed samples were diluted to 200 μl with GT buffer containing 50% glycerol, spotted onto poly-lysine slides, and visualized by wide-field microscopy using a 60x oil immersion objective.

5.7 Cell biology protocols

5.7.1 Plasmids, RNA interference and transfections

Afadin/LGN Project

For knockdown of human Afadin, four unique 29-mer shRNA constructs in lentiviral vectors were tested in HeLa cells (OriGene Technologies, TL311457). The two most effective hairpins (Afadin shRNA-1, GCAGTCGTCAACAGATGGTGAGCATGAT; and Afadin shRNA-2, CTCTGTGGTGACACTGGAAGTAGCAAAGC) were further used to study the effect of Afadin ablation in mitotic HeLa cells. Caco-2 cells were infected with Afadin shRNA-2-expressing lentiviruses to generate a stable cell line devoid of Afadin. To rescue the misorientation phenotype of HeLa cells expressing the Afadin shRNA-2 hairpin, an shRNA-resistant mCherry-tagged rat long Afadin construct was generated by targeted mutagenesis introducing four silent base substitutions in the region targeted by the shRNA-2 hairpin. To obtain an Afadin$^{\Delta ACTIN}$ variant unable to interact with LGN, the construct was further engineered by deletion of residues 1714–1751 of rat long Afadin, corresponding to the LGN-binding stretch encoded by residues 1709–1747 of human

Afadin isoform 4. To obtain the Afadin$^{\Delta ACTIN}$ mutant, residues 1519–1690 were deleted from the rat Afadin gene, corresponding to residues 1514–1685 of isoform 4 of human Afadin (Fig. 9). mCherry-Afadin wild-type, mCherry-Afadin$^{\Delta ACTIN}$, and mCherry-Afadin$^{\Delta ACTIN}$ were subcloned into a pCDH vector under the UbC promoter (SBI System Biosciences) and transfected into HeLa cells with Lipofectamine reagent (Invitrogen) according to the manufacturer's instructions.

Aurora-A/NuMA Project

HeLa cell lines stably expressing mCherry-NuMA^{Cter} mutants were generated using the pCDH vector. For knocking-down human NuMA, four unique 29- mer shRNA in lentiviral vectors carrying a GFP reporter and puromycin resistance were tested in HeLa cells (catalogue number TL311065; OriGene Technologies). The most effective hairpin (5'CATTATGATGCCAAGAAGCAGCAGAACCA3') was used to generate a stably interfered HeLa cell line. Transfection was conducted following the manufacture's instruction using either Lipofectamine or Oligofectamine (both from Invitrogen) for plasmids or siRNA, respectively. For spindle orientation rescue experiments, NuMA-ablated HeLa cells were transfected with sh-resistant pCDH-mCherry- NuMA wild-type or S1969A mutant.

5.7.2 Cell treatments

Afadin/LGN Project

For all the experiments, HeLa cells were cultured on fibronectin (5 μg/ml; Roche) and synchronized by a single thymidine block. Cells were treated with 2.5 mM thymidine (Sigma, T1895) for 24 hours, released, and fixed for immunofluorescence after 8 hours. Latrunculin A (Sigma, L5163) was added to the medium 30 minutes before fixation.

Aurora-A/NuMA Project

For all experiments shown, cells were plated on fibronectin-coated coverslip (5 μg/ml,

Roche). HeLa cultures were pre-synchronized by thymidine block/release. The indicated amounts of MLN8237 (Selleck Chemicals) were added to the medium 6 hours after release, and cells were fixed after 9-10 hours from release. hTERT-RPE-1 cultures were synchronized by 100 μM Monastrol (Biomol International) for 16 hours, with the addition of MLN8237 during the last 2 hours of treatment. After 2 hours of Monastrol wash-out, cells grown in complete medium plus MLN8237 were fixed. Synchronization of HeLa cells in prometaphase was performed by adding 5 μM STLC (S-trityl-L- cysteine, Sigma) for 16 hours.

5.7.3 Immunofluorescence staining and quantification

Afadin/LGN Project

For detecting NuMA and Afadin, cells were fixed with methanol at −20 °C for 10 minutes. For detection of LGN, p150^{Glued} and actin, cells were fixed with 4% paraformaldehyde for 10 minutes at room temperature; this was followed by permeabilization with PBS and 0.3% Triton X-100 for 5 min. Cells were stained with rabbit anti-Afadin (polyclonal, raised against fragment 1514–1824 of human Afadin isoform 4; working dilution 1:500; produced in house; mouse anti-LGN (monoclonal, raised against human full-length LGN; working dilution 1:5; produced in house, mouse anti-NuMA (monoclonal, raised against fragment 1861–2001 of human NuMA; working dilution 1:3,000; produced in house, and p150^{Glued} (1:600, BD 610473). F-actin was visualized with TRITC-conjugated phalloidin (diluted 1:10 for HeLa cells and 1:50 for Caco-2 cysts, Sigma P1951), Quantification of cortical signals of LGN, NuMA and p150^{Glued} were conducted on confocal sections of metaphase cells in Fiji as follows. A 30-pixel-wide line was manually drawn from the spindle pole to the nearest cellular cortex perpendicularly to the metaphase plate, to obtain the intensity profile of the immunostained proteins along the line. The protein at the cortex was calculated by integrating the profile on a 30-pixel area centered at the peak of the profile, whereas the protein in the cytosol was quantified by integrating the same area 30

pixels away from the peak toward the DNA.

Aurora-A/NuMA Project

Cells grown on coverslips were fixed as follow: a) −20 °C methanol for 10 minutes to visualize NuMA and $p150^{Glued}$ at the cortex b) 4% paraformaldehyde (PFA) for 10 minutes at room temperature, followed by permeabilization with PBS and 0.1 % Triton X-100 for 5 minutes, to detect NuMA staining at poles and LGN. Cells were blocked with PBS containing 0.05 % Tween 20 and 3% BSA for one hour, and incubated 1-2 hours with primary antibodies at room temperature. Depending on the experiment, cells were stained with a monoclonal mouse antibody anti-LGN (Mapelli lab; 1:5), a monoclonal mouse antibody anti-NuMA (Mapelli lab; 1:3000), anti-$p150^{Glued}$ (BD, 610473, 1:1000), anti-α-tubulin (Abcam, ab4074; 1:50 or Sigma-Aldrich B-5-1-2; 1:3000), anti-γ- tubulin (Sigma-Aldrich, GTU-88; 1:1000, or Cy3 conjugated Sigma-Aldrich, C7604; 1:200). DNA was stained with DAPI. To quantify the fluorescence intensity of endogenous NuMA at the spindle poles, the signal of NuMA inside a α-tubulin mask was integrated using the Fiji software. To quantify the levels of mCherry-$NuMA^{Cter}$ at the spindle poles, mCherry signals within a α-tubulin mask were integrated, and compared to the amount of mCherry-$NuMA^{Cter}$ in the cytosol measured by integrating the mCherry signal of the same α-tubulin mask positioned in the cytoplasm area. Quantification of cortical signals of LGN, NuMA and $p150^{Glued}$ were conducted on confocal sections of metaphase cells in Fiji as follows. A 2.7 μm-wide line was manually drawn from the spindle pole to the nearest cellular cortex perpendicularly to the metaphase plate, to obtain the intensity profile of the immunostained proteins along the line. The "protein at the cortex" was calculated by integrating the profile on a 1.35 μm-large area centered at the peak of the profile, whereas the "protein in the cytosol" was quantified by integrating the same area 2.7 μm away from the peak towards the DNA.

5.7.4 Spindle orientation analysis

Spindle orientation was monitored with HeLa and hTERT-RPE-1 cells grown on fibronectin-coated coverslips. In this condition, wild-type cells divided with the spindle axis parallel to the substratum. To quantify the spindle tilt, metaphase cells were fixed and stained with anti-NuMA antibody and DAPI. Cells were imaged in x-z optical sections passing through the spindle poles. Spindle-axis angles with respect to the substratum were measured with the angle tool of Fiji.

5.7.5 FRAP analysis

HeLa cells plated were transfected with GFP-NuMA or mCherry-NuMA. After 24 hours, cells were synchronized with a single thymidine block and analyzed 8 hours after the release. To inhibit Aurora-A, 50 nM MLN8237 were added 5 hours after thymidine release. FRAP was performed on an UltraVIEW-VoX spinning-disk confocal system (PerkinElmer) equipped with an EclipseTi inverted microscope (Nikon) provided with a Nikon Perfect Focus System, an integrated FRAP PhotoKinesis unit (PerkinElmer), and a Hamamatsu CCD camera (C9100-50) and driven by Volocity software (Improvision; Perkin Elmer). All images were acquired through a 60× oil-immersion ob. GFP and mCherry signals were excited with a 488 nm and 561 nm 50 mW diode lasers, respectively. Photobleaching was performed on a 5 μm diameter circular region around one of the spindle poles. After bleaching, images were acquired every 2 seconds for 5 minutes. Analysis of the recovery curves was conducted using a custom macro in ImageJ. Briefly, the mean intensity value in the bleached area was measured, corrected for the background and for the acquisition photobleaching, and the curves were then normalized to the prebleaching mean intensity values. Recovery measurements were quantified by fitting normalized fluorescence intensities of bleached areas to a one-phase exponential association for GFP-NuMA by a custom-software of MatLab.

6. REFERENCES

1. Caussinus, E., and Gonzalez, C. (2005). Induction of tumor growth by altered stem-cell asymmetric division in Drosophila melanogaster. Nat Genet *37*, 1125-1129.
2. Bergstralh, D.T., Lovegrove, H.E., and St Johnston, D. (2015). Lateral adhesion drives reintegration of misplaced cells into epithelial monolayers. Nat Cell Biol *17*, 1497-1503.
3. Nakajima, Y., Meyer, E.J., Kroesen, A., McKinney, S.A., and Gibson, M.C. (2013). Epithelial junctions maintain tissue architecture by directing planar spindle orientation. Nature *500*, 359-362.
4. Williams, S.E., and Fuchs, E. (2013). Oriented divisions, fate decisions. Current opinion in cell biology *25*, 749-758.
5. Vorhagen, S., and Niessen, C.M. (2014). Mammalian aPKC/Par polarity complex mediated regulation of epithelial division orientation and cell fate. Experimental cell research *328*, 296-302.
6. Scadden, D.T. (2014). Nice neighborhood: emerging concepts of the stem cell niche. Cell *157*, 41-50.
7. Batlle, E., Henderson, J.T., Beghtel, H., van den Born, M.M., Sancho, E., Huls, G., Meeldijk, J., Robertson, J., van de Wetering, M., Pawson, T., et al. (2002). Beta-catenin and TCF mediate cell positioning in the intestinal epithelium by controlling the expression of EphB/ephrinB. Cell *111*, 251-263.
8. Tanaka-Okamoto, M., Itoh, Y., Miyoshi, J., Mizoguchi, A., Mizutani, K., Takai, Y., and Inoue, M. (2014). Genetic ablation of afadin causes mislocalization and deformation of Paneth cells in the mouse small intestinal epithelium. PloS one *9*, e110549.
9. Habib, S.J., Chen, B.C., Tsai, F.C., Anastassiadis, K., Meyer, T., Betzig, E., and Nusse, R. (2013). A localized Wnt signal orients asymmetric stem cell division in vitro. Science *339*, 1445-1448.
10. Kraut, R., Chia, W., Jan, L.Y., Jan, Y.N., and Knoblich, J.A. (1996). Role of inscuteable in orienting asymmetric cell divisions in Drosophila. Nature *383*, 50-55.
11. Schober, M., Schaefer, M., and Knoblich, J.A. (1999). Bazooka recruits Inscuteable to orient asymmetric cell divisions in Drosophila neuroblasts. Nature *402*, 548-551.
12. Culurgioni, S., Alfieri, A., Pendolino, V., Laddomada, F., and Mapelli, M. (2011). Inscuteable and NuMA proteins bind competitively to Leu-Gly-Asn repeat-enriched protein (LGN) during asymmetric cell divisions. Proc Natl Acad Sci U S A *108*, 20998-21003.
13. Siller, K.H., Cabernard, C., and Doe, C.Q. (2006). The NuMA-related Mud protein binds Pins and regulates spindle orientation in Drosophila neuroblasts. Nat Cell Biol *8*, 594-600.
14. Izumi, Y., Ohta, N., Hisata, K., Raabe, T., and Matsuzaki, F. (2006). Drosophila Pins-binding protein Mud regulates spindle-polarity coupling and centrosome organization. Nat Cell Biol *8*, 586-593.
15. Yamashita, Y.M., Jones, D.L., and Fuller, M.T. (2003). Orientation of asymmetric stem cell division by the APC tumor suppressor and centrosome. Science *301*, 1547-1550.
16. Williams, S.E., Beronja, S., Pasolli, H.A., and Fuchs, E. (2011). Asymmetric cell divisions promote Notch-dependent epidermal differentiation. Nature *470*, 353-358.
17. Lechler, T., and Fuchs, E. (2005). Asymmetric cell divisions promote stratification and differentiation of mammalian skin. Nature *437*, 275-280.
18. Niessen, M.T., Scott, J., Zielinski, J.G., Vorhagen, S., Sotiropoulou, P.A., Blanpain, C.d., Leitges, M., and Niessen, C.M. (2013). aPKCλ controls epidermal homeostasis and stem cell fate through regulation of division orientation. J Cell Biol *202*, 887-900.
19. Hao, Y., Du, Q., Chen, X., Zheng, Z., Balsbaugh, J.L., Maitra, S., Shabanowitz, J., Hunt, D.F., and Macara, I.G. (2010). Par3 controls epithelial spindle orientation by aPKC-mediated phosphorylation of apical Pins. Curr Biol *20*, 1809-1818.
20. Zheng, Z., Zhu, H., Wan, Q., Liu, J., Xiao, Z., Siderovski, D.P., and Du, Q. (2010). LGN regulates mitotic spindle orientation during epithelial morphogenesis. J Cell Biol *189*, 275-288.
21. Jaffe, A.B., Kaji, N., Durgan, J., and Hall, A. (2008). Cdc42 controls spindle orientation to position the apical surface during epithelial morphogenesis. J Cell Biol *183*, 625-633.

22. Toyoshima, F., and Nishida, E. (2007). Integrin-mediated adhesion orients the spindle parallel to the substratum in an EB1- and myosin X-dependent manner. Embo J *26*, 1487-1498.
23. Kotak, S., Busso, C., and Gonczy, P. (2012). Cortical dynein is critical for proper spindle positioning in human cells. J Cell Biol *199*, 97-110.
24. Woodard, G.E., Huang, N.N., Cho, H., Miki, T., Tall, G.G., and Kehrl, J.H. (2011). Ric-8A and Gi alpha recruit LGN, NuMA, and dynein to the cell cortex to help orient the mitotic spindle. Mol Cell Biol *30*, 3519-3530.
25. Du, Q., and Macara, I.G. (2004). Mammalian Pins is a conformational switch that links NuMA to heterotrimeric G proteins. Cell *119*, 503-516.
26. Kiyomitsu, T., and Cheeseman, I.M. (2012). Chromosome- and spindle-pole-derived signals generate an intrinsic code for spindle position and orientation. Nat Cell Biol.
27. Peyre, E., Jaouen, F., Saadaoui, M., Haren, L., Merdes, A., Durbec, P., and Morin, X. (2011). A lateral belt of cortical LGN and NuMA guides mitotic spindle movements and planar division in neuroepithelial cells. J Cell Biol *193*, 141-154.
28. Saadaoui, M., Machicoane, M., di Pietro, F., Etoc, F., Echard, A., and Morin, X. (2014). Dlg1 controls planar spindle orientation in the neuroepithelium through direct interaction with LGN. J Cell Biol *206*, 707-717.
29. Bergstralh, D.T., Lovegrove, H.E., and St Johnston, D. (2013). Discs large links spindle orientation to apical-basal polarity in Drosophila epithelia. Curr Biol *23*, 1707-1712.
30. Tuncay, H., and Ebnet, K. (2016). Cell adhesion molecule control of planar spindle orientation. Cell Mol Life Sci *73*, 1195-1207.
31. Kimple, R.J., Kimple, M.E., Betts, L., Sondek, J., and Siderovski, D.P. (2002). Structural determinants for GoLoco-induced inhibition of nucleotide release by Galpha subunits. Nature *416*, 878-881.
32. Jia, M., Li, J., Zhu, J., Wen, W., Zhang, M., and Wang, W. (2012). Crystal structures of the scaffolding protein LGN reveal the general mechanism by which GoLoco binding motifs inhibit the release of GDP from Galphai. J Biol Chem *287*, 36766-36776.
33. David, N.B., Martin, C.A., Segalen, M., Rosenfeld, F., Schweisguth, F., and Bellaiche, Y. (2005). Drosophila Ric-8 regulates Galphai cortical localization to promote Galphai-dependent planar orientation of the mitotic spindle during asymmetric cell division. Nat Cell Biol *7*, 1083-1090.
34. Bellaiche, Y., and Gotta, M. (2005). Heterotrimeric G proteins and regulation of size asymmetry during cell division. Curr Opin Cell Biol *17*, 658-663.
35. Kiyomitsu, T., and Cheeseman, I.M. (2013). Cortical dynein and asymmetric membrane elongation coordinately position the spindle in anaphase. Cell *154*, 391-402.
36. Zhu, J., Wen, W., Zheng, Z., Shang, Y., Wei, Z., Xiao, Z., Pan, Z., Du, Q., Wang, W., and Zhang, M. (2011). LGN/mInsc and LGN/NuMA complex structures suggest distinct functions in asymmetric cell division for the Par3/mInsc/LGN and Galphai/LGN/NuMA pathways. Molecular cell *43*, 418-431.
37. Yuzawa, S., Kamakura, S., Iwakiri, Y., Hayase, J., and Sumimoto, H. (2011). Structural basis for interaction between the conserved cell polarity proteins Inscuteable and Leu-Gly-Asn repeat-enriched protein (LGN). Proc Natl Acad Sci U S A *108*, 19210-19215.
38. Takayanagi, H., Yuzawa, S., and Sumimoto, H. (2015). Structural basis for the recognition of the scaffold protein Frmpd4/Preso1 by the TPR domain of the adaptor protein LGN. Acta Crystallogr F Struct Biol Commun *71*, 175-183.
39. Pan, Z., Shang, Y., Jia, M., Zhang, L., Xia, C., Zhang, M., Wang, W., and Wen, W. (2013). Structural and biochemical characterization of the interaction between LGN and Frmpd1. Journal of molecular biology *425*, 1039-1049.
40. Pan, Z., Zhu, J., Shang, Y., Wei, Z., Jia, M., Xia, C., Wen, W., Wang, W., and Zhang, M. (2013). An autoinhibited conformation of LGN reveals a distinct interaction mode between GoLoco motifs and TPR motifs. Structure *21*, 1007-1017.
41. Smith, N.R., and Prehoda, K.E. (2011). Robust spindle alignment in Drosophila neuroblasts by ultrasensitive activation of pins. Molecular cell *43*, 540-549.
42. Nipper, R.W., Siller, K.H., Smith, N.R., Doe, C.Q., and Prehoda, K.E. (2007). Galphai generates multiple Pins activation states to link cortical polarity and spindle orientation in Drosophila neuroblasts. Proc Natl Acad Sci U S A *104*, 14306-14311.

43. Johnston, C.A., Hirono, K., Prehoda, K.E., and Doe, C.Q. (2009). Identification of an Aurora-A/PinsLINKER/Dlg spindle orientation pathway using induced cell polarity in S2 cells. Cell *138*, 1150-1163.
44. Speicher, S., Fischer, A., Knoblich, J., and Carmena, A. (2008). The PDZ protein Canoe regulates the asymmetric division of Drosophila neuroblasts and muscle progenitors. Curr Biol *18*, 831-837.
45. Bellaiche, Y., Radovic, A., Woods, D.F., Hough, C.D., Parmentier, M.L., O'Kane, C.J., Bryant, P.J., and Schweisguth, F. (2001). The Partner of Inscuteable/Discs-large complex is required to establish planar polarity during asymmetric cell division in Drosophila. Cell *106*, 355-366.
46. Zhu, J., Shang, Y., Xia, C., Wang, W., Wen, W., and Zhang, M. (2011). Guanylate kinase domains of the MAGUK family scaffold proteins as specific phospho-protein-binding modules. Embo J *30*, 4986-4997.
47. Sans, N., Wang, P.Y., Du, Q., Petralia, R.S., Wang, Y.X., Nakka, S., Blumer, J.B., Macara, I.G., and Wenthold, R.J. (2005). mPins modulates PSD-95 and SAP102 trafficking and influences NMDA receptor surface expression. Nat Cell Biol *7*, 1179-1190.
48. Segalen, M., Johnston, C.A., Martin, C.A., Dumortier, J.G., Prehoda, K.E., David, N.B., Doe, C.Q., and Bellaiche, Y. (2010). The Fz-Dsh planar cell polarity pathway induces oriented cell division via Mud/NuMA in Drosophila and zebrafish. Dev Cell *19*, 740-752.
49. Dewey, E.B., Sanchez, D., and Johnston, C.A. (2015). Warts phosphorylates mud to promote pins-mediated mitotic spindle orientation in Drosophila, independent of Yorkie. Curr Biol *25*, 2751-2762.
50. Keder, A., Rives-Quinto, N., Aerne, B.L., Franco, M., Tapon, N., and Carmena, A. (2015). The hippo pathway core cassette regulates asymmetric cell division. Curr Biol *25*, 2739-2750.
51. Banon-Rodriguez, I., Galvez-Santisteban, M., Vergarajauregui, S., Bosch, M., Borreguero-Pascual, A., and Martin-Belmonte, F. (2014). EGFR controls IQGAP basolateral membrane localization and mitotic spindle orientation during epithelial morphogenesis. Embo J *33*, 129-145.
52. Johnston, C.A., Manning, L., Lu, M.S., Golub, O., Doe, C.Q., and Prehoda, K.E. (2013). Formin-mediated actin polymerization cooperates with Mushroom body defect (Mud)-Dynein during Frizzled-Dishevelled spindle orientation. J Cell Sci *126*, 4436-4444.
53. Yang, Y., Liu, M., Li, D., Ran, J., Gao, J., Suo, S., Sun, S.C., and Zhou, J. (2014). CYLD regulates spindle orientation by stabilizing astral microtubules and promoting dishevelled-NuMA-dynein/dynactin complex formation. Proc Natl Acad Sci U S A *111*, 2158-2163.
54. Kikuchi, K., Niikura, Y., Kitagawa, K., and Kikuchi, A. (2010). Dishevelled, a Wnt signalling component, is involved in mitotic progression in cooperation with Plk1. Embo J *29*, 3470-3483.
55. Madrzak, J., Fiedler, M., Johnson, C.M., Ewan, R., Knebel, A., Bienz, M., and Chin, J.W. (2015). Ubiquitination of the Dishevelled DIX domain blocks its head-to-tail polymerization. Nat Commun *6*, 6718.
56. Bienz, M. (2014). Signalosome assembly by domains undergoing dynamic head-to-tail polymerization. Trends Biochem Sci *39*, 487-495.
57. Machicoane, M., de Frutos, C.A., Fink, J., Rocancourt, M., Lombardi, Y., Garel, S., Piel, M., and Echard, A. (2014). SLK-dependent activation of ERMs controls LGN-NuMA localization and spindle orientation. J Cell Biol *205*, 791-799.
58. Mitsushima, M., Toyoshima, F., and Nishida, E. (2009). Dual role of Cdc42 in spindle orientation control of adherent cells. Mol Cell Biol *29*, 2816-2827.
59. Lancaster, O.M., and Baum, B. (2014). Shaping up to divide: Coordinating actin and microtubule cytoskeletal remodelling during mitosis. Seminars in cell & developmental biology.
60. di Pietro, F., Echard, A., and Morin, X. (2016). Regulation of mitotic spindle orientation: an integrated view. EMBO Rep *17*, 1106-1130.
61. Zheng, Z., Wan, Q., Liu, J., Zhu, H., Chu, X., and Du, Q. (2013). Evidence for dynein and astral microtubule-mediated cortical release and transport of Galphai/LGN/NuMA complex in mitotic cells. Mol Biol Cell *24*, 901-913.

62. Zhu, M., Settele, F., Kotak, S., Sanchez-Pulido, L., Ehret, L., Ponting, C.P., Gonczy, P., and Hoffmann, I. (2013). MISP is a novel Plk1 substrate required for proper spindle orientation and mitotic progression. J Cell Biol *200*, 773-787.
63. Kwon, M., Bagonis, M., Danuser, G., and Pellman, D. (2015). Direct Microtubule-Binding by Myosin-10 Orients Centrosomes toward Retraction Fibers and Subcortical Actin Clouds. Dev Cell *34*, 323-337.
64. Fink, J., Carpi, N., Betz, T., Betard, A., Chebah, M., Azioune, A., Bornens, M., Sykes, C., Fetler, L., Cuvelier, D., et al. (2011). External forces control mitotic spindle positioning. Nat Cell Biol *13*, 771-778.
65. Thery, M., Racine, V., Pepin, A., Piel, M., Chen, Y., Sibarita, J.B., and Bornens, M. (2005). The extracellular matrix guides the orientation of the cell division axis. Nat Cell Biol *7*, 947-953.
66. Reinsch, S., and Karsenti, E. (1994). Orientation of spindle axis and distribution of plasma membrane proteins during cell division in polarized MDCKII cells. J Cell Biol *126*, 1509-1526.
67. Baker, J., and Garrod, D. (1993). Epithelial cells retain junctions during mitosis. J Cell Sci *104 (Pt 2)*, 415-425.
68. den Elzen, N., Buttery, C.V., Maddugoda, M.P., Ren, G., and Yap, A.S. (2009). Cadherin adhesion receptors orient the mitotic spindle during symmetric cell division in mammalian epithelia. Mol Biol Cell *20*, 3740-3750.
69. Tuncay, H., Brinkmann, B.F., Steinbacher, T., Schurmann, A., Gerke, V., Iden, S., and Ebnet, K. (2015). JAM-A regulates cortical dynein localization through Cdc42 to control planar spindle orientation during mitosis. Nat Commun *6*, 8128.
70. Xia, J., Swiercz, J.M., Banon-Rodriguez, I., Matkovic, I., Federico, G., Sun, T., Franz, T., Brakebusch, C.H., Kumanogoh, A., Friedel, R.H., et al. (2015). Semaphorin-Plexin Signaling Controls Mitotic Spindle Orientation during Epithelial Morphogenesis and Repair. Dev Cell *33*, 299-313.
71. Bosveld, F., Markova, O., Guirao, B., Martin, C., Wang, Z., Pierre, A., Balakireva, M., Gaugue, I., Ainslie, A., Christophorou, N., et al. (2016). Epithelial tricellular junctions act as interphase cell shape sensors to orient mitosis. Nature *530*, 495-498.
72. Fujiwara, Y., Goda, N., Tamashiro, T., Narita, H., Satomura, K., Tenno, T., Nakagawa, A., Oda, M., Suzuki, M., Sakisaka, T., et al. (2015). Crystal structure of afadin PDZ domain-nectin-3 complex shows the structural plasticity of the ligand-binding site. Protein Sci *24*, 376-385.
73. Sawyer, J.K., Harris, N.J., Slep, K.C., Gaul, U., and Peifer, M. (2009). The Drosophila afadin homologue Canoe regulates linkage of the actin cytoskeleton to adherens junctions during apical constriction. J Cell Biol *186*, 57-73.
74. Wee, B., Johnston, C.A., Prehoda, K.E., and Doe, C.Q. (2011). Canoe binds RanGTP to promote Pins(TPR)/Mud-mediated spindle orientation. J Cell Biol *195*, 369-376.
75. Lorger, M., and Moelling, K. (2006). Regulation of epithelial wound closure and intercellular adhesion by interaction of AF6 with actin cytoskeleton. J Cell Sci *119*, 3385-3398.
76. Saito, S., Matsushima, M., Shirahama, S., Minaguchi, T., Kanamori, Y., Minami, M., and Nakamura, Y. (1998). Complete genomic structure DNA polymorphisms, and alternative splicing of the human AF-6 gene. DNA Res *5*, 115-120.
77. Mandai, K., Nakanishi, H., Satoh, A., Obaishi, H., Wada, M., Nishioka, H., Itoh, M., Mizoguchi, A., Aoki, T., Fujimoto, T., et al. (1997). Afadin: A novel actin filament-binding protein with one PDZ domain localized at cadherin-based cell-to-cell adherens junction. J Cell Biol *139*, 517-528.
78. Ooshio, T., Irie, K., Morimoto, K., Fukuhara, A., Imai, T., and Takai, Y. (2004). Involvement of LMO7 in the association of two cell-cell adhesion molecules, nectin and E-cadherin, through afadin and alpha-actinin in epithelial cells. J Biol Chem *279*, 31365-31373.
79. Zhadanov, A.B., Provance, D.W., Jr., Speer, C.A., Coffin, J.D., Goss, D., Blixt, J.A., Reichert, C.M., and Mercer, J.A. (1999). Absence of the tight junctional protein AF-6 disrupts epithelial cell-cell junctions and cell polarity during mouse development. Curr Biol *9*, 880-888.

80. Yamamoto, H., Maruo, T., Majima, T., Ishizaki, H., Tanaka-Okamoto, M., Miyoshi, J., Mandai, K., and Takai, Y. (2013). Genetic deletion of afadin causes hydrocephalus by destruction of adherens junctions in radial glial and ependymal cells in the midbrain. PloS one *8*, e80356.
81. Yang, Z., Zimmerman, S., Brakeman, P.R., Beaudoin, G.M., 3rd, Reichardt, L.F., and Marciano, D.K. (2013). De novo lumen formation and elongation in the developing nephron: a central role for afadin in apical polarity. Development *140*, 1774-1784.
82. Tawa, H., Rikitake, Y., Takahashi, M., Amano, H., Miyata, M., Satomi-Kobayashi, S., Kinugasa, M., Nagamatsu, Y., Majima, T., Ogita, H., et al. (2010). Role of afadin in vascular endothelial growth factor- and sphingosine 1-phosphate-induced angiogenesis. Circulation research *106*, 1731-1742.
83. Xu, Y., Chang, R., Peng, Z., Wang, Y., Ji, W., Guo, J., Song, L., Dai, C., Wei, W., Wu, Y., et al. (2015). Loss of polarity protein AF6 promotes pancreatic cancer metastasis by inducing Snail expression. Nat Commun *6*, 7184.
84. Fournier, G., Cabaud, O., Josselin, E., Chaix, A., Adelaide, J., Isnardon, D., Restouin, A., Castellano, R., Dubreuil, P., Chaffanet, M., et al. (2011). Loss of AF6/afadin, a marker of poor outcome in breast cancer, induces cell migration, invasiveness and tumor growth. Oncogene *30*, 3862-3874.
85. Nik-Zainal, S., Davies, H., Staaf, J., Ramakrishna, M., Glodzik, D., Zou, X., Martincorena, I., Alexandrov, L.B., Martin, S., Wedge, D.C., et al. (2016). Landscape of somatic mutations in 560 breast cancer whole-genome sequences. Nature *534*, 47-54.
86. Kotak, S., and Gonczy, P. (2013). Mechanisms of spindle positioning: cortical force generators in the limelight. Current opinion in cell biology *25*, 741-748.
87. Wang, G., Jiang, Q., and Zhang, C. (2014). The role of mitotic kinases in coupling the centrosome cycle with the assembly of the mitotic spindle. J Cell Sci *127*, 4111-4122.
88. Merdes, A., Heald, R., Samejima, K., Earnshaw, W.C., and Cleveland, D.W. (2000). Formation of spindle poles by dynein/dynactin-dependent transport of NuMA. J Cell Biol *149*, 851-862.
89. Merdes, A., Ramyar, K., Vechio, J.D., and Cleveland, D.W. (1996). A complex of NuMA and cytoplasmic dynein is essential for mitotic spindle assembly. Cell *87*, 447-458.
90. Kotak, S., Busso, C., and Gonczy, P. (2013). NuMA phosphorylation by CDK1 couples mitotic progression with cortical dynein function. Embo J *32*, 2517-2529.
91. Zheng, Z., Wan, Q., Meixiong, G., and Du, Q. (2014). Cell cycle-regulated membrane binding of NuMA contributes to efficient anaphase chromosome separation. Mol Biol Cell *25*, 606-619.
92. Seldin, L., Poulson, N.D., Foote, H.P., and Lechler, T. (2013). NuMA localization, stability, and function in spindle orientation involve 4.1 and Cdk1 interactions. Mol Biol Cell *24*, 3651-3662.
93. Mattagajasingh, S.N., Huang, S.C., Hartenstein, J.S., Snyder, M., Marchesi, V.T., and Benz, E.J. (1999). A nonerythroid isoform of protein 4.1R interacts with the nuclear mitotic apparatus (NuMA) protein. J Cell Biol *145*, 29-43.
94. Kotak, S., Busso, C., and Gonczy, P. (2014). NuMA interacts with phosphoinositides and links the mitotic spindle with the plasma membrane. Embo J *33*, 1815-1830.
95. Haren, L., and Merdes, A. (2002). Direct binding of NuMA to tubulin is mediated by a novel sequence motif in the tail domain that bundles and stabilizes microtubules. J Cell Sci *115*, 1815-1824.
96. Du, Q., Taylor, L., Compton, D.A., and Macara, I.G. (2002). LGN blocks the ability of NuMA to bind and stabilize microtubules. A mechanism for mitotic spindle assembly regulation. Curr Biol *12*, 1928-1933.
97. Silk, A.D., Holland, A.J., and Cleveland, D.W. (2009). Requirements for NuMA in maintenance and establishment of mammalian spindle poles. J Cell Biol *184*, 677-690.
98. Matsumura, S., Hamasaki, M., Yamamoto, T., Ebisuya, M., Sato, M., Nishida, E., and Toyoshima, F. (2011). ABL1 regulates spindle orientation in adherent cells and mammalian skin. Nat Commun *3*, 626.
99. Kettenbach, A.N., Schweppe, D.K., Faherty, B.K., Pechenick, D., Pletnev, A.A., and Gerber, S.A. (2011). Quantitative phosphoproteomics identifies substrates and functional modules of Aurora and Polo-like kinase activities in mitotic cells. Sci Signal *4*, rs5.

100. Toughiri, R., Li, X., Du, Q., and Bieberich, C.J. (2012). Phosphorylation of NuMA by Aurora-A kinase in PC-3 prostate cancer cells affects proliferation, survival and interphase NuMA localization. Journal of cellular biochemistry.
101. Asteriti, I.A., Giubettini, M., Lavia, P., and Guarguaglini, G. (2011). Aurora-A inactivation causes mitotic spindle pole fragmentation by unbalancing microtubule-generated forces. Molecular cancer *10*, 131.
102. Miyahara, M., Nakanishi, H., Takahashi, K., Satoh-Horikawa, K., Tachibana, K., and Takai, Y. (2000). Interaction of nectin with afadin is necessary for its clustering at cell-cell contact sites but not for its cis dimerization or trans interaction. J Biol Chem *275*, 613-618.
103. Zhang, Y.L., and Zhang, Z.Y. (1998). Low-affinity binding determined by titration calorimetry using a high-affinity coupling ligand: a thermodynamic study of ligand binding to protein tyrosine phosphatase 1B. Anal Biochem *261*, 139-148.
104. Carminati, M., Cecatiello, V., and Mapelli, M. (2016). Crystallization and X-ray diffraction of LGN in complex with the actin-binding protein afadin. Acta Crystallogr F Struct Biol Commun *72*, 145-151.
105. Kabsch, W. (2010). Integration, scaling, space-group assignment and post-refinement. Acta Crystallogr D Biol Crystallogr *66*, 133-144.
106. Winter, G., Lobley, C.M., and Prince, S.M. (2013). Decision making in xia2. Acta Crystallogr D Biol Crystallogr *69*, 1260-1273.
107. McCoy, A.J., Grosse-Kunstleve, R.W., Adams, P.D., Winn, M.D., Storoni, L.C., and Read, R.J. (2007). Phaser crystallographic software. Journal of applied crystallography *40*, 658-674.
108. Emsley, P., Lohkamp, B., Scott, W.G., and Cowtan, K. (2010). Features and development of Coot. Acta Crystallogr D Biol Crystallogr *66*, 486-501.
109. Adams, P.D., Afonine, P.V., Bunkoczi, G., Chen, V.B., Davis, I.W., Echols, N., Headd, J.J., Hung, L.W., Kapral, G.J., Grosse-Kunstleve, R.W., et al. (2010). PHENIX: a comprehensive Python-based system for macromolecular structure solution. Acta Crystallogr D Biol Crystallogr *66*, 213-221.
110. Radulescu, A.E., and Cleveland, D.W. (2010). NuMA after 30 years: the matrix revisited. Trends in cell biology *20*, 214-222.
111. Wiese, C., Wilde, A., Moore, M.S., Adam, S.A., Merdes, A., and Zheng, Y. (2001). Role of importin-beta in coupling Ran to downstream targets in microtubule assembly. Science *291*, 653-656.
112. Ferrari, S., Marin, O., Pagano, M.A., Meggio, F., Hess, D., El-Shemerly, M., Krystyniak, A., and Pinna, L.A. (2005). Aurora-A site specificity: a study with synthetic peptide substrates. Biochem J *390*, 293-302.
113. Cheeseman, I.M., Anderson, S., Jwa, M., Green, E.M., Kang, J., Yates, J.R., 3rd, Chan, C.S., Drubin, D.G., and Barnes, G. (2002). Phospho-regulation of kinetochore-microtubule attachments by the Aurora kinase Ipl1p. Cell *111*, 163-172.
114. Forth, S., Hsia, K.C., Shimamoto, Y., and Kapoor, T.M. (2014). Asymmetric friction of nonmotor MAPs can lead to their directional motion in active microtubule networks. Cell *157*, 420-432.
115. Carminati, M., Gallini, S., Pirovano, L., Alfieri, A., Bisi, S., and Mapelli, M. (2016). Concomitant binding of Afadin to LGN and F-actin directs planar spindle orientation. Nat Struct Mol Biol *23*, 155-163.
116. Birukova, A.A., Tian, X., Tian, Y., Higginbotham, K., and Birukov, K.G. (2013). Rap-afadin axis in control of Rho signaling and endothelial barrier recovery. Mol Biol Cell *24*, 2678-2688.
117. Iwasawa, N., Negishi, M., and Oinuma, I. (2012). R-Ras controls axon branching through afadin in cortical neurons. Mol Biol Cell *23*, 2793-2804.
118. Carmena, A., Makarova, A., and Speicher, S. (2011). The Rap1-Rgl-Ral signaling network regulates neuroblast cortical polarity and spindle orientation. J Cell Biol *195*, 553-562.
119. Gallini, S., Carminati, M., De Mattia, F., Pirovano, L., Martini, E., Oldani, A., Asteriti, I.A., Guarguaglini, G., and Mapelli, M. (2016). NuMA Phosphorylation by Aurora-A Orchestrates Spindle Orientation. Curr Biol *26*, 458-469.
120. Regan, J.L., Sourisseau, T., Soady, K., Kendrick, H., McCarthy, A., Tang, C., Brennan, K., Linardopoulos, S., White, D.E., and Smalley, M.J. (2013). Aurora A kinase regulates

mammary epithelial cell fate by determining mitotic spindle orientation in a Notch-dependent manner. Cell reports *4*, 110-123.

121. van den Ent, F., and Lowe, J. (2006). RF cloning: a restriction-free method for inserting target genes into plasmids. J Biochem Biophys Methods *67*, 67-74.
122. Kantardjieff, K.A., and Rupp, B. (2003). Matthews coefficient probabilities: Improved estimates for unit cell contents of proteins, DNA, and protein-nucleic acid complex crystals. Protein Sci *12*, 1865-1871.
123. Weichenberger, C.X., and Rupp, B. (2014). Ten years of probabilistic estimates of biocrystal solvent content: new insights via nonparametric kernel density estimate. Acta Crystallogr D Biol Crystallogr *70*, 1579-1588.
124. Carlier, M.F., Criquet, P., Pantaloni, D., and Korn, E.D. (1986). Interaction of cytochalasin D with actin filaments in the presence of ADP and ATP. J Biol Chem *261*, 2041-2050.
125. Scita, G., Tenca, P., Areces, L.B., Tocchetti, A., Frittoli, E., Giardina, G., Ponzanelli, I., Sini, P., Innocenti, M., and Di Fiore, P.P. (2001). An effector region in Eps8 is responsible for the activation of the Rac-specific GEF activity of Sos-1 and for the proper localization of the Rac-based actin-polymerizing machine. J Cell Biol *154*, 1031-1044.
126. Ciferri, C., Pasqualato, S., Screpanti, E., Varetti, G., Santaguida, S., Dos Reis, G., Maiolica, A., Polka, J., De Luca, J.G., De Wulf, P., et al. (2008). Implications for kinetochore-microtubule attachment from the structure of an engineered Ndc80 complex. Cell *133*, 427-439.

7. APPENDIX: Publications

nature structural & molecular biology

Concomitant binding of Afadin to LGN and F-actin directs planar spindle orientation

Manuel Carminati[1,4], Sara Gallini[1,4], Laura Pirovano[1], Andrea Alfieri[1,3], Sara Bisi[2] & Marina Mapelli[1]

Polarized epithelia form by oriented cell divisions in which the mitotic spindle aligns parallel to the epithelial plane. To orient the mitotic spindle, cortical cues trigger the recruitment of NuMA–dynein–based motors, which pull on astral microtubules via the protein LGN. We demonstrate that the junctional protein Afadin is required for spindle orientation and correct epithelial morphogenesis of Caco-2 cysts. Molecularly, Afadin binds directly and concomitantly to F-actin and to LGN. We determined the crystallographic structure of human Afadin in complex with LGN and show that it resembles the LGN–NuMA complex. In mitosis, Afadin is necessary for cortical accumulation of LGN and NuMA above the spindle poles, in an F-actin–dependent manner. Collectively, our results depict Afadin as a molecular hub governing the enrichment of LGN and NuMA at the cortex. To our knowledge, Afadin is the first-described mechanical anchor between dynein and cortical F-actin.

Oriented cell divisions are essential for morphogenesis during embryonic development and for homeostasis of adult organisms[1]. Divisions within the plane of epithelia, or planar divisions, shape the architecture of epithelial sheets. Conversely, vertical divisions along the apicobasal axis have been associated with asymmetric fate specification and stratification[2,3]. Consistently with this observation, the impairment of spindle-orientation pathways leads to developmental defects[3,4] and has been correlated with tumor-like proliferation and age disorders[5–7].

Oriented divisions rely on the coordination between spindle position and cortical polarity. In planar epithelial divisions, the spindle axis is maintained within the epithelial plane by microtubule motors localized at the lateral membrane. The core constituents of these force-generating machines are trimeric complexes formed by the nuclear mitotic apparatus protein (NuMA), the switch molecule LGN and the $G_{\alpha i}$ subunit of heterotrimeric G proteins, all of which are conserved in eukaryotes including nematodes and mammals[8]. Genetic and cellular characterization of spindle dynamics in several systems has suggested that at mitotic entry LGN is targeted to the plasma membrane by direct interaction of its C-terminal region with multiple $G_{\alpha i}$ molecules, whose myristoyl group inserts into the lipid bilayer[1,9]. The N-terminal tetratricopeptide repeat (TPR) domain of LGN (hereafter LGN^{TPR}) acts as a cortical receptor for NuMA that is released in the cytoplasm upon nuclear-envelope breakdown and associates with the motor dynein. Mechanistically, the minus end–directed movement of dynein–dynactin engaged at the membrane with NuMA and LGN results in pulling forces that act on astral microtubules and are able to position the spindle[10]. What restricts LGN and NuMA to the lateral cortex during planar divisions is largely unclear.

Members of the disc large (Dlg) family that localize at the baso-lateral membrane have been reported to promote planar divisions in chick neural progenitors[11], in *Drosophila* imaginal discs and in follicular epithelium[12,13]. Molecularly, Dlg favors the lateral enrichment of an LGN variant phosphorylated on the linker region between the TPR domain and the $G_{\alpha i}$-binding sites, and it acts on the spindle through the kinesin GAKIN (Khc-73 in flies)[14–16]. In asymmetrical apicobasal divisions in flies and vertebrates, the stem cell–specific adaptor Inscuteable bridges LGN and the polarity proteins Par3–Par6–aPKC, which are localized at the apical site[17,18]. Whether other LGN and NuMA tethers to the cortex exist remains unexplored to date.

Genetic studies in *Drosophila* have shown that the membrane-associated Canoe (Afadin in mammals) contributes to spindle alignment of neuroblasts and muscle progenitors[19,20] and interacts with Pins (LGN in mammals)[21]. Interestingly, ablation of Canoe (Afadin) in these systems prevents cortical enrichment of Mud, the counterpart of NuMA in flies. The vertebrate ortholog of Canoe is Afadin (or AF6), whose longest splicing variants are expressed ubiquitously[22]. In vertebrate epithelia, Afadin organizes adherens junctions, together with a plethora of other junctional constituents including nectins, α-catenin, p120, LMO7, occludin and claudin[23,24]. Consistently with this function, the Afadin knockout is embryonically lethal in mice[25], whereas its tissue-specific ablations cause severe morphogenetic defects in the brain[26], nephrons[27] and lymphatic system[28]. Loss of Afadin in the small intestine induces dislodging of the Paneth cells (the niche of intestinal stem cells) from the base of the crypt, thus suggesting a role for Afadin in regulating the intestinal stem-cell compartment[29]. The domain structure of Afadin consists of several Ras-association domains, followed by a forkhead (FH) domain, a Dilute domain (DIL) and a PDZ domain responsible for the interaction with nectins[30] and Dishevelled[31] (**Fig. 1b**). Whether human Afadin binds to LGN to promote spindle positioning is not known.

[1]Department of Experimental Oncology, European Institute of Oncology, Milan, Italy. [2]Fondazione Italiana Ricerca sul Cancro Institute of Molecular Oncology, Milan, Italy. [3]Present address: Department of Biosciences, Università degli Studi di Milano, Milan, Italy. [4]These authors contributed equally to this work. Correspondence should be addressed to M.M. (marina.mapelli@ieo.eu).

Received 20 June 2015; accepted 26 November 2015; published online 11 January 2016; doi:10.1038/nsmb.3152

Afadin was initially identified as a filamentous actin (F-actin) binding protein. Long and short isoforms of Afadin differ in the C-terminal region, which in both vertebrates and flies is the portion of the molecule binding to F-actin[32]. Interestingly, recent evidence has suggested a major role of the actomyosin cytoskeleton in spindle positioning in several cellular systems[33,34]. In HeLa cells, chemical depolymerization of F-actin, or ablation of actin-binding proteins required for cortical integrity, abrogates the cortical accumulation of LGN and NuMA and leads to misoriented divisions[35–37]. This phenotype has been ascribed to global changes in the stiffness of the plasma membrane and hence changes in its ability to counterbalance dynein-based forces. The possibility that more direct molecular links exist between the actomyosin cortex and mechanoenzyme positioning the spindle is currently unexplored.

To understand whether and how the actin-binding protein Afadin contributes to planar divisions, we set out to investigate its spindle-orientation functions in polarized epithelia and its interactions with LGN and NuMA. Our studies uncover a new role of Afadin in governing spindle orientation in Caco-2 three-dimensional cysts and HeLa cells, and elucidate the molecular mechanism underlying this function. Most notably, we show that Afadin acts as a direct molecular bridge between the actomyosin cortex, LGN and dynein, and that this function is essential for planar divisions and correct epithelial morphogenesis.

RESULTS

Ablation of Afadin induces mitotic-spindle misorientation

To begin to address the mitotic function of Afadin, we generated a polyclonal antibody recognizing the C-terminal portion of isoform 4 of human Afadin, which we will refer to as Afadin (**Supplementary Fig. 1a**). In HeLa cells, Afadin was uniformly cortical from prometaphase to anaphase, and it colocalized with LGN and NuMA at the polar regions of the cell cortex, whereas in telophase it accumulated at the cortical region in proximity to the cleavage furrow (**Fig. 1a**). The cortical enrichment of Afadin in mitosis prompted us to investigate whether it could be implicated in spindle positioning. To explore this possibility, we developed two lentiviral short hairpin RNAs (hereafter shRNA-1/2) targeting human Afadin, which, compared to control shRNA, produced ~80% knockdown (**Fig. 1c**,**d** and **Supplementary Fig. 1b**). We then created HeLa cell lines in which Afadin was stably depleted and visualized the mitotic-spindle orientation of synchronized cells plated on fibronectin-coated coverslips. Under these conditions, unperturbed cells aligned the spindle axis parallel to the substratum, whereas cells with defective orientation mechanisms underwent misoriented divisions (**Fig. 1e**). In both cell lines with stable Afadin knockdown, we observed spindle randomization, with an average spindle angle of 13.9° or 15.4°, compared to 7.6° in cells expressing control shRNA, and spindle angular distributions skewed toward larger values than those in wild-type cells (**Fig. 1f**). Importantly, the misorientation phenotype observed in the Afadin-depleted cells was comparable to that displayed by HeLa cells lacking LGN or NuMA (**Supplementary Fig. 1c–e**). Collectively, these results indicate that Afadin contributes to defining the spindle alignment of adherent cells in culture.

Afadin competes with NuMA for LGN binding

Accurate spindle positioning in metaphase is dependent on the association of LGN with NuMA, which occurs via direct interaction between the TPR domain of LGN and the C-terminal portion of NuMA[17].

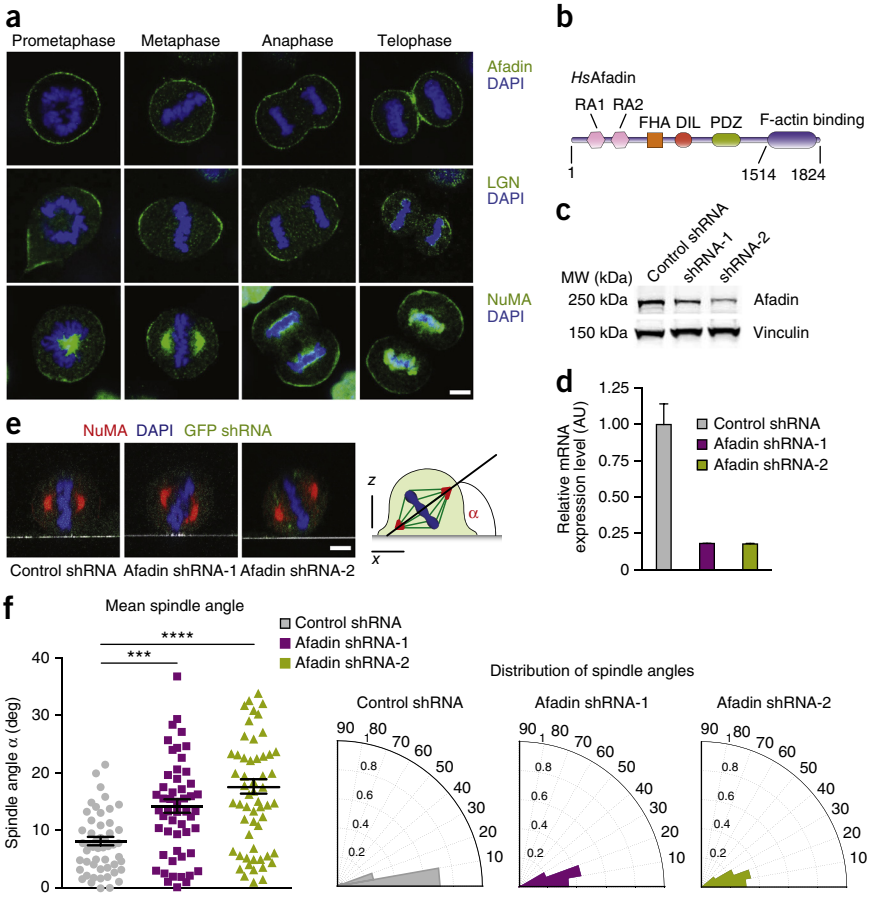

Figure 1 Afadin is required to orient the mitotic spindle in HeLa cells. (**a**) Cortical localization of endogenous Afadin in HeLa cells cultured on fibronectin-coated coverslips. (**b**) Schematic representation of the domain structure of long isoforms of human Afadin (*Hs*Afadin) consisting of two Ras-association domains (RA1 and RA2), a forkhead domain, a Dilute domain (DIL) and a PDZ (PSD95–Dlg–ZO-1) domain, followed by a C-terminal F-actin–binding region. (**c**,**d**) Immunoblot (**c**) and quantitative PCR analysis (**d**) from lysates of HeLa cells with stable Afadin knockdown, showing the efficiency of the shRNA-based depletions. Original images of the blots can be found in **Supplementary Data Set 1**. Levels of Afadin mRNA were normalized to the GAPDH internal control. Bar graphs represent mean + s.d. of 3 independent experiments. MW, molecular weight. (**e**) Representative confocal *z*-sections of mitotic HeLa cells infected with control or Afadin-targeting shRNAs stained for NuMA and DNA (DAPI). The plane of the coverslip is visible as a white line. Right, schematic representation of the experimental setting. (**f**) Quantification of the mitotic-spindle alignment to the plane of the coverslip of wild-type and Afadin-knockdown HeLa cells. Scatter plots (center line, mean; error bars, s.e.m.) and radial histograms illustrate the distributions of the spindle-axis angles for the three cell lines. $^{****}P < 0.0001$; $^{***}P < 0.001$ by two-sided Kruskal-Wallis test between control and Afadin shRNA–expressing cells from three independent experiments with $n = 51$ cells for control shRNA, $n = 52$ for Afadin shRNA-1 and $n = 56$ for Afadin shRNA-2. Scale bars, 5 μm.

To uncover the functional contribution of Afadin to spindle positioning, we purified to homogeneity the C-terminal domain of Afadin encompassing residues 1514–1824 (hereafter Afadin^{Cter}) and tested its direct interaction with LGN^{TPR} and NuMA$_{1861–1928}$. Size-exclusion chromatography (SEC) and static light scattering analyses (not shown) revealed that Afadin^{Cter} enters a stoichiometric 1:1 complex with LGN^{TPR} (**Fig. 2a**) but is unable to bind NuMA$_{1861–1928}$ (**Fig. 2b**). Importantly, when the three proteins were loaded simultaneously on a sizing column, LGN^{TPR} coeluted with NuMA$_{1861–1928}$ but not with Afadin^{Cter} (**Fig. 2c**), thus indicating that the binding of LGN to Afadin and to NuMA is mutually exclusive and that NuMA is a higher-affinity ligand of LGN than Afadin is. We obtained analogous results with the corresponding domains of the *Drosophila* orthologs Canoe, Pins and Mud (**Supplementary Fig. 2**). Thus, we conclude that the molecular events accounting for the mitotic function of Afadin are evolutionarily conserved.

To further dissect the requirements for the interaction of Afadin with LGN, we mapped the minimal binding domains between the two proteins. Afadin^{Cter} is predicted to form two helical domains joined by a poorly structured linker region (**Supplementary Fig. 3**). We used this information to design complementary constructs of Afadin^{Cter} fused to a GST moiety. Then we verified the ability of the truncated proteins to bind LGN in a pulldown experiment performed with GST-Afadin fragments immobilized on glutathione-Sepharose (GSH) beads and purified LGN^{TPR} in solution. Of the tested constructs, only Afadin$_{1709–1746}$ associated with LGN^{TPR} to the same extent observed for the entire Afadin^{Cter} (**Fig. 2d**). Moreover, measurement of the strength of the binary interaction of Afadin$_{1709–1746}$ and Afadin^{Cter} with LGN^{TPR} revealed that the two constructs displayed similar binding affinities, with dissociation constants of 5.6 ± 0.5 μM and 2.0 ± 0.6 μM respectively (**Figs. 2e** and **3h**). This evidence confirms that Afadin$_{1709–1746}$ encompasses the entire LGN-binding region. We next used the same pulldown assay to assess whether all the eight TPRs of LGN were essential for the association with Afadin$_{1709–1746}$. Deletion of the first or the last TPR of LGN abrogated binding (**Fig. 2f**), thus indicating that the dimer interface spans the integral LGN^{TPR} domain.

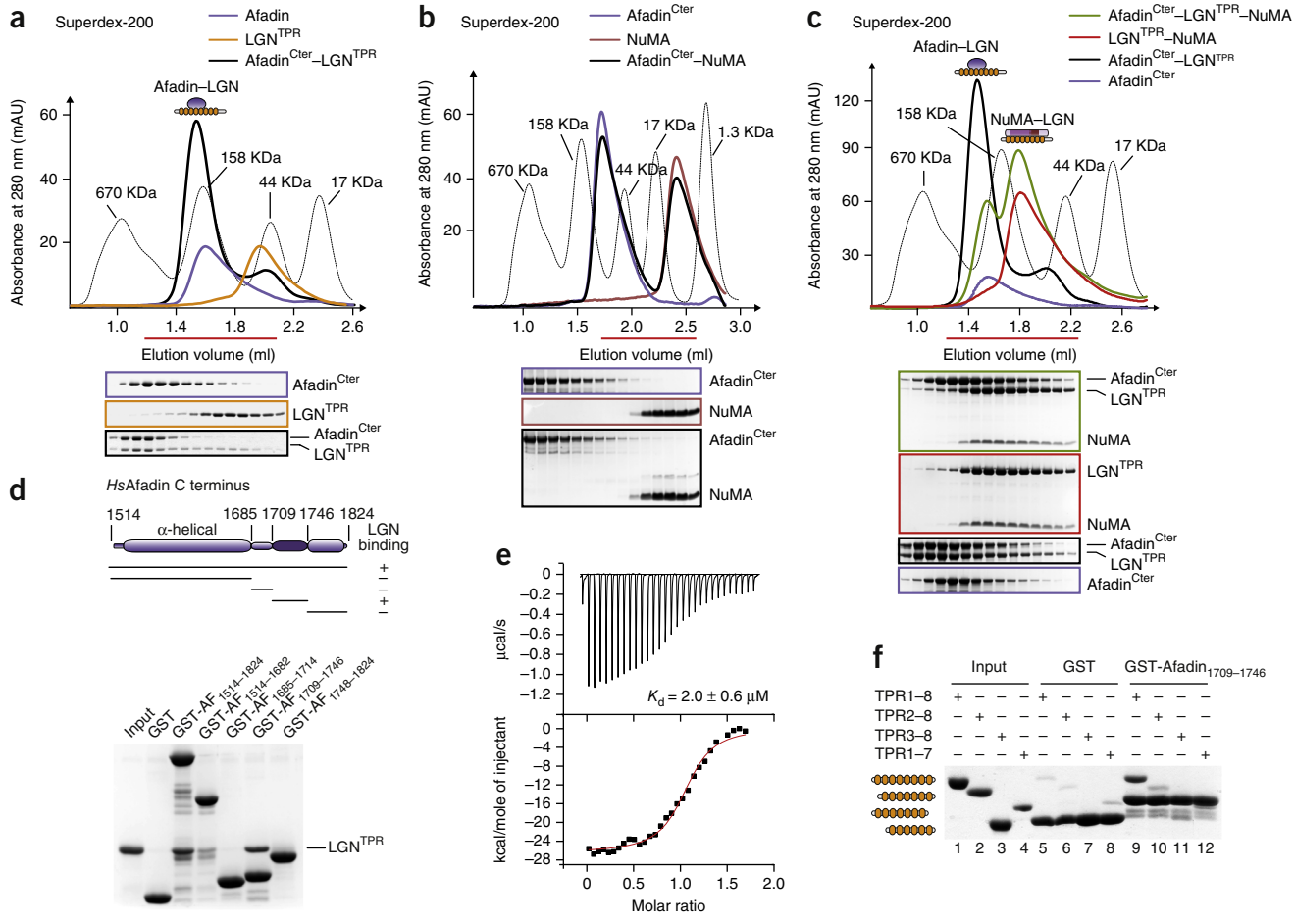

Figure 2 Afadin binds directly to LGN competitively with NuMA. (**a**) SEC elution profile of the stoichiometric complex formed between Afadin^{Cter} and LGN^{TPR} mixed at 15 μM concentration, and Coomassie-stained SDS-PAGE of the peak fractions indicated by the horizontal red bar. The elution profile of globular markers is indicated as a dashed gray line. Individual runs of Afadin^{Cter} and LGN^{TPR} are shown for comparison. SDS-PAGE gels are ordered from top to bottom, as indicated in the color keys. (**b**) SEC elution profile as in **a**, with incubation of Afadin^{Cter} with NuMA$_{1861–1928}$. (**c**) SEC elution profile with simultaneous loading of equimolar amounts of Afadin^{Cter}, LGN^{TPR} and NuMA$_{1861–1928}$. These proteins eluted in two distinct peaks (green trace). (**d**) Mapping, through GST pulldown, of the minimal region of Afadin^{Cter} retaining binding to LGN^{TPR}. SDS-PAGE of the bound fraction of complementary fragments of Afadin^{Cter} (1 μM) adsorbed on glutathione (GSH) beads and incubated with 5 μM of purified LGN^{TPR} is shown. (**e**) Measurement of the binding affinity between Afadin^{Cter} and LGN^{TPR} by isothermal titration calorimetry (ITC). K_d is reported as mean ± error of fitting of the ITC data with the isotherm (red line). (**f**) Binding assay with 1 μM of GST-Afadin$_{1709–1746}$ on GSH beads, incubated with 5 μM of LGN constructs encompassing different sets of TPRs.

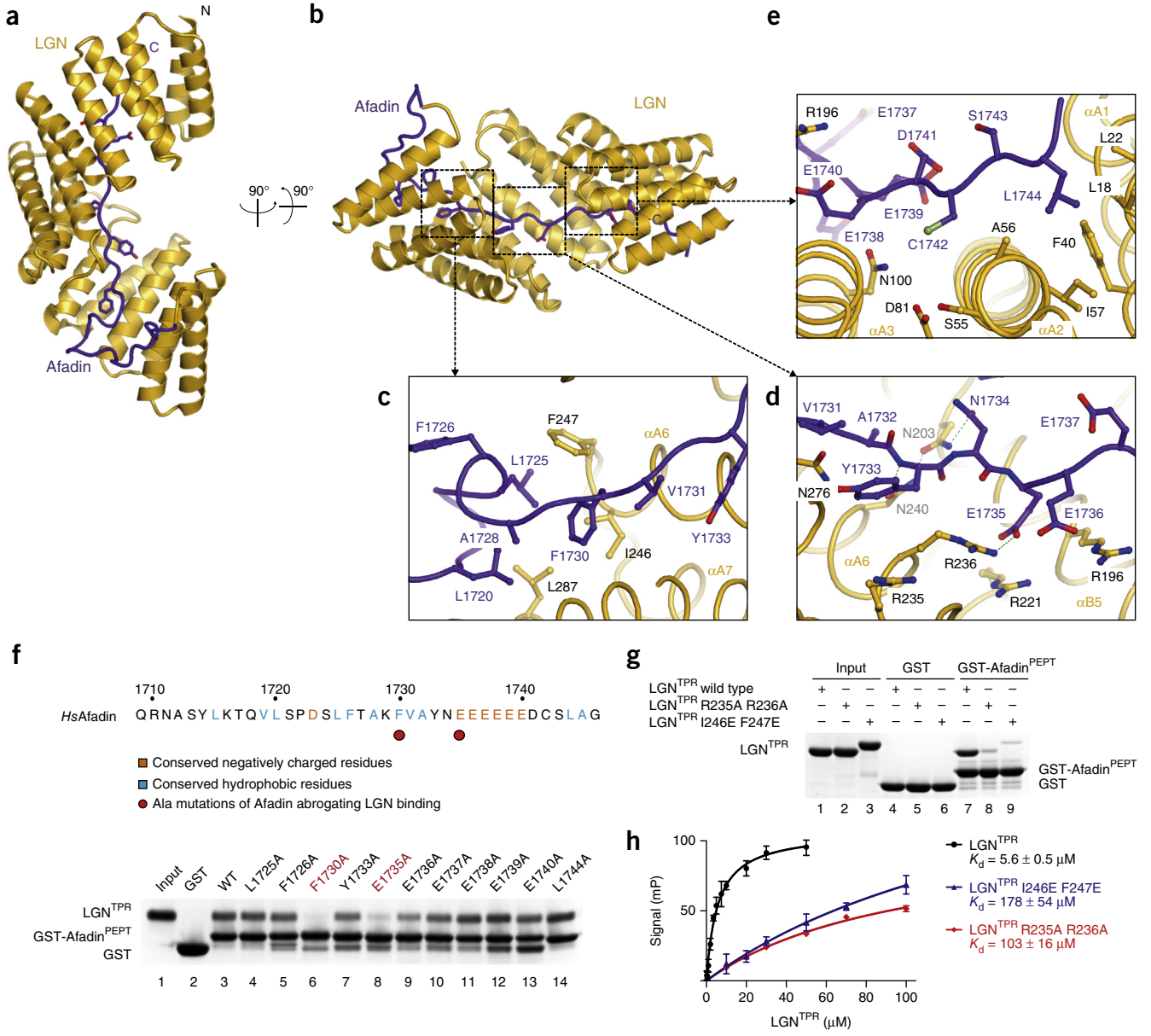

Figure 3 Structure and analysis of the interface between LGN^{TPR} and Afadin^{PEPT}. (**a**,**b**) Cartoon representation of the LGN^{TPR}-Afadin^{PEPT} fusion protein viewed at the indicated orientations. Gold, LGN^{TPR}; purple, Afadin^{PEPT}. (**c**–**e**) Enlarged views of three modules of the interaction interface between LGN^{TPR} and Afadin^{PEPT}. (**f**) Top, primary sequence of Afadin^{PEPT}, colored according to sequence conservation. Cyan, hydrophobic residues; orange, negatively charged residues. Bottom, biochemical validation of the Afadin-LGN interface by mutational analysis. GST pulldown assays performed with GST-Afadin^{PEPT} carrying the indicated alanine substitutions are shown. WT, wild type. (**g**) GST pulldown assays performed with LGN^{TPR} variants carrying double mutations in residues facing Phe1730^{AF} and Glu1735^{AF}. (**h**) Fluorescence polarization measurements of the binding affinity between a synthetic fluorescein-labeled Afadin^{PEPT} and LGN^{TPR}, either wild type or mutated at the LGN-Afadin interface. Error bars, s.d. (n = 3 independent experiments).

Architecture of the Afadin–LGN^{TPR} complex

To gain insight into the organizational principles of the Afadin–LGN complex, we took advantage of the acquired biochemical knowledge to engineer a chimeric construct in which Afadin$_{1709–1746}$ (hereafter Afadin^{PEPT}) was fused C terminally to LGN^{TPR} (residues 15–350). The chimera readily yielded cubic crystals diffracting to 2.9-Å resolution. We determined the structure by molecular replacement and refined it to an R_{free} of 25.5 and R_{work} of 20.6, with good stereochemistry (**Table 1**). The final model includes residues 15–350 of LGN and 1709–1745 of Afadin, the last ten of which are visible only in one of the two copies present in the asymmetric unit.

The LGN^{TPR} domain folds as a crescent moon whose inner concave groove holds the elongated Afadin^{PEPT} (**Fig. 3a**,**b**). The Afadin-LGN^{TPR} interface where the LGN^{TPR} scaffold wraps around the Afadin^{PEPT} with an opposite chain directionality buries an extended contact area of ~1,990 Å^2.

Each TPR repeat consists of a pair of antiparallel helices, termed A and B, connected by short loops. The eight TPRs of LGN stack side by side, forming a contiguous right-handed twisted array, with a layer of A helices facing the inner surface[38]. With the exception of the first 12 residues running parallel to the TPR-8 of LGN, the Afadin^{PEPT} traces along the axis of the LGN^{TPR} α-solenoid,

Table 1 Data collection and refinement statistics

	LGN–Afadin
Data collection	
Space group	$P2_13$
Cell dimensions	
a, *b*, *c* (Å)	169.8
α, β, γ (°)	90.0
Resolution (Å)	45.4–2.9 (2.98–2.9)[a]
R_{merge}	5.7 (71.6)
$I / \sigma I$	14.6 (1.5)
Completeness (%)	96.3 (95.8)
Redundancy	3.4 (3.2)
Refinement	
Resolution (Å)	45.4–2.9
No. reflections	34,817
R_{work} / R_{free}	20.6 / 25.2
No. atoms	
Protein	5,732
SO_4^{2-} ions	15
B factors	
Protein	81
SO_4^{2-} ions	105
r.m.s. deviations	
Bond lengths (Å)	0.01
Bond angles (°)	1.15

[a]Values in parentheses are for highest-resolution shell.

primarily contacting the A helices of each TPR. The position of asparagine residues of the invariant Leu-Gly-Asn (LGN) triplets present on the A helices defines a ridge stabilizing the extended conformation of Afadin^{PEPT} via hydrogen bonds with main chain atoms. Interestingly, the overall conformation of the assembly is reminiscent of the topology observed for LGN^{TPR} in complex with other ligands such as NuMA and Inscuteable[38,39], thus providing a molecular explanation for the observed competitive binding of Afadin and NuMA to LGN (**Fig. 2c**).

The dimer interface can be subdivided into three segments of Afadin^{PEPT}. The first segment (Afadin residues 1720–1731) starts with a zigzagging hairpin and later stretches in an antiparallel fashion on TPR-6 and TPR-7. Here, hydrophobic residues on both sides of the dimer create a hydrophobic pocket centered at Phe1730^{AF}, Ile246^{LGN} and Phe247^{LGN} (**Fig. 3c**). The second segment, comprising Afadin residues 1732–1741, is negatively charged and docks on the central TPRs, contributing to the Afadin-LGN interface primarily with polar interactions between a glutamate stretch of Afadin and a conserved arginine of LGN (**Fig. 3d**). Notably, this charge complementarity dominating the binding interface is a feature common to all LGN^{TPR} ligands characterized to date[40]. Finally, the third fragment, comprising residues 1742–1745 of Afadin^{PEPT}, extends over the A helices of the first TPRs of LGN, and Leu1744^{AF} protrudes into a conserved hydrophobic pocket (**Fig. 3e**). This structural arrangement suggests that all the three modules work synergistically to hook the Afadin^{PEPT} onto the LGN scaffold. We tested this hypothesis in GST pulldown assays. First we introduced specific mutations into GST-Afadin^{PEPT} and analyzed whether they could impair binding to wild-type LGN^{TPR}. Consistently with the structure, single replacement of Phe1730^{AF} or Glu1735^{AF} with alanine abrogated binding (**Fig. 3f**). Next, we asked whether substitutions of LGN residues interacting with Phe1730^{AF} and Glu1735^{AF} would affect the binding of LGN^{TPR} to GST-Afadin^{PEPT}. Double replacement of Ile246^{LGN}-Phe247^{LGN} with glutamate, or of Arg235^{LGN}-Arg236^{LGN} with alanine, completely abolished binding (**Fig. 3g**), thus underscoring the key role of these LGN residues at the dimer interface. Quantitative measurements of the binding affinity by fluorescence polarization confirmed that Afadin^{PEPT} binds mutated LGN^{TPR} with an affinity two orders of magnitude lower than that for binding to wild-type LGN (**Fig. 3h**). In summary, our structural analysis revealed that Afadin^{PEPT} threads through the superhelix of LGN^{TPR} and that the structural determinants for the specific recognition are Phe1730^{AF} and Glu1735^{AF}.

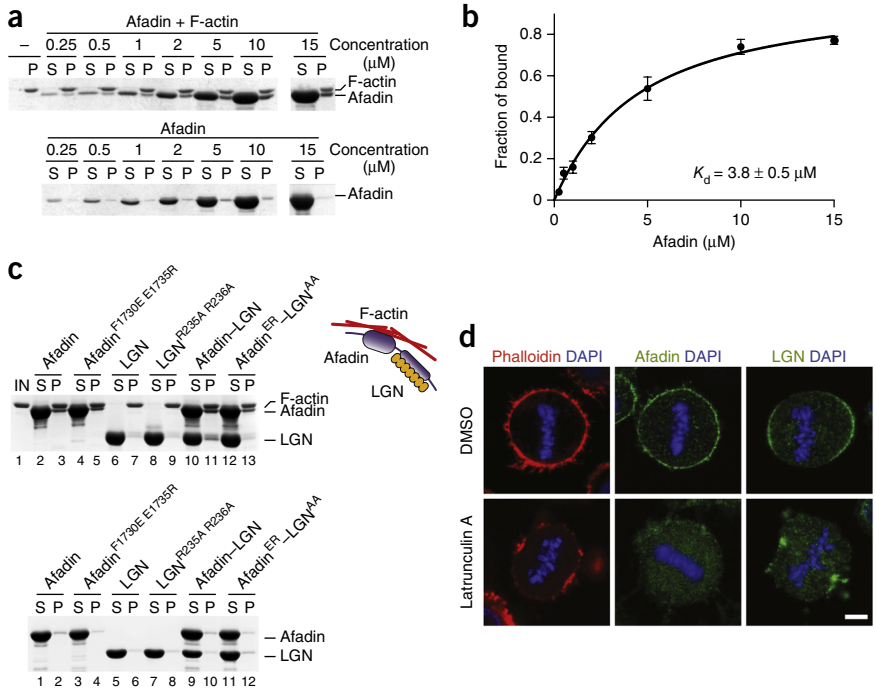

Figure 4 Afadin mediates the interaction of LGN with the actomyosin cortex. (**a**) High-speed co-sedimentation of increasing concentrations of Afadin^{Cter} with 1 μM of F-actin. Coomassie-stained SDS-PAGE of pellet (P) and supernatant (S) fractions for each Afadin concentration. (**b**) Quantification of the co-sedimentation assay by densitometric analysis. Error bars, s.d. ($n = 3$ independent experiments). (**c**) As in **a**, performed at saturating concentrations of Afadin^{Cter} (9 μM) in the presence of equal amounts of LGN^{TPR}. Analyses were carried out with wild-type Afadin^{Cter} and LGN^{TPR} or with the mutants Afadin$^{F1730E\ E1735R}$ and LGN$^{R235A\ R236A}$. In, F-actin input. (**d**) HeLa cells in metaphase treated with DMSO (top row) or 1 μM Latrunculin A (bottom row), fixed and stained for actin (phalloidin), Afadin or LGN. Scale bar, 5 μm.

Afadin mediates the interaction of LGN with F-actin

At mitotic entry, the actin cytoskeleton reorganizes in a mesh of ordered actin filaments and associated proteins known as the cortex, which mediates cell rounding. Growing evidence supports the notion that cortical functions are required for correct spindle

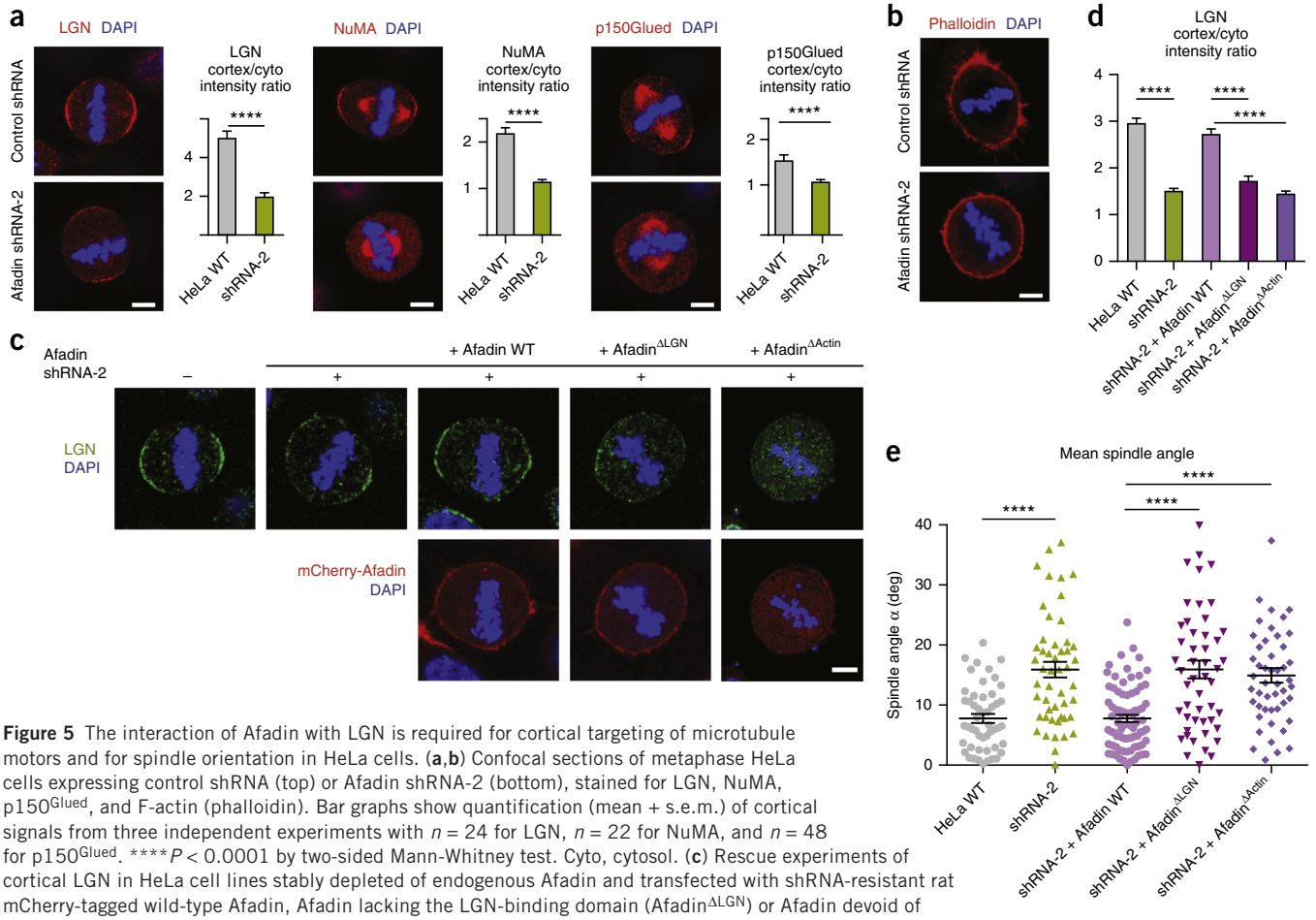

Figure 5 The interaction of Afadin with LGN is required for cortical targeting of microtubule motors and for spindle orientation in HeLa cells. (**a**,**b**) Confocal sections of metaphase HeLa cells expressing control shRNA (top) or Afadin shRNA-2 (bottom), stained for LGN, NuMA, p150^{Glued}, and F-actin (phalloidin). Bar graphs show quantification (mean + s.e.m.) of cortical signals from three independent experiments with $n = 24$ for LGN, $n = 22$ for NuMA, and $n = 48$ for p150^{Glued}. ****$P < 0.0001$ by two-sided Mann-Whitney test. Cyto, cytosol. (**c**) Rescue experiments of cortical LGN in HeLa cell lines stably depleted of endogenous Afadin and transfected with shRNA-resistant rat mCherry-tagged wild-type Afadin, Afadin lacking the LGN-binding domain (Afadin$^{\Delta LGN}$) or Afadin devoid of the actin-binding domain (Afadin$^{\Delta Actin}$). Bottom, localization of the transfected mCherry-Afadin constructs. (**d**) Quantification of cortical LGN in three independent rescue experiments with $n = 50$ for wild-type HeLa cells, $n = 58$ for Afadin shRNA-2 expressing cells, $n = 59$ for Afadin-depleted cells transfected with wild-type Afadin, $n = 37$ for Afadin-depleted cells transfected with Afadin$^{\Delta LGN}$, and $n = 41$ for Afadin-depleted cells transfected with Afadin$^{\Delta Actin}$ (mean + s.e.m.). ****$P < 0.0001$ by two-sided Kruskal-Wallis test. (**e**) Distributions of mitotic-spindle angles in metaphase for Afadin shRNA rescue experiments. Mean ± s.e.m. are shown for three independent experiments with $n = 50$ for wild-type HeLa cells, $n = 50$ for Afadin shRNA-2 expressing cells, $n = 78$ for Afadin-depleted cells transfected with wild-type Afadin, $n = 50$ for Afadin-depleted cells transfected with Afadin$^{\Delta LGN}$, and $n = 49$ for Afadin-depleted cells transfected with Afadin$^{\Delta Actin}$. ****$P < 0.0001$; by one-way ANOVA Tukey's test. Scale bars in **a**–**c**, 5 µm. Throughout figure, *n*, number of cells analyzed.

positioning, although no mechanistic link between spindle-orientation proteins and F-actin has been identified to date. Intriguingly, long isoforms of Afadin have been reported to associate with F-actin. To verify whether the Afadin^{Cter} construct that interacts with LGN contains the actin-binding domain, we performed high-speed co-sedimentation assays with 1 µM F-actin. Under these conditions, Afadin^{Cter} stoichiometrically associated with F-actin, with a dissociation constant of 3.8 ± 0.5 µM (**Fig. 4a**,**b**). SEC analysis revealed that the same Afadin^{Cter} construct did not enter a complex with globular (G) actin, even at concentrations ten-fold higher than those used in co-sedimentation assays (**Supplementary Fig. 4a**), thus suggesting that Afadin recognizes specific features of the actin filaments' lattice. We mapped the boundaries of the Afadin actin-binding region to residues 1514–1682 (**Supplementary Fig. 4b**). The finding that the actin-binding domain of Afadin is just upstream of the LGN-binding stretch prompted us to explore the possibility that Afadin could act as a molecular bridge between LGN and F-actin. To test this hypothesis, we repeated the Afadin co-sedimentation assays in the presence of LGN^{TPR}. As expected, LGN^{TPR} in isolation was present in the supernatant, whereas it co-sedimented with F-actin when it was in complex with Afadin^{Cter} (**Fig. 4c**). Consistently with this finding, mutations disrupting the Afadin^{Cter}–LGN^{TPR} dimer interface prevented LGN co-sedimentation with F-actin (**Fig. 4c**). To assess whether Afadin also functions as a physical tether between actin filaments and LGN in cells, we treated mitotic HeLa cells with 1 µM of the actin-depolymerizing drug Latrunculin A, which disassembled the acto-myosin cortex almost completely (**Fig. 4d**). Under these conditions, Afadin disappeared from the plasma membrane and redistributed uniformly in the cytoplasm, whereas LGN accumulated aberrantly at the spindle poles, as previously reported[37]. Together these findings highlight the importance of Afadin as a molecular link between LGN and F-actin *in vitro* and *in vivo*.

Afadin aids in planar division by localizing LGN at the cortex

According to the current model, the assembly of force generators is initiated at metaphase by recruitment of LGN to the plasma membrane by the direct interaction with several myristoylated $G_{\alpha i}$ moieties. Whether this interaction is sufficient to anchor dynein at the cell cortex while it pulls toward the spindle poles is currently unclear. To assess the putative role of Afadin in securing dynein–dynactin

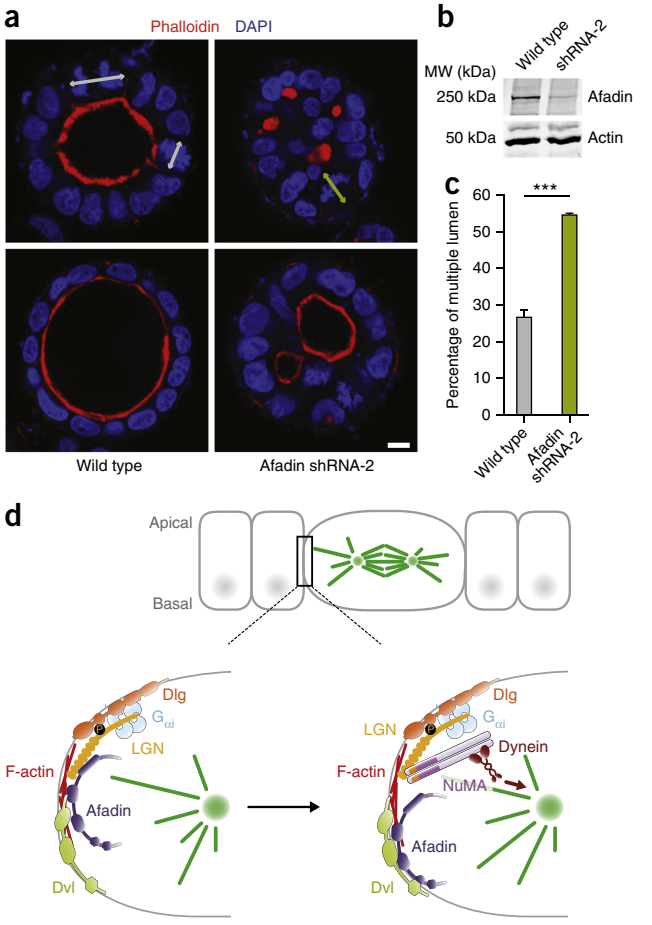

Figure 6 Role of Afadin in Caco-2 planar cell divisions and cystogenesis. (**a**) Confocal sections of the equatorial region of Caco-2 cysts grown from wild-type cells (left) or cells lacking Afadin (right). The orientation of the spindle axis in mitotic cells is indicated with double-arrowed lines. Scale bar, 10 µm. (**b**) Depletion of endogenous Afadin in the Caco-2 cell line used for cystogenesis experiments, verified by western blotting of lysates from Caco-2. Original images of the blots can be found in **Supplementary Data Set 1**. (**c**) Quantification of defective cystogenesis as a percentage of cysts with a single lumen in wild-type or Afadin-ablated Caco-2 cells. Mean ± s.d. are shown ($n = 107$ wild-type cysts and $n = 97$ Afadin-ablated cysts from 3 independent experiments). $***P < 0.001$ by two-sided Fisher's exact test between control cysts and Afadin shRNA-2 expressing cysts. (**d**) Schematic representation of the mitotic function of Afadin supported by our study. Afadin localizes at adherens junctions of polarized epithelia and instructs the localization of microtubule motors by concomitant binding to cortical F-actin and LGN. LGN is anchored to the lateral membrane by direct simultaneous interactions with Afadin, $G_{\alpha i}{}^{GDP}$ and Dlg. Dlg recognizes the phosphorylated linker region of LGN (left). In the presence of the higher-affinity ligand NuMA, LGN dissociates from Afadin and recruits NuMA–dynein at the cortex, and microtubule-pulling forces ensue. Evidence in flies suggests that the direct association of Afadin with Dishevelled (Dvl) might contribute indirectly to targeting NuMA at the cortex.

at the actomyosin cortex, we set out to analyze the consequences of Afadin depletion on the distributions of LGN and NuMA in mitotic HeLa cells. Loss of Afadin significantly reduced the levels of LGN at the cortex in metaphase and anaphase, and prevented cortical recruitment of NuMA and dynactin (**Fig. 5a** and **Supplementary Fig. 5a**), thus indicating that cortical targeting of microtubule motors relies on the presence of Afadin. Conversely, the cortical distribution of Afadin was not altered by depletion of LGN or NuMA (**Supplementary Fig. 5b**), a result indicating that Afadin acts upstream of LGN and NuMA in recruiting spindle motors at the cortex. It is known that defects in the actin cytoskeleton can alter the localization of LGN and NuMA in mitosis[35,41]. To assess whether the depletion of Afadin could perturb cortical distribution of LGN and NuMA by simply disrupting the actomyosin integrity, we visualized cortical actin in Afadin-knockdown cells. Phalloidin staining showed that the actomyosin organization in the absence of Afadin was undistinguishable from that in wild-type cells (**Fig. 5b**), thus suggesting that the molecular mechanism accounting for the LGN and NuMA mislocalization phenotype is downstream of the actin cytoskeleton.

From the direct binding between Afadin and LGN that we had uncovered, we reasoned that Afadin might bring LGN to the cortex by interacting with its TPR domain. To test this hypothesis, we set out to rescue mitotic defects of Afadin-ablated cells by expressing shRNA-resistant mCherry-Afadin mutants. The association of Afadin with LGN^{TPR} is mediated by a number of main chain hydrogen bonds in addition to the polar and hydrophobic interaction contributed by the side chains of $Phe1730^{AF}$ and $Glu1735^{AF}$. Therefore, for the rescue experiments we designed an Afadin mutant lacking the entire stretch involved in LGN^{TPR} binding, referred to as $Afadin^{\Delta LGN}$. In Afadin shRNA-2 HeLa cells, mCherry-$Afadin^{WT}$ localized uniformly to the cell cortex (**Supplementary Fig. 5c**,**d**) and was able to restore normal levels of cortical LGN and NuMA (**Fig. 5c**,**d** and **Supplementary Fig. 5f**). However, the analogous overexpression of the $Afadin^{\Delta LGN}$ mutant did not restore the cortical distribution of LGN nor NuMA in spite of localizing properly at the actomyosin cortex. Thus, we conclude that the binding surface between $Afadin^{Cter}$ and LGN^{TPR} is required to establish correct polar accumulation of LGN and NuMA at the cortex in metaphase. To assess whether Afadin is the direct link between the actomyosin cortex and the spindle apparatus, we generated an additional Afadin mutant devoid of the actin-binding region that we had identified earlier (**Supplementary Fig. 4b**), termed $Afadin^{\Delta Actin}$ henceforth. Interestingly, mCherry-$Afadin^{\Delta Actin}$ localized poorly at the cortex (**Supplementary Fig. 5d**,**e**), thus indicating that in isolated cells in culture Afadin is recruited to the membrane by direct interaction with cortical F-actin. Consistently with the notion that Afadin acts upstream of LGN in the spindle-orientation pathway, $Afadin^{\Delta Actin}$ did not restore targeting of LGN at the cortex (**Fig. 5c**,**d**).

We then asked whether impairment of LGN recruitment at the membrane could provide the molecular explanation for the spindle-misorientation phenotype observed upon Afadin knockdown. Spindle-angle analysis revealed that mCherry-$Afadin^{WT}$ almost completely rescued the defects of spindle alignment in Afadin-depleted cells, whereas $Afadin^{\Delta LGN}$ and $Afadin^{\Delta Actin}$ did not (**Fig. 5e**). Together, these results indicate that Afadin acts as a scaffolding module coordinating the correct assembly of force generators at the cortex and hence the spindle orientation.

Afadin is an adhesion protein required for timely stabilization of cell-cell junctions during epithelia formation[42]. To understand the functional relevance of the spindle-orientation role of Afadin in the morphogenesis of polarized epithelia, we analyzed the growth of three-dimensional Caco-2 cysts. Wild-type Caco-2 cells underwent planar divisions, forming monolayered cellular spheres with the apical side facing the inner lumen (**Fig. 6a**). In contrast, cysts grown from Caco-2 cells lacking Afadin failed to organize a single lumen and displayed spindle-orientation defects (**Fig. 6a–c**) similar to those observed after LGN ablation[43]. As observed in HeLa cells, Afadin ablation did not disrupt the uniform distribution of cortical F-actin

in Caco-2 mitotic cells (**Supplementary Fig. 6**). This evidence demonstrates that Afadin is required for planar divisions and for correct epithelial morphogenesis.

DISCUSSION

In this study, we report the structural and functional characterization of the direct interaction between Afadin, LGN and F-actin, and provide a molecular explanation for a new role of Afadin in coordinating planar cell divisions.

In adherent HeLa cells, Afadin distributes uniformly at the cortex throughout mitosis, and from metaphase to anaphase it colocalizes with LGN and NuMA at polar regions above the spindle poles. Consistently with this, we discovered that Afadin interacts directly with LGN^{TPR}, through a fragment spanning Afadin residues 1709–1746. The crystallographic structure of $Afadin_{1709–1746}$ in complex with LGN^{TPR} revealed that the Afadin peptide lines the inner surface of the TPR superhelical arrangement, as secured by a number of main chain hydrogen bonds and specific contacts from the side chains of $Phe1730^{AF}$ and $Glu1735^{AF}$. The topology of the interaction is reminiscent of that of other LGN-binding partners involved in spindle orientation, such as NuMA, Inscuteable and Frmpd1–4 (refs. 17,38,39,44); therefore, it is not surprising that the association of LGN with Afadin and NuMA is mutually exclusive. Importantly, we found that such a network of competitive interactions is conserved among *Drosophila* orthologs, thus suggesting that the molecular function of Afadin is shared across species. Structural superposition of the TPR domain of LGN in complex with the known ligands, including Afadin, led to the definition of the LGN-binding motif [FW]-X(2,8)-[EQY]-X-E-X(5)-[QDE]-X(1,2)-[KRC]-X(0,1)-[LIV], where X stands for any residue. Unfortunately, the substantial variability in the number of residues accommodated between the conserved positions and in the manner in which side chains rearrange to recognize the TPR surface makes this consensus poorly predictive.

How does Afadin contribute to the recruitment of force generators at the cortex in cells? One option is that Afadin belongs to higher-order oligomers, in which multiple LGN molecules engage with either Afadin or NuMA. We suspect that such complexes would be energetically unfavorable because, in the absence of limiting-concentration conditions and topological constraints, the high-affinity LGN ligand NuMA would occupy all the available sites. Loss of Afadin perturbs the polar enrichment of LGN in mitosis and abolishes cortical accumulation of NuMA and dynein. This phenotype can be observed both in metaphase, when NuMA is known to be directed to the cortex by LGN-mediated mechanisms[35,45], and in anaphase, when the levels of cortical NuMA increase, owing to its direct interactions with the plasma membrane[41,45,46]. The evidence that in metaphase the removal of the LGN-binding motif from Afadin abolishes NuMA targeting at the cortex supports a sequential recruitment model wherein LGN is first recruited at the membrane by Afadin, binds to $G_{\alpha i}$ and is later handed to NuMA, which is a higher-affinity LGN ligand (**Fig. 6d**). The molecular events underlying the cross-talk between Afadin and NuMA might be more sophisticated in anaphase and may involve LGN-independent mechanisms. Interestingly, induced cell polarity assays in *Drosophila* S2 cells have shown that the Ras-association domains of Canoe (Afadin) bind to Ran^{GTP} and are essential for cortical targeting of Mud (NuMA) with Pins (LGN)[21]. Ran-dependent cortical regulation of LGN has recently been reported in HeLa cells[47], although in this system active Ran appears to be required to exclude force generators from the cortical regions above chromosomes rather than to cause active cortical recruitment. In addition, Canoe (Afadin) and F-actin regulators have recently been implicated in the Dishevelled-mediated cortical accumulation of Mud (NuMA) in *Drosophila* S2 cells[31]; this result seems to suggest that Afadin belongs to localized cortical landmarks transducing external signals to the spindle apparatus to properly orient the divisions[48].

Increasing evidence points to a prominent role of the actomyosin cortex in mitotic rounding in spindle alignment[34]. The need for an intact actin cytoskeleton for spindle positioning is reflected in the requirement for a number of actin regulators including ERM family members[49], Cdc42 (ref. 50) and focal-adhesion molecules such as β1 integrin[18]. However, how signals sensed by the actomyosin cortex are communicated to spindle-orienting motors is, to date, largely unclear. The ability of Afadin to simultaneously bind LGN and cortical F-actin makes it the first-identified direct molecular bridge between the mitotic spindle and the actomyosin cortex, to our knowledge. Afadin associates with the TPR domain of LGN and acts in conjunction with $G_{\alpha i}$ and other cortical anchoring mechanisms, including Dlg[11], thus ensuring timely targeting of NuMA–dynein at the membrane. Experiments able to dissect the temporal sequence of events involved in force-generator assembly *in vivo* will be key to illuminating how these cortical cues synergize at the membrane.

In vertebrate epithelia, Afadin is found at the adherens junctions[51], thus implying that it can act as a lateral cue restricting LGN at the lateral cortex to orient the mitotic spindle planarly. In line with this hypothesis, we show that Caco-2 cells lacking Afadin are unable to undergo planar division and to form three-dimensional cysts with a single lumen. Whether defective cystogenesis of Afadin-depleted Caco-2 cells is caused solely by misoriented divisions or also by impaired cell-cell contacts remains an important open question. The knowledge that Afadin acts as a major organizer of epithelial cell-cell junctions and as a hub for small–G protein signaling makes it an ideal candidate to transduce information from the extracellular signals and mechanoproperties of the cortex to the spindle to direct spindle positioning. In this respect, it would be interesting to investigate the role of Afadin in cellular systems able to switch from planar to vertical divisions, such as skin progenitors[52], neuroepithelia[11] and mammary epithelia[53].

METHODS

Methods and any associated references are available in the online version of the paper.

Accession codes. Coordinates and structure factors have been deposited in the Protein Data Bank under accession code PDB 5A6C.

Note: Any Supplementary Information and Source Data files are available in the online version of the paper.

ACKNOWLEDGMENTS

We are grateful to S. Pasqualato and V. Cecatiello of the Crystallography Unit of the European Institute of Oncology for technical support. We thank E. Martini and D. Parazzoli of the Cogentech Facility for help with image analysis. We thank scientists at the X06DA beamline at the Swiss Light Source and the ID23-2 beamline at the European Synchrotron Radiation Facility for valuable help with data collection. We are grateful to all members of the Mapelli laboratory, F. Villa, G. Scita, A. Disanza, S. Santaguida and A. De Antoni for scientific discussions, and to A. Musacchio for careful reading of the manuscript. We thank Y. Takai (Kobe University Graduate School of Medicine, Japan) for sharing the rat Afadin cDNA. This work was supported by grants from the Italian Association for Cancer Research (AIRC) to M.M., the Italian Ministry of Health to M.M. and BioStruct-X (FP7/2007-2013, grant agreement 283570).

AUTHOR CONTRIBUTIONS

M.C. conducted the biochemical and structural biology experiments, and S.G. performed cell biology experiments and analysis. A.A. designed Afadin mutants, L.P. helped with the cell biology, and S.B. provided purified actin. M.M. supervised the project and wrote the manuscript.

COMPETING FINANCIAL INTERESTS
The authors declare no competing financial interests.

1. Morin, X. & Bellaïche, Y. Mitotic spindle orientation in asymmetric and symmetric cell divisions during animal development. *Dev. Cell* **21**, 102–119 (2011).
2. Lancaster, M.A. & Knoblich, J.A. Spindle orientation in mammalian cerebral cortical development. *Curr. Opin. Neurobiol.* **22**, 737–746 (2012).
3. Williams, S.E., Beronja, S., Pasolli, H.A. & Fuchs, E. Asymmetric cell divisions promote Notch-dependent epidermal differentiation. *Nature* **470**, 353–358 (2011).
4. Pease, J.C. & Tirnauer, J.S. Mitotic spindle misorientation in cancer: out of alignment and into the fire. *J. Cell Sci.* **124**, 1007–1016 (2011).
5. Gonzalez, C. Spindle orientation, asymmetric division and tumour suppression in *Drosophila* stem cells. *Nat. Rev. Genet.* **8**, 462–472 (2007).
6. Knoblich, J.A. Asymmetric cell division: recent developments and their implications for tumour biology. *Nat. Rev. Mol. Cell Biol.* **11**, 849–860 (2010).
7. Noatynska, A., Gotta, M. & Meraldi, P. Mitotic spindle (DIS)orientation and DISease: cause or consequence? *J. Cell Biol.* **199**, 1025–1035 (2012).
8. Kotak, S. & Gönczy, P. Mechanisms of spindle positioning: cortical force generators in the limelight. *Curr. Opin. Cell Biol.* **25**, 741–748 (2013).
9. Du, Q. & Macara, I.G. Mammalian Pins is a conformational switch that links NuMA to heterotrimeric G proteins. *Cell* **119**, 503–516 (2004).
10. Kotak, S., Busso, C. & Gönczy, P. Cortical dynein is critical for proper spindle positioning in human cells. *J. Cell Biol.* **199**, 97–110 (2012).
11. Saadaoui, M. *et al.* Dlg1 controls planar spindle orientation in the neuroepithelium through direct interaction with LGN. *J. Cell Biol.* **206**, 707–717 (2014).
12. Bergstralh, D.T., Lovegrove, H.E. & St Johnston, D. Discs large links spindle orientation to apical-basal polarity in *Drosophila* epithelia. *Curr. Biol.* **23**, 1707–1712 (2013).
13. Nakajima, Y., Meyer, E.J., Kroesen, A., McKinney, S.A. & Gibson, M.C. Epithelial junctions maintain tissue architecture by directing planar spindle orientation. *Nature* **500**, 359–362 (2013).
14. Johnston, C.A., Hirono, K., Prehoda, K.E. & Doe, C.Q. Identification of an Aurora-A/PinsLINKER/Dlg spindle orientation pathway using induced cell polarity in S2 cells. *Cell* **138**, 1150–1163 (2009).
15. Zhu, J. *et al.* Guanylate kinase domains of the MAGUK family scaffold proteins as specific phospho-protein-binding modules. *EMBO J.* **30**, 4986–4997 (2011).
16. Johnston, C.A., Doe, C.Q. & Prehoda, K.E. Structure of an enzyme-derived phosphoprotein recognition domain. *PLoS One* **7**, e36014 (2012).
17. Culurgioni, S., Alfieri, A., Pendolino, V., Laddomada, F. & Mapelli, M. Inscuteable and NuMA proteins bind competitively to Leu-Gly-Asn repeat-enriched protein (LGN) during asymmetric cell divisions. *Proc. Natl. Acad. Sci. USA* **108**, 20998–21003 (2011).
18. Lechler, T. & Fuchs, E. Asymmetric cell divisions promote stratification and differentiation of mammalian skin. *Nature* **437**, 275–280 (2005).
19. Speicher, S., Fischer, A., Knoblich, J. & Carmena, A. The PDZ protein Canoe regulates the asymmetric division of *Drosophila* neuroblasts and muscle progenitors. *Curr. Biol.* **18**, 831–837 (2008).
20. Carmena, A., Makarova, A. & Speicher, S. The Rap1-Rgl-Ral signaling network regulates neuroblast cortical polarity and spindle orientation. *J. Cell Biol.* **195**, 553–562 (2011).
21. Wee, B., Johnston, C.A., Prehoda, K.E. & Doe, C.Q. Canoe binds RanGTP to promote Pins(TPR)/Mud-mediated spindle orientation. *J. Cell Biol.* **195**, 369–376 (2011).
22. Mandai, K. *et al.* Afadin: a novel actin filament-binding protein with one PDZ domain localized at cadherin-based cell-to-cell adherens junction. *J. Cell Biol.* **139**, 517–528 (1997).
23. Niessen, C.M. & Gottardi, C.J. Molecular components of the adherens junction. *Biochim. Biophys. Acta* **1778**, 562–571 (2008).
24. Ooshio, T. *et al.* Cooperative roles of Par-3 and afadin in the formation of adherens and tight junctions. *J. Cell Sci.* **120**, 2352–2365 (2007).
25. Zhadanov, A.B. *et al.* Absence of the tight junctional protein AF-6 disrupts epithelial cell-cell junctions and cell polarity during mouse development. *Curr. Biol.* **9**, 880–888 (1999).
26. Yamamoto, H. *et al.* Genetic deletion of afadin causes hydrocephalus by destruction of adherens junctions in radial glial and ependymal cells in the midbrain. *PLoS One* **8**, e80356 (2013).
27. Yang, Z. *et al. De novo* lumen formation and elongation in the developing nephron: a central role for afadin in apical polarity. *Development* **140**, 1774–1784 (2013).
28. Tawa, H. *et al.* Role of afadin in vascular endothelial growth factor- and sphingosine 1-phosphate-induced angiogenesis. *Circ. Res.* **106**, 1731–1742 (2010).
29. Tanaka-Okamoto, M. *et al.* Genetic ablation of afadin causes mislocalization and deformation of Paneth cells in the mouse small intestinal epithelium. *PLoS One* **9**, e110549 (2014).
30. Kobayashi, R. *et al.* s-Afadin binds more preferentially to the cell adhesion molecules nectins than l-afadin. *Genes Cells* **19**, 853–863 (2014).
31. Johnston, C.A. *et al.* Formin-mediated actin polymerization cooperates with Mushroom body defect (Mud)-Dynein during Frizzled-Dishevelled spindle orientation. *J. Cell Sci.* **126**, 4436–4444 (2013).
32. Lorger, M. & Moelling, K. Regulation of epithelial wound closure and intercellular adhesion by interaction of AF6 with actin cytoskeleton. *J. Cell Sci.* **119**, 3385–3398 (2006).
33. Théry, M., Jiménez-Dalmaroni, A., Racine, V., Bornens, M. & Jülicher, F. Experimental and theoretical study of mitotic spindle orientation. *Nature* **447**, 493–496 (2007).
34. Lancaster, O.M. & Baum, B. Shaping up to divide: coordinating actin and microtubule cytoskeletal remodelling during mitosis. *Semin. Cell Dev. Biol.* **34**, 109–115 (2014).
35. Seldin, L., Poulson, N.D., Foote, H.P. & Lechler, T. NuMA localization, stability, and function in spindle orientation involve 4.1 and Cdk1 interactions. *Mol. Biol. Cell* **24**, 3651–3662 (2013).
36. Kiyomitsu, T. & Cheeseman, I.M. Cortical dynein and asymmetric membrane elongation coordinately position the spindle in anaphase. *Cell* **154**, 391–402 (2013).
37. Zheng, Z. *et al.* Evidence for dynein and astral microtubule-mediated cortical release and transport of Gαi/LGN/NuMA complex in mitotic cells. *Mol. Biol. Cell* **24**, 901–913 (2013).
38. Zhu, J. *et al.* LGN/mInsc and LGN/NuMA complex structures suggest distinct functions in asymmetric cell division for the Par3/mInsc/LGN and Gαi/LGN/NuMA pathways. *Mol. Cell* **43**, 418–431 (2011).
39. Yuzawa, S., Kamakura, S., Iwakiri, Y., Hayase, J. & Sumimoto, H. Structural basis for interaction between the conserved cell polarity proteins Inscuteable and Leu-Gly-Asn repeat-enriched protein (LGN). *Proc. Natl. Acad. Sci. USA* **108**, 19210–19215 (2011).
40. Mapelli, M. & Gonzalez, C. On the inscrutable role of Inscuteable: structural basis and functional implications for the competitive binding of NuMA and Inscuteable to LGN. *Open Biol.* **2**, 120102 (2012).
41. Kotak, S., Busso, C. & Gönczy, P. NuMA phosphorylation by CDK1 couples mitotic progression with cortical dynein function. *EMBO J.* **32**, 2517–2529 (2013).
42. Indra, I., Troyanovsky, R. & Troyanovsky, S.M. Afadin controls cadherin cluster stability using clathrin-independent mechanism. *Tissue Barriers* **2**, e28687 (2014).
43. Zheng, Z. *et al.* LGN regulates mitotic spindle orientation during epithelial morphogenesis. *J. Cell Biol.* **189**, 275–288 (2010).
44. Pan, Z. *et al.* Structural and biochemical characterization of the interaction between LGN and Frmpd1. *J. Mol. Biol.* **425**, 1039–1049 (2013).
45. Zheng, Z., Wan, Q., Meixiong, G. & Du, Q. Cell cycle-regulated membrane binding of NuMA contributes to efficient anaphase chromosome separation. *Mol. Biol. Cell* **25**, 606–619 (2014).
46. Kotak, S. & Gönczy, P. NuMA phosphorylation dictates dynein-dependent spindle positioning. *Cell Cycle* **13**, 177–178 (2014).
47. Kiyomitsu, T. & Cheeseman, I.M. Chromosome- and spindle-pole-derived signals generate an intrinsic code for spindle position and orientation. *Nat. Cell Biol.* **14**, 311–317 (2012).
48. Ségalen, M. *et al.* The Fz-Dsh planar cell polarity pathway induces oriented cell division via Mud/NuMA in *Drosophila* and zebrafish. *Dev. Cell* **19**, 740–752 (2010).
49. Machicoane, M. *et al.* SLK-dependent activation of ERMs controls LGN-NuMA localization and spindle orientation. *J. Cell Biol.* **205**, 791–799 (2014).
50. Jaffe, A.B., Kaji, N., Durgan, J. & Hall, A. Cdc42 controls spindle orientation to position the apical surface during epithelial morphogenesis. *J. Cell Biol.* **183**, 625–633 (2008).
51. Ooshio, T. *et al.* Involvement of LMO7 in the association of two cell-cell adhesion molecules, nectin and E-cadherin, through afadin and alpha-actinin in epithelial cells. *J. Biol. Chem.* **279**, 31365–31373 (2004).
52. Williams, S.E., Ratliff, L.A., Postiglione, M.P., Knoblich, J.A. & Fuchs, E. Par3-mInsc and Gαi3 cooperate to promote oriented epidermal cell divisions through LGN. *Nat. Cell Biol.* **16**, 758–769 (2014).
53. Elias, S. *et al.* Huntingtin regulates mammary stem cell division and differentiation. *Stem Cell Reports* **2**, 491–506 (2014).

ONLINE METHODS

Protein expression and purification. GST-LGN$_{15–350}$, GST-NuMA$_{1861–1928}$, and the chimeric fusion protein GST-LGN$_{15–350}$-Afadin$_{1709–1746}$ (LGN^{TPR}-Afadin^{PEPT} in the text) were cloned into the pGEX-6P1 vector (GE Healthcare) and expressed in BL21 *Escherichia coli* cells. Cells were lysed in 0.1 M Tris-HCl, pH 8, 0.3 M NaCl, 10% glycerol, 0.5 mM EDTA, and 1 mM DTT, and cleared for 1 h at 100,000*g*. Cleared lysates were affinity purified by incubation with glutathione–Sepharose-4 Fast-Flow beads (GE Healthcare). After washing of the beads, fusion proteins retained on the beads were incubated with PreScission protease (GE Healthcare) overnight at 4 °C to remove the GST tag. The cleaved material was eluted from the beads in a desalting buffer consisting of 20 mM Tris-HCl, pH 8, 40 mM NaCl, 5% glycerol, and 1 mM DTT, and loaded on Resource-Q or Resource-S ion-exchange columns. *Drosophila* Canoe$_{1755–2051}$, Mud$_{1895–2094}$, and Pins$_{25–406}$ (Pins^{TPR}) were purified similarly. For crystallization experiments, the fusion protein LGN^{TPR}-Afadin^{PEPT} was further purified on a Superdex-200 column equilibrated in 10 mM HEPES, pH 7.5, 0.15 M NaCl, and 5% glycerol. Afadin point mutations were generated by QuikChange site-directed mutagenesis (Stratagene) according to the manufacturer's instructions. All clones were sequence verified.

Crystallization and crystal-structure determination. Crystallization experiments of LGN^{TPR}-Afadin^{PEPT} (10 mg/ml) were performed at the IEO Crystallography Unit. Diffraction-quality crystals were obtained by manual optimization of the initial conditions in hanging drops at 15 °C; 1 µl of protein was mixed with an equal volume of reservoir solution containing 1.5 M ammonium sulfate and 0.1 M Tris-HCl, pH 8.25. Crystals were cryoprotected by soaking in reservoir buffer supplemented with 20% ethylene glycol and were flash frozen in liquid nitrogen. X-ray diffraction data were collected at beamline X06DA (PXIII) of the SLS (Villigen, Switzerland), and beamline ID23-2 at the ESRF (Grenoble, France). The cubic crystals belonged to space group $P2_13$. Initial phases were obtained by molecular replacement (MR) with the TPR domain of LGN as a search model (PDB 3RO2). The model was then completed with iterative cycles of manual building and restrained refinement with PHENIX[54]. The two copies of LGN^{TPR}-Afadin^{PEPT} present in the asymmetric unit were identical except for part of the C-terminal region of one of the Afadin peptides, for which the density was poor. The final model had 95% of its residues in the favored regions of the Ramachandran plot, 5% in the additionally allowed regions and 0% Ramachandran outliers. Data processing and refinement statistics are presented in **Table 1**.

***In vitro* binding assays.** For pulldown assays, 1 µM GST-Afadin fragments were immobilized on GSH beads and incubated for 1 h on ice with 5 µM LGN^{TPR} in 10 mM HEPES, pH 7.5, 0.1 M NaCl, 5% glycerol, and 0.1% Tween20. After washing of the beads, proteins bound to the beads were separated by SDS-PAGE and detected by Coomassie staining.

Isothermal titration calorimetry. The thermodynamic parameters of the association between Afadin^{Cter} and LGN^{TPR} were measured in an ITC displacement experiment, in which the relatively low-affinity reaction between Afadin and LGN was coupled to the high-affinity binding of LGN^{TPR} to the Inscuteable$_{25–58}$ peptide[17]. All reagents were dialyzed overnight against 10 mM HEPES, pH 7.5, and 0.15 M NaCl. ITC measurements were performed at 25 °C on a MicroCal VP-ITC calorimeter. In a preliminary experiment, 12 µM of LGN^{TPR} in the cell was titrated with 10-µl injections of Inscuteable$_{25–58}$ at 90 µM. Heats of ligand binding were corrected by subtraction of the average heat of ligand dilution after saturation and fitted to a single-site binding model with the Origin-7.0 package (MicroCal). Analysis of the integrated heats yielded an association constant K_{Insc} of $6.3 \pm 1.8 \times 10^7$ M^{-1}, a value fully in line with previous reports[2]. In a second calorimetric experiment, Inscuteable$_{25–58}$ at the same concentration used in the first experiment was injected in a cell containing 12 µM of LGN^{TPR} and 30 µM of Afadin^{Cter}. The presence of the low-affinity ligand in the cell affected the association of Insc$_{25–58}$ with LGN^{TPR}, as revealed by the analysis of the binding isotherm performed with the standard single-site binding model, which resulted in an apparent association constant K_{app} of $4.0 \times 10^6 \pm 5.7 \times 10^5$ M^{-1}. The measured K_{Insc} and K_{app} were then used to derive the association constant K_{Af} for the binding of Afadin^{Cter} to LGN^{TPR} with the following equation:

$$K_{Af} = [(K_{Insc} / K_{app}) - 1] \times 1/[Af]$$

where [Af] is the concentration of Afadin in the cell during the measurement of K_{app}.

Fluorescence polarization. Fluorescence polarization measurements were performed on an Infinite F200 (Tecan). A fixed concentration (40 nM) of fluorescein-labeled Afadin^{PEPT} (United Biosystems) was incubated with increasing concentrations of the indicated LGN^{TPR} construct in 10 mM HEPES, pH 7.5, and 0.15 M NaCl. The corresponding K_d values were calculated by fitting the fluorescence polarization curves in Prism (GraphPad Software) with the following quadratic equation:

$$Y = B \times ((0.04 + x + K_d) - \mathrm{sqrt}(\mathrm{sqr}(0.04 + x + K_d) - 4 \times 0.04 \times x))/(2 \times 0.04)$$

where Y is the intensity of the fluorescence polarization signal, B is the maximum polarization signal at saturation, x is the concentration of LGN^{TPR} in micromolar, and 0.04 µM is the constant concentration of Afadin^{PEPT}.

Actin co-sedimentation assays. For co-sedimentation assays, actin was purified as previously described[55]. Actin co-sedimentation assays were conducted according to Scita *et al.*[56]. In brief, purified rabbit G-actin was allowed to polymerize into filamentous actin (F-actin) for 20 min at room temperature in F buffer (5 mM Tris-HCl, pH 7.8, 0.2 mM ATP, 1 mM DTT, 0.1 mM $CaCl_2$, 1 mM $MgCl_2$ and 0.1 M KCl). Polymeric F-actin (1 µM) was incubated with increasing concentrations of His-Afadin^{Cter} for 15 min at room temperature and was subsequently ultracentrifuged for 25 min at 400,000*g* at 4 °C. Pellet and supernatant fractions were separated by SDS-PAGE and visualized by Coomassie staining. For each concentration of Afadin^{Cter}, densitometric quantification of the band in the pellet was performed with ImageLab (Bio-Rad). Normalized binding data were obtained by dividing the values of the pellet fractions at each point by the maximum value of the pellet at saturation. Normalized binding data were fitted to the quadratic equation

$$Y = B \times ((1 + x + K_d) - \mathrm{sqrt}(\mathrm{sqr}(1 + x + K_d) - 4 \times 1 \times x))/(2 \times 1)$$

where Y is the fraction of Afadin in the pellet at each concentration point, B is the maximum value of Afadin in the pellet at saturation, x is the concentration of Afadin incubated with F-actin expressed in micromolar, and 1 µM is the constant concentration of F-actin. Fitting and K_d calculation were carried out in GraphPad Prism. Qualitative co-sedimentation assays of Afadin^{Cter} in complex to LGN^{TPR} were carried out similarly with 9 µM of both proteins and 1 µM F-actin.

Culture conditions, antibodies and immunostaining. HeLa cells were cultured in Dulbecco's Modified Eagle's Medium (DMEM) supplemented with 10% FBS, 1% L-glutamine and antibiotics. For all the experiments, HeLa cells were cultured on fibronectin (5 µg/ml; Roche) and synchronized by a single thymidine block. Cells were treated with 2.5 mM thymidine (Sigma, T1895) for 24 h, released, and fixed for immunofluorescence after 8 h. Latrunculin A (Sigma, L5163) was added into the medium 30 min before fixation.

For knockdown of human Afadin, four unique 29-mer shRNA constructs in lentiviral vectors carrying a GFP reporter and puromycin resistance were tested in HeLa cells (OriGene Technologies, TL311457). The two most effective hairpins (Afadin shRNA-1, GCAGTCGTCAACAAGATGGTGAGCATGAT; and Afadin shRNA-2, CTCTGTGGTGACACTGGAAGTAGCAAAGC) were further used to study the effect of Afadin ablation in mitotic HeLa cells. Caco-2 cells were infected with Afadin shRNA-2–expressing lentiviruses to generate a stable cell line devoid of Afadin. Transcript depletion was verified by quantitative PCR with TaqMan assays (Life Technologies, Hs00984486_m1 for human Afadin). Samples were amplified with primers and probes for human Afadin and GAPDH as a housekeeping gene. For depletion of NuMA, a lentiviral vector carrying a GFP reporter and puromycin resistance, and expressing the NuMA shRNA CAUUAUGAUG

doi:10.1038/nsmb.3152

CCAAGAAGCAGCAGAACCA was used (OriGene Technologies, TL311065). For knockdown of LGN, small interfering RNA (siRNA) oligos with the following sense sequence were used: 5′-CCAUGGAUGUAGUGGGAAAUU-3′ (Thermo Scientific, Dharmacon). As a control, scrambled siRNAs with the sense sequence 5′-AGACGAACAAGUCACCGACUU-3′ were used. Transient transfections of 50 nM of siRNAs were conducted with RNAiMAX (Invitrogen), according to the manufacturer's instructions. Protein depletion was monitored by western blotting and immunofluorescence.

To rescue the misorientation phenotype of HeLa cells expressing the Afadin shRNA-2 hairpin, an shRNA-resistant mCherry-tagged rat long Afadin construct was generated by targeted mutagenesis introducing four silent base substitutions in the region targeted by the shRNA-2 hairpin. To obtain an Afadin$^{\Delta LGN}$ variant unable to interact with LGN, the construct was further engineered by deletion of residues 1714–1751 of rat long Afadin, corresponding to the LGN-binding stretch encoded by residues 1709–1747 of human Afadin isoform 4. To obtain the Afadin$^{\Delta Actin}$ mutant, residues 1519–1690 were deleted from the rat Afadin gene, corresponding to residues 1514–1685 of isoform 4 of human Afadin (**Supplementary Fig. 4**).

mCherry-Afadin wild-type, mCherry-Afadin$^{\Delta LGN}$, and mCherry-Afadin$^{\Delta Actin}$ were subcloned into a pCDH vector under the UbC promoter (SBI System Biosciences) and transfected into HeLa cells with Lipofectamine reagent (Invitrogen) according to the manufacturer's instructions.

Caco-2 cells were cultured in DMEM supplemented with 20% FCS, 1% L-glutamine, 0.1% $NaHCO_3$, and 0.1% nonessential amino acids. To produce cysts, Caco-2 cells were diluted in complete medium supplemented with 2.5% Matrigel (BD) and seeded on solidified Matrigel at a dilution of 6,000 cells/well in eight-well chamber slides (Lab-Tek). After 6 d of culture, cysts were fixed for 30 min in 4% PFA and permeabilized for 30 min with 0.5% Triton X-100. Statistical analysis of cystogenesis was performed in Prism with Fisher's exact test.

Immunofluorescence and immunoblotting. For detecting NuMA and Afadin, cells were fixed with methanol at −20 °C for 10 min. For detection of LGN, p150^{Glued} and actin, cells were fixed with 4% paraformaldehyde for 10 min at room temperature; this was followed by permeabilization with PBS and 0.3% Triton X-100 for 5 min. Cells were stained with rabbit anti-Afadin (polyclonal, raised against fragment 1514–1824 of human Afadin isoform 4; working dilution 1:500; produced in house; **Figs. 1c** and **6b**; validation in **Supplementary Fig. 1b**), mouse anti-LGN (monoclonal, raised against human full-length LGN; working dilution 1:5; produced in house; validation in **Supplementary Fig. 1c**), mouse anti-NuMA (monoclonal, raised against fragment 1861–2001 of human NuMA; working dilution 1:3,000; produced in house; validation in **Supplementary Fig. 1c**), and p150^{Glued} (1:600, BD 610473) followed by donkey anti-rabbit and anti-mouse Alexa Fluor 488 (ThemoFisher-Scientific A-21206 and A-21202, respectively), and anti-mouse and anti-rabbit Alexa Fluor674 (ThemoFisher-Scientific A-31571 and A-31573, respectively). F-actin was visualized with TRITC-conjugated phalloidin (diluted 1:10 for HeLa cells and 1:50 for Caco-2 cysts, Sigma P1951); DNA was stained with DAPI. For immunoblotting, the rabbit anti-Afadin antibody was used at a dilution of 1:500. Original images of blots used in this study can be found in **Supplementary Data Set 1**.

Microscopy. Confocal microscopy was performed on a Leica TCS SP2 confocal microscope equipped with violet (405 nm), blue (488 nm), yellow (561 nm), and red (633 nm) excitation laser lines. A 63× oil-immersion objective lens (HCX Plan-Apochromat 63× NA 1.4 Lbd Bl; Leica) was used for analysis. Image acquisition conditions were set to remove channel cross-talk, optimize spectral detection bands, and scan modalities.

Spindle-orientation analysis. Spindle orientation was monitored with HeLa cells grown on fibronectin-coated coverslips. In this condition, wild-type cells divided with the spindle axis parallel to the substratum. To quantify the spindle tilt, metaphase HeLa cells were fixed and stained with anti-NuMA antibody and DAPI. Cells were imaged in x-z optical sections passing through the spindle poles. Spindle-axis angles with respect to the substratum were measured with the angle tool of Fiji. Statistical analyses of spindle-angle distributions were performed with Prism (GraphPad Software) and plotted in angular histograms with a custom-written macro for MatLab. Statistical analysis of the data was performed in Prism with Kruskal-Wallis tests (**Fig. 1f**), one-way ANOVA Tukey's tests (**Fig. 5e**) or Mann-Whitney tests (**Supplementary Fig. 1**).

Quantification of cortical signal in mitotic cells. Quantification of cortical signals of LGN, NuMA and p150^{Gued} were conducted on confocal sections of metaphase cells in Fiji as follows. A 30-pixel-wide line was manually drawn from the spindle pole to the nearest cellular cortex perpendicularly to the metaphase plate, to obtain the intensity profile of the immunostained proteins along the line. The protein at the cortex was calculated by integrating the profile on a 30-pixel area centered at the peak of the profile, whereas the protein in the cytosol was quantified by integrating the same area 30 pixels away from the peak toward the DNA. Statistical analysis of the data was performed in Prism with Mann-Whitney tests (**Fig. 5a** and **Supplementary Fig. 5b**) or Kruskal-Wallis tests (**Fig. 5d** and **Supplementary Fig. 5e**,**f**).

54. Adams, P.D. *et al.* PHENIX: a comprehensive Python-based system for macromolecular structure solution. *Acta Crystallogr. D Biol. Crystallogr.* **66**, 213–221 (2010).
55. Carlier, M.F., Criquet, P., Pantaloni, D. & Korn, E.D. Interaction of cytochalasin D with actin filaments in the presence of ADP and ATP. *J. Biol. Chem.* **261**, 2041–2050 (1986).
56. Scita, G. *et al.* An effector region in Eps8 is responsible for the activation of the Rac-specific GEF activity of Sos-1 and for the proper localization of the Rac-based actin-polymerizing machine. *J. Cell Biol.* **154**, 1031–1044 (2001).

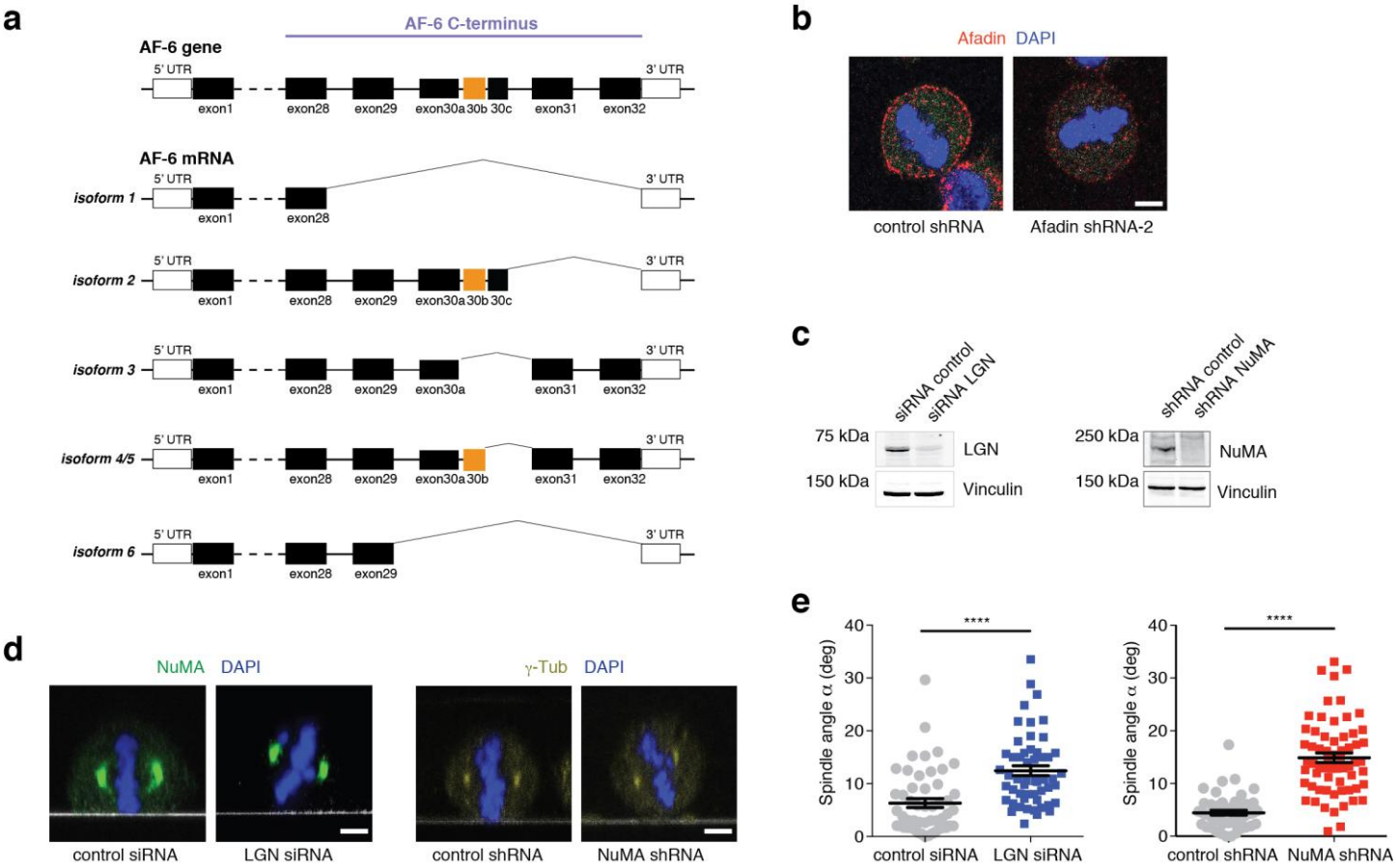

Supplementary Figure 1

Characterization of Afadin-, LGN- and NuMA-specific antibodies, and spindle angle analysis in LGN-depleted and NuMA-depleted HeLa cells.

(a) Scheme of human Afadin (also known as AF-6 or MLLT4) gene, and its splice variants. The AF-6 gene is located on human chromosome 6, and consists of 32 exons. Alternative splicing produces six transcripts differing in their C-terminal region. Human Afadin isoforms 1 and 6 stop at exons 28 and 29 respectively, and are similar to *short* variant of rat Afadin (also known as *s-Afadin*), which was reported to be unable to bind to F-actin. Human Afadin isoforms 2, 3, 4 and 5 are similar to *long* rat Afadin (*l*-Afadin), which binds to F-actin. Isoforms 4 and 5 differ for the presence of additional 11 residues between exon 28 and 29. The LGN-binding site of Afadin characterized in this study is coded by exon 30 (highlighted in orange), and is present in all human long isoforms except isoform-3. (**b**) Specificity of the Afadin antibody. Confocal sections of mitotic HeLa cells expressing a control shRNA and shRNA targeting Afadin (Afadin shRNA-2), fixed and stained for endogenous Afadin. Afadin staining was lost in Afadin shRNA-2 expressing cells. The scale bar corresponds to 5 μm. (**c**) Immunoblot analysis of mitotic lysates of HeLa cells transiently interfered for LGN (left) or stably depleted of NuMA (left) showing the efficiency of the protein depletions. (**d**) Representative confocal z-sections of mitotic HeLa cells depleted for LGN (left) or NuMA (right), with the corresponding controls. LGN-depleted cells are stained with NuMA (green) and DAPI (blue), while NuMA-ablated cells are visualized with γ-tubulin (dark yellow) and DAPI (blue). The plane of the coverslip is visible as a white line. (**e**) Quantification of mitotic spindle alignment performed as in Fig. 1 (with means ± SEM), showing mean angular tilts of about 14.9° for NuMA-depleted cells, and 12.5° for LGN-ablated cells. **** indicates a statistical difference of $P < 0.0001$ by Mann-Whitney test between interfered and control cells from three independent experiments with $n > 50$. Scale bars correspond to 5 μM.

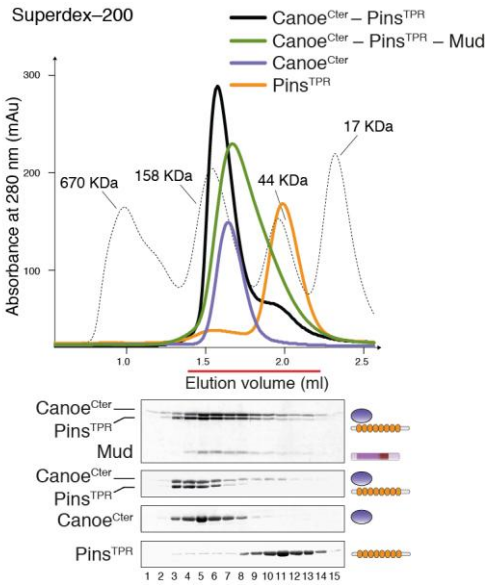

Supplementary Figure 2

Canoe (Afadin) binds directly to Pins (LGN) and competes with Mud (NuMA).

SEC analysis and corresponding Coomassie-blue stained SDS-PAGE of the competitive interactions between the C-terminal portion of *Drosophila* Canoe (encompassing residues 1755-2051), Pins(LGN)^{TPR} (spanning residues 25-406) and Mud$_{1895\text{-}2094}$. At equimolar concentration, Canoe(Afadin)^{Cter} enters a stoichiometric complex with Pins(LGN)^{TPR} eluting in fractions 3-6 (black trace). Addition to the mix of equimolar amounts of Mud$_{1895\text{-}2094}$ results in a complex of Mud$_{1895\text{-}2094}$–Pins(LGN)^{TPR} eluting slightly earlier than Canoe(Afadin)^{Cter} in isolation (fractions 4-7). This analysis demonstrates that Canoe(Afadin) and Mud(NuMA) are mutually exclusive interactors of Pins(LGN)^{TPR}, with Mud(NuMA) displaying higher affinity.

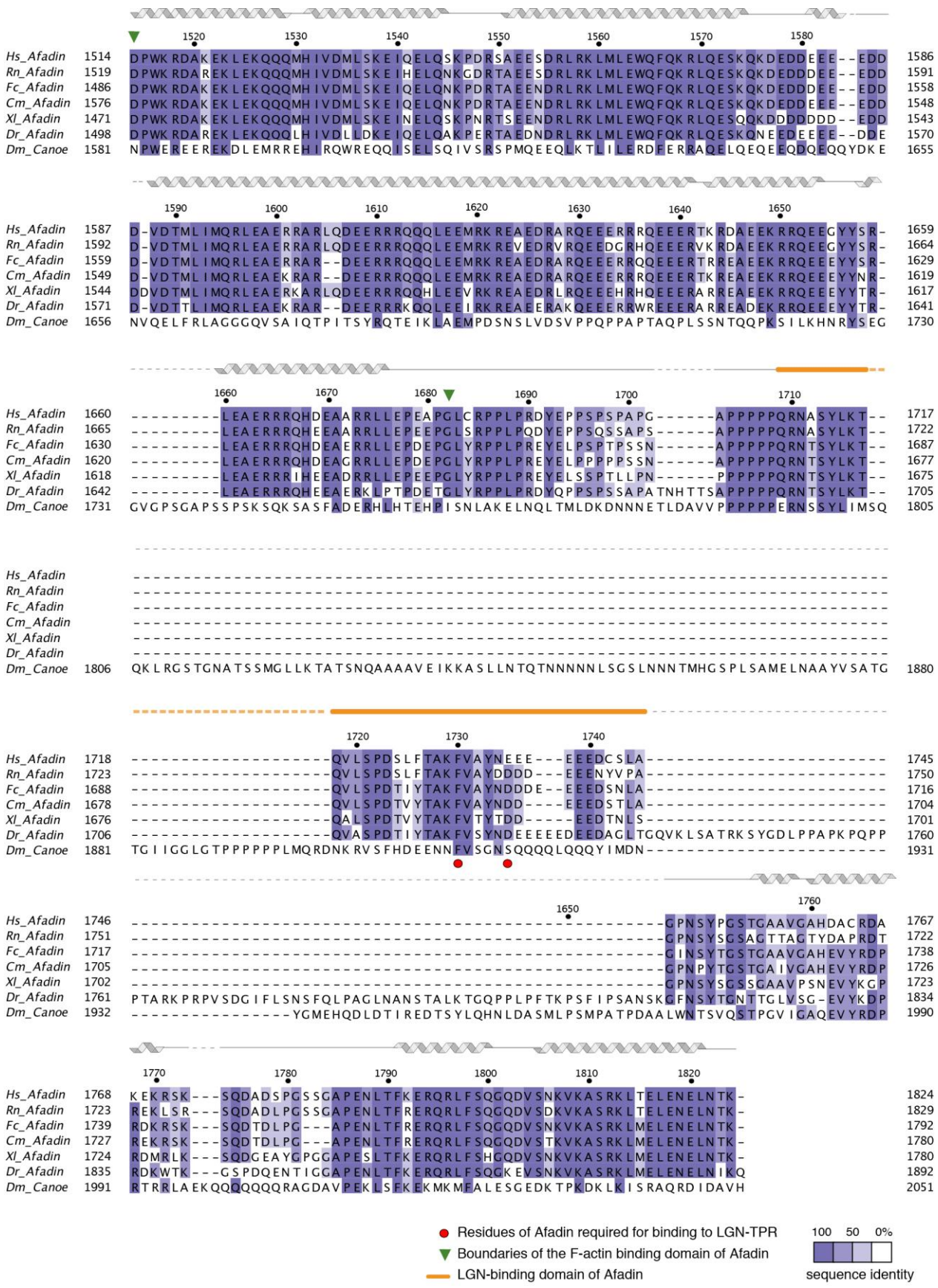

Nature Structural & Molecular Biology: doi:10.1038/nsmb.3152

Supplementary Figure 3

Sequence alignment of the C terminus of Afadin long isoforms.

Afadin residues are colored based on the conservation calculated on the alignment of seven orthologues of *Homo sapiens, Rattus norvegicus, Falco cherrug, Chelonia mydas, Xenopus laevis, Danio rerio and Drosophila melanogaster.* The orange line highlights the Afadin fragment directly in contact with the LGN^{TPR} domain according to the crystallographic structure, with the $Phe1730^{AF}$ and $Glu1735^{AF}$ labeled as red circles. The F-actin binding region of Afadin determined experimentally (Supplementary Figure 4b) is upstream of the LGN-binding stretch, and is predicted to adopt a helical conformation, as depicted in light gray (secondary structure prediction was performed using the server https://www.predictprotein.org/).

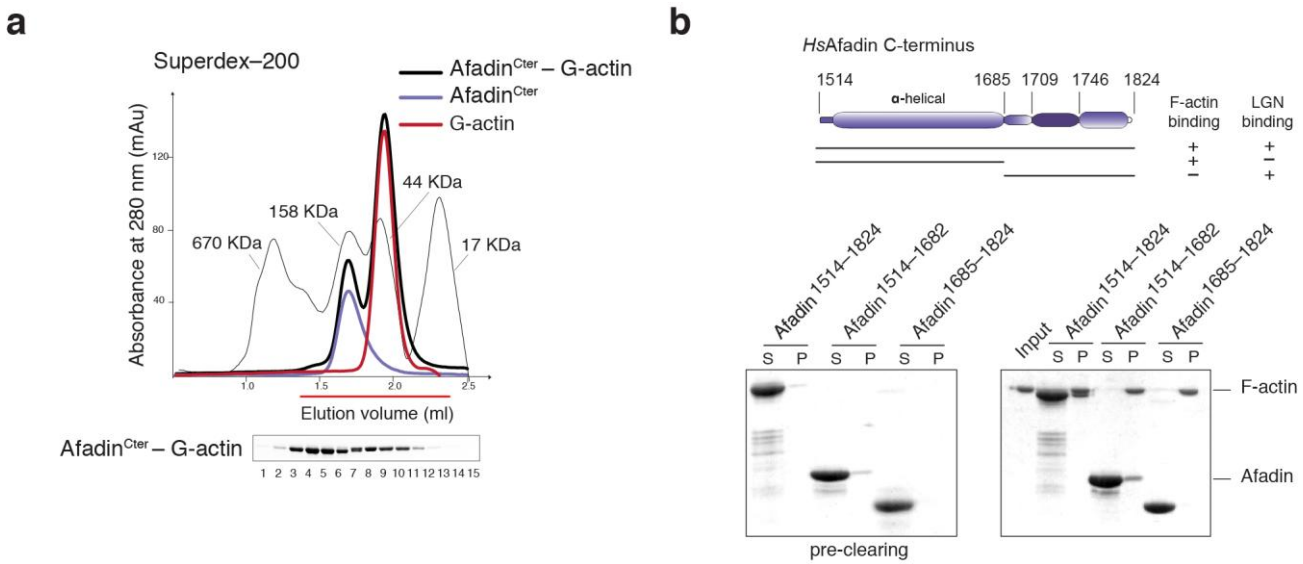

Supplementary Figure 4

Biochemical characterization of the interaction between Afadin^{Cter} and actin.

(a) Afadin does not bind to globular actin (G-actin). SEC analysis and corresponding SDS-PAGE showing that at 150 μM concentration of both species Afadin^{Cter} and monomeric G-actin do not form a complex. The elution profiles of Afadin^{Cter} and G-actin are also shown as references for the individual runs. Despite having similar molecular weight, Afadin^{Cter} elutes near the globular 158 kDa marker (lanes 3-6 of the SDS-PAGE), whereas G-actin elutes in the later fractions 7-10. (**b**) Afadin binds to F-actin through a region lying upstream to the LGN binding site. High-speed cosedimentation assay of two complementary fragments of Afadin^{Cter} (residues 1514-1824) with F-actin, showing that the actin-binding domain of human Afadin spans residues 1514-1682, upstream of the LGN-binding domain (colored in purple in the top scheme). Supernatant and pellet fractions of an analogous high-speed sedimentation experiment performed in the absence of F-actin are shown as a control of cosedimentation specificity.

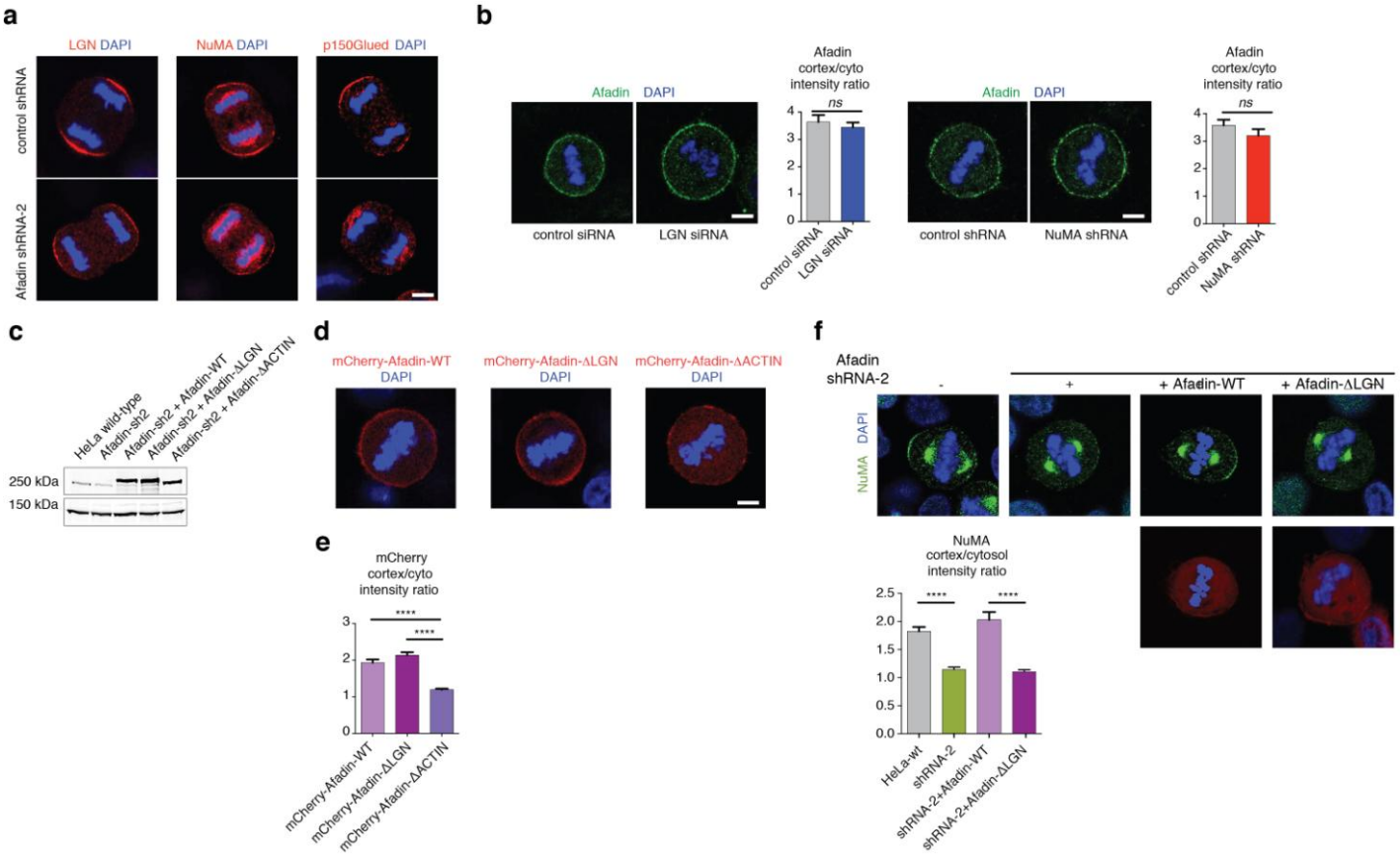

Supplementary Figure 5

Analysis of spindle motors in Afadin-depleted HeLa anaphases, localization of Afadin rescue constructs and NuMA rescue experiments.

(**a**) Ablation of Afadin in HeLa cells impairs cortical localization of LGN, NuMA and Dynactin in anaphase**.** Confocal sections of control shRNA (top) and Afadin shRNA-2 expressing HeLa cells (bottom) in anaphase stained for LGN, NuMA, and $p150^{Glued}$. Chromosomes are visualized with DAPI (blue). (**b**) Immunostaining of endogenous Afadin in mitotic HeLa cells interfered for LGN (left) or NuMA (right) with the corresponding controls. DNA is stained with DAPI. Quantification of cortical signals revealed that the cortical accumulation of Afadin is not altered by loss of LGN nor NuMA. (**c-d**) mCherry-Afadin rescue constructs. Immunoblot and immunostaining of HeLa cells transiently transfected with mCherry-Afadin, mCherry-Afadin-ΔLGN, or mCherry-Afadin-ΔACTIN showing the expression levels and the cortical localization of the shRNA-2 resistant rescue constructs. (**e**) Quantification of cortical mCherry-Afadin constructs analyzed in (d) showing that the F-actin binding domain of Afadin is required for the correct localization of the protein at the cortex. **** indicates $P < 0.0001$ by Kruskal-Wallis test from three independent experiments with $n > 40$. (**f**) Rescue experiment of cortical NuMA in HeLa cells stably depleted of Afadin, and transfected with shRNA-2 resistant mCherry-tagged rat Afadin wild-type, Afadin-ΔLGN, or Afadin-ΔACTIN. Quantification of cortical NuMA signals indicates that only Afadin wild-type rescues the cortical localization of NuMA in metaphase. The bottom panels show the mCherry-signal of the transfected cells. Under the conditions of methanol fixation used to visualize cortical NuMA, the cortical mCherry signal of all the rescue constructs is lost. **** indicates $P < 0.0001$ by Kruskal-Wallis test from three independent experiments with $n > 32$. Scale bars correspond to 5 μm.

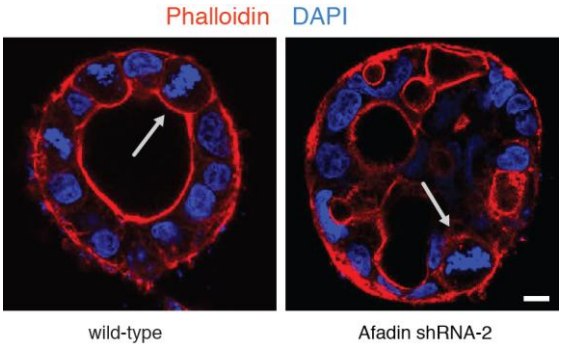

Supplementary Figure 6

Distribution of cortical F-actin in metaphases of Caco-2 cells, either wild type or lacking Afadin in three-dimensional cysts.

Cysts of Caco-2 cells wild-type or stably interfered for Afadin stained with DAPI (blue) and TRITC-conjugated Phalloidin (red). Confocal sections of the equatorial region of the cysts show that in mitotic cells (indicated by grey arrows) cortical F-actin distributes uniformly all around the plasma membrane regardless of the presence of Afadin.

STRUCTURAL BIOLOGY COMMUNICATIONS

ISSN 2053-230X

Crystallization and X-ray diffraction of LGN in complex with the actin-binding protein afadin

Manuel Carminati,[a] Valentina Cecatiello[a,b] and Marina Mapelli[a]*

[a]Department of Experimental Oncology, European Institute of Oncology, Via Adamello 16, 20139 Milan, Italy, and [b]IFOM, The FIRC Institute of Molecular Oncology, Via Adamello 16, 20139 Milan, Italy. *Correspondence e-mail: marina.mapelli@ieo.eu

Received 15 December 2015
Accepted 15 January 2016

Edited by R. L. Stanfield, The Scripps Research Institute, USA

Keywords: LGN; spindle orientation; fusion proteins.

Supporting information: this article has supporting information at journals.iucr.org/f

Asymmetric stem-cell divisions are fundamental for morphogenesis and tissue homeostasis. They rely on the coordination between cortical polarity and the orientation of the mitotic spindle, which is orchestrated by microtubule pulling motors recruited at the cortex by NuMA–LGN–Gαi complexes. LGN has emerged as a central component of the spindle-orientation pathway that is conserved throughout species. Its domain structure consists of an N-terminal TPR domain associating with NuMA, followed by four GoLoco motifs binding to Gαi subunits. The LGN^{TPR} region is also involved in interactions with other membrane-associated proteins ensuring the correct cortical localization of microtubule motors, among which is the junctional protein afadin. To investigate the architecture of LGN^{TPR} in complex with afadin, a chimeric fusion protein with a native linker derived from the region of afadin upstream of the LGN-binding domain was generated. The fusion protein behaves as a globular monomer in solution and readily crystallizes in the presence of sulfate-containing reservoirs. The crystals diffracted to 3.0 Å resolution and belonged to the cubic space group $P2_13$, with unit-cell parameter a = 170.3 Å. The structure of the engineered protein revealed that the crystal packing is promoted by the coordination of sulfate ions by residues of the afadin linker region and LGN^{TPR}.

1. Introduction

Asymmetric cell divisions regulate the position and the fate choice of daughter cells, with an impact on numerous phenotypes of multicellular organisms both during development and in adulthood (Knoblich, 2010). Asymmetric cell divisions are attained by the unequal segregation of cell-fate defining components and by differential positioning of siblings within the tissue. In several stem-cell systems, only daughters retaining contact with a specialized microenvironment called the niche will maintain stemness. The asymmetric outcome of a cell division requires tight coordination between cellular polarity and the division plane, and hence the mitotic spindle axis (Morin & Bellaïche, 2011). Spindle coupling to polarity cues involves the recruitment at spatially restricted cortical sites of molecular devices known as force generators, the main task of which is to capture astral microtubules emanating from the spindle poles and to establish pulling forces. One of the main players in the spindle-orientation pathway is the scaffolding protein LGN (where LGN stands for Leu-Gly-Asn repeat-enriched protein), which is found to be conserved from nematodes to mammals. From a topological standpoint, LGN

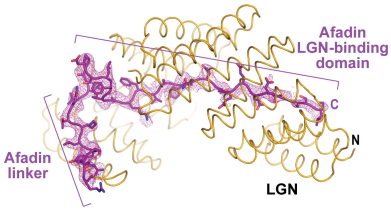

Table 1
Macromolecule-production information.

Source organism	*Homo sapiens*
DNA source	Synthetic
Forward primer	GAAATTTCAAGAGAGGTTGGGGATCAGCGAAACGCCTCCTACCTCAAA
Reverse primer	AAACAAAATTATTACTAGTGTCGACTTATCCTGCTAGGCTGCAGTCCTC
Cloning vector	pGEX-6P1
Expression vector	pGEX-6P1
Expression host	*E. coli* BL21 Rosetta
Sequence of LGN^{TPR}-afadin^{PEPT}†	**GPLGS**ASCLELALEGERLCKSGDCRAGVSFFEAAVQVGTEDLKTLSAIYSQLGNAYFYLHDYAKALEYHHHDLTLARTIGDQLGEAKASGNLGNTLKVLGNFDEAIVCCQRHLDISRELNDKVGEARALYNLGNVYHAKGKSFGCPGPQDVGEFPEEVRDALQAAVDFYEENLSLVTALGDRAAQGRAFGNLGNTHYLLGNFRDAVIAHEQRLLIAKEFGDKAAERRAYSNLGNAYIFLGEFETASEYYKKTLLLARQLKDRAVEAQSCYSLGNTYTLLQDYEKAIDYHLKHLAIAQELNDRIGEGRACWSLGNAYTALGNHDQAMHFAEKHLEISREVGDQRNASYLKTQVLSPDSLFTAKFVAYNEEEEEEDCSLAG

† The afadin^{PEPT} sequence is underlined.

has been depicted as a molecular switch (Du & Macara, 2004) that is held inhibited in interphase by intramolecular interactions and opens up in mitosis to bind several interactors including the Gαi subunits of heterotrimeric G proteins, the stem cell-specific cortical adaptor Inscuteable (Schaefer *et al.*, 2000; Mapelli & Gonzalez, 2012) and the major regulator of the microtubule motor dynein/dynactin, NuMA (nuclear mitotic apparatus protein; Du *et al.*, 2001). Less characterized ligands of LGN such as the actin-binding protein afadin have recently been identified in *Drosophila* (Wee *et al.*, 2011). In vertebrates, afadin is known as a junctional protein that is localized at the zona adherens and is required for epithelial organization (Ooshio *et al.*, 2007). Whether afadin is the positional cue restricting LGN at the lateral membrane during oriented epithelial divisions is an open issue, the elucidation of which will benefit from structural studies of the LGN–afadin interaction.

Structure–function analysis conducted in chicken neuroepithelial cells (Peyre *et al.*, 2011), skin progenitors (Williams *et al.*, 2011) and monolayered epithelia (Zheng *et al.*, 2010) revealed that the function of LGN as a hub conveying mitotic signals that instruct spindle orientation is intimately connected to its domain structure. The C-terminal half of the molecule harbours four GoLoco motifs responsible for the recruitment of LGN at the membrane by direct binding to Gαi subunits anchored to the lipid bilayer *via* myristoyl groups. The N-terminal domain of LGN consists of a contiguous array of eight tetratricopeptide repeats (TPRs) stacking in a superhelical arrangement. TPR motifs are degenerate 34-amino-acid units characterized by two antiparallel α-helices, generally referred to as A and B, which form the inner and outer surface of the superhelix, respectively (Das *et al.*, 1998). Intriguingly, most of the structurally characterized LGN^{TPR} interacting partners recognize the inner surface of the TPR scaffold *via* an intrinsically unstructured stretch that aligns perpendicularly with all eight A helices (Culurgioni *et al.*, 2011; Zhu *et al.*, 2011; Takayanagi *et al.*, 2015; Yuzawa *et al.*, 2011). Spiralling of the TPR α-solenoid around the elongated peptides results in a reduction of the intrinsic conformational flexibility of the helical array, which has proven to be a prerequisite for crystallizability of the domain. An analogous conformational stabilization of the TPRs has been observed in the complex of LGN^{TPR} with the last two LGN-GoLoco motifs, which recapitulates the architecture of the inhibited closed form of the molecule (Pan *et al.*, 2013).

Similar to other ligands such as Inscuteable and NuMA, the minimal LGN^{TPR}-binding region of afadin consists of a 37-residue peptide, which we will refer to as afadin^{PEPT}. Initial attempts to crystallize a complex reconstituted from purified LGN^{TPR} and a synthetic version of afadin^{PEPT} were not successful. Therefore, to gain insights into the architecture of the LGN^{TPR}–afadin^{PEPT} interaction, we engineered a chimeric protein carrying the LGN-binding region of afadin fused C-terminally to the LGN^{TPR} domain. We show that the afadin peptide of this chimeric protein is recognized intramolecularly by the TPR domain and that it stabilizes a compact conformation of the LGN^{TPR} superhelix required for the growth of diffraction-quality crystals. We also show that the amino-acid composition of the linker between the minimal interacting fragments of the two proteins is crucial in promoting crystal packing in sulfate-containing crystallization conditions.

2. Materials and methods

2.1. Generation of the chimeric fusion protein and macromolecule production

To reconstitute the interaction between human LGN (UniProt code B2RAL8) and afadin (UniProt code P55196, isoform 4), we used an LGN^{TPR} construct encompassing residues 15–350 and a fragment of afadin spanning residues 1709–1746 (afadin^{PEPT}). To stabilize the LGN^{TPR}–afadin^{PEPT} interaction, the sequence of afadin^{PEPT} was covalently linked to the C-terminus of LGN^{TPR} by means of a native polypeptide sequence derived from the ten residues of afadin upstream of afadin^{PEPT}. The entire sequence of the fusion protein is shown in Table 1, with afadin^{PEPT} underlined. To generate the chimeric construct, a two-step restriction-free cloning approach was employed (van den Ent & Löwe, 2006; Supplementary Fig. S1). Firstly, the coding sequence of the linker-afadin^{PEPT} cDNA was amplified using 50-base primers designed for the insertion of the PCR product into a previously generated pGEX-6P1-LGN^{TPR} vector. The forward primer carried a 24-base overlap with the vector, which was complementary to the 3′-end of the LGN^{TPR} construct, followed by 25 bases of linker-afadin^{PEPT}. The reverse primer annealed on the pGEX-6PI vector with 24 bases complementary to the 3′-end of the point of insertion. The amplified PCR fragment was cleaned using a PCR purification kit (Qiagen) and diluted to 100 ng µl^{-1}. A second amplification was conducted using 2–4 µl of the PCR fragment previously produced to prime the PCR reaction of *PfuTurbo* polymerase (Agilent Technologies) on 50 ng pGEX-6P1-LGN^{TPR} vector in 50 µl reaction mixture. The amplification

protocol consisted of 35 cycles, with an elongation step of 15 min. Once completed, 9 µl of the PCR reaction was treated with DpnI (New England Biolabs) for 2 h at 310 K to digest the methylated parental plasmid and subsequently transformed into *Escherichia coli* DH10 competent cells (Top10, Invitrogen). Positive clones containing the GST-LGN^{TPR}-afadin^{PEPT} fusion gene were confirmed by DNA sequencing.

The chimeric construct GST-LGN^{TPR}-afadin^{PEPT} was expressed in *E. coli* BL21 Rosetta cells grown to an OD of 0.6 by induction with 0.5 m*M* IPTG overnight at 291 K (Table 1). Harvested cells were resuspended in 0.1 *M* Tris–HCl pH 8, 0.3 *M* NaCl, 10% glycerol, 0.5 m*M* EDTA, 1 m*M* DTT and were lysed with a French press. Lysates were cleared for 1 h at 100 000*g* before incubation with Glutathione Sepharose 4 Fast Flow beads (GE Healthcare) for 2 h at 277 K. After washes in lysis buffer supplemented with 0.7 *M* NaCl, the GST-fusion protein retained on the beads was incubated with PreScission protease (GE Healthcare) in a 1:50 weight ratio overnight at 277 K to remove the GST tag. The cleaved material, which retained the residues GPLGS preceding the LGN sequence (shown in bold in Table 1), was eluted from the beads in a desalting buffer consisting of 20 m*M* Tris–HCl pH 8, 40 m*M* NaCl, 5% glycerol, 1 m*M* DTT and loaded onto a Resource Q ion-exchange column (GE Healthcare). The protein was eluted with a 40–350 m*M* NaCl gradient over 20 column volumes. Peak fractions were analyzed by SDS–PAGE and pooled for a subsequent purification step on a preparative Superdex 200 size-exclusion chromatography (SEC) column equilibrated in 10 m*M* HEPES pH 7.5, 0.15 *M* NaCl, 5% glycerol. Peak fractions eluted from the SEC column were pooled and concentrated to about 12 mg ml^{-1} using Vivaspin concentrators (Sartorius). The sample was stored at 193 K prior to use. Typically, about 7 mg pure protein was obtained starting from 1 l culture. The LGN^{TPR} used for SEC and native gel analyses was purified similarly, with a yield of about 3 mg pure protein from 1 l culture.

The LGN^{TPR}-afadin^{PEPT} construct has a molecular mass of about 41 kDa. Analytical SEC analysis revealed that the LGN^{TPR}-afadin^{PEPT} fusion elutes at the same volume as the LGN^{TPR}:afadin^{PEPT} complex assembled with a synthetic afadin peptide, but is slightly delayed compared with LGN^{TPR} in isolation (Fig. 1*a*). This result suggested that the LGN^{TPR}-afadin^{PEPT} chimera runs as a monodisperse monomer in solution, with an overall shape and hydrodynamical properties similar to those of the LGN^{TPR}:afadin^{PEPT} complex. To further corroborate this hypothesis, we compared the behaviour of the three samples on 12% Tris–glycine native PAGE (37:1 acrylamide:bisacrylamide). While LGN^{TPR} in isolation migrates on a native gel as a smear of multiple bands, the LGN^{TPR}-afadin^{PEPT} fusion runs with higher mobility as a single population (Fig. 1*b*), indicating that the fused afadin^{PEPT} stabilizes a compact conformation of the LGN^{TPR} superhelix. Consistently, the LGN^{TPR}:afadin^{PEPT} complex is less retarded than LGN^{TPR} but is more heterogeneous than the chimeric fusion construct. Collectively, these results provide good evidence that the fused peptide of afadin binds the TPR scaffold intramolecularly, inducing a homogeneous conformational rearrangement, rather than binding to a different molecule and causing heterogeneous aggregation.

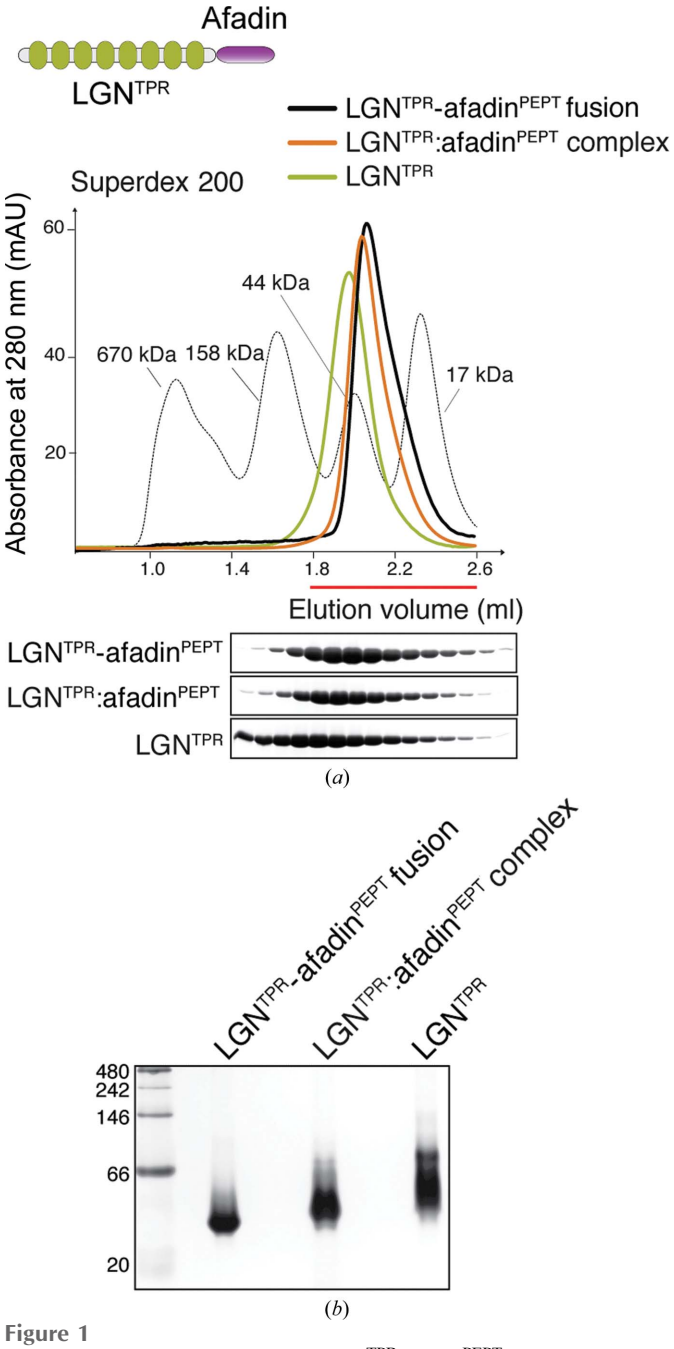

Figure 1
Biochemical characterization of LGN^{TPR}-afadin^{PEPT}. (*a*) Comparative SEC analysis of LGN^{TPR}-afadin^{PEPT}, LGN^{TPR} and the LGN^{TPR}:afadin^{PEPT} complex performed on a Superdex 200 5/150 column (GE Healthcare) at 100 µ*M* concentration. For this analysis, the LGN^{TPR} complex was assembled by mixing synthetic afadin^{PEPT} with LGN^{TPR} in a 1:1.3 molar ratio. The protein elution profiles are overlaid with the trace of globular molecular-weight markers (grey dashed line). For all samples, the peak fractions were separated by SDS–PAGE and visualized by Coomassie staining. At the top left corner a schematic representation of the domain structure of the chimeric protein is shown, with LGN^{TPR} coloured green and afadin^{PEPT} purple. (*b*) The conformational heterogeneity of the LGN^{TPR}-afadin^{PEPT} fusion, the LGN^{TPR}:afadin^{PEPT} complex and LGN^{TPR} was assessed by native PAGE followed by Coomassie staining. Native molecular-weight markers (NativeMark, Life Technologies) are displayed in the first lane (labelled in kDa).

Table 2
Crystallization.

Method	Sitting drop	Sitting drop	Hanging drop	Hanging drop, seeding
Plate type	96 × 3 well	96 × 3 well	24 well	24 well
Temperature (K)	293	293	288	277
Protein concentration (mg ml^{-1})	10	10	8	5
Buffer composition of protein solution	10 m*M* Na HEPES pH 7.5, 0.15 *M* NaCl, 5% glycerol, 4.5 m*M* TCEP	10 m*M* Na HEPES pH 7.5, 0.15 *M* NaCl, 5% glycerol, 4.5 m*M* TCEP	10 m*M* Na HEPES pH 7.5, 0.15 *M* NaCl, 5% glycerol, 4.5 m*M* TCEP	10 m*M* Na HEPES pH 7.5, 0.15 *M* NaCl, 5% glycerol, 4.5 m*M* TCEP
Composition of reservoir solution	0.1 *M* Na HEPES pH 7, 1.6 *M* ammonium sulfate	0.1 *M* bis-tris propane pH 7, 3.5 *M* sodium formate	0.1 *M* Tris–HCl pH 8, 1.4 *M* ammonium sulfate	0.1 *M* bis-tris propane pH 7, 1.0 *M* DL-malic acid
Initial hit	AmSO4 E10	SaltRX C7	AmSO4 E10	SaltRX C9
Volume and ratio of drop	100 nl (1:1 ratio)	100 nl (1:1 ratio)	1 µl (1:1 ratio)	1 µl (1:1 ratio)
Volume of reservoir (µl)	100	100	300	300
Screened using X-rays	No	No	Yes	Yes

These findings are consistent with the micromolar affinity that afadin^{PEPT} displays for LGN^{TPR} (with a dissociation constant K_d of 5.6 µ*M*; Carminati *et al.*, 2016).

2.2. Crystallization

Initial crystallization trials of the LGN^{TPR}-afadin^{PEPT} sample utilized the commercial sparse-matrix screens SaltRX (Hampton Research), AmSO4 (Qiagen), JCSG-plus and Structure Screen 1 + 2 (Molecular Dimensions) and were conducted in sitting-drop vapour-diffusion format using a Cartesian Honeybee nanodispenser (Genomic Solutions) in three-square-well CrystalQuick Greiner plates. At the two concentrations tested (10 and 5 mg ml^{-1}), 100 nl protein solution was mixed with an equal volume of reservoir solution at 293 K. Crystals appeared at 10 mg ml^{-1} after 1 d in about 20% of the salting-out conditions containing sulfate, phosphate, formate or malic acid ions at pH values between 7.0 and 8.5. The same crystallization trials conducted on a sample of LGN^{TPR} in complex with synthetic afadin^{PEPT} were unsuccessful. Since four of the linker residues present in the chimera have charged side chains, we reasoned that these linker residues could be crucial in promoting nucleation in the presence of high concentrations of multivalent ions. We selected conditions E10 from the AmSO4 kit (0.1 *M* Na HEPES pH 7, 1.6 *M* ammonium sulfate) and C7 and C9 from the SaltRX kit (0.1 *M* bis-tris propane pH 7, 3.5 *M* sodium formate and 0.1 *M* bis-tris propane pH 7, 1.2 *M* DL-malic acid pH 7.0, respectively) for manual optimization. All three conditions could be reproduced in hanging drops in 24-well VDX plates (Hampton Research) by mixing 1 µl protein solution with 1 µl reservoir solution. Under these conditions, crystallogenesis was very rapid at 293 K, yielding showers of small crystals in about 2 h or multiple crystals in the case of malic acid (Figs. 2*a* and 2*b*). To slow the crystal growth, we decided to perform grid screens around 0.1 *M* Na HEPES pH 7, 1.6 *M* ammonium sulfate at 288 K. The concentration of ammonium sulfate was varied from 1.35 to 1.6 *M* in 50 m*M* increments at pH values ranging from 7.5 to 8.25. Using this approach, single cubic crystals of around 0.5 mm in size (Fig. 2*c*) grew overnight. Further attempts to slow crystal nucleation were conducted at 277 K, seeding drops set up with a protein concentration of 5 mg ml^{-1} and a reservoir solution consisting of 0.1 *M* Tris–HCl pH 8.0, 1.4 *M* ammonium sulfate after 3 h of equilibration (Table 2). Analogous optimizations were conducted around 0.1 *M* bis-tris propane pH 8.0, 3.5 *M* sodium formate and around 0.1 *M* bis-tris propane pH 7.0, 1.2 *M* malic acid. Single large crystals suitable for diffraction experiments were obtained at 288 K with 1.3 *M* ammonium sulfate or 1.0 *M* DL-malic acid or by seeding the same conditions at 277 K. To improve the crystal

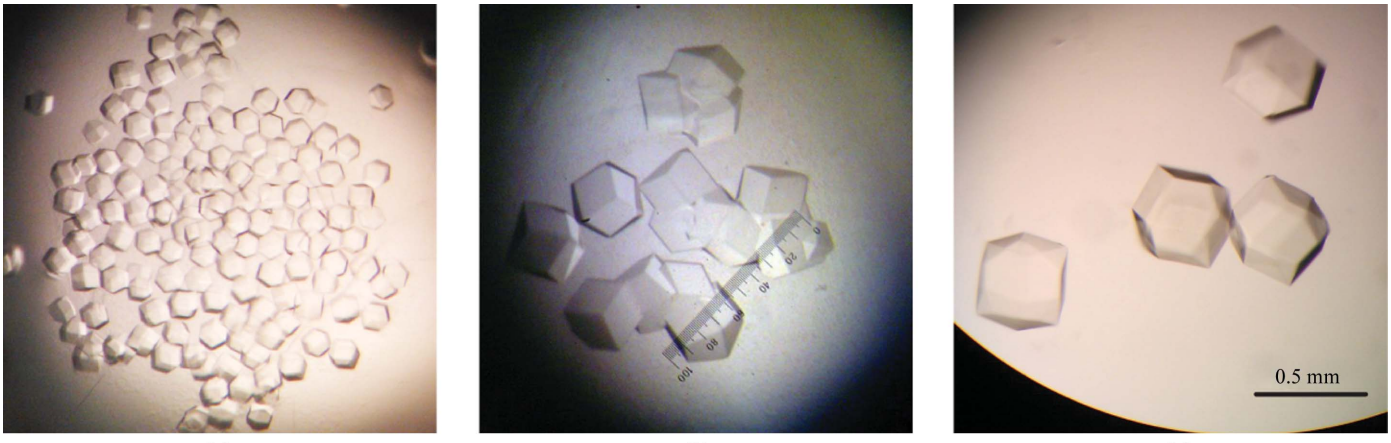

(*a*) (*b*) (*c*)

Figure 2
(*a*, *b*) Initial crystals of LGN^{TPR}-afadin^{PEPT} grown manually by hanging-drop vapour diffusion in ammonium sulfate or malic acid. (*c*) After optimization at 288 K or seeding at 277 K, single cubic crystals of about 0.5 mm in size appear after 1 d of crystallization.

packing an additional additive screen was performed starting from these latter conditions, which unfortunately did not change either the crystal morphology or diffraction properties. As the crystals were fragile, they were cryoprotected by stepwise addition of ethylene glycol directly to the crystallization drops to a final concentration of 20% for 10–30 min prior to flash-cooling in liquid nitrogen.

2.3. Data collection and processing

X-ray diffraction data for LGN^{TPR}-afadin^{PEPT} crystals were collected on beamline X06DA at the Swiss Light Source (SLS), Villigen, Switzerland and on beamline ID23-2 at the European Synchrotron Radiation Facility, Grenoble, France. Data were processed using *XDS* (Kabsch, 2010) implemented in *xia*2 (Winter *et al.*, 2013). The crystals diffracted to a resolution of about 3.0 Å (Fig. 3*a*) and belonged to the cubic space group $P2_13$. The unit-cell parameters are consistent with two copies of the fusion protein per asymmetric unit, with a Matthews coefficient of 4.8 Å^3 Da^{-1} and a solvent content of 75%. The high solvent content partly explains the modest resolution of the data despite the relatively large dimensions of the crystals, as often observed by Kantardjieff & Rupp (2003) and Weichenberger & Rupp (2014). Based on the Patterson function, no translational pseudosymmetry exists between the two molecules in the asymmetric unit. The structure of LGN^{TPR}-afadin^{PEPT} was determined by molecular replacement with *Phaser* (McCoy *et al.*, 2007) using the coordinates of mouse LGN^{TPR} solved previously in complex with NuMA (PDB entry 3ro2; Zhu *et al.*, 2011) as a search model. The afadin peptide was built manually by iterative cycles in *Coot* (Emsley *et al.*, 2010) and refinement in *PHENIX* (Adams

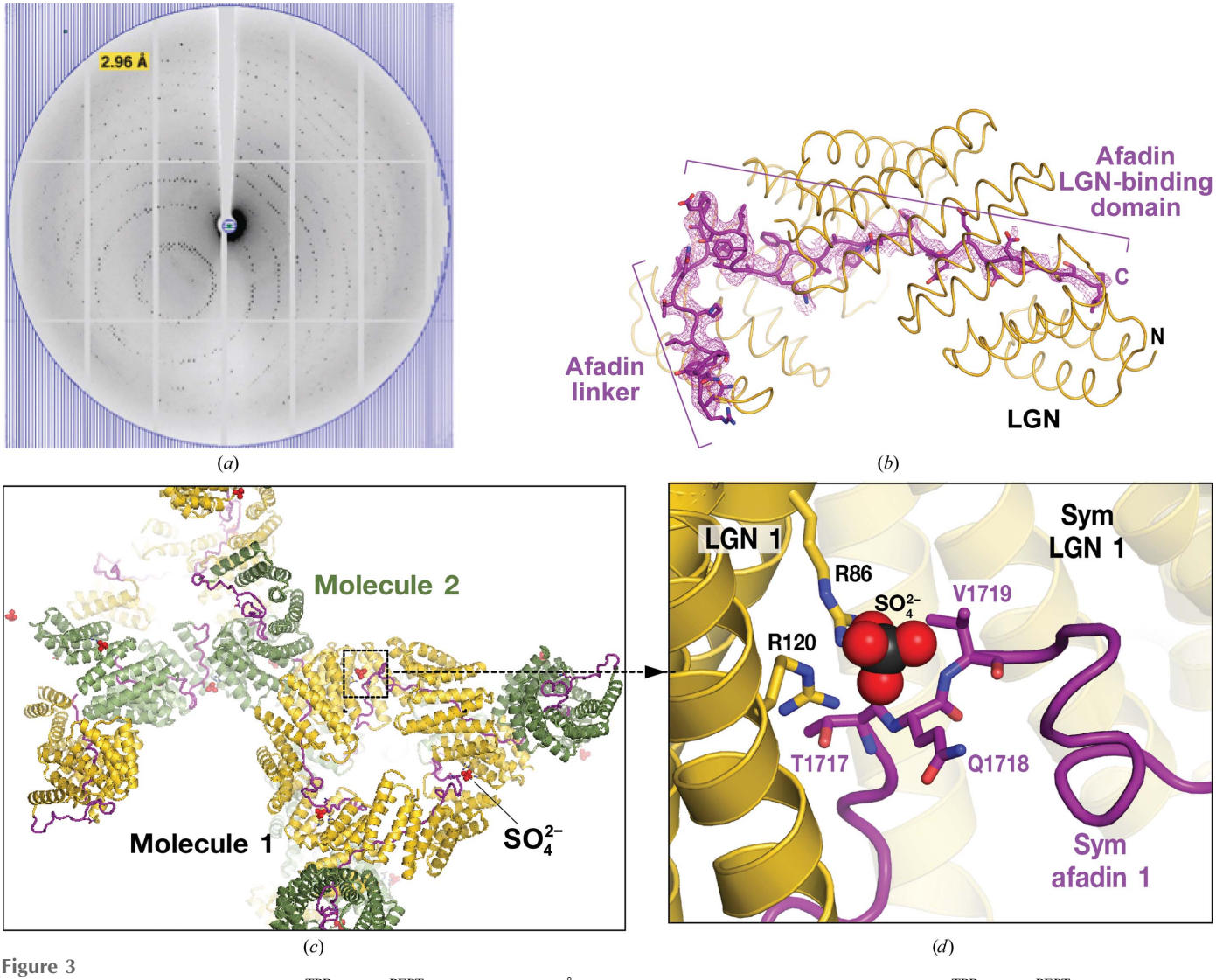

Figure 3
Diffraction and packing of the LGN^{TPR}-afadin^{PEPT} crystals. (*a*) 3.0 Å resolution X-ray diffraction pattern of LGN^{TPR}-afadin^{PEPT} obtained using a synchrotron-radiation source on beamline X06DA at the Swiss Light Source. (*b*) LGN^{TPR}-afadin^{PEPT} model and composit OMIT electron-density map displayed around the afadin^{PEPT} region contoured at the 1.0σ level. (*c*) Crystal lattice of LGN^{TPR}-afadin^{PEPT} with the two molecules of the asymmetric unit shown as gold and green cartoons and the sulfate ions shown as red spheres. For all molecules, the native linker of afadin^{PEPT} is displayed in purple. (*d*) Enlarged view of the crystal contacts contributed to by the side chains of Arg86^{LGN} and Arg120^{LGN} and Gln1718^{afadin} of the two LGN^{TPR}-afadin^{PEPT} fusion proteins present in the asymmetric unit.

Table 3
Data collection and processing.

Values in parentheses are for the outer shell.

Diffraction source	X06DA, SLS
Wavelength (Å)	1.008
Temperature (K)	100
Detector	PILATUS 2M
Crystal-to-detector distance (mm)	305
Rotation range per image (°)	0.3
Total rotation range (°)	60.3
Exposure time per image (s)	5
Space group	$P2_13$
a, b, c (Å)	170.3
α, β, γ (°)	90
Mosaicity (°)	0.2
Resolution range (Å)	69.5–3.00 (3.07–3.00)
Total No. of reflections	223474
No. of unique reflections	33516
Completeness (%)	99.9 (100.0)
Multiplicity	6.7 (6.4)
$\langle I/\sigma(I)\rangle$	18.6 (2.5)
R_{meas}	0.109 (1.022)
Overall B factor from Wilson plot (Å^2)	75.6

et al., 2010). The current model was refined at 3.0 Å resolution to an R_{free} of 26.7% and an R_{work} of 23.3%, with good electron density for the afadin^{PEPT} residues (Fig. 3*b*). Data-collection statistics are given in Table 3. The sulfate ions, which were contained in the reservoir, are coordinated by Arg86^{LGN}, Arg120^{LGN} and by Gln1718^{afadin} of afadin^{PEPT} belonging to a symmetry-related molecule, thus promoting crystal packing (Figs. 3*c* and 3*d*). Importantly, direct contacts between the very C-terminus of afadin^{PEPT} of one of the molecules in the asymmetric unit (namely residues Cys-Ser-Leu-Ala) and the TPR repeats of the second molecule in the same asymmetric unit also contribute to the crystal packing. However, crystals of LGN^{TPR} in complex with synthetic afadin^{PEPT} grown by seeding with nuclei of the LGN^{TPR}-afadin^{PEPT} fusion protein, which retain the afadin^{PEPT} contacts but lack those of the linker region, were very tiny (0.03–0.05 µm in size) and diffracted only to about 30 Å resolution. Thus, we conclude that the presence of the afadin linker is the molecular explanation for the good diffraction quality of the crystals of the LGN^{TPR}-afadin^{PEPT} chimera.

3. Results and discussion

In this study, we report the generation and crystallization of a fusion protein between the LGN^{TPR} domain and its binding peptide from afadin as an instrumental step in obtaining well diffracting crystals of the two interacting proteins. Chimeric fusions between low-affinity interactors are known to promote the formation of stoichiometric complexes for structural studies (Pellegrini *et al.*, 2002). Although natively occurring interdomain linkers consist of residues as diverse as Pro, Arg, Phe, Thr, Glu and Gln (George & Heringa, 2002; Kobe *et al.*, 2015), historically for crystallization purposes the linker region between the two binding domains has been chosen as the shortest flexible stretch of glycines and serines that allows unrestrained recognition of the two partners (Reddy Chichili *et al.*, 2013). For our structural investigations, we decided to covalently join LGN^{TPR} to the LGN-binding domain of afadin using the sequence of afadin upstream of the minimal LGN-binding peptide. When mixed with multivalent anion-containing reservoirs, the resulting chimeric fusion readily yielded cubic crystals. The structure of the fusion construct revealed that crystal packing is contributed to by positively charged residues of LGN^{TPR} and a Gln side chain of the afadin linker, which coordinate sulfate ions. This evidence explains the improved crystallizability of the chimera compared with LGN^{TPR} in complex with synthetic afadin^{PEPT}, which yielded only poorly diffracting crystals upon seeding with nuclei of the chimeric fusion construct. Thus, we can conclude that in this case the use of a native linker sequence coupled the advantage of forming stable complexes between LGN and afadin with the beneficial effect of having chemically active side chains of the linker promoting crystal packing.

Interestingly, the topology of LGN^{TPR}-afadin^{PEPT} is reminiscent of the recognition mode of other helical repeat-containing proteins with their cognate ligands, such as E-cadherin in complex with β-catenin (Huber & Weis, 2001) and karyopherin α bound to NLS peptides (Conti *et al.*, 1998). We predict that the engineering method presented in this study will be particularly successful in investigating the organizational principles of similar α-solenoids in complex with their binding partners.

Acknowledgements

This work was supported by the Italian Foundation for Cancer Research (AIRC), the Italian Ministry of Health and Bio-Struct-X (FP7/2007–2013, grant agreement No. 283570). We are grateful to the IEO Crystallography Unit for technical support and to the members of the Mapelli laboratory for scientific discussion. We thank the scientists at the X06DA beamline at SLS and at the ID23-2 beamline at the ESRF for help with data collection.

References

Adams, P. D. *et al.* (2010). *Acta Cryst.* D**66**, 213–221.
Carminati, M., Gallini, S., Pirovano, L., Alfieri, A., Bisi, S. & Mapelli, M. (2016). *Nature Struct. Mol. Biol.*, doi:10.1038/nsmb.3152.
Conti, E., Uy, M., Leighton, L., Blobel, G. & Kuriyan, J. (1998). *Cell*, **94**, 193–204.
Culurgioni, S., Alfieri, A., Pendolino, V., Laddomada, F. & Mapelli, M. (2011). *Proc. Natl Acad. Sci. USA*, **108**, 20998–21003.
Das, A. K., Cohen, P. W. & Barford, D. (1998). *EMBO J.* **17**, 1192–1199.
Du, Q. & Macara, I. G. (2004). *Cell*, **119**, 503–516.
Du, Q., Stukenberg, P. T. & Macara, I. G. (2001). *Nature Cell Biol.* **3**, 1069–1075.
Emsley, P., Lohkamp, B., Scott, W. G. & Cowtan, K. (2010). *Acta Cryst.* D**66**, 486–501.
Ent, F. van den & Löwe, J. (2006). *J. Biochem. Biophys. Methods*, **67**, 67–74.
George, R. A. & Heringa, J. (2002). *Protein Eng.* **15**, 871–879.
Huber, A. H. & Weis, W. I. (2001). *Cell*, **105**, 391–402.
Kabsch, W. (2010). *Acta Cryst.* D**66**, 133–144.
Kantardjieff, K. A. & Rupp, B. (2003). *Protein Sci.* **12**, 1865–1871.
Knoblich, J. A. (2010). *Nature Rev. Mol. Cell Biol.* **11**, 849–860.
Kobe, B., Ve, T. & Williams, S. J. (2015). *Acta Cryst.* F**71**, 861–869.
Mapelli, M. & Gonzalez, C. (2012). *Open Biol.* **2**, 120102.

McCoy, A. J., Grosse-Kunstleve, R. W., Adams, P. D., Winn, M. D., Storoni, L. C. & Read, R. J. (2007). *J. Appl. Cryst.* **40**, 658–674.
Morin, X. & Bellaïche, Y. (2011). *Dev. Cell*, **21**, 102–119.
Ooshio, T., Fujita, N., Yamada, A., Sato, T., Kitagawa, Y., Okamoto, R., Nakata, S., Miki, A., Irie, K. & Takai, Y. (2007). *J. Cell Sci.* **120**, 2352–2365.
Pan, Z., Zhu, J., Shang, Y., Wei, Z., Jia, M., Xia, C., Wen, W., Wang, W. & Zhang, M. (2013). *Structure*, **21**, 1007–1017.
Pellegrini, L., Yu, D. S., Lo, T., Anand, S., Lee, M., Blundell, T. L. & Venkitaraman, A. R. (2002). *Nature (London)*, **420**, 287–293.
Peyre, E., Jaouen, F., Saadaoui, M., Haren, L., Merdes, A., Durbec, P. & Morin, X. (2011). *J. Cell Biol.* **193**, 141–154.
Reddy Chichili, V. P., Kumar, V. & Sivaraman, J. (2013). *Protein Sci.* **22**, 153–167.
Schaefer, M., Shevchenko, A., Shevchenko, A. & Knoblich, J. A. (2000). *Curr. Biol.* **10**, 353–362.
Takayanagi, H., Yuzawa, S. & Sumimoto, H. (2015). *Acta Cryst.* F**71**, 175–183.
Wee, B., Johnston, C. A., Prehoda, K. E. & Doe, C. Q. (2011). *J. Cell Biol.* **195**, 369–376.
Weichenberger, C. X. & Rupp, B. (2014). *Acta Cryst.* D**70**, 1579–1588.
Williams, S. E., Beronja, S., Pasolli, H. A. & Fuchs, E. (2011). *Nature (London)*, **470**, 353–358.
Winter, G., Lobley, C. M. C. & Prince, S. M. (2013). *Acta Cryst.* D**69**, 1260–1273.
Yuzawa, S., Kamakura, S., Iwakiri, Y., Hayase, J. & Sumimoto, H. (2011). *Proc. Natl Acad. Sci. USA*, **108**, 19210–19215.
Zheng, Z., Zhu, H., Wan, Q., Liu, J., Xiao, Z., Siderovski, D. P. & Du, Q. (2010). *J. Cell Biol.* **189**, 275–288.
Zhu, J., Wen, W., Zheng, Z., Shang, Y., Wei, Z., Xiao, Z., Pan, Z., Du, Q., Wang, W. & Zhang, M. (2011). *Mol. Cell*, **43**, 418–431.

Article

Current Biology

NuMA Phosphorylation by Aurora-A Orchestrates Spindle Orientation

Highlights

- Aurora-A contributes to spindle orientation by controlling NuMA cortical targeting
- Phosphorylation of Ser1969^{NuMA} by Aurora-A governs NuMA mobility at spindle poles
- NuMA residues 2002–2115 bind to microtubules, independently of Aurora-A
- NuMA binds simultaneously microtubules and the spindle orientation protein LGN

Authors

Sara Gallini, Manuel Carminati, Fabiola De Mattia, ..., Italia Anna Asteriti, Giulia Guarguaglini, Marina Mapelli

Correspondence

giulia.guarguaglini@uniroma1.it (G.G.), marina.mapelli@ieo.eu (M.M.)

In Brief

Gallini et al. identify NuMA phosphorylation as the determinant for the Aurora-A spindle orientation function. In metaphase, Aurora-A governs the distribution of NuMA between poles and cortex by phosphorylating Ser1969^{NuMA}, which controls NuMA mobility at poles. A novel microtubule-binding domain of NuMA is identified compatible with LGN binding.

Gallini et al., 2016, Current Biology *26*, 458–469
February 22, 2016
http://dx.doi.org/10.1016/j.cub.2015.12.051

CellPress

CellPress

Current Biology
Article

NuMA Phosphorylation by Aurora-A Orchestrates Spindle Orientation

Sara Gallini,[1] Manuel Carminati,[1] Fabiola De Mattia,[2] Laura Pirovano,[1] Emanuele Martini,[3,4] Amanda Oldani,[3,4] Italia Anna Asteriti,[2] Giulia Guarguaglini,[2,*] and Marina Mapelli[1,*]

[1]Department of Experimental Oncology, European Institute of Oncology, Via Adamello 16, 20139 Milan, Italy
[2]Institute of Molecular Biology and Pathology, CNR National Research Council, c/o Department of Biology and Biotechnology, Sapienza University of Rome, Via degli Apuli 4, 00185 Rome, Italy
[3]Cogentech S.c.a.r.l., Via Adamello 16, 20139 Milan, Italy
[4]IFOM, the FIRC Institute of Molecular Oncology, Via Adamello 16, 20139 Milan, Italy
*Correspondence: giulia.guarguaglini@uniroma1.it (G.G.), marina.mapelli@ieo.eu (M.M.)
http://dx.doi.org/10.1016/j.cub.2015.12.051

SUMMARY

Spindle positioning is essential for tissue morphogenesis and homeostasis. The signaling network synchronizing spindle placement with mitotic progression relies on timely recruitment at the cell cortex of NuMA:LGN:Gαi complexes, in which NuMA acts as a receptor for the microtubule motor Dynein. To study the implication of Aurora-A in spindle orientation, we developed protocols for the partial inhibition of its activity. Under these conditions, in metaphase NuMA and Dynein accumulate abnormally at the spindle poles and do not reach the cortex, while the cortical distribution of LGN remains unperturbed. FRAP experiments revealed that Aurora-A governs the dynamic exchange between the cytoplasmic and the spindle pole-localized pools of NuMA. We show that Aurora-A phosphorylates directly the C terminus of NuMA on three Ser residues, of which Ser1969 determines the dynamic behavior and the spindle orientation functions of NuMA. Most interestingly, we identify a new microtubule-binding domain of NuMA, which does not overlap with the LGN-binding motif. Our study demonstrates that in metaphase the direct phosphorylation of NuMA by Aurora-A controls its cortical enrichment, and that this is the major event underlying the spindle orientation functions of Aurora-A in transformed and non-transformed cells in culture. Phosphorylation of NuMA by Aurora-A does not affect its affinity for microtubules or for LGN but rather determines the mobility of the protein at the spindle poles. The finding that NuMA can associate concomitantly with LGN and microtubules suggests that its microtubule-binding activity contributes to anchor Dynein-loaded microtubule +TIPs at cortical sites with LGN.

INTRODUCTION

The organization and functions of the mitotic spindle are essential for proper execution of mitosis. Sophisticated mechanisms ensure the formation of a bipolar spindle with highly dynamic properties. In addition, regulatory networks operate to properly position the spindle within the cell. Coupling of the mitotic spindle axis with cell polarity is particularly relevant in mitotic epithelial cells during morphogenesis and regeneration, because it defines the position of the cell division plane [1, 2]. Intrinsic mechanisms of spindle placement are active also in adherent cells in culture to stabilize the spindle before anaphase onset [3]. Spindle placement is achieved by recruitment of microtubule motors at cortical domains in conjunction with membrane-associated proteins. The core constituents of these force-generating machines are trimeric complexes formed by the nuclear mitotic apparatus protein NuMA, the switch molecule LGN, and the Gαi subunit of heterotrimeric G-proteins, all of which are found conserved from nematodes to mammals [3, 4].

NuMA is a master regulator of spindle functions, implicated not only in spindle placement, but also in spindle organization and maintenance [5]. Consistent with these two activities, in mitotic HeLa cells NuMA localizes both at spindle poles and at cortical regions above the poles [6]. NuMA operates in large multiprotein complexes mainly as an adaptor of the microtubule motor Dynein/Dynactin, to which it binds with its N-terminal domain [7]. Depending on the cellular context, the C-terminal portion has been reported to associate with LGN [8], Eg5 [9], cortical 4.1R/G [10, 11], and also directly with microtubules [8, 12] and the plasma membrane [13, 14]. During spindle assembly, the interaction of NuMA with Dynein/Dynactin promotes microtubule tethering to the poles and aster focusing [15–17]. In metaphase, binding of NuMA to Dynein/Dynactin is essential for the recruitment of Dynein to the cortex, where it exerts minus-end directed pulling forces on astral microtubules in order to position the spindle [6, 7]. To coordinate spindle functions with cell-cycle progression, the mitotic activities of NuMA must be tightly controlled in time and space. At mitotic entry, NuMA localization and activities respond to mitotic Ran^{GTP} signaling [18], and to several phosphorylation events. From prometaphase to metaphase, the phosphorylation of NuMA on Thr2055 by CDK1 negatively regulates the direct association of the protein to the plasma membrane [11, 14, 19]. Experiments in HeLa cells revealed that the activity of Plk1 at the poles assists spindle centering by decreasing the affinity of NuMA for Dynein/Dynactin [6], while phosphorylation of NuMA by Abl1 is required to couple the spindle axis with NuMA:LGN cortical crescents [20]. Studies in *C. elegans* embryos showed that

the phosphorylation of the NuMA-related LIN-5 protein by aPKC reduces microtubule-pulling forces at the anterior site to promote asymmetric spindle positioning [21]. Recently, in vitro studies and proteomic screenings identified NuMA among the substrates of Aurora-A [22, 23]. However, whether these putative phosphosites affect spindle alignment is currently unexplored.

The Aurora-A kinase governs spindle assembly [24]. In human cells, its activity orchestrates the organization of the spindle poles by influencing microtubule nucleation and dynamics [25–29]. Historically, key functions of Aurora-A in spindle alignment and maintenance of self-renewing have been documented in *Drosophila* SOP cells and neuroblasts, mainly by regulation of the Par3/Par6/aPKC activity [30, 31]. In the same systems, Aurora-A has been shown to promote spindle orientation by phosphorylating LGN/Pins, this way favoring its association with cortical Dlg [32]. Whether Aurora-A can contribute in flies or vertebrates to spindle orientation in other ways is an interesting open issue. More indirect evidence of the involvement of Aurora-A in spindle alignment came from overexpression studies in mammary stem cells [33] and colon cancer cells [34]. Recently, partial inhibition of Aurora-A with low doses of the chemical inhibitor MLN8237 has been reported to induce misorientation of cell division in human U2OS cells in culture [35].

Based on the common functions of Aurora-A and NuMA in orienting cell divisions, and on their colocalization at the spindle poles, we set out to address whether and how Aurora-A could influence the spindle orientation activities of NuMA directly. In this study, we demonstrate that in metaphase Aurora-A controls the recruitment of NuMA/Dynein at the cortex by direct phosphorylation of NuMA, and that this event recapitulates the spindle orientation activities of Aurora-A in transformed and non-transformed cells in culture. In addition, we identify a new microtubule-binding domain of NuMA, which is not required for spindle pole targeting but might secure NuMA/Dynein complexes to the cortex together with LGN.

RESULTS

Reduced Aurora-A Activity Results in Spindle Misorientation in HeLa and hTERT-RPE-1 Cells

Under conditions of complete Aurora-A inactivation, cells are strongly delayed in prometaphase with highly disorganized spindles, thus precluding the possibility of studying the role of the kinase in spindle orientation. However, partial inhibition of Aurora-A by low doses of MLN8237 has been shown to cause spindle misorientation in cultured cells without preventing mitotic progression [35]. Thus, to investigate the molecular events underlying the spindle orientation functions of Aurora-A, we established conditions to inactivate the kinase in HeLa cells to an extent that still allows a fraction of mitoses to form a bipolar spindle and congress chromosomes in a metaphase plate.

Preliminary setup experiments indicated that in HeLa cells 50 nM MLN8237 are required to inactivate partially Aurora-A (Figure 1A, left panel; Figure S1A), leaving the activity of Aurora-B unaffected (Figure S1A). Importantly, under these conditions, about 30% of mitoses assembled a bipolar spindle and formed a metaphase plate (Figures S1A and S1B). Depletion of Aurora-A by small-RNA interfering (RNAi) oligos in HeLa cells or treatment of hTERT-RPE-1 cells with 100 nM MLN8237 results in an analogous Aurora-A inactivation, with a good proportion of metaphases (Figures 1A, S1C, and S1D). Thus, we set out to use these MLN8237 and RNAi conditions to study the spindle orientation functions of Aurora-A in cultured cells.

Time-lapse video-recording analyses of HeLa and hTERT-RPE-1 cells under the partial Aurora-A inhibiting conditions established above revealed that between 15% and 30% of bipolar divisions were misoriented, with the two forming daughters partially overlapping rather than being adjacent (Figures 1B and 1C; Movies S1 and S2). We ruled out that misoriented divisions occurred as a result of delayed anaphase onset by assessing the correct orientation of HeLa cultures slowed by MG132 treatment/release (Figure S1E). Measuring of the spindle axis angles with respect to the substrate in fixed cells plated on fibronectin-coated coverslips showed that the phenotype observed upon partial Aurora-A inhibition reflected a misorientation of the mitotic spindle in metaphase (Figure 1D). The orientation defect observed upon partial Aurora-A inactivation is comparable to the one reported for NuMA and LGN ablation [7], although less penetrant than the misorientation resulting from β1-integrin loss [36].

These results indicate that either partially depleting or chemically inactivating Aurora-A in human cultured cells alters the orientation of the mitotic spindle and results in misoriented divisions.

Aurora-A Activity Is Required for the Correct Distribution of NuMA in Metaphase Cells

In order to investigate whether the misorientation phenotype observed upon Aurora-A inactivation reflected defects in the localization of the main players of the spindle orientation pathway, we analyzed the distribution of LGN, NuMA, and the Dynactin subunit $p150^{Glued}$ by immunofluorescence (Figures 2 and S2). LGN distribution at the cell cortex was comparable in control and MLN8237-treated HeLa metaphases (Figure 2A). Conversely, upon Aurora-A inhibition NuMA was clearly displaced from the cortex, and concomitantly accumulated at the spindle poles (Figures 2B and S2B). A similar relocalization was observed for $p150^{Glued}$ in MLN8237-treated HeLa cells, although to a lower extent (Figure S2A). Quantitative image analyses (see Supplemental Experimental Procedures for details) demonstrated that treatment with 50 nM MLN8237 induces a 6-fold enrichment of NuMA at spindle poles, and a concomitant loss of its cortical signal (Figures 2B and S2B). Comparable results were obtained following RNAi-mediated Aurora-A inactivation (Figures 2C and S2B, lower panels), as well as in MLN8237-treated (100 nM) hTERT-RPE-1 metaphases (Figures 2D and S2C), indicating that Aurora-A activity is required for the correct localization of NuMA in mitosis. Consistent with this idea, transient overexpression of a kinase inactive Aurora-A mutant induced partial relocalization of NuMA from the cell cortex to spindle poles, a phenotype that is consistent with a dominant-negative effect (Figure S2D).

Based on the observed perturbation of the mitotic distribution of NuMA, we reasoned that, when Aurora-A activity is lowered, NuMA is somehow trapped at spindle poles, thus depleting the cytosolic fraction able to reach the cortex. To test this

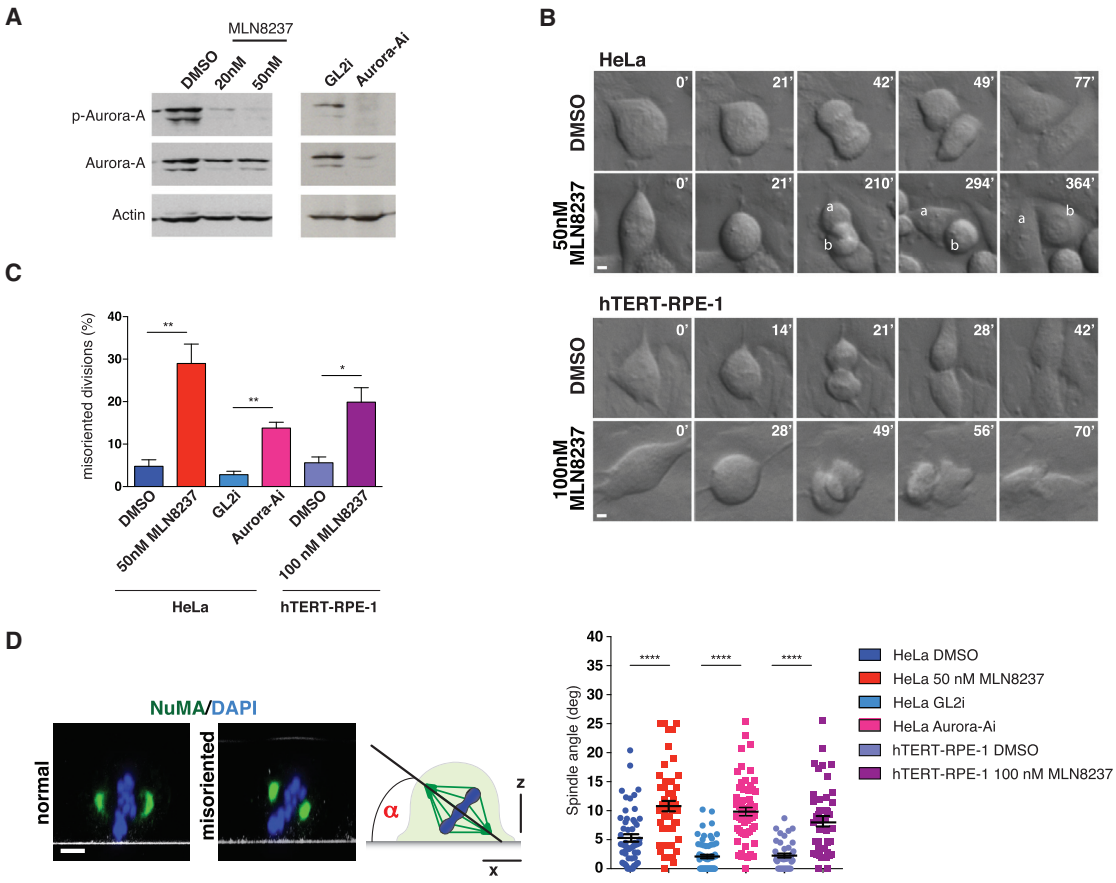

Figure 1. Aurora-A Is Required for the Correct Orientation of the Mitotic Spindle

(A) Immunoblotting of phospho-Thr-288-Aurora-A (p-Aurora-A) and Aurora-A in mitotic extracts of HeLa cells treated with DMSO or MLN8237 (left) or interfered (right) for luciferase (GL2i) or Aurora-A (Aurora-Ai). Actin was used as loading control.

(B) Still frames from time-lapse video recording of HeLa and hTERT-RPE-1 cells dividing parallel to the substrate when treated with DMSO (top rows) or misoriented in presence of MLN8237 (bottom rows). Minutes from the round-up are indicated on top-right corner of each frame. *a* and *b* mark daughters derived from the filmed division. Scale bars, 5 μm.

(C) Quantification (%) of the occurrence of the phenotype shown in B in HeLa (DMSO or 50 nM MLN8237; GL2i or Aurora-Ai) and hTERT-RPE-1 (DMSO or 100 nM MLN8237) cells. Means ± SEM are shown. Analyzed bipolar mitoses: n > 150 for all conditions, from three independent experiments. **p < 0.01 and *p < 0.05 by unpaired t test.

(D) Left: representative confocal z-sections of metaphase HeLa cells treated with DMSO or 50 nM MLN8237 stained for NuMA (green) and DAPI (blue). In the sections, the plane of the coverslip is visible as a white line. Scale bar, 5 μm. A schematic representation of the mitotic spindle angle measured is also shown. Right: scatterplots illustrate the distribution of the angle measured between the spindle axis and the plane of the coverslip in cells treated as in (C). Means ± SEM are shown; n > 40 from three independent experiments by Mann-Whitney test. ****p < 0.0001. See also Figure S1.

hypothesis, we measured the mobility of transiently transfected GFP-NuMA at the spindle poles by fluorescence recovery after photobleaching (FRAP) analysis in control or MLN8237-treated mitotic HeLa cells (Figure 2E). The half-time for the recovery ($t_{1/2}$) of the fluorescence signal after photobleaching in unperturbed conditions was about 50 s, confirming the existence of a mobile fraction of NuMA at spindle poles previously reported [11, 37]. In Aurora-A-inhibited cells, the half-time for the recovery significantly increased compared to untreated cells, and concomitantly the fluorescence intensity at plateau diminished indicating a reduction of the mobile fraction of NuMA at the poles from 60 to about 40%. Together these data indicate that the activity of Aurora-A controls the mobility of NuMA at spindle poles, establishing the correct dynamic exchange between the polar and cortical pools of NuMA.

Loss of Cortical NuMA Causes Spindle Misorientation in Aurora-A-Inhibited Cells

In mitosis, NuMA is the molecular connection between the microtubule motor Dynein and cortical receptors formed by LGN:Gαi complexes [7]. The evidence that MLN8237 treatment causes loss of NuMA from the cortical sites leaving LGN unperturbed prompted us to investigate whether ectopic targeting of NuMA at the membrane could bypass the requirement of Aurora-A for spindle orientation. To address this possibility, we generated a chimeric protein (Figure 3A) carrying the GoLoco region of LGN, encompassing residues 359–677, fused C-terminally to GFP-NuMA (GFP-NuMA-GoLoco hereon) [6]. We first tested the localization of GFP-NuMA-GoLoco in mitotic HeLa cells upon transient transfection. In metaphase, the chimera was recruited in a cortical belt at the plasma membrane at higher levels than

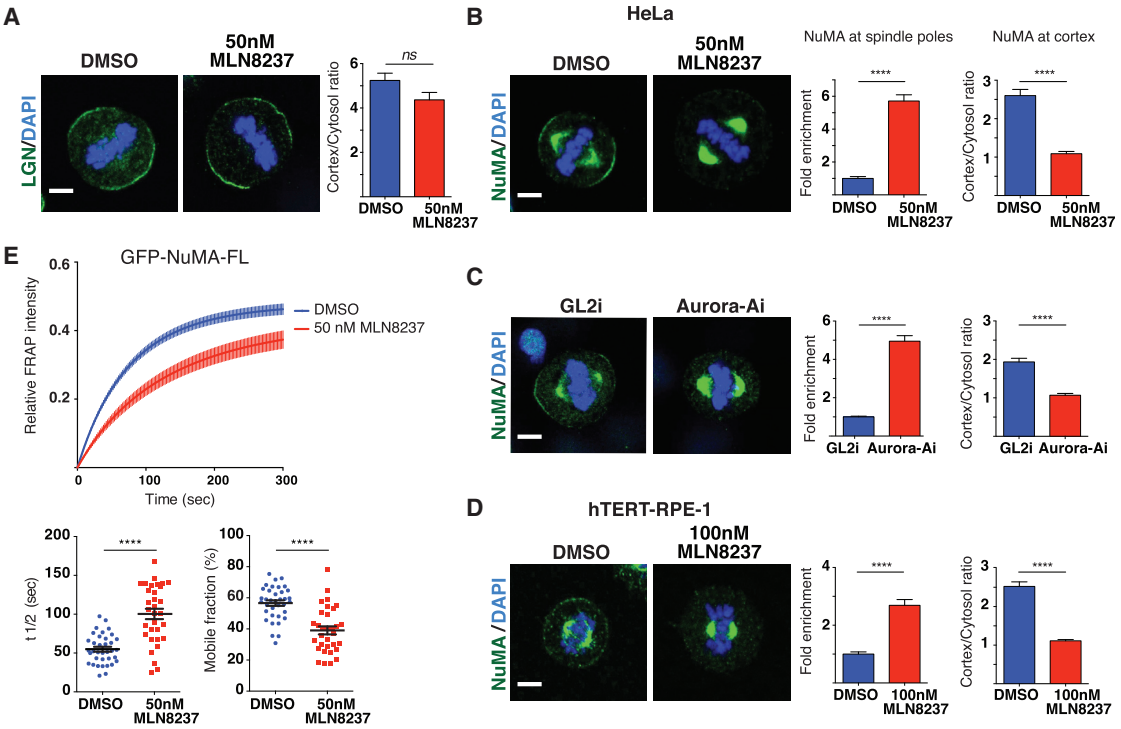

Figure 2. Aurora-A Inhibition Perturbs the Localization of NuMA in Metaphase

(A) Immunofluorescence analysis of endogenous LGN (green) in HeLa cells treated with DMSO or MLN8237. Histograms represent the LGN cortical-to-cytosol fluorescence ratio (means ± SEM; n > 30 from three independent experiments). *ns*, non-significant statistical difference by Mann-Whitney test.

(B) Immunofluorescence analysis of endogenous NuMA (green) in HeLa cells treated with DMSO or MLN8237. Histograms show the quantification of the signal intensity at the spindle poles as fold change relative to control (means ± SEM; n > 40 from three independent experiments) and the cortex-to-cytosol fluorescence ratio (means ± SEM; n > 30 from three independent experiments).

(C) Analysis as in (B) of endogenous NuMA in control GL2- (GL2i) or Aurora-A-interfered (Aurora-Ai) HeLa cells. n > 50 for polar NuMA and n > 40 for cortical NuMA, from three independent experiments.

(D) Immunofluorescence analysis of endogenous NuMA in hTERT-RPE-1 cells treated with DMSO or MLN8237. Levels of NuMA at the spindle poles and at the cortex are quantified as in (B) from three independent experiments with n > 40, for both cortical and polar NuMA.

(E) FRAP analysis in HeLa cells of full-length GFP-NuMA in the presence of DMSO or MLN8237. Recovery profiles of bleached GFP spindle poles signal are plotted over 5 min (top). The dot plots (bottom) show the distribution of $t_{1/2}$ (s) and the mobile fraction (%) of GFP-NuMA at the spindle poles (means ± SEM; n > 40 from three independent experiments).

****p < 0.0001 by Mann-Whitney test in (B)–(D) and by unpaired t test in (E). Scale bars, 5 μm. See also Figure S2.

GFP-NuMA, while it displayed a weaker localization at the spindle poles (Figure 3B). Upon MLN8237 treatment, GFP-NuMA-GoLoco accumulated at the spindle poles as observed for GFP-NuMA and for the endogenous protein (Figure 2); however, a pool of the protein was still visible at the cortex (Figure 3B). To evaluate the orientation of cell divisions in GFP-NuMA-GoLoco-expressing cells treated with MLN8237, we monitored the position of the spindle poles (detected by GFP signal) and of the forming daughters (monitored by differential interference contrast [DIC]) in video-recording time-lapse experiments (Figure 3C; Movies S3 and S4) and compared them with the divisions of GFP-NuMA-expressing cells. As expected, a large fraction of cells transfected with GFP-NuMA misaligned the spindle when treated with MLN8237. Conversely, the percentage of misoriented divisions of cells expressing GFP-NuMA-GoLoco did not increase upon MLN8237 addition (Figure 3D). We also observed that expression of GFP-NuMA-GoLoco per se tended to enhance the number of misoriented cells compared to GFP-NuMA (shown by the "DMSO" columns in the histograms of Figure 3D). We speculate that this phenotype might be caused by enhanced targeting of NuMA to the cortex by the GoLoco domain. Notably, the presence of GFP-NuMA-GoLoco also partially rescued the mitotic delay induced by MLN8237 treatment (Figure 3C) [35]. Collectively, these results demonstrate that loss of NuMA is the major molecular determinant for the misorientation phenotype observed upon Aurora-A inhibition.

The Distribution of NuMA in Metaphase Is Regulated by Direct Aurora-A Phosphorylation

To gain a mechanistic understanding of the events underlying the NuMA-dependent spindle misorientation phenotype observed upon Aurora-A inhibition, we set out to test the hypothesis that direct phosphorylation of NuMA by Aurora-A governs its mitotic distribution. We decided to start our analysis using a C-terminal fragment of NuMA spanning residues 1821–2115 (referred to as $NuMA^{Cter}$ hereon), which starts right after the coiled-coil region, is unable to dimerize, and contains Aurora-A phosphosites identified previously [22] (Figure 4A). We purified

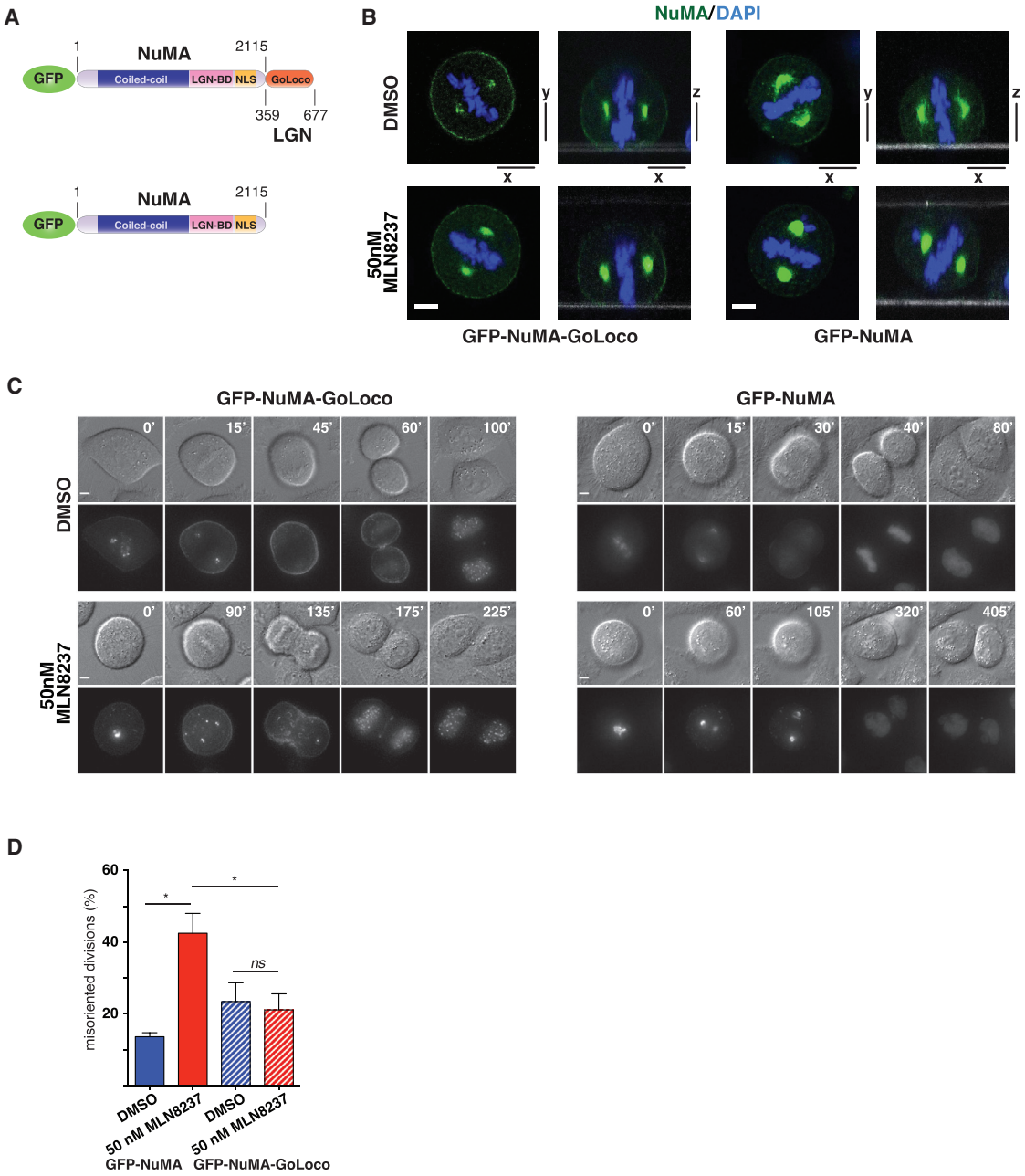

Figure 3. Ectopic Targeting of NuMA at the Cortex Rescues the MLN8237-Induced Misorientation Phenotype

(A) Schematic representation of GFP-NuMA full-length and GFP-NuMA-GoLoco.

(B) Confocal x-y and x-z sections of HeLa cells transfected with GFP-NuMA-GoLoco and GFP-NuMA in presence of DMSO (top) or MLN8237 (bottom). NuMA is visualized by GFP signal and DNA by DAPI. Scale bars, 5 μm.

(C) DIC (top) and GFP-fluorescent (bottom) images from time-lapse video recording of mitotic HeLa cells expressing GFP-NuMA-GoLoco or GFP-NuMA and treated with DMSO or MLN8237. Minutes from the round-up are indicated. Scale bars, 5 μm.

(D) Quantification (%) of misoriented bipolar divisions of HeLa cells treated as in (C) (means ± SEM; for all conditions n > 45 from three independent experiments). *$p < 0.05$; ns, non-significant statistical difference by unpaired t test.

NuMA^{Cter} from bacterial sources and performed an in vitro kinase assay. Upon incubation with purified Aurora-A, NuMA^{Cter} displayed three phosphorylated species, which disappeared in the presence of MLN8237 (Figure 4B). In line with previous findings [22], mass spectrometry analysis of the phosphorylated bands established that the phosphorylation occurred on three serine residues of NuMA^{Cter} conforming to the Aurora-A consensus site, namely, Ser1969, Ser1991, and Ser2047 (Figure 4A). Consistently, alanine substitution of these three serines abrogated phosphorylation of NuMA^{Cter} (Figure 4B), confirming that in vitro Aurora-A phosphorylates NuMA^{Cter} on Ser1969, 1991, and 2047.

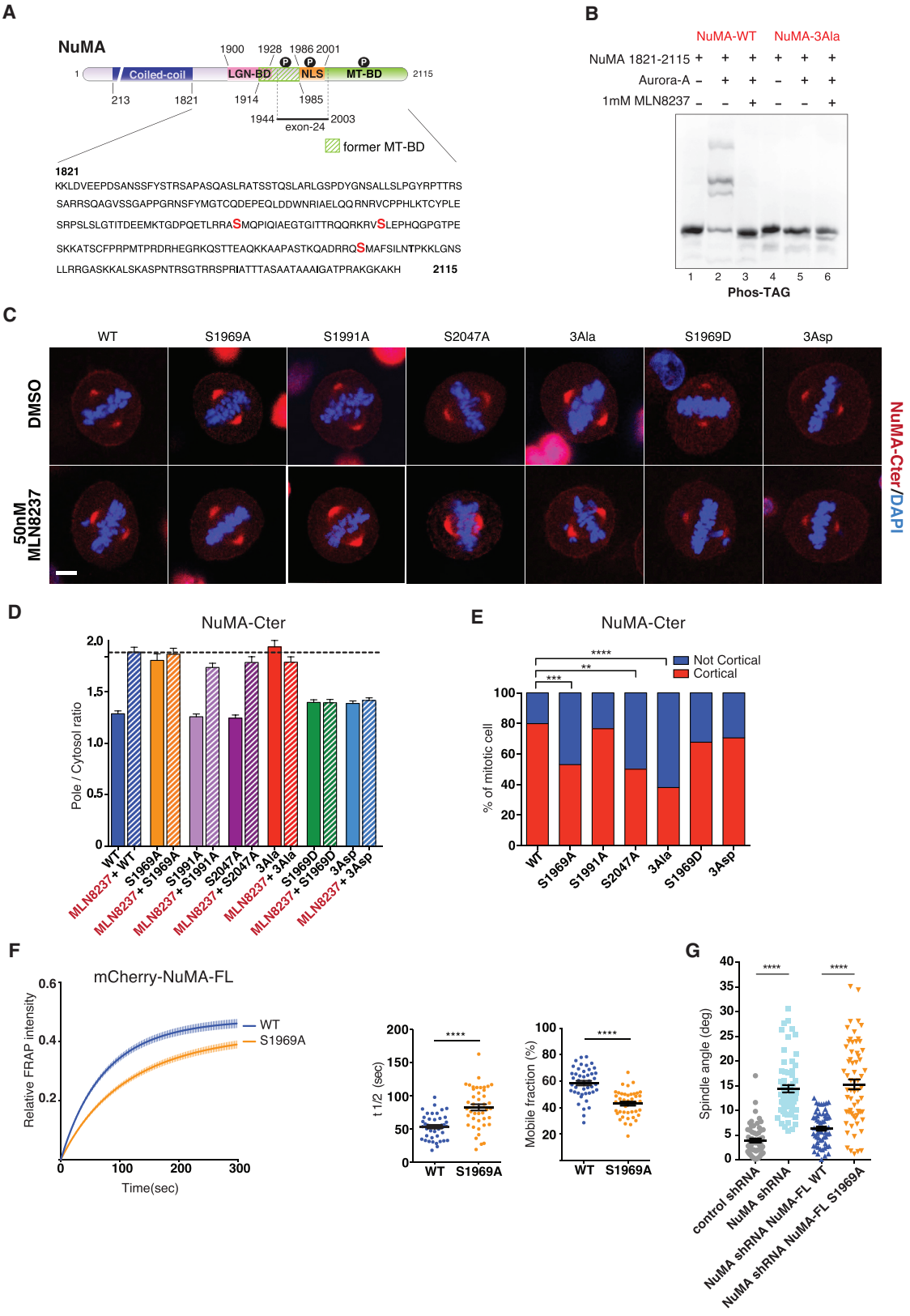

Figure 4. Direct Phosphorylation of the C-Terminal Region of NuMA by Aurora-A Influences NuMA Localization in Metaphase

(A) Schematic representation of the domain structure of NuMA, enlarged on the C-terminal portion spanning residues 1821–2115 (NuMA^{Cter} in the text and below). Fragments with known functions are highlighted with different colors including the LGN-binding domain (residues 1900–1928, pink), the *old* MT-binding domain

(legend continued on next page)

To explore the physiological relevance of the identified phosphosites in mitosis, we generated HeLa cell lines stably expressing mCherry-tagged NuMA^{Cter} wild-type or mutated either to alanines or to aspartic acids in the three serine phosphosites, singularly or in combination. Immunoblot analysis of the lysates confirmed that all cell lines expressed equal amounts of NuMA^{Cter}, and that the overexpression levels of the C-terminal fragments driven by Ubc promoter were of the same order of magnitude of endogenous NuMA (Figure S3A). We then analyzed the mitotic distribution of mCherry-NuMA^{Cter} mutants in unperturbed cells and in cells treated with 50 nM MLN8237 (Figure 4C). In metaphase, wild-type NuMA^{Cter} localized at the spindle poles, where it accumulated aberrantly upon Aurora-A inhibition (Figures 4C and 4D), mirroring what observed for the endogenous protein (Figure 2). A similar behavior was observed with the NuMA^{Cter}-Ser1991-Ala and NuMA^{Cter}-Ser2047-Ala mutants. Interestingly, substitution of Ser1969 with Ala sufficed to determine the constitutive enrichment of NuMA^{Cter} at the spindle poles, as efficiently as the 3Ala mutant, and both mutants became insensitive to MLN8237 treatment. Conversely, phosphomimetic replacement of Ser1969 with aspartic acid, alone or in combination with Ser1991-Asp and Ser2047-Asp mutations (3 Asp), resulted in NuMA^{Cter} mutant proteins localizing at the spindle poles as the wild-type, but unable to enrich upon MLN8237 treatment. These results suggested that Ser1969^{NuMA} plays a pivotal role in determining the levels of NuMA^{Cter} at the spindle poles. We reasoned Ser1969^{NuMA} could work as a priming site to allow the subsequent phosphorylation of Ser1991 and Ser2047. To test this possibility, we compared the kinetics of phosphorylation in vitro of NuMA^{Cter} wild-type and NuMA^{Cter}-Ser1969-Ala and found that they were unchanged (Figure S3B), indicating that no priming occurs. Thus, we conclude that the polar accumulation of NuMA^{Cter} observed in metaphase upon MLN8237 treatment mirrors the redistribution previously described for endogenous NuMA under the same conditions (Figure 2), and that the major determinant is the Aurora-A phosphosite Ser1969.

Beside polar accumulation, inhibition of Aurora-A prevents cortical targeting of NuMA (Figure 2). To assess whether the three phosphosites identified above impact on the cortical recruitment of NuMA, we analyzed the cortical enrichment of mCherry-tagged NuMA^{Cter} mutants (Figure S3C). Since the low expression levels of cell lines stably expressing mCherry-NuMA^{Cter} mutants did not allow a reliable quantification of cortical signals, we resorted to transiently transfect the same constructs in HeLa cells and monitor the presence of cortical mCherry fluorescence (Figure S3C). Single substitutions of Ser1969 and Ser2047 to Ala reduced NuMA^{Cter} localization at the plasma membrane to the same extent observed for the combined mutation of the three phosphosites to alanine, whereas replacement of Ser1969 with Asp, alone or together with Ser1991-Asp and Ser2047-Asp, did not alter significantly cortical NuMA^{Cter} levels (Figure 4E).

To address the relevance of Ser1969^{NuMA} phosphorylation by Aurora-A in the context of the full-length protein, we first generated a HeLa cell line stably depleted of NuMA by infection with a short-hairpin RNA (shRNA) targeting human NuMA (Figure S3D). We then used this cell line to study the mobility and orientation functions of a sh-resistant mCherry-NuMA^{S1969A} mutant. Upon photobleaching, the mCherry signal of wild-type NuMA recovered with rates undistinguishable from GFP-NuMA transfected in HeLa cells, whereas the Ser1969Ala-mutated protein displayed slower recovery rates (Figure 4F). Most notably, the mobility of the Ser1969Ala mutant mirrors the one of the wild-type protein in cells treated with 50 nM MLN8237 (cf. Figures 4F and 2E). We conclude that the phosphorylation of Ser1969^{NuMA} sets the correct cycling rates of the protein at the spindle poles in metaphase.

Based on the FRAP analysis, we asked whether the reduced spindle pole mobility of the NuMA^{S1969A} phosphomutant could recapitulate the spindle misorientation phenotype occurring upon Aurora-A inhibition. Spindle angle analysis revealed that transfected mCherry-NuMA^{WT} rescues almost completely the spindle alignment defects of NuMA-depleted cells, whereas NuMA^{S1969A} does not (Figures 4G and S3E).

Collectively, these results indicate that NuMA is a direct substrate of Aurora-A, and that in metaphase the specific phosphorylation of the Ser1969^{NuMA} prevents aberrant accumulation of the protein at the spindle poles allowing its membrane targeting at the cortex, this way promoting correct spindle orientation.

Binding of NuMA to Microtubules Is Independent of Aurora-A

The evidence that Aurora-A inhibition leads to accumulation of NuMA at the spindle poles indicates that a receptor for NuMA

(residues 1914–1985, dashed green) and the nuclear localization signal (NLS, residues 1986–2001, orange). The MT-binding domain identified in this study encompassing residues 2002–2115 is in green. In the primary sequence of NuMA^{Cter}, the Aurora-A phospho-serines Ser1969, Ser1991 and Ser2047 are in red.

(B) Coomassie-blue-stained Phos-TAG SDS-PAGE of the in vitro kinase assay performed with the purified kinase domain of Aurora-A and NuMA^{Cter} wild-type (NuMA-WT) or with Ser1969, Ser1991, and Ser2047 mutated into alanine (NuMA-3Ala). Samples in lanes 3 and 6 contained MLN8237 in the reaction buffer. The purified NuMA^{Cter} samples used as substrates are loaded in lanes 1 and 4 as controls.

(C) Confocal images of metaphase HeLa cells stably expressing mCherry-NuMA^{Cter} wild-type or the following mutants: S1969A/D, S1991A, S2047A, S1969-S1991-S2047 mutated into alanine (3Ala) or aspartic acid (3Asp). Representative images from cultures treated with DMSO (top) or 50 nM MLN8237 (bottom) are shown. Scale bar, 5 μm.

(D) Quantification of the mCherry fluorescence ratio between poles and cytosol in the experimental conditions of (C) (means ± SEM; n > 20 from three independent experiments).

(E) Analysis of the mCherry signal at the cortex in metaphase HeLa cells expressing mCherry-NuMA^{Cter} mutants. The percentage of cells displaying cortical mCherry signal is plotted in red (n > 40 from three independent experiments) ****p < 0.0001, ***p < 0.001, and **p < 0.01 by Fisher's exact test.

(F) FRAP analysis in NuMA-ablated HeLa cells transiently transfected with full-length mCherry-NuMA wild-type or S1969A mutant. Recovery profiles of bleached mCherry spindle poles signal plotted over 5 min (left). Dot plots (right) show the distribution of $t_{1/2}$ (s) and the mobile fraction (%) of mCherry-NuMA proteins at the spindle poles (means ± SEM; n > 44 from three independent experiments). ****p < 0.0001 by unpaired t test.

(G) Quantification of mitotic spindle angle of NuMA-depleted HeLa cells transiently transfected with full-length mCherry-NuMA wild-type or S1969A mutant. Means ± SEM; n > 50 from three independent experiments. ****p < 0.0001 by Kruskal-Wallis test. See also Figure S3.

exists at the spindle poles, whose affinity is modulated by the activity of the kinase. The major phosphosite that influences the mobility of NuMA at the poles in MLN8237-treated cells, Ser1969^{NuMA}, lies in the region that was previously shown to bind directly microtubules (see Figure 4A). Thus, we set out to test whether the phosphorylation of NuMA by Aurora-A could affect its affinity for microtubules. Cosedimentation of purified NuMA^{Cter} with taxol-stabilized microtubules revealed that phosphorylation by Aurora-A or replacement of the three serine phosphosites with Asp did not alter the binding affinity of NuMA^{Cter} for microtubules in vitro (Figure 5A). Cosedimentation of mCherry-NuMA^{Cter} from mitotic lysates with increasing concentrations of microtubules confirmed that, under the same conditions used for the studies in cells, Aurora-A inhibition did not alter the affinity of NuMA^{Cter} for microtubules (Figure 5B).

Dimeric constructs of NuMA encompassing the microtubule-binding domain (MT-binding in the following) have been recently shown to bundle microtubules [38]. To assess whether this activity could be modulated by Aurora-A, we generated dimeric GST-fusion proteins of NuMA^{Cter} and two complementary subdomains spanning residues 1821–2001 and 2002–2115, respectively. The ability of the fusion proteins to stabilize and bundle microtubules was tested in a microtubule formation assay. Regardless of Aurora-A phosphorylation, both NuMA^{Cter} and NuMA$^{2002–2115}$ proteins bundled efficiently microtubules, whereas NuMA$^{1821–2001}$ induced only polymerization of short microtubules, similarly to the GST control (Figures 5C and S4A). These results confirmed that Aurora-A does not impair the microtubule association properties of NuMA. They were also unexpected since the NuMA fragment 1821–2001 containing the previously mapped MT-binding domain did not affect microtubule organization. Cosedimentation experiments with the three C-terminal NuMA fragments used in the microtubule bundling assay revealed that NuMA$^{2002–2115}$ cosediments with microtubules as the entire NuMA^{Cter}, while NuMA$^{1821–2001}$ does not (Figure 5D).

We next tested whether microtubule binding was implicated in the localization of NuMA at the spindle poles. To this aim, we generated three NuMA constructs encompassing the old MT-binding domain (NuMA$^{1821–2002}$), the newly identified MT-binding domain (NuMA^{Cter}Δexon-24), or both (NuMA^{Cter}) (see scheme in Figure 4A), and tested their ability to localize at the spindle poles when transfected in HeLa cells. In metaphase, mCherry-NuMA$^{1821–2002}$ localized at the spindle poles almost to the same extent of NuMA^{Cter} (Figure 5E, left and central panels), indicating that direct microtubule binding is not required for the recruitment of NuMA at the spindle poles. Conversely, ablation of the fragment 1943–2004, corresponding to exon 24 of human NuMA (exon 22 of mouse NuMA [17]), resulted in a NuMA^{Cter} deletion mutant largely impaired in pole targeting (Figure 5E, right panel).

The newly discovered MT-binding domain of NuMA lies downstream of the LGN-binding stretch, spanning residues 1900–1928 (Figure 4A), rather than overlapping with it as previously believed. This observation opens the possibility that a single molecule of NuMA forms a complex with both LGN and microtubules. To test this hypothesis, we cosedimented microtubules with NuMA fragments containing only the LGN-binding region (NuMA$^{1821–2001}$), the MT-binding domain (NuMA$^{2002–2115}$), or both (NuMA^{Cter}) in the presence of equimolar amounts of the TPR domain of LGN (LGN^{TPR} in the following). In line with our expectations, only the entire NuMA^{Cter} was found in the microtubule pellet fraction with LGN^{TPR} (Figure 5F). Binding assays conducted with GST-LGN^{TPR} adsorbed on beads and phosphorylated NuMA^{Cter} in solution revealed that Aurora-A does not enhance the affinity of NuMA for LGN (Figure S4B).

In summary, our analyses revealed that (1) the phosphorylation of Aurora-A on NuMA^{Cter} does not alter the microtubule organizing activity of NuMA or its binding to LGN; (2) the fragment of NuMA spanning residues 2002–2115 contains a MT-binding domain, while residues 1821–2001 are not involved in microtubule binding; and (3) NuMA^{Cter} can associate simultaneously with LGN and microtubules.

DISCUSSION

Aurora kinases are master regulators of mitosis involved in spindle assembly and positioning. Here, we report that the direct phosphorylation of NuMA by Aurora-A on Ser1969 and Ser2047 regulates its cortical recruitment in metaphase, and in this way the correct orientation of the mitotic spindle of adherent cells in culture. In addition, we identify a new MT-binding domain on the C-terminal portion of NuMA, which is dispensable for the localization of the protein at the spindle poles and is compatible with its association to LGN, suggesting a role in spindle positioning.

Aurora-A has been implicated in orienting symmetric and asymmetric divisions from nematodes to mammals [1, 2, 33, 35]. In asymmetric divisions of *Drosophila* neuroblasts, Aurora-A controls the establishment of apico-basal polarity by phosphorylating Lgl [39–41], this way affecting indirectly also spindle positioning. Our studies reveal that the kinase activity of Aurora-A controls spindle alignment of unpolarized cells by governing the distribution of NuMA in metaphase. Partial ablation or chemical inhibition of Aurora-A in metaphase causes excessive accumulation of NuMA at the spindle poles, thus preventing its cortical recruitment with LGN. Ectopic targeting of NuMA at the cortex by chimeric fusion of the GoLoco domain of LGN at the C terminus of the protein restores almost completely the alignment defects observed in MLN8237-treated HeLa cells, demonstrating that in this system the recruitment of NuMA at the cortex in metaphase is required and sufficient to align the spindle parallel to the substratum.

Studies in fly neuroblasts suggested that Aurora-A promotes spindle alignment by phosphorylating Pins/LGN on a conserved Ser residue in the linker region between the TPR domain and the GoLoco motifs [32]. Phosphorylation of this Ser residue seems to play a role for spindle orientation also in MDCK cysts [42] and neuroepithelial cells [43], although it is not clear whether in vertebrate LGN is a direct substrate of Aurora-A. Under the conditions of partial Aurora-A inhibition that we used for our studies, we did not observe a significant reduction in the levels of cortical LGN in metaphase. We conclude that in HeLa cells, cortical targeting of LGN is less sensitive than NuMA's one to the kinase activity of Aurora-A. Whether this behavior holds true in proliferating tissues remains an interesting open question.

Aurora-A inhibition results in aberrant accumulation of NuMA at the spindle poles accompanied by reduced mobility, implying that in normal conditions the affinity of NuMA for spindle pole components is diminished by Aurora-A phosphorylation. The

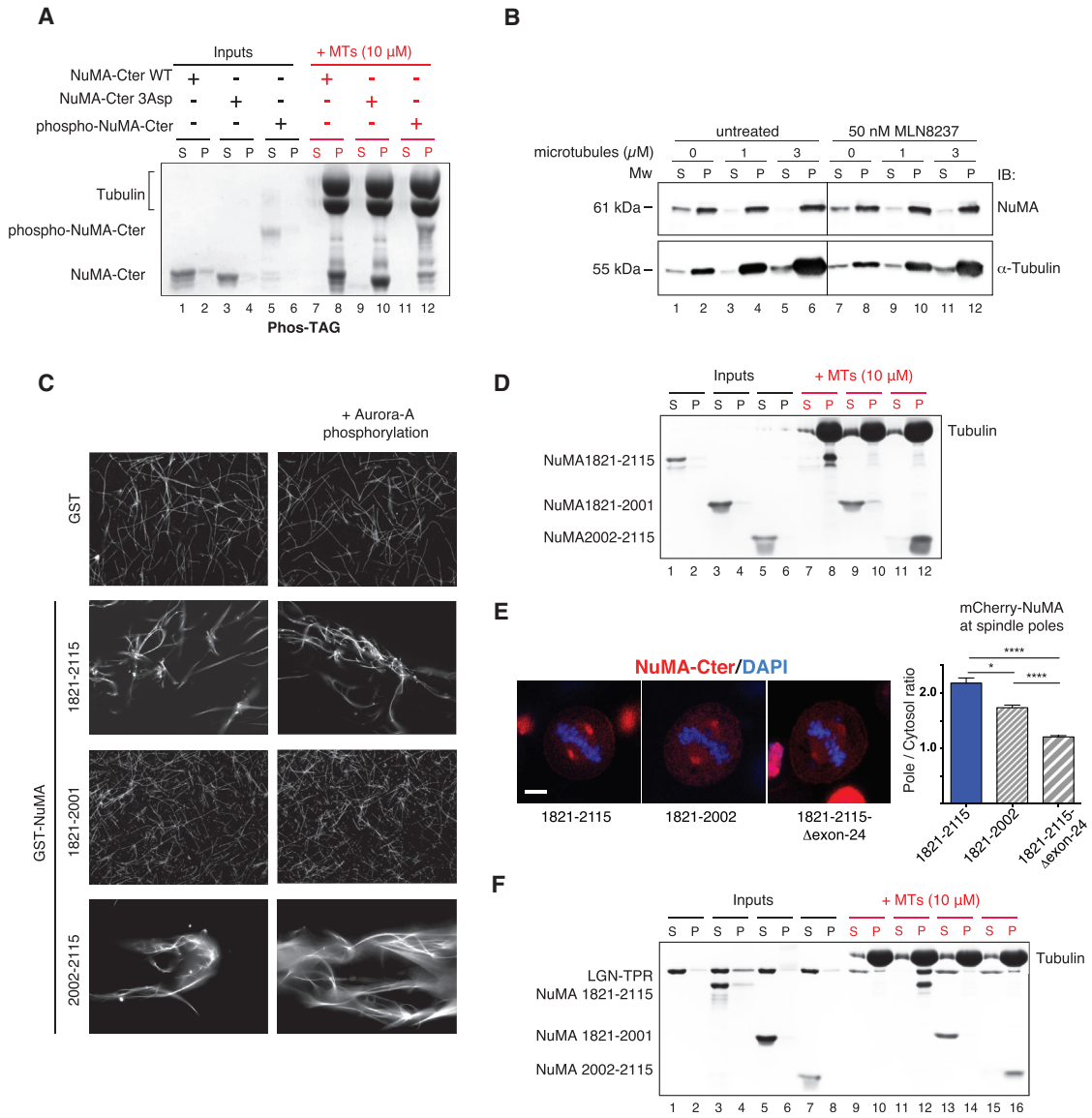

Figure 5. Direct Binding of NuMA to Microtubules Occurs through a Region Downstream of the LGN-Binding Domain and Is Not Affected by Aurora-A Phosphorylation

(A) Cosedimentation of 2 µM NuMA^{Cter} with polymeric tubulin (MTs). Wild-type NuMA^{Cter} unmodified or phosphorylated by Aurora-A, and NuMA^{Cter}-3Asp (S1969-S1991-S2047 replaced with Asp) were tested. The supernatant (S) and pellet (P) fractions were analyzed on a Phos-TAG SDS-PAGE followed by Coomassie staining (lanes 7–12). The solubility of NuMA^{Cter} in the absence of microtubules was also tested (lanes 1–6).

(B) Lysates of prometaphase-arrested mCherry-NuMA^{Cter}–expressing HeLa cells were cosedimented with increasing amounts of exogenous microtubules. The microtubule binding ability of mCherry-NuMA^{Cter} was assessed in untreated (lanes 1–6) and 50 nM MLN8237-treated (lanes 7–12) lysates. NuMA^{Cter} and microtubules in the pellet (P) and supernatant (S) fractions were detected by immunoblotting using anti-NuMA and anti-α-tubulin antibodies.

(C) Representative images of in vitro microtubule bundling assays performed with rhodamine-labeled tubulin in the presence of GST-NuMA$^{1821–2115}$, GST-NuMA$^{1821–2001}$, and GST-NuMA$^{2002–2115}$, or GST as control. Experiments were performed both with unmodified (left panels) and phosphorylated NuMA fragments (right panels and Figure S4A).

(D) Cosedimentation of NuMA^{Cter} fragments with polymeric tubulin (MTs), performed as in (A).

(E) Confocal sections of metaphase HeLa cells transiently expressing the entire mCherry-NuMA^{Cter} (residues 1821–2115) or its deletions Δ2003–2115 and Δ1944–2003 (Δexon-24). Histograms represent the quantification of the mCherry signal at the spindle poles with respect to cytoplasm (means ± SEM; n > 30 from three independent experiments). ****p < 0.0001 and *p < 0.05 by Kruskal-Wallis test. Scale bar, 5 µm.

(F) Microtubule cosedimentation assays conducted as in (D) in the presence of 1 µM LGN^{TPR}.

See also Figure S4.

evidence that in MLN8237-treated cells the monomeric C-terminal construct of NuMA, spanning residues 1821–2115, exhibits the same polar enrichment displayed by endogenous NuMA allowed us to use this construct to dissect the effects of Aurora-A on NuMA at a molecular scale, both in vivo and in vitro. In line with previous proteomic data [22], we showed

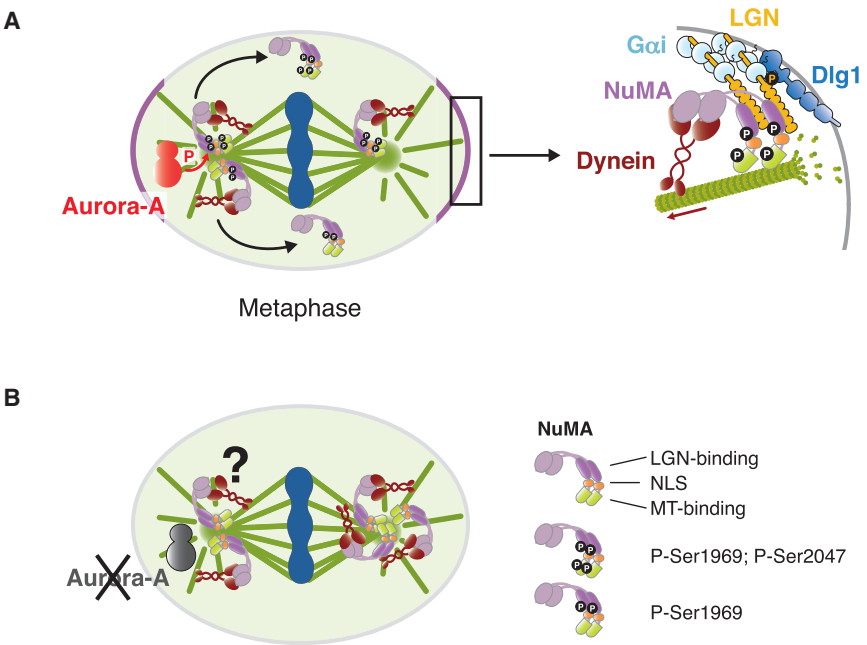

Figure 6. Schematic Representation of the Role of Aurora-A in Regulating the Distribution of NuMA in Metaphase

(A) In unperturbed conditions, Aurora-A at the spindle poles phosphorylates NuMA on Ser1969 and Ser2047 enhancing its mobility and allowing a pool of NuMA to reach the polar regions of the cortex above the spindle poles (left panel). The receptor for NuMA at the cortex is LGN, which, in turn, is recruited to the plasma membrane by interaction with four Gαi moieties anchored to the lipid bilayer via myristoyl groups. Phosphorylated LGN is further secured to the membrane by interaction with Dlg1. The N terminus of NuMA associates with Dynein/Dynactin, while the C-terminal portion binds concomitantly to LGN and to microtubules, this way stabilizing the contacts between the Dynein/Dynactin motors and the depolymerizing microtubule lattice (right panel).

(B) Aurora-A inhibition results in aberrant accumulation of unphosphorylated NuMA at the spindle poles, and simultaneous loss of NuMA from the cortex. The receptor of NuMA at the spindle poles whose affinity is reduced by Aurora-A phosphorylation is still unknown (indicated as a question mark).

that in vitro Aurora-A phosphorylates NuMA on Ser1969, Ser1991, and Ser2047 and demonstrated that the Ser1969 phosphosite is the determinant of the polar accumulation of NuMA observed in the presence of MLN8237. In particular, we found that replacement of Ser1969 with Ala on NuMA^{Cter} recapitulates the enrichment at the poles observed upon Aurora-A inhibition, whereas substitution of Ser2047 with Ala influences only cortical recruitment. In NuMA-ablated cells, the same Ser1969Ala substitution on full-length NuMA reduces the mobility of the protein at the spindle poles and impairs its spindle orientation functions. We propose that in metaphase the two phosphosites Ser1969 and Ser2047 synergize to guarantee the correct distribution of NuMA between poles and cortex (Figure 6). These results somehow differ from what reported by Kettenbach and colleagues on the distribution of the NuMA-Ser1969Glu mutant [22], likely because their analyses were conducted with full-length NuMA able to dimerize with the endogenous protein.

In mitosis Aurora-A controls the polar levels of p150^{Glued}, the Dynactin subunit implicated in spindle organization, by direct phosphorylation on Ser19 [44]. The finding that NuMA^{Cter} enriches at the spindle poles upon Aurora-A inhibition despite being unable to interact with Dynein/Dynactin [7] suggests that Aurora-A can coordinate activities of NuMA and Dynactin at the spindle pole independently and synergically. Conversely, the Aurora-A-mediated loss of Dynactin from the cortex (Figure S2) likely reflects the lack of cortical NuMA.

The evidence that the phosphosite playing a prominent role in setting normal amounts of NuMA at the spindle poles, Ser1969, lies in a fragment that was previously implicated in microtubule binding prompted us to test the idea that Aurora-A could regulate the interaction between NuMA and microtubules. Microtubule cosedimentation and forming assays revealed that the kinase activity of Aurora-A does not influence the affinity of NuMA for microtubules or its microtubule organizing ability. Most importantly these analyses led to the identification of a new MT-binding domain of NuMA contained in the fragment 2002–2115. Regardless of Aurora-A activity, we also found that the association of NuMA^{Cter} with microtubules is not essential for targeting of the protein to the spindle poles, hinting at the possibility that the direct association of NuMA to microtubules is important in processes other than spindle pole assembly [17]. The finding that the newly discovered MT-binding domain is compatible with the concomitant binding of NuMA to LGN and microtubules suggests that it can sustain spindle orientation. We propose that this MT-binding domain of NuMA works at the cortex, to stabilize the interaction between LGN-engaged NuMA molecules and microtubule +TIPs, this way assisting the Dynein-mediated sliding of cortical LGN:NuMA complexes along the depolymerizing microtubules (Figure 6). This hypothesis is consistent with the propensity of the MT-binding activity of NuMA to promote minus-end directed movements [38].

In developing tissues, the coordination of the spindle axis with respect to cortical polarity is a prerequisite for asymmetric cell divisions because it defines the unequal segregation of fate determinants and niche contacts [45, 46]. In the majority of the asymmetrically dividing systems analyzed so far, in metaphase NuMA polarizes at the apical site above one of the spindle poles [11, 47–50] and promotes spindle alignment along the apico-basal axis (or anterior-posterior axis in *C. elegans* zygotes) [51]. Therefore, our findings bear major implications in the context of vertebrate stem cell divisions. We believe that the relevance of the Aurora-A/NuMA pathway in the self-renewal of embryonic and adult stem cells will be an exciting direction for future experiments.

EXPERIMENTAL PROCEDURES

Plasmids and Small Interfering Oligonucleotides

Full-length cDNA encoding NuMA (NCBI Reference Sequence: NM_006185) was subcloned in a pCDH vector with an N-terminal GFP or mCherry tag, under the control of a weak Ubc promoter (System Biosciences, CD615B). For

the construction of pCDH-GFP-NuMA-GoLoco, the GoLoco domain of LGN encompassing residues 359–677 was first amplified by PCR and then subcloned into a pCDH-GFP-NuMA vector at the C terminus of NuMA. The NuMA C-terminal fragments encompassing residues 1821–2115 (referred to as $NuMA^{Cter}$ in the text), residues 1821–2002, and the $NuMA^{Cter}$-Δ1944–2003 ($NuMA^{Cter}$-Δexon-24 in the text) were inserted into a pCDH lentiviral vector fused to a mCherry tag. For biochemical assays, $NuMA^{Cter}$, NuMA-1821–2001, and NuMA-2002–2115 were cloned in pETM14, while LGN-1-409 (LGN^{TPR}) was cloned in pGEX6P1. All point mutations were generated with the QuikChange mutagenesis kit (Stratagene) according to the manufacturer's guidelines. All constructs were sequence verified. The sense sequences of the small interfering RNA (siRNA) (Applied Biosystems/Ambion) targeting Aurora-A and luciferase (GL2) are 5′AUGCCCUGUCUUACUGUCAdTdT3′ and 5′CGUACGCGGAAUACUUCGAdTdT3′.

Additional detailed methodological information can be found in the Supplemental Experimental Procedures.

SUPPLEMENTAL INFORMATION

Supplemental Information includes Supplemental Experimental Procedures, four figures, and four movies and can be found with this article online at http://dx.doi.org/10.1016/j.cub.2015.12.051.

AUTHOR CONTRIBUTIONS

Conceptualization, M.M. and G.G.; Methodology, E.M. and A.O.; Investigation, S.G., M.C., F.D.M., L.P., and I.A.A.; Writing, M.M. and G.G.; Funding Acquisition, M.M. and G.G.

ACKNOWLEDGMENTS

We are grateful to Dario Parazzoli of the Cogentech Facility and the Nikon Reference Centre at IBPM for imaging experiments. We thank all members of the M.M. and G.G. labs, Giorgio Scita, Stefano Santaguida, Anna De Antoni, and Patrizia Lavia for scientific discussions and careful reading of the manuscript. This work is supported by the Italian Association for Cancer Research (AIRC IG-12877 and MFAG-13350), the Italian Ministry of Health, CNR-InterOmics Flagship Project - grant IBISA, and PNR-CNR Aging Program 2012-2014. I.A.A. was supported by a Fondazione Umberto Veronesi fellowship.

Received: September 4, 2015
Revised: November 30, 2015
Accepted: December 16, 2015
Published: January 28, 2016

REFERENCES

1. Morin, X., and Bellaïche, Y. (2011). Mitotic spindle orientation in asymmetric and symmetric cell divisions during animal development. Dev. Cell *21*, 102–119.
2. Gillies, T.E., and Cabernard, C. (2011). Cell division orientation in animals. Curr. Biol. *21*, R599–R609.
3. Kotak, S., and Gönczy, P. (2013). Mechanisms of spindle positioning: cortical force generators in the limelight. Curr. Opin. Cell Biol. *25*, 741–748.
4. Du, Q., and Macara, I.G. (2004). Mammalian Pins is a conformational switch that links NuMA to heterotrimeric G proteins. Cell *119*, 503–516.
5. Radulescu, A.E., and Cleveland, D.W. (2010). NuMA after 30 years: the matrix revisited. Trends Cell Biol. *20*, 214–222.
6. Kiyomitsu, T., and Cheeseman, I.M. (2012). Chromosome- and spindle-pole-derived signals generate an intrinsic code for spindle position and orientation. Nat. Cell Biol. *14*, 311–317.
7. Kotak, S., Busso, C., and Gönczy, P. (2012). Cortical dynein is critical for proper spindle positioning in human cells. J. Cell Biol. *199*, 97–110.
8. Du, Q., Stukenberg, P.T., and Macara, I.G. (2001). A mammalian Partner of inscuteable binds NuMA and regulates mitotic spindle organization. Nat. Cell Biol. *3*, 1069–1075.
9. Iwakiri, Y., Kamakura, S., Hayase, J., and Sumimoto, H. (2013). Interaction of NuMA protein with the kinesin Eg5: its possible role in bipolar spindle assembly and chromosome alignment. Biochem. J. *451*, 195–204.
10. Kiyomitsu, T., and Cheeseman, I.M. (2013). Cortical dynein and asymmetric membrane elongation coordinately position the spindle in anaphase. Cell *154*, 391–402.
11. Seldin, L., Poulson, N.D., Foote, H.P., and Lechler, T. (2013). NuMA localization, stability, and function in spindle orientation involve 4.1 and Cdk1 interactions. Mol. Biol. Cell *24*, 3651–3662.
12. Haren, L., and Merdes, A. (2002). Direct binding of NuMA to tubulin is mediated by a novel sequence motif in the tail domain that bundles and stabilizes microtubules. J. Cell Sci. *115*, 1815–1824.
13. Kotak, S., and Gönczy, P. (2014). NuMA phosphorylation dictates dynein-dependent spindle positioning. Cell Cycle *13*, 177–178.
14. Zheng, Z., Wan, Q., Meixiong, G., and Du, Q. (2014). Cell cycle-regulated membrane binding of NuMA contributes to efficient anaphase chromosome separation. Mol. Biol. Cell *25*, 606–619.
15. Gaglio, T., Saredi, A., and Compton, D.A. (1995). NuMA is required for the organization of microtubules into aster-like mitotic arrays. J. Cell Biol. *131*, 693–708.
16. Merdes, A., Heald, R., Samejima, K., Earnshaw, W.C., and Cleveland, D.W. (2000). Formation of spindle poles by dynein/dynactin-dependent transport of NuMA. J. Cell Biol. *149*, 851–862.
17. Silk, A.D., Holland, A.J., and Cleveland, D.W. (2009). Requirements for NuMA in maintenance and establishment of mammalian spindle poles. J. Cell Biol. *184*, 677–690.
18. Wiese, C., Wilde, A., Moore, M.S., Adam, S.A., Merdes, A., and Zheng, Y. (2001). Role of importin-beta in coupling Ran to downstream targets in microtubule assembly. Science *291*, 653–656.
19. Kotak, S., Busso, C., and Gönczy, P. (2013). NuMA phosphorylation by CDK1 couples mitotic progression with cortical dynein function. EMBO J. *32*, 2517–2529.
20. Matsumura, S., Hamasaki, M., Yamamoto, T., Ebisuya, M., Sato, M., Nishida, E., and Toyoshima, F. (2012). ABL1 regulates spindle orientation in adherent cells and mammalian skin. Nat. Commun. *3*, 626.
21. Galli, M., Muñoz, J., Portegijs, V., Boxem, M., Grill, S.W., Heck, A.J., and van den Heuvel, S. (2011). aPKC phosphorylates NuMA-related LIN-5 to position the mitotic spindle during asymmetric division. Nat. Cell Biol. *13*, 1132–1138.
22. Kettenbach, A.N., Schweppe, D.K., Faherty, B.K., Pechenick, D., Pletnev, A.A., and Gerber, S.A. (2011). Quantitative phosphoproteomics identifies substrates and functional modules of Aurora and Polo-like kinase activities in mitotic cells. Sci. Signal. *4*, rs5.
23. Toughiri, R., Li, X., Du, Q., and Bieberich, C.J. (2013). Phosphorylation of NuMA by Aurora-A kinase in PC-3 prostate cancer cells affects proliferation, survival, and interphase NuMA localization. J. Cell. Biochem. *114*, 823–830.
24. Nikonova, A.S., Astsaturov, I., Serebriiskii, I.G., Dunbrack, R.L., Jr., and Golemis, E.A. (2013). Aurora A kinase (AURKA) in normal and pathological cell division. Cell. Mol. Life Sci. *70*, 661–687.
25. Hirota, T., Kunitoku, N., Sasayama, T., Marumoto, T., Zhang, D., Nitta, M., Hatakeyama, K., and Saya, H. (2003). Aurora-A and an interacting activator, the LIM protein Ajuba, are required for mitotic commitment in human cells. Cell *114*, 585–598.
26. Marumoto, T., Honda, S., Hara, T., Nitta, M., Hirota, T., Kohmura, E., and Saya, H. (2003). Aurora-A kinase maintains the fidelity of early and late mitotic events in HeLa cells. J. Biol. Chem. *278*, 51786–51795.
27. Burgess, S.G., Peset, I., Joseph, N., Cavazza, T., Vernos, I., Pfuhl, M., Gergely, F., and Bayliss, R. (2015). Aurora-A-Dependent Control of TACC3 Influences the Rate of Mitotic Spindle Assembly. PLoS Genet. *11*, e1005345.
28. De Luca, M., Brunetto, L., Asteriti, I.A., Giubettini, M., Lavia, P., and Guarguaglini, G. (2008). Aurora-A and ch-TOG act in a common pathway in control of spindle pole integrity. Oncogene *27*, 6539–6549.

29. Asteriti, I.A., Giubettini, M., Lavia, P., and Guarguaglini, G. (2011). Aurora-A inactivation causes mitotic spindle pole fragmentation by unbalancing microtubule-generated forces. Mol. Cancer *10*, 131.
30. Wang, H., Somers, G.W., Bashirullah, A., Heberlein, U., Yu, F., and Chia, W. (2006). Aurora-A acts as a tumor suppressor and regulates self-renewal of *Drosophila* neuroblasts. Genes Dev. *20*, 3453–3463.
31. Lee, C.Y., Andersen, R.O., Cabernard, C., Manning, L., Tran, K.D., Lanskey, M.J., Bashirullah, A., and Doe, C.Q. (2006). *Drosophila* Aurora-A kinase inhibits neuroblast self-renewal by regulating aPKC/Numb cortical polarity and spindle orientation. Genes Dev. *20*, 3464–3474.
32. Johnston, C.A., Hirono, K., Prehoda, K.E., and Doe, C.Q. (2009). Identification of an Aurora-A/PinsLINKER/Dlg spindle orientation pathway using induced cell polarity in S2 cells. Cell *138*, 1150–1163.
33. Regan, J.L., Sourisseau, T., Soady, K., Kendrick, H., McCarthy, A., Tang, C., Brennan, K., Linardopoulos, S., White, D.E., and Smalley, M.J. (2013). Aurora A kinase regulates mammary epithelial cell fate by determining mitotic spindle orientation in a Notch-dependent manner. Cell Rep. *4*, 110–123.
34. Ertych, N., Stolz, A., Stenzinger, A., Weichert, W., Kaulfuß, S., Burfeind, P., Aigner, A., Wordeman, L., and Bastians, H. (2014). Increased microtubule assembly rates influence chromosomal instability in colorectal cancer cells. Nat. Cell Biol. *16*, 779–791.
35. Asteriti, I.A., Di Cesare, E., De Mattia, F., Hilsenstein, V., Neumann, B., Cundari, E., Lavia, P., and Guarguaglini, G. (2014). The Aurora-A inhibitor MLN8237 affects multiple mitotic processes and induces dose-dependent mitotic abnormalities and aneuploidy. Oncotarget *5*, 6229–6242.
36. Toyoshima, F., and Nishida, E. (2007). Integrin-mediated adhesion orients the spindle parallel to the substratum in an EB1- and myosin X-dependent manner. EMBO J. *26*, 1487–1498.
37. Kisurina-Evgenieva, O., Mack, G., Du, Q., Macara, I., Khodjakov, A., and Compton, D.A. (2004). Multiple mechanisms regulate NuMA dynamics at spindle poles. J. Cell Sci. *117*, 6391–6400.
38. Forth, S., Hsia, K.C., Shimamoto, Y., and Kapoor, T.M. (2014). Asymmetric friction of nonmotor MAPs can lead to their directional motion in active microtubule networks. Cell *157*, 420–432.
39. Bell, G.P., Fletcher, G.C., Brain, R., and Thompson, B.J. (2014). Aurora kinases phosphorylate lgl to induce mitotic spindle orientation in *Drosophila* epithelia. Curr. Biol. *25*, 61–68.
40. Carvalho, C.A., Moreira, S., Ventura, G., Sunkel, C.E., and Morais-de-Sa, E. (2014). Aurora a triggers lgl cortical release during symmetric division to control planar spindle orientation. Curr. Biol. *25*, 53–60.
41. Wirtz-Peitz, F., Nishimura, T., and Knoblich, J.A. (2008). Linking cell cycle to asymmetric division: Aurora-A phosphorylates the Par complex to regulate Numb localization. Cell *135*, 161–173.
42. Hao, Y., Du, Q., Chen, X., Zheng, Z., Balsbaugh, J.L., Maitra, S., Shabanowitz, J., Hunt, D.F., and Macara, I.G. (2010). Par3 controls epithelial spindle orientation by aPKC-mediated phosphorylation of apical Pins. Curr. Biol. *20*, 1809–1818.
43. Saadaoui, M., Machicoane, M., di Pietro, F., Etoc, F., Echard, A., and Morin, X. (2014). Dlg1 controls planar spindle orientation in the neuroepithelium through direct interaction with LGN. J. Cell Biol. *206*, 707–717.
44. Reboutier, D., Troadec, M.B., Cremet, J.Y., Chauvin, L., Guen, V., Salaun, P., and Prigent, C. (2013). Aurora A is involved in central spindle assembly through phosphorylation of Ser 19 in P150Glued. J. Cell Biol. *201*, 65–79.
45. Gönczy, P. (2002). Mechanisms of spindle positioning: focus on flies and worms. Trends Cell Biol. *12*, 332–339.
46. Knoblich, J.A. (2010). Asymmetric cell division: recent developments and their implications for tumour biology. Nat. Rev. Mol. Cell Biol. *11*, 849–860.
47. Lechler, T., and Fuchs, E. (2005). Asymmetric cell divisions promote stratification and differentiation of mammalian skin. Nature *437*, 275–280.
48. Izumi, Y., Ohta, N., Hisata, K., Raabe, T., and Matsuzaki, F. (2006). *Drosophila* Pins-binding protein Mud regulates spindle-polarity coupling and centrosome organization. Nat. Cell Biol. *8*, 586–593.
49. Siller, K.H., Cabernard, C., and Doe, C.Q. (2006). The NuMA-related Mud protein binds Pins and regulates spindle orientation in *Drosophila* neuroblasts. Nat. Cell Biol. *8*, 594–600.
50. Bowman, S.K., Neumüller, R.A., Novatchkova, M., Du, Q., and Knoblich, J.A. (2006). The *Drosophila* NuMA Homolog Mud regulates spindle orientation in asymmetric cell division. Dev. Cell *10*, 731–742.
51. Lorson, M.A., Horvitz, H.R., and van den Heuvel, S. (2000). LIN-5 is a novel component of the spindle apparatus required for chromosome segregation and cleavage plane specification in Caenorhabditis elegans. J. Cell Biol. *148*, 73–86.

Current Biology, Volume *26*

Supplemental Information

NuMA Phosphorylation by Aurora-A Orchestrates Spindle Orientation

Sara Gallini, Manuel Carminati, Fabiola De Mattia, Laura Pirovano, Emanuele Martini, Amanda Oldani, Italia Anna Asteriti, Giulia Guarguaglini, and Marina Mapelli

SUPPLEMENTAL FIGURES

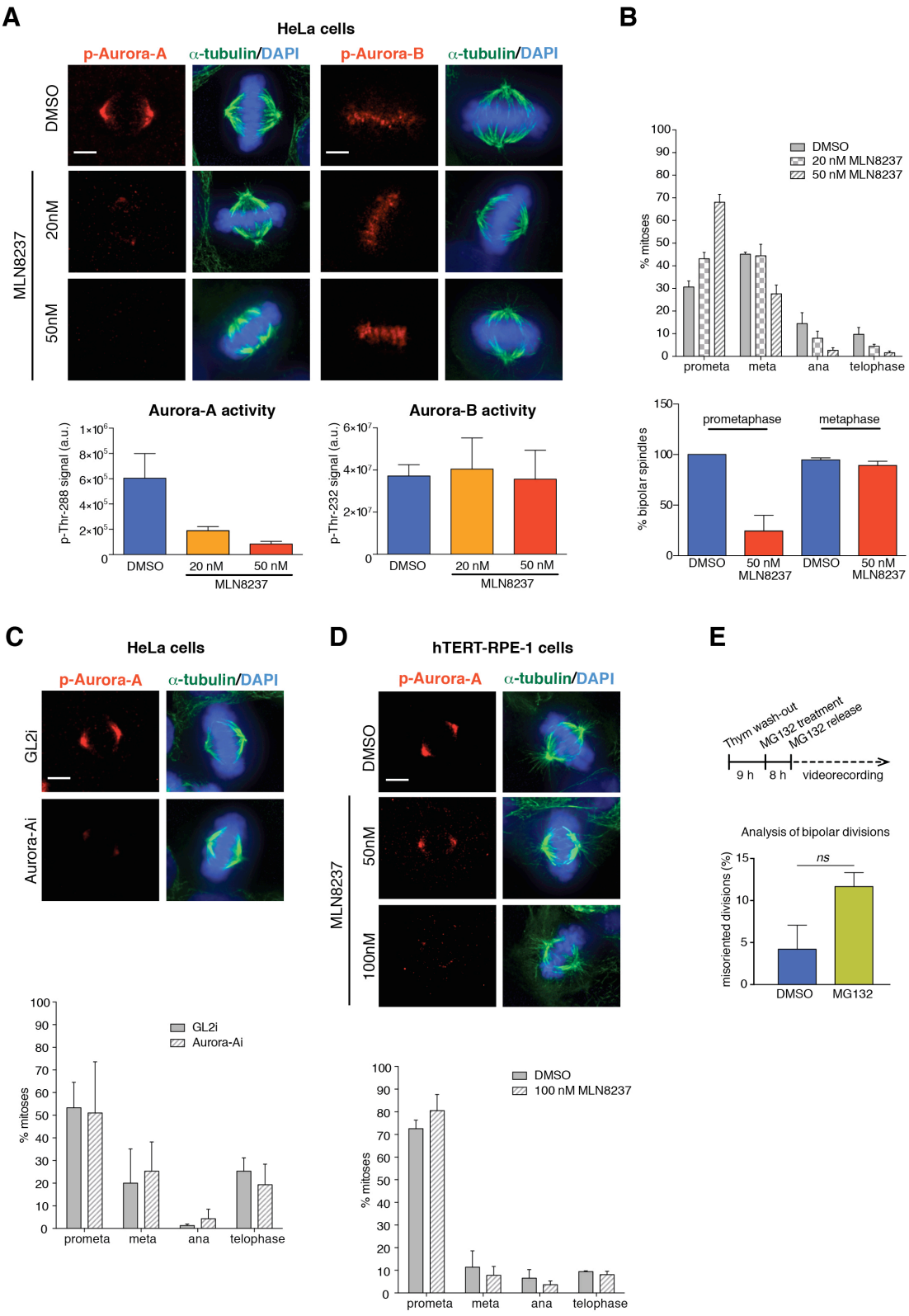

Gallini - Figure S1

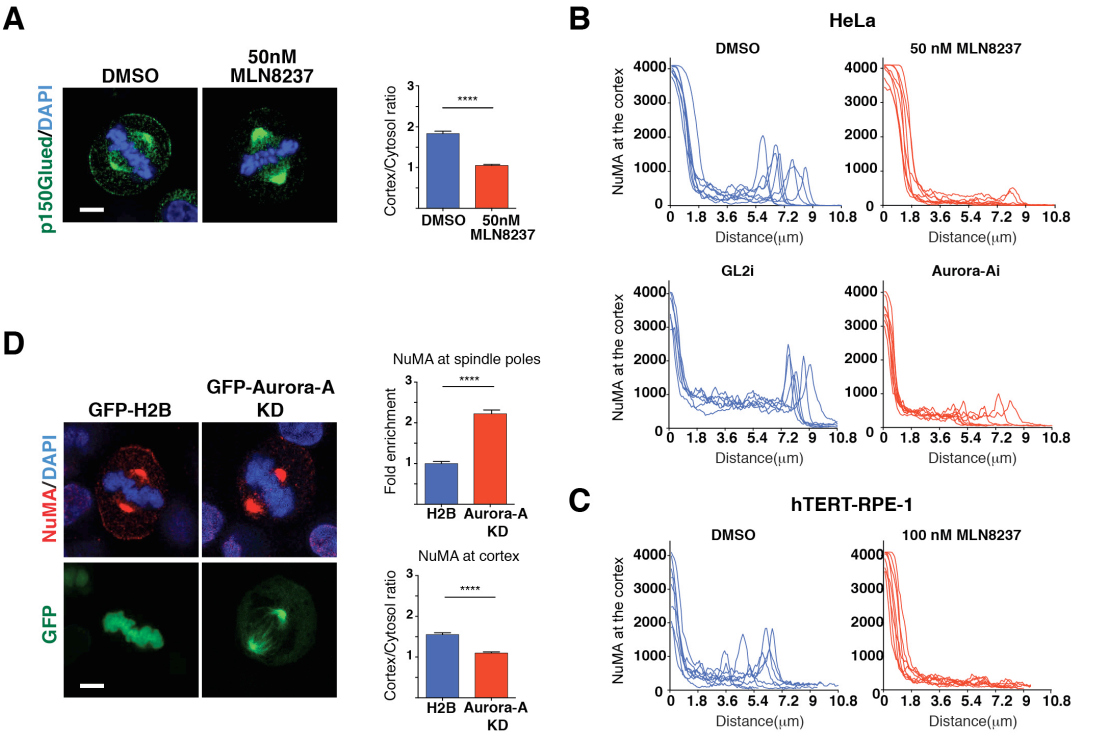

Gallini - Figure S2

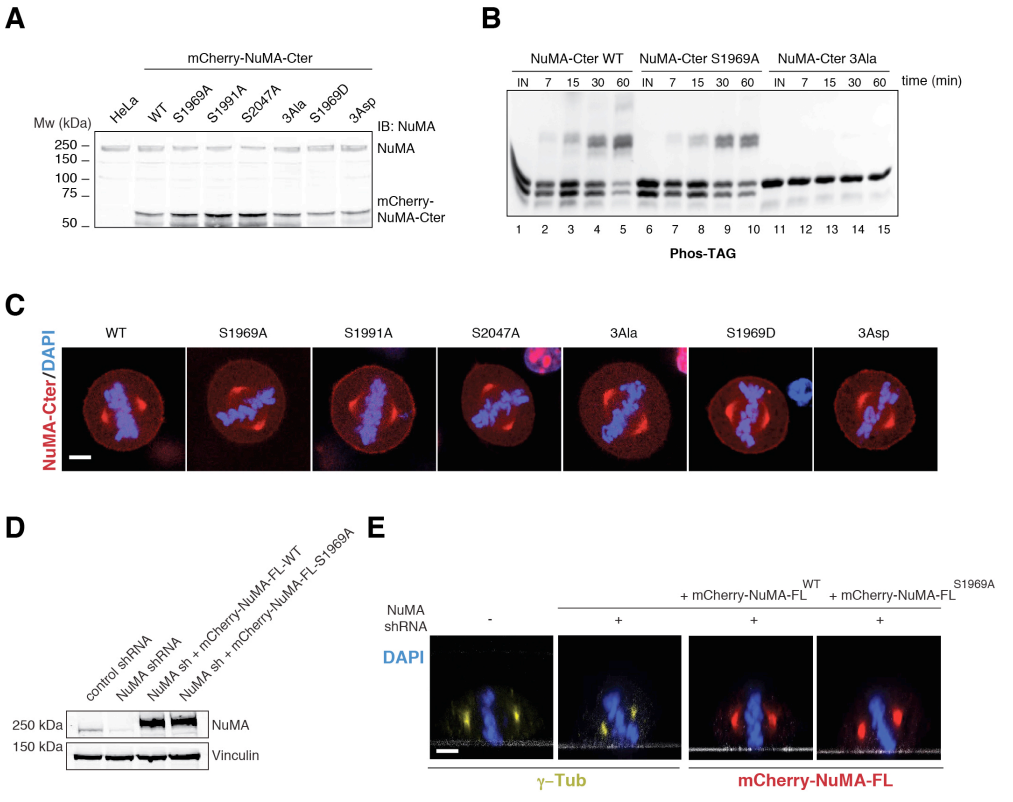

Gallini - Figure S3

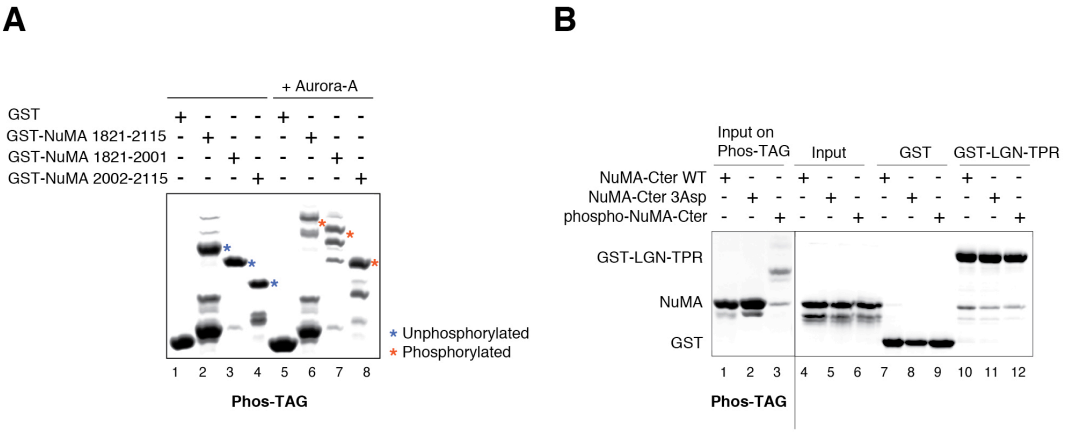

Gallini - Figure S4

SUPPLEMENTAL LEGENDS

Figure S1, Related to Figure 1. Set up of partial Aurora-A inhibition in mitotic HeLa and hTERT-RPE-1 cells. (**A**) Immunofluorescence analysis of phospho-Thr288-Aurora-A (p-Aurora-A, red) or phospho-Thr232-Aurora-B (p-Aurora-B, red) in HeLa cells released from thymidine block and treated with DMSO or MLN8237 (20 nM and 50 nM). The spindle is visualized with α-tubulin (green); DNA is stained with DAPI (blue). Histograms show the intensity values (a.u., arbitrary units) of the signals at the centrosomes (p-Aurora-A) or at the chromosomes (p-Aurora-B) corrected for external background. Means ± SD; n > 70, from three independent experiments. (**B**) Top: histograms (means ± SD) showing the distribution of cells in different mitotic phases in the conditions described above; n > 300 mitoses, from three independent experiments. Bottom: histograms showing the percentage of prometaphases and metaphases with bipolar spindles (means ± SD, n > 100 from three independent experiments). (**C**) Analysis of Aurora-A activity in HeLa cells interfered for Aurora-A. GL2i was used as control. (**D**) Analysis of Aurora-A activity in hTERT-RPE-1 cells treated with DMSO or MLN8237 (100 nM). Cells were stained and analyzed as in A-B. For GL2i/Aurora-Ai: n > 300, from three independent experiments. For hTERT-RPE-1 cells: n > 400, from two independent experiments. Scale bars: 5 μm. (**E**) Time-lapse analysis of MG132-treated HeLa cells. The experimental protocol is shown starting from thymidine wash-out. Only cells that were in prometaphase at the time of MG132 release, and hence had been MG132-delayed, have been analyzed (n > 100 mitotic divisions, from three experiments). Control mitoses (n > 100, from three experiments) were also analyzed. Histograms (mean ± SEM) show the percentage of misoriented bipolar divisions, calculated as in Figure 1C. *n.s.* : non significant; unpaired *t*-test.

Figure S2, Related to Figure 2. Partial inhibition of Aurora-A perturbs the distribution of p150^{Glued} and NuMA in metaphase. (**A**) Immunostaining of p150^{Glued} (green) in HeLa cells treated with DMSO or MLN8237. Histograms represent the p150^{Glued} cortical-to-cytosol fluorescence ratio (means ± SEM; n > 45, from three independent experiments). ****: p < 0.0001 by Mann-Whitney test. (**B**) Representative line-scan profiles of NuMA signal measured from spindle poles to cell cortex in metaphase HeLa cells treated with DMSO or MLN8237 (top row), or interfered for luciferase (GL2i) or Aurora-A (Aurora-Ai)(bottom row). (**C**) Representative line-scan profiles as in (B) of hTERT-RPE-1 cells treated with DMSO or MLN8237. (**D**) Immunofluorescence analysis of endogenous NuMA (red) in HeLa cells transiently transfected with GFP-Aurora-A-D274A (kinase dead, KD, a generous gift of Prof. Erich A. Nigg) or GFP-H2B as control. Histograms represent the quantification of the signal intensity of NuMA at the spindle poles compared to control (means ± SEM; n > 30 from three independent experiments, upper plot), and the cortex-to-cytosol fluorescence ratio (means ± SEM; n >

45 from three independent experiments, bottom plot). ****: $p < 0.0001$ by Mann-Whitney test. All scale bars: 5 μm.

Figure S3, Related to Figure 4. Activity of Aurora-A on the NuMA^{Cter} fragment. (**A**) Anti-NuMA immunoblotting of lysates of HeLa cells wild-type, or stably expressing mCherry-NuMA^{Cter} constructs. (**B**) Time-course of the *in vitro* phosphorylation by Aurora-A of NuMA^{Cter} wild-type, S1969A, or 3Ala. Reactions were stopped at different time points, and analysed by Phos-TAG SDS-PAGE Coomassie-stained. (**C**) Confocal images of metaphase HeLa cells transiently transfected with mCherry-NuMA^{Cter} mutants. The fragments analyzed are wild-type, S1969A/D, S1991A, S2047A, and S1969-S1991-S2047 mutated into alanine (3Ala) or to aspartic acid (3Asp). To visualize NuMA^{Cter} localization at the cortex, images were acquired at saturating conditions of the mCherry-signal at the poles. (**D**) Immunoblot of NuMA-ablated HeLa cells transiently transfected with sh-resistant mCherry-NuMA wild-type or S1969A mutant. Vinculin was used as a loading control. (**E**) Representative confocal z-sections of mitotic HeLa cells stably interfered for NuMA, transfected or not with mCherry-NuMA wild-type or S1969A mutant. Spindle poles were visualized by γ-tubulin (wild-type and sh-NuMA HeLa cells) or mCherry (sh-NuMA HeLa cells expressing mCherry-NuMA wild-type or S1969A mutant). Scale bars: 5 μm.

Figure S4, Related to Figure 5. Aurora-A phosphorylation of NuMA does not influence its binding to LGN. (**A**) Coomassie-stained Phos-TAG SDS-PAGE of the GST-NuMA^{Cter} fragments used in the *in vitro* bundling assays of Figure 5C. Unmodified species are indicated with blue asterisks (lanes 2-4), whereas Aurora-A phosphorylated corresponding bands are marked with red asterisks (lanes 6-8). (**B**) *In vitro* pull-down assay performed with GST-LGN^{TPR} absorbed on glutathione beads and purified NuMA^{Cter} in solution. After washes, species retained on beads were separated by SDS-PAGE and Coomassie-stained. The NuMA^{Cter} samples used in the pull-down experiment were also separately loaded on a Phos-TAG SDS-PAGE to monitor their phosphorylation status (lanes 1-3).

SUPPLEMENTAL EXPERIMENTAL PROCEDURES

Cell culture and drug treatments

HeLa and hTERT-RPE-1 cells were grown at 37 ^{o}C in a 5 % CO_2 atmosphere, in complete Dulbecco's Modified Eagle's Medium (DMEM) or MEM with Earle's Salts/Ham's F12 (1:1) respectively. For all experiments shown, cells were plated on fibronectin-coated coverslip (5 μg/ml, Roche). HeLa cultures for experiments in Figures 1-4 were pre-synchronized by thymidine block/release. The indicated amounts of MLN8237 (Selleck Chemicals) were added to the medium 6 hours after release, and cells were fixed after 9-10 hours from release or video-recorded from the moment of MLN8237 addition. hTERT-RPE-1 cultures were synchronized by 100 μM Monastrol (Biomol International) for 16 hours, with the addition of MLN8237 during the last 2 hours of treatment. After 2 hours of Monastrol wash-out, cells grown in complete medium plus MLN8237 were fixed, or video-recorded from the time of wash-out for the following 24 hours. Only cells entering mitosis after Monastrol-release were analysed. Synchronization of HeLa cells in prometaphase was performed by adding 5 μM STLC (S-trityl-L-cysteine, Sigma) for 16 hours. Mock-treated cultures were incubated with DMSO. MG132 treatment (Santa Cruz Biotechnology, sc-201270, 10 μM) was performed 9 hours after thymidine wash-out, for the following 8 hours. Cultures released in MG132-free medium were video-recorded for the following 12 hours (microscope settings as in Figure 1C). HeLa cell lines stably expressing mCherry-NuMA^{Cter} mutants were generated using the pCDH vector. For knocking-down human NuMA, four unique 29-mer shRNA in lentiviral vectors carrying a GFP reporter and puromycin resistance were tested in HeLa cells (catalogue number TL311065; OriGene Technologies). The most effective hairpin (5'CATTATGATGCCAAGAAGCAGCAGAACCA3') was used to generate a stably interfered HeLa cell line.

Transfection

Transfection was conducted following the manufacture's instruction using either Lipofectamine or Oligofectamine (both from Invitrogen) for plasmids or siRNA, respectively. For spindle orientation rescue experiments, NuMA-ablated HeLa cells were transfected with sh-resistant pCDH-mCherry-NuMA wild-type or S1969A mutant.

Transfected cultures were synchronized and MLN8237 treated as described above. siRNAs were used at 80 nM, and asynchronously growing cultures were fixed 48 hours after transfection. In time-lapse experiments, cultures were video-recorded starting 24 hours after siRNA transfection, for the following 48 hours.

Immunofluorescence

Cells grown on coverslips were fixed as follow: a) −20 °C methanol for 10 minutes to visualize NuMA and $p150^{Glued}$ at the cortex and phospho-Thr288-Aurora-A; b) 4 % paraformaldehyde (PFA) for 10 minutes at room temperature, followed by permeabilization with PBS and 0.1 % Triton X-100 for 5 minutes, to detect NuMA staining at poles, LGN and phospho-Thr232-Aurora-B; c) pre-extraction with PHEM containing 0.3 % Triton X-100 for 4 minutes, followed by 10 minutes in 4 % PFA in PBS and 5 minutes in 0.3 % Triton X-100 (all at room temperature) for NuMA staining in hTERT-RPE1 cells. Cells were blocked with PBS containing 0.05 % Tween 20 and 3 % BSA for one hour, and incubated 1-2 hours with primary antibodies at room temperature. Secondary antibody incubation was carried out for 1 hour at room temperature. Depending on the experiment, cells were stained with a monoclonal mouse antibody anti-LGN (Mapelli lab; 1:5), a monoclonal mouse antibody anti-NuMA (Mapelli lab; 1:3000), anti-$p150^{Glued}$ (BD, 610473, 1:1000), anti-phospho-Thr288-Aurora-A (Cell Signalling, C39D8; 1:100), anti-phospho-Thr232-Aurora-B (BioLegend, Poly6361; 1:50), anti-α-tubulin (Abcam, ab4074; 1:50 or Sigma-Aldrich B-5-1-2; 1:3000), anti-pericentrin (Abcam, ab4448; 2 μg/ml); anti-γ-tubulin (Sigma-Aldrich, GTU-88; 1:1000, or Cy3 conjugated Sigma-Aldrich, C7604; 1:200). DNA was stained with DAPI.

Microscopy on fixed samples

Confocal microscopy was performed on a Leica TCS SP2 AOBS confocal microscope controlled by Leica Confocal Software. For all analysis, a 63x oil-immersion objective lens (HCX Plan-Apochromat 63x N.A. 1.4 Lbd Bl; Leica) was used. Image acquisition conditions were set to remove channel crosstalk, optimizing spectral detection bands, and scanning modalities. Images were processed with the Fiji software [S1]. For Figure S1, widefield microscopy was performed using a Nikon Eclipse 90i microscope equipped with a oil immersion Plan Fluor 100x objective (N.A. 1.3; Nikon) and a Qicam Fast 1394 CCD camera (QImaging). Image acquisition, deconvolution and Extended Depth of Focus on z-serial optical sections were performed using Nis-Elements HC 4.2 (Nikon); images were further processed with Adobe Photoshop CS 8.0.

Spindle orientation analysis

To quantify the spindle tilt, cells were plated on fibronectin. Metaphase fixed cells were imaged in x-z optical sections passing through the spindle poles. Spindle axis angles with respect to the substratum were measured with the angle tool of Fiji. For hTERT-RPE-1 cells, the angle of inclination of the mitotic spindle was also measured using the mathematical formula "arctan(xy/z)", with "xy" being the distance between centrosomes in the maximum intensity projection, and "z" being the distance between centrosomes along the z-axis. For rescue experiments of Figure 4G, only mCherry-NuMA transfected cells with total mCherry intensity lower than $4x10^7$ a.u. were analysed. Statistical analysis of the data was performed in Prism with the Mann-Whitney test.

Measurements of the fluorescence intensity at the spindle poles and at the cortex

To quantify the fluorescence intensity of endogenous NuMA at the spindle poles, the signal of NuMA inside a α-tubulin mask was integrated using the Fiji software. To quantify the levels of mCherry-$NuMA^{Cter}$ at the spindle poles, mCherry signals within a α-tubulin mask were integrated, and compared to the amount of mCherry-$NuMA^{Cter}$ in the cytosol measured by integrating the mCherry signal of the same α-tubulin mask positioned in the cytoplasm area. Quantification of cortical signals of LGN, NuMA and $p150^{Glued}$ were conducted on confocal sections of metaphase cells in Fiji as follows. A 2.7 μm-wide line was manually drawn from the spindle pole to the nearest cellular cortex perpendicularly to the metaphase plate, to obtain the intensity profile of the immunostained proteins along the line. The "protein at the cortex" was calculated by integrating the profile on a 1.35 μm-large area centered at the peak of the profile, whereas the "protein in the cytosol" was quantified by integrating the same area 2.7 μm away from the peak towards the DNA. Statistical analysis of the data was performed in Prism with the Mann-Whitney test. For quantification of Figure 4E, $NuMA^{Cter}$ was classified as *cortical* when the mCherry signal of the "protein at the cortex" was at least 1.3-fold higher than the "protein in the cytosol" signal. Statistical analysis of the data was performed in Prism with the Fisher's exact test.

Time-lapse acquisition and analysis
Misoriented cell divisions of HeLa and hTERT-RPE-1 cells seeded in 4-well micro-slides were analyzed in time-lapse experiments using an Eclipse Ti inverted microscope (Nikon) and a 40x (Plan Fluor, N.A. 0.60, DIC, Nikon) objective. During the whole observation cells were kept in a microscope stage incubator at 37 °C and 5 % CO_2. DIC images were acquired every 7 minutes over 24/48 hours using a DS-Qi1Mc camera and the NIS-Elements AR 3.22 software (Nikon). Image and movie processing were performed with NIS-Elements HC 4.2. For rescue experiments, HeLa cells were plated on 28 mm glasses coated with fibronectin. Cells were transfected with either full length GFP-NuMA or GFP-NuMA-GoLoco. After 24h, cells were thymidine-synchronized and MLN8237-treated as described above. Live cell imaging was performed using a DeltaVision Elite imaging system (Applied Precision) driven by softWoRx software and equipped with a CoolSNAP HQ2 CCD camera (Photometrics) and an environmental chamber maintained at 37 °C in 5 % CO_2. Images were acquired using an Olympus 60x/1.42 Plan Apo N oil immersion objective for 16 hours every 5 minutes at 3 μm steps for a total thickness of 27 μm.

FRAP analysis
HeLa cells plated on 28 mm glasses coated with fibronectin were transfected with GFP-NuMA or mCherry-NuMA. After 24 hours, cells were synchronized with a single thymidine block and analyzed 8 hours after the release. To inhibit Aurora-A, 50 nM MLN8237 were added 5 hours after thymidine release. FRAP was performed on an UltraVIEW-VoX spinning-disk confocal system (PerkinElmer) equipped with an EclipseTi inverted microscope (Nikon) provided with a Nikon Perfect Focus System, an integrated FRAP PhotoKinesis unit (PerkinElmer), and a Hamamatsu CCD camera (C9100-50) and driven by Volocity software (Improvision; Perkin Elmer). All images were acquired through a 60× oil-immersion objective (Nikon Plan Apo VC, N.A. 1.4). GFP and mCherry signals were excited with a 488 nm and 561 nm 50 mW diode lasers, respectively. Photobleaching was performed on a 5 μm diameter circular region around one of the spindle poles. After defining the region of interest, to bleach the fluorescence the lasers were used at the maximum power for 30 cycles for GFP-NuMA, or 40 cycles for mCherry-NuMA. After bleaching, images were acquired every 2 seconds for 5 minutes. Analysis of the recovery curves was conducted using a custom macro in ImageJ. Briefly, the mean intensity value in the bleached area was measured, corrected for the background and for the acquisition photobleaching, and the curves were then normalized to the prebleaching mean intensity values. Recovery measurements were quantified by fitting normalized fluorescence intensities of bleached areas to a one-phase exponential association for GFP-NuMA by a custom-software of MatLab. Statistical analysis of the data was performed in Prism with the unpaired *t*-test.

Statistical analysis
Data were tested for normality using D'Agostino-Pearson omnibus normality test. For time-lapse and FRAP experiments, differences between means were tested by unpaired *t*-test for normal data, while non-normal data were analysed by Mann-Whitney test. For the contingency tables of Figure 4E the Fisher's exact test was applied. Spindle orientation analyses were performed by Mann-Whitney or Kruskal-Wallis test. GraphPad Prism 6.0 software was used. The criterion for statistical significance was set at $p < 0.05$.

Protein expression and purification
Fragments of human NuMA spanning residues 1821-2115, 1821-2001 and 2002-2115 were cloned into a pETM14 vector (Novagen) in frame with a hexa-histidine tag. After expression in BL21 Rosetta E. *coli* cells, all proteins were purified by nickel affinity and cation-exchange chromatography. For microtubule forming assays, the same NuMA fragments were cloned into a pGEX-6PI vector (GE Healthcare). GST-fusion proteins were purified on gluthatione beads (GSH, GE-Healthcare), eluted and dialyzed against 10 mM Hepes pH 7.5, 0.15 M NaCl, and 5 % glycerol before storage at -80 °C. The TPR domain of human LGN encompassing residues 1-409 (LGN^{TPR} in the text) was cloned in pGEX-6P1, and purified on GSH beads followed by GST-tag removal with PreScission protease.

***In vitro* kinase assays**
Kinase assays were carried out using 1 ng of the purified kinase domain of Aurora-A (generous gift of Prof. Richard Bayliss) incubated with 2 μM of the $NuMA^{Cter}$ fragments. The reagents were incubated for 30 minutes at 30° C in kinase buffer consisting of 20 mM Hepes pH 7.5, 5 mM $MgCl_2$, 0.2 M KCl, 0.5 mM EGTA, 2 mM DTT, 0.25 mM $NaVO_4$, and 1 mM ATP. To inhibit Aurora-A, 1 mM of MLN8237 was added to the reaction mix. For the phosphorylation time-course, kinase reactions were stopped at 7, 15, 30, or 60 minutes by addition of SDS-loading buffer. To discriminate the phospho-

proteins from their non phosphorylated counterparts, samples were separated by Phos-TAG SDS-PAGE (Wako Rure Chemical Industries,Ltd, AAL-107), and stained with Coomassie blue.

Microtubule co-sedimentation assays

Tubulin (Cytoskeleton Inc.) was polymerized into stable microtubules according to the producer's instructions, and microtubule cosedimentation assays were carried out as in Ciferri et al. [S2]. Briefly, for microtubule-binding reactions, microtubules were diluted to a final concentration of 9 μM in general tubulin (GT) buffer (80 mM PIPES pH 6.8, 1 mM $MgCl_2$, 1 mM EGTA) supplemented with 1 mM GTP, 50 μM Paclitaxel, and 60 mM NaCl. 1 μM $NuMA^{Cter}$ fragments were added to a final volume of 50 μl. Reactions were incubated at room temperature for 15 minutes, transferred onto 100 μl of cushion buffer (80 mM PIPES pH 6.8, 1 mM $MgCl_2$, 1 mM EGTA, 50 μM Paclitaxel, 50 % glycerol), and ultracentrifuged for 15 minutes at 400,000 g at 25 °C. To monitor phosphorylated species cosedimenting with microtubules (Figure 5A), samples were loaded on a Phos-TAG SDS-PAGE. To assess whether NuMA could associate simultanelously with microtubules and with LGN, the cosedimentation assays were repeated in the presence of 1 μM LGN^{TPR}.

To perform microtubule cosedimentation experiments with cell extracts, HeLa cells stably expressing mCherry-$NuMA^{Cter}$ and synchronized with STLC in prometaphase, with or without MLN8237, as described above, were lysed in JS buffer (75 mM Hepes pH 7.5, 1.5 mM EGTA, 1.5 mM $MgCl_2$, 0.15 M KCl, 0.1 % NP40, 15 % glycerol) supplemented with protease and phosphatase inhibitors. Cleared lysates were subjected to ultracentrifugation at 400,000 *g* at 25 °C for 15 minutes with microtubules previously polymerized.

In *vitro* microtubule forming assay

Microtubule forming assays were performed according to Du et al. [S3]. Briefly, rhodamine-labeled and unlabeled tubulin were mixed at a 1:10 ratio at a concentration of 36 μM with GT buffer supplemented with 1 mM GTP, and incubated with 25 μM GST-$NuMA^{Cter}$ fragments. 5 μl of the reactions were kept at 37 °C for 4 minutes, and later fixed for 3 minutes at room temperature with 45 μl GT complemented with 1% glutaraldehyde. Fixed samples were diluted to 200 μl with GT buffer containing 50 % glycerol, spotted onto poly-lysine slides, and visualized by widefield microscopy using a 60x oil immersion objective.

GST pull-down

For pull-down assays, 1μM of GST-LGN^{TPR} was immobilized on GSH-beads, and incubated for 1 hour on ice with 2 μM $NuMA^{Cter}$ wild-type, carrying the 3Asp mutation, or phosphorylated by Aurora-A in a buffer consisting of 10 mM Hepes pH 7.5, 0.15 M NaCl, 5 % glycerol, 0.1 % Tween 20. After washes, proteins bound to beads were separated by SDS-PAGE, and detected by Coomassie staining.

Immunoblotting

For immunoblots of Figure 1 and Figure S3A, mitotic cells collected by shake off were lysed in RIPA buffer (50nM Tris-HCl pH 8.0, 150 nM NaCl, 1 % NP40, 1mM EGTA, 0.25 % sodium deoxycholate), with protease and phosphatase inhibitors. 50 μg of extracts were resolved by electrophoresis, and transferred on a nitrocellulose membrane. Blocking and antibody incubations were performed at room temperature in TBS containing 0.1 % Tween 20 and 1 % low fat milk, or in TBS containing 0.1 % Tween 20 and 5 % BSA for anti-phospho-Aurora-A hybridization. The antibodies used are: mouse anti-Aurora-A (1:250 BD Transduction Laboratories), rabbit anti-phospho-Aurora-A (Thr288) (1:500; C39D8; Cell Signaling Technology), goat α-actin (0.4 μg/ml, I-19; SantaCruz Biotechnology). The mouse monoclonal anti-NuMA antibody was used at a dilution of 1:200, and the anti-α-tubulin at 1:1500 (Abcam ab4074).

Supplemental References

S1. Schindelin, J., Arganda-Carreras, I., Frise, E., Kaynig, V., Longair, M., Pietzsch, T., Preibisch, S., Rueden, C., Saalfeld, S., Schmid, B., et al. (2012). Fiji: an open-source platform for biological-image analysis. Nat Methods *9*, 676-682.

S2. Ciferri, C., Pasqualato, S., Screpanti, E., Varetti, G., Santaguida, S., Dos Reis, G., Maiolica, A., Polka, J., De Luca, J.G., De Wulf, P., et al. (2008). Implications for kinetochore-microtubule attachment from the structure of an engineered Ndc80 complex. Cell *133*, 427-439.

S3. Du, Q., Taylor, L., Compton, D.A., and Macara, I.G. (2002). LGN blocks the ability of NuMA to bind and stabilize microtubules. A mechanism for mitotic spindle assembly regulation. Curr Biol *12*, 1928-1933.

ACKNOWLEDGEMENTS

First of all, I would like to thank all the members of my group Sara, Laura, Vale, Smari and Cristina for their help, their collaboration and their support throughout these four years. Each one of you has contributed to make every single day much easier and funny. You are amazing group mates!

I am grateful to my boss Marina that, with her enthusiasm and determination, has been a great mentor for my PhD studies. I also thank her for giving me the opportunity to join her group, to work on these exciting projects, and for encouraging me every time I needed.

My thanks also go to the previous members of our lab, especially to Simone, which taught me everything at the very beginning, and to Andrea. The members of the IEO crystallography unit Silvia, Valentina and Sebastiano have also been of support to my studies. Also, I thank Sebastiano and Fabrizio for introducing me to X-ray crystallography.

Finally, I would like to thank my internal supervisor Prof. Giorgio Scita, and my external PhD supervisor Prof. Neil Q McDonald. A special mention goes to Dr. Paolo Maiuri and to Prof. Carien Niessen for agreeing to serve as my PhD examiners.